Numerical Study of Some Fluid Flow Problems by B-Spline Differential Quadrature Method

Thesis Submitted for the Award of the Degree of

DOCTOR OF PHILOSOPHY

in

Mathematics

By

Rajesh Kumar Chandrawat

41800037

Supervised By

Dr. Varun Joshi

LOVELY PROFESSIONAL UNIVERSITY
PUNJAB
2022

Declaration of Authorship

I, Rajesh Kumar Chandrawat, declare that this thesis titled, 'Numerical Study of Some Fluid Flow Problems by B-Spline Differential Quadrature Method Basis Functions' and the work presented in it are my own. I confirm that:

- This work was done wholly or mainly while in candidature for a research degree at this University.
- Where any part of this thesis has previously been submitted for a degree or any other qualification at this University or any other institution, this has been clearly stated.
- Where I have consulted the published work of others, this is always clearly attributed.
- Where I have quoted from the work of others, the source is always given. Except for such quotations, this thesis is entirely my work.
- I have acknowledged all primary sources of help.
- The thesis is based on my work and jointly with others, and I have clarified exactly what others did and what I have contributed to myself.

Signed: 

Date: 02/03/2022

Certificate

The thesis titled **"Numerical Study of Some Fluid Flow Problems by B-Spline Differential Quadrature Method Basis Functions"** submitted by **Mr. Rajesh Kumar Chandrawat** for the award of the degree of Doctor of Philosophy has been carried out under my supervision at the Department of Mathematics, Lovely Professional University, Punjab, India. The matter presented in this thesis is original and has not been submitted to any other University or institute to award any degree or diploma. The work is comprehensive, complete, and fit for evaluation.

Dr. Varun Joshi

Assistant Professor,

Department of Mathematics,

Lovely Professional University,

Punjab, India.

Acknowledgments

First of all, I would like to thank the Almighty for granting perseverance. I want to express my gratitude to my esteemed supervisor – Dr. Varun Joshi, Assistant Professor, Department of Mathematics, Lovely Professional University, Phagwara, for his patience, guidance, and support throughout this work. I was honestly very fortunate to have the opportunity to work with him as a student, and it was both an honor and a privilege to work with him.

I take this opportunity to express my sincere thanks to Dr. Amit Singh, and Dr. Ramesh Katta, Department of Mathematics Symbiosis University Pune, Dr. Osman Beg University of Salford United Kingdom, Dr. Dharmendra Tripathi NIT Uttarakhand for their valuable support and help without which it would not have been possible for me to complete this work.

I do not find enough words with which I can express my feeling of thanks to my friends Dr. Varun Kumar, Dr. Kulwinder Singh, Dr. Gurpreet Singh, Dr. Deepak Kumar, Dr. Ratesh, Dr. Pankaj, and Dr. Vikas Sharma Department of Mathematics, Lovely Professional University, Phagwara, for their help, inspiration, and moral support, and belief in me which went a long way in the successful completion of my work.

I would like to express my sincere gratitude to Mr. Varun Kumra Lovely Professional University and his team for providing the help in technical writing and presentation style, and I found this guidance to be extremely valuable.

I thank all those who have contributed directly or indirectly to this work. Lastly, and more importantly, I would like to thank my family for their years of unyielding love and encouragement. They have always wanted the best for me, and I admire my parent's and wife's determination and sacrifice to put me through my Ph.D.

List of Figures

List of tables

Contents

Abstract

Immiscible fluid regimes are essential for multi-component hydrodynamics in nature and industry, including lubrication and coating processes, oil and gas extraction in a petroleum reservoir, biofluids rheology, physicochemical separation techniques, water, and steam tapping in a geothermal reservoir, and sediment transportation. Such flows typically contain interfacial conditions and are characterized by mass (species) diffusion. Motivated by applications in viscous magnetohydrodynamic duct flow processing, biological fluid flow modelling, and non-Newtonian multiphase flow processing, in the present thesis, the comprehensive mathematical model and computational simulation with the modified cubic B-spline-Differential Quadrature method (MCB-DQM) is described for the unsteady flow of some immiscible fluids.

Different combinations of immiscible liquids, i.e., Newtonian and Eringen micropolar, Eringen micropolar and Saffman dusty (fluid-particle suspension), Saffman dusty and non-dusty, micropolar and micropolar-dusty, are considered through horizontal channels with stable and moving interface schemes. Three applied pressure gradients are studied for constrained values of the control parameters: constant, periodic, and decaying. The coupled partial differential equations for each scheme flow are formulated and numerically solved under physically realistic boundary conditions using the modified cubic B-spline-Differential Quadrature method (MCB-DQM). According to the particular scheme flow, microrotation (angular velocity) of Eringen liquid, fluids and particle-phase velocities, fluids and particle-phase temperatures, interface evolution between immiscible fluids are visualized graphically for the effects of the critical hydrodynamic, magnetic, thermal, and solute parameters.

The thesis is organized into 7 chapters. Chapter 1 is introductory and contains the basic definitions relevant to the immiscible fluid flow problems, governing mathematical equations, a brief literature survey, the research gap, and the objective of the research.

Furthermore, the research methodology modified cubic B-spline-differential quadrature method (MCB-DQM) is also present in this chapter.

In Chapter 2, the unsteady laminar flow of two immiscible fluids, namely Eringen micropolar and Newtonian liquids, is taken in a horizontal channel with stable and moving interface schemes. Each scheme flow is driven by a constant, periodic, and decreasing pressure gradient, and the numerical solutions are obtained using the modified cubic B-spline-differential quadrature technique (MCB-DQM). The effects of essential fluid parameters, such as Reynolds number, viscosity ratio, pressure gradients, micro-polarity parameter, and time on fluid velocities and micro rotation, are depicted using the stable interface scheme. The advection and tracking of the interface with time, wave number, Micropolar parameter, various pressure gradients, and amplitude for the moving interface scheme.

In Chapter 3, a detailed mathematical model and computation using the modified cubic B-spine-Differential Quadrature method (MCB-DQM) for the unsteady flow of two immiscible fluids- dusty (fluid-particle suspension) and Eringen micropolar fluids- through horizontal channels with two separate schemes are described: first through nonporous plates with the stable interface, second through nonporous plates with interface evolution. Particle concentration effects in the dusty fluid cause mass transfer to occur. The stable liquid-liquid interface between two immiscible fluids is studied for the first scheme. In the second scheme, it is considered that the interface moves from one location to another, which may be severely distorted; hence, the volume of fluid (VOF) technique is coupled with the continuous surface approach model, and an interface tracking is proposed. Linear velocity, micro-rotation (Eringen angular velocity), and interface evolution are visualized graphically for the effects of the critical hydrodynamic parameters, i. e., Reynolds number, Froude number, the particle concentration parameter, Eringen micropolar material parameter, volume fraction parameter, pressure gradient, time, viscosity ratio, and density ratio.

Chapter 4 includes the generalized Couette flow of two immiscible Saffman dusty (fluid-particle suspension) and pure (non-dusty) fluids through the horizontal duct with heat transfer. The heat transfer, mass transfer, and interface tracking analysis are

numerically proposed using MCB-DQM. The flow is explored under three separate geometries: first for nonporous plates with the stable interface, second for porous plates with the sight of suction and injection, and third for nonporous plates with interface evolution—the effects of emerging thermo-fluid parameters, i. e. Eckert (dissipation), Reynolds, Prandtl, and Froude numbers, particle concentration parameter, volume fraction parameter, pressure gradient, time, and the ratio of viscosities, densities, thermal conductivities, and specific heats on velocity and temperature characteristics are illustrated through graphs. A detailed appraisal of the physics is included. Validation is also conducted through skin friction coefficient and Nusselt number.

Chapter 5 aims to investigate the effects of Ion slip, Viscous dissipation, Joule heating, and Hall current on time-dependent plain and genialized Couette flow of two immiscible fluids. In the horizontal duct with heat transmission, two non-Newtonian incompressible magnetohydrodynamic fluids are considered: micropolar and dusty (fluid-particle suspension). The coupled partial differential equations for fluids and particle phases are developed, and the velocities, temperatures, and microrotation profiles are determined using MCB-DQM. The influence of the magnetic, thermal, and other pertinent parameters, i. e. Hartman, Eckert (dissipation), Reynolds, and Prandtl numbers, micropolar, Hall, ion-slip, and particle concentration parameter, the ratio of viscosities, densities, and time on velocity, microrotation, and temperature characteristics are illustrated through graphs. The skin friction coefficient and Nusselt number are computed, and the accuracy of MCB-DQM is also explored with a limiting case.

Chapter 6 includes a mathematical and computational study of the unsteady two-dimensional flow of electrically conducting immiscible dusty and non-dusty fluids with interface evolution (moving) through a horizontal channel. Hall current and ion slip effects are incorporated in the model as they feature novel ionic working fluid regimes in chemical and nuclear engineering, for example. The Saffman two-phase model is deployed for the dusty fluid, and the Newtonian model is used for the non-dusty liquid. The fluid-fluid interface is expected to be chaotic and distorted from one location to the next; hence, a single momentum equation is coupled for evaluating the interface profiles

using the VOF (Volume of fluid) approach. The enhanced B-spline differential quadrature method solves the modelled coupled-partial differential equations with appropriate boundary conditions. The impact of magnetic (Hartmann) number, Hall and ion slip numbers, Froude number, capillary number, wave number, Reynolds number, amplitude, viscosity ratio, and time on the interface profile is computed and visualized.

In Chapter 7, the thesis concludes with a broad summary and findings for the whole research and a brief remark on future work scope.

Chapter 1 Introduction

A fluid is a substance that continually flows or deforms when it is subjected to shear stress or external force. The flow model can monitor the conduct of fluids such as liquids, gases, and natural and industrial fluids in various states, whether at rest or in operation. Determining forces and moments on jets, measuring the volume flow rate of petroleum via tubes, forecasting weather trends, and modelling fission bomb explosions are some of the uses of hydrodynamics. Fluid flow modelling is used to render and control complex multi-dimensional fluid flows. The natural and industrial fluid systems like atmospheric gas dispersion, oil and gas industry, piston pump, leak rapture, and spill-related fire analysis can be predicted and estimated using these models. In general, fluid flow analysis of any system has been traditionally divided into two parts; experimental and modelling and simulation. Compared to experimental analysis, simulations give a detailed study at a lesser cost and time. Numerical methods can be used to demonstrate the eventual real effects of specific experiments.

As a result, computational fluid dynamics is employed in a wide range of industrial applications involving fluid flow, such as automotive, aerospace, power generation, and so on. It is helpful for the design and optimization of wind tunnel models, nozzle flow application, smoke propagation assessment, development of the biomedical device, and development of the electronic, microelectronic, and microfluidic devices. Flow patterns for turbo-machinery and air-jet weaving machines can be analyzed by fluid flow modelling. The motion of a fluid is subjected to fluid properties, including velocity, density, flow geometry, space, time, and unbalanced forces. In fluid mechanics, the diagnostic approach differs based on the type of flow pattern.

1.1 Types of Fluid flow

The numerous factors are involved in distinct ways as the flow passes through a point, a path, or a channel. The fluid flow can be classified based on time, space, flow pattern, and geometry. The following Figure 1.1 depicts the different types of fluid flow.

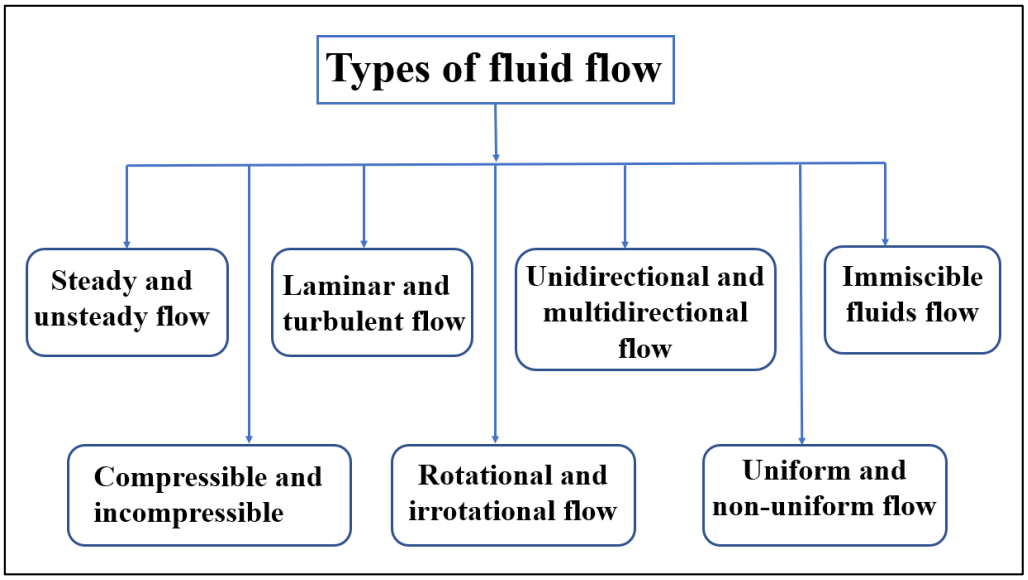

Figure 1.1: Types of the fluid flow

1.1.1 Steady and unsteady flow

The flow is said to be steady if the fluid parameters, such as velocity and pressure, do not change with time, while the flow is described as unsteady if the fluid characteristics depend on time.

1.1.2 Laminar and turbulent flow

The fluid flow in which fluid particles follow a smooth pathway to move in distinct fluid layers and do not merge macroscopically is called laminar flow. We can forecast the streaming trend at any point in time. In the laminar flow, all successive layers are parallel to one another. The fluid flow in which fluid particles follow an irregular pathway to move and merge in distinct parallel fluid layers is known as turbulent flow.

1.1.3 Immiscible fluids flow

Immiscible fluids are the compositions of two or more liquids that do not mix and do not dissolve. They're the liquids that don't mix in the same way at particular proportions, and within the subsurface, immiscible fluids travel in discrete phases. Kerosene and water, water and steam in a geothermal reservoir, and corn syrup and vegetable oil are some common examples of instances of immiscible fluid flow.

1.1.4 Unidirectional and multidirectional flow

Unidirectional and multidirectional flow relates to the number of spatial coordinates needed to describe a flow. In a uniform flow, fluid characteristics such as velocity are a function of time and a single spatial coordinate, but in a multidirectional flow, fluid parameters are a function of time and two or more spatial coordinates.

1.1.5 Compressible and incompressible flow

The compressible flow consists of compressible fluid whose density varies from one point to other. The density of fluid flow is constant in incompressible flow, and gases are compressible, but liquids are often incompressible.

1.1.6 Rotational and irrotational flow

The form of flow wherein the fluid particles spin on their own axes while traveling along the streamlines is known as rotational flow when fluid particles travel along streamlines and do not spin around their axis, which is known as irrotational flow.

1.1.7 Uniform and non-uniform flow

The fluid flow is uniform if the flow characteristics stay similar with distance along the flow route. And if the flow characteristics change and are different at different places along the flow channel, the flow pattern is non-uniform. The cross-section area should stay unchanged for a uniform flow. A liquid's passage via a tube with a constant

diameter is an example of uniform flow, and the flow via a tube with varying diameters would be non-uniform.

1.2 Types of Fluids

Fluids are categorized according to how they behave when the property of viscosity and density changes. Viscosity acts as a frictional force in fluid particles, resisting them to move, and it opposes fluid flow and causes relative motion between fluid layers underneath it. The following Figure 1.2 shows a detailed description of different types of fluids based on viscosity and compressibility:

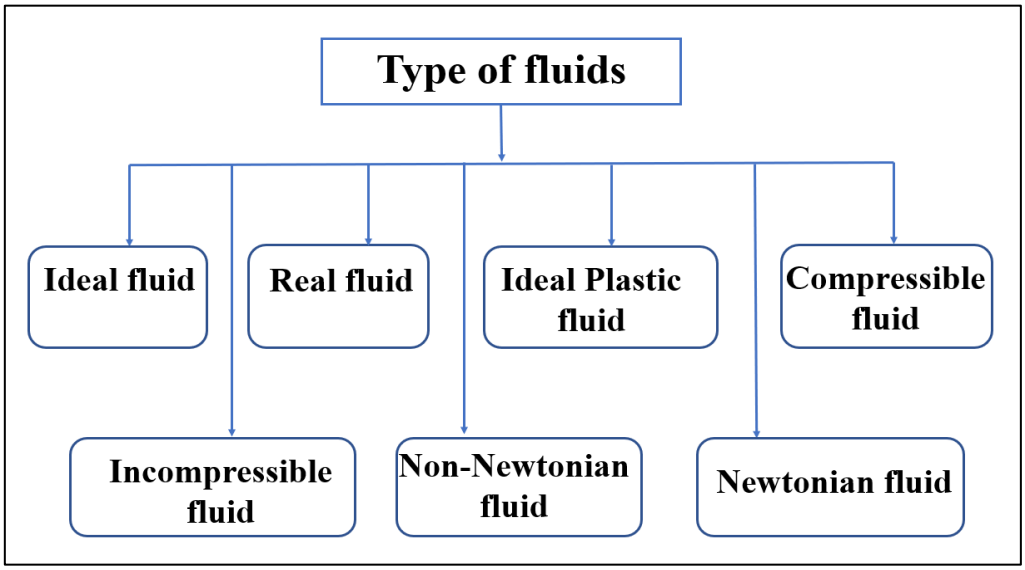

Figure 1.2: Type of the fluids

1.2.1 Ideal and Real fluid

The fluids in which viscosity is non-zero are called viscous or real fluid. Viscous fluid provides resistance to fluid flow and possesses a high viscosity level, for example, Honey, milk, and petrol. The incompressible fluids with zero viscosity(frictionless) are

said to be non-viscous or ideal fluids. Because all fluids possess certain viscosity, there is no ideal fluid in reality.

1.2.2 Ideal plastic fluid

Ideal plastic fluid is a fluid with shear stress more significant than the yield stress and shear stress proportionate to the velocity gradient, for example, water suspension of clay.

1.2.3 Compressible and incompressible fluids

Compressibility is a term used to describe a fluid's ability to be compressed. If the density of fluid changes with time and space, it is said to be compressible fluid, and if the density is constant, then the fluid is known to be incompressible. In this scenario, the viscosity might be either zero or non-zero. Liquids such as water, honey, milk, oil, etc., are examples of incompressible fluids, while gases like liquid petroleum and oxygen are compressible fluids.

1.2.4 Newtonian Fluid

Newtonian fluids have contributed significantly to fluid dynamics of Turbulence and multiphase motions over the last two centuries. Isaac Newton did some pioneering work for liquids, among many other discoveries, and he observed that most fluids have only a temperature effect on viscosity. Viscosity is the quantity that characterizes a fluid’s resistance to flow. A substantial viscous liquid withstands the friction, and a low viscosity fluid moves quickly. Highly viscous substances, such as sugar, syrup, and honey, require more time to pour than less vicious, such as milk. Although the cream may be heavier than milk, it is generally less concentrated and less dense, as cream floats on top of milk. Many small molecular compounds such as polymeric solutions, non-molecular acid, molten metal solutions, salts, etc., manifested that the shear stress is proportional to the shear rate at a constant temperature, pressure, and the viscosity is

such a constant of proportionality. These fluids are generally referred to as Newtonian fluids.

The Mathematical expression for Newton's law of viscosity is defined as follows:

$$\tau_s = \mu_n \frac{du_n}{\partial y}. \tag{1.1}$$

Here $\frac{du_n}{\partial y}$ is the velocity gradient of Newtonian fluid velocity u_n in *y-axis* direction and μ_n is the viscosity of the Newtonian fluid. τ_s is the shear stress.

The governing equation of mass and heat transfer for Newtonian fluid with density (ρ_n) and viscosity (μ_n) can be seen in [1]–[4] as follows:

The continuity equation:

$$\frac{\partial \rho_n}{\partial t} + \nabla.(\rho_n \overrightarrow{u_n}) = 0. \tag{1.2}$$

For incompressible Newtonian fluid flow, $(\nabla.\overrightarrow{u_n} = 0)$.

The mass transfer equation:

$$\rho_n \left(\frac{\partial \overrightarrow{u_n}}{\partial t} + (\overrightarrow{u_n}.\nabla)\overrightarrow{u_n} \right) = -\nabla p + \mu_n \nabla^2 \overrightarrow{u_n} + \overrightarrow{f_b}. \tag{1.3}$$

Here ∇p is the pressure term. $\overrightarrow{f_b}$ is the body forces acting on the whole fluid mass, which may include gravitational, electrical, drag, and magnetic force.

The heat transfer equation:

$$\rho_n c_n \left(\frac{\partial T_n}{\partial t} + (\overrightarrow{u_n}.\nabla)T_n \right) = \kappa_n \nabla^2 T + \mu_n \Phi. \tag{1.4}$$

Here c_n, κ_n are the specific heat capacity and thermal conductivity of the Newtonian fluid. Φ is the viscous dissipation term with u_n, v_n, w_n components of the Newtonian fluid velocity vector $\overrightarrow{u_n}$ in the direction of *x*, *y*, and *z*, respectively, as follows.

$$\Phi = 2\left[\left(\frac{\partial u_n}{\partial x}\right)^2 + \left(\frac{\partial v_n}{\partial x}\right)^2 + \left(\frac{\partial w_n}{\partial x}\right)^2\right] + \left[\begin{matrix}\left(\frac{\partial u_n}{\partial y} + \frac{\partial v_n}{\partial x}\right)^2 + \left(\frac{\partial v_n}{\partial z} + \frac{\partial w_n}{\partial y}\right)^2 \\ + \left(\frac{\partial w_n}{\partial x} + \frac{\partial u_n}{\partial z}\right)^2\end{matrix}\right]. \quad (1.5)$$

1.2.5 Non-Newtonian Fluid

Several fluids differ significantly from Newton's law of viscosity. Such fluids are classified as non-Newtonian fluids, and non-Newtonian fluid is characterized by a nonlinear relationship between shear stress and strain rate. Non-Newtonian fluids include sperm, intrauterine fluids, tar, resins, heavy oils, blood, slurries, lubricants, and chyme. One of the imperative types of non-Newtonian liquids is the micropolar liquid which grabbed the interest of the scientists to the enhancement of a few theories in this area.

1.3 Micropolar fluid

The flow propensity of most physiological fluids with various physical structures is not sufficiently analyzed by the Navier Stokes equation alone. In this aspect, some researchers have related physiological or bio-fluid behavior to non-Newtonian models of fluids.

Eringen [5] sought a non-Newtonian model of micropolar fluids to analyze the continuum with a suspension nature, a collection of organized particles comprising mass and velocity, and a substructure. In such fluids, the material volume element includes a microvolume element that can rotate and translate regardless of the macro volume movement. This model incorporates two independent kinematic vector fields-one representing the translation velocities of fluid particles and the other representing the particles' angular (spin) velocities, called microrotation vectors. Micropolar fluids are found in engineering science. They have an extensive spectrum of functionalities in short waves for heat-conducting fluids, lubrication analysis, multi-component media hydrodynamics, and flow separation principle. Micropolar fluids include

microelements with spin characteristics along their axis. Human blood and plasma, anisotropic fluids, and polymer solutions are common micropolar fluid examples.

According to Eringen [6], micropolar fluids are a particular class of microfluidics that exhibit micro-rotational stiffness and effects. This form of fluid is anisotropic fluid nanocrystals made up of dumbbell molecules. Studies of micropolar fluids have recently received considerable attention due to their applications in several processes that occur in the industry. Such applications include suspension solutions, solidifying liquid crystals, animal blood, and exotic lubricants. Therefore, the micropolar fluid theory offers a precise fluid model that involves polymers and spinning particles by including the micro rotational momentum equation and the classical momentum equation.

Devakar and Raje [2] presented the unsteady MHD flow of immiscible micropolar and Newtonian fluids inside the parallel plate and found the effect of numerous fluid parameters on flow velocity and temperature profile. Chen *et al*. [7] evaluated the overall impact of heat radiation on micropolar fluid flow across a bendy surface. The optically thick limit approach is used for the radiation flow, and a modified variant of the heat transfer equation is constructed. Aski *et al*. [8] studied injective micropolar flow in a permeable duct and used suction and injection to control the flow. Pandey and Tripathi [9] aimed to simulate an unstable peristaltic flow of micropolar liquid in a finite length duct. Abbas *et al*. [10] studied a continuous two-dimensional micropolar dynamic and modified a micropolar fluid that arises at an orthogonal stagnation point. The significance of micropolar fluid boundary layer motion and heat exchange over an increasingly porous sheet was reviewed by Aurangzaib *et al*. [11]. Rashidi *et al.* [12] analyzed a detailed investigation of the 2-D stationary flow of the heat transmission properties for an incompressible micropolar fluid towards a heated shrinking surface. They found an effective technique for analytic solutions named Homotopic analysis for velocity and temperature distributions and to investigate the constantly mixed convection of a micropolar fluid in 2-D stationary flows around a vertically diminishing sheet. Before that, Srinivasa and Shiferaw [13] also used the Homotopic analysis method to compute the effects of cross-diffusion on micropolar convection flow in a

channel, and then Jangili *et al.* [14] too used a homotopy method to compute the entropy generate rate in hydromagnetic micropolar buoyancy-driven flow in solar ducts. Mekheimer and Kot [15] analyzed the stenotic hemodynamic flow of micropolar fluids with applications in diseased tapered arteries. Wang *et al*. [16] examined the motion of micropolar fluids into a micro parallel system with applications in industrial flow separation in chemical engineering systems. The analytical study of the flow provided by a transparent sphere rotating slowly and steadily in an incompressible micropolar fluid is investigated by P. Aparna *et al.* [17]. The solutions for energy and concentration equations, angular momentum, and governing momentum have been investigated. Rao *et al*. [18] have worked on an incompressible micropolar fluid and the problem of longitudinal fluctuations of a circular cylinder along its axis of symmetry in an isotropic micropolar fluid. Wang *et al*. [19] implemented the micropolar fluid flow into a microchannel using the user-defined function and then examined the mass transfer analysis. Bég *et al.* [20] considered the micropolar fluid in the inclined channel investigated the linear momentum and angular momentum of micropolar flow with hydromagnetic source effects.Saad and Faltas [21] derived the thermophoretic velocity and torque for semi-infinite micropolar fluid with Fourier thermal conductivities. Mehryan *et al.* [22] investigated natural convection inside a porous embedded channel filled with micropolar nanofluid. Kumar and Chawla [23] have studied the effect of Mass and Heat transfer for a two-dimensional micropolar fluid flow that oscillates through a porous infinitely moving plate in the presence of a transverse magnetic field in a porous media. The analysis of hybrid nanoparticle suspension in micropolar fluids has been assessed comprehensively by Ghadikolaei *et al.* [24]–[26]. Kaneez *et al.* [27] exhibits the major aspect of micro-structured and dust particles in viscoelastic micropolar fluid with heat energy transportation.

MHD (magnetohydrodynamics) is the behavioural analysis of electrically conducting fluids such as plasmas, electrolytes, and liquid metals. The magnetic force affects a micropolar fluid's angular and translation momentum. There has been a need to

simulate a magnetohydrodynamics flow employing micro-elements that can spin asymmetrically inside the fluid over the past two decades.

Many excellent studies of theoretical magnetofluid dynamics in channels have been reported utilizing various numerical methods and featuring multiple phenomena, including mass and heat transfer. Cowley [28] identified that the essential parameters arising in viscous hydromagnetic (MHD) flows are the Hartmann number (ratio of Lorentz force to viscous force) and the magnetic interaction parameter ratio of Lorentz force to inertial body force). Under the MHD effect, heat transfer and flow with variable viscosity inside a duct containing micropolar fluid have been investigated by Javed and Siddiqui [29]. Tetbirt *et al.* [30] presented a numerical investigation of the magneto-hydrodynamic flow of micropolar and viscous fluids in a vertical duct. Nabwey and Mahdy [31] extensively studied the transient MHD boundary layer flow micropolar hybrid nanofluid. Ahmad and Nadeem [32] investigated the micropolar fluid with dust and hybrid nanoparticles suspension and enhanced the heat transfer effect. The analysis of nanotube suspension in MHD micropolar dusty fluid has been reported by Eid and Mabood [33]. Makinde *et al.* [34] described a numerical analysis for MHD melting micropolar fluid in heat control processing systems. Soundalgekar and Aranake [35] investigated the MHD Couette flow of an electrically conducting, viscous incompressible non-Newtonian polar (couple stress) fluid. They derived closed-form solutions for the velocity, current density, and the skin-friction at the lower duct wall. They evaluated the force required to move the upper plate and the coefficient of mass flux for several scenarios. The MHD effect on micropolar nanofluid is studied by Hsiao [36]. The blood flow with floating magnetic Zinc-oxide nanoparticles in the arteries is analyzed by Zhang *et al.* [37]. The impact of applied transversely uniform magnetic field on unsteady MHD micropolar fluid flow with heat distribution in channels was addressed by Ashraf *et al*. [38]. Further studies of micropolar fluid dynamics include non-isothermal Hall hydromagnetic channel flow by Bég *et al*. [39], reactive oscillating micropolar thermo-solutal channel in Shamshuddin *et al.* [40] flow and on ion-slip micropolar gas dynamics in a rectangular duct Bég *et al.* [41].

1.3.1 Governing equations of micropolar fluid

Let ρ_m is the density coefficient, μ_m is the viscosity coefficient of micropolar fluid, which possesses the linear velocity vector $\overrightarrow{u_m}$, the angular velocity vector $\vec{M}$. Micropolar fluid flow field equations are given following Eringen [5] and Lukaszewicz [42].

The continuity equation:

$$\frac{\partial \rho_m}{\partial t} + \nabla.(\rho_m \overrightarrow{u_m}) = 0. \tag{1.6}$$

For incompressible Newtonian fluid flow, $(\nabla.\overrightarrow{u_m} = 0)$.

The translation momentum equation:

$$\rho_m \left(\frac{\partial \overrightarrow{u_m}}{\partial t} + \nabla \left(\frac{\overrightarrow{u_m}^2}{2} \right) - \overrightarrow{u_m} \times (\nabla \times \overrightarrow{u_m}) \right) = \begin{bmatrix} \rho_m \overrightarrow{f_b} - \nabla p + \kappa_m \nabla \times \vec{M} - \\ (\mu_m + \kappa_m) \nabla \times \nabla \times \overrightarrow{u_m} + \\ (\gamma_1 + 2\mu_m + \kappa_m) \nabla (\nabla.\overrightarrow{u_m}) \end{bmatrix}. \tag{1.7}$$

Here body force per unit mass is $\overrightarrow{f_b}$, the fluid pressure at any point is p, vortex viscosity is κ_m, $\gamma_1$is the second viscosity.

The angular momentum equation:

$$\rho_m \tau \left(\frac{\partial \vec{M}}{\partial t} - (\overrightarrow{u_m}.\nabla)\vec{M} \right) = \begin{bmatrix} (\alpha_m + \beta_m + \omega_m) \nabla (\nabla.\vec{M}) \\ -\omega_m \nabla \times \nabla \times \vec{M} - 2\kappa_m \vec{M} \\ +\kappa_m \nabla \times \overrightarrow{u_m} + \rho_m \overrightarrow{f_b} \end{bmatrix}. \tag{1.8}$$

Here τ is the gyration parameter, The constants $\alpha_m, \beta_m,$ and ω_m are the are gyro-viscosity coefficients.

The equation of heat transfer:

$$\rho_m C_m \left(\frac{\partial \overrightarrow{T_m}}{\partial t} - (\overrightarrow{u_m}.\nabla)\overrightarrow{T_m} \right) = \begin{bmatrix} -p(\nabla.\overrightarrow{u_m}) + \nabla.\left(K_m \nabla \overrightarrow{T_m}\right) + \gamma_1 (\nabla.\overrightarrow{u_m})^2 + \\ \alpha_m \left(\nabla.\vec{M}\right)^2 + 4\kappa_m \left(\frac{1}{2}\nabla \times \overrightarrow{u_m} - \vec{M}\right)^2 + \\ 2\mu_m (D:D) + \omega_m \left(\nabla\vec{M}:\nabla\vec{M}\right) + \beta_m \left(\nabla\vec{M}:\nabla\vec{M}^T\right) \end{bmatrix}. \quad (1.9)$$

Here C_m is specific heat capacity, K_m is the thermal conductivity of micropolar fluid. $\overrightarrow{T_m}$ is the temperature of the fluid, D is the deformation tensor.

The heat transfer capacity of both Newtonian and non-Newtonian fluids largely depends on their thermal conductivities. However, in order to increase the thermal conductivity of such fluids, micro-sized crystals (dust particles) must be integrated into the particular fluid. It can be used for combustion, crude oil filtering, and electrostatic precipitation.

1.4 Dusty fluid

In many industrial problems, like splitting of the matter mostly from a fluid, oil and gas industry, petroleum filtration, polymer technology, transportation procedures, sometimes the pure form of fluid is hardly accessible. Similarly, some fluids include impurities such as dust particles and external entities, and these types of fluids are known as dusty fluids. Dusty flows or fluid-particle suspension dynamics have been of interest to engineers for many decades. These flows generally feature a homogenous liquid (velocity phase) carrying small dust particles (solid phase) and are also an example of a two-phase system. They arise in aerodynamics [43], chemical engineering fluidized beds [44], spinning bioreactors [45], liquid metal processing, [46], nozzle systems in propulsion [47], cosmical hydrodynamics [48], and solid oxide fuel cells (SOFCs) [49].

Early work on modelling dusty fluids for the Newtonian case was reported by Saffman [50], who proposed a dusty fluid framework taking into consideration the impact of suspended particles on laminar flow stability. Marble [51] later generalized Saffman's analysis and provided a broader perspective of dusty flows deriving boundary value problems in which the dusty particles (of small volume fraction) do not interact with

the momentum, heat, and mass transfer in such media. Marble's approach also popularized the use of momentum inverse Stokes number, particle loading parameter, and temperature inverse Stokes number, which have become the basis for many subsequent dimensionless mathematical flow models. Dusty flows have also been explored in atmospheric fluid mechanics, notably foggy suspensions [52] and debris-laden tornados (swirling cone models) [53]. A number of boundary layers and fully developed flow configurations have also been studied in dusty (fluid–particle) suspension flows. Allaham and Peddieson [54] used a finite difference technique to compute the fluid (Newtonian), and particle-phase velocity components in swirling Von Karman flow noted the particle phase viscosity and solid surface boundary conditions impact considerably on the dynamics. Manuilovich [55] investigated the transient flow of a dilute gas-particle dusty mixture in a plane channel under the action of a constant longitudinal pressure gradient and transverse gravity force, with asymptotic and numerical methods for the cases of both monodisperse and polydisperse particles. Bilal *et al*. [56] studied the viscoelastic dusty fluid-free convective hydromagnetic Couette flow in a rotating frame using a Poincare-Light Hill Technique. They computed the particle and fluid phase velocities and derived expressions for skin friction, and the Nusselt number (the rate of heat transfer) are also calculated. It was observed that stronger rotation decelerates both dust particle phase and fluid phase velocities. Osiptsov [57] used Van Dyke's matched asymptotic expansion method to compute the dusty laminar boundary layer flow from both plane and curved surfaces, scrutinizing the impact of particle accumulation in the boundary layers and the effects of particles on the friction and heat fluxes. Debnath and Ghosh [58] considered dusty fluids' oscillatory hydromagnetic channel flow and computed the mass transfer for the fluid and particle phase. Dey [59] analyzed the non-Newtonian dusty channel convective flow problem with viscous heating effects. Pulsatile time-dependent dusty pumping in a channel was examined by Datta *et al.* [60] using Laplace transform techniques. Vajravelu *et al*. [61] studied temperature-dependent fluid property effects in magnetized convective boundary layer flow in a dusty fluid over a stretching sheet with the second-order implicit finite difference scheme known as the Keller–Box method and perturbation methods. They observed that transverse fluid phase velocity

is damped with elevation in the fluid-particle interaction parameter both with and without a magnetic field. Kumar and Sarma [62] used the least-squares finite element method to simulate the steady flow of a fluid–particle suspension generated by stretching a wall, noting that both fluid and particle-phase velocities are suppressed with increment in particle loading fluid-particle interaction parameters. They also observed that dusty particle density attains a peak at the plate (sheet) surface. Dalal *et al.* [63] presented central and second upwind finite difference computational solutions for natural convection of a dusty fluid in an infinite rectangular channel with differentially heated vertical walls and adiabatic horizontal walls. They noted that the heat transfer rate at the channel walls (Nusselt number) is reduced with an increase in the mass concentration of dust particles, whereas it is boosted with a higher thermal buoyancy effect (Rayleigh number). Gretler and Regenfelder [64] developed similar solutions for adiabatic strong blast shock waves of variable energy propagating in a dusty gas using an equilibrium-flow condition and simulating the variable energy input via a driving piston (decelerated, constant velocity, or accelerated) with a time-dependent power law. They tabulated extensive results for the effects of mass concentration of the solid particles and the ratio of the density of solid particles to the constant initial density of the gas. Saqib *et al*. [65] used a two-phase Brinkman model with Laplace and Hankel transform to develop exact analytical solutions for magnetic blood flow in a cylindrical tube with Newtonian fluid and uniformly distributed magnetite dusty particles. Park and Rosner [66] computed laminar flow mass, momentum, and energy-transfer rate coefficients over a wide range of particle mass loadings, dimensionless particle relaxation times (Stokes numbers), dimensionless thermophoretic diffusivities, and gas Reynolds numbers in steady axisymmetric "dusty-gas" flow between two infinite disks. They identified a new "critical" Strokes number (for incipient particle impaction) on the particle mass loading and the wall/gas temperature ratio for dust-laden gas motion towards "overheated" solid surfaces. Takhar *et al*. [67] deployed a complex variable method to study the transient magnetic flow of a dusty viscous liquid in a spinning channel with Hall current effects, elucidating in detail the impact of Strouhal and Stokes numbers on particle and fluid phase velocities at both weak and strong magnetic fields. Chamkha [68] derived closed-

form solutions for dual-phase velocities, displacement thicknesses, and skin friction for dusty Newtonian flow in a channel with perforated walls considering both suction and injection (blowing) effects. Bég *et al*. [69] used a variational finite element method to compute the steady, laminar nonlinear natural convection dusty flow with heat generation in a vertical channel containing a non-Darcian porous medium. They computed both fluid/particle-phase velocity and temperatures, noting that fluid velocity is strongly damped with porous drag forces and magnetic field, whereas particle-phase velocity is weakly reduced. They further noted that higher inverse momentum Stokes number suppresses fluid phase velocity but elevates particle-phase velocity. Further recent studies of dusty transport in channels have been reported by Mukhopadhyay *et al*. [70] using a finite volume method for a wavy-walled duct, Bég *et al*.[71] using differential transform methods with Padé approximants for dusty blood flow under thermal buoyancy effects, and Palani and Kim [72] with a Crank–Nicholson finite difference method for external cylinder coating dusty boundary layer.

1.4.1 Governing equations of dusty fluid flow

The net volume transfer of fluid is affected by the dust particle disbursed in the fluid; hence the drag force is modelled by the volume transfer coefficient ζ_T. The governing equation of mass and heat transfer for dusty fluid with density (ρ_d) and viscosity (μ_d) can be seen in [73], [74] as follows.

The continuity equation:

$$\frac{\partial \emptyset}{\partial t} + \nabla.(1-\emptyset)\overrightarrow{u_d} = 0, \tag{1.10}$$

$$\frac{\partial \emptyset}{\partial t} + \nabla.\emptyset\overrightarrow{u_p} = 0. \tag{1.11}$$

For incompressible Newtonian fluid flow, $(\nabla.\overrightarrow{u_d} = 0)$.

The mass transfer equation:

$$\rho_n(1-\emptyset).\left(\frac{\partial\overrightarrow{u_d}}{\partial t}+(\overrightarrow{u_d}.\nabla)\overrightarrow{u_d}\right)=\begin{bmatrix}(1-\emptyset)(-\nabla p+\mu_d\nabla^2\overrightarrow{u_d})-\\ \zeta_T\rho_p\emptyset(\overrightarrow{u_d}-\overrightarrow{u_p})\end{bmatrix}. \tag{1.12}$$

$$\rho_p\emptyset\left(\frac{\partial\overrightarrow{u_p}}{\partial t}+(\overrightarrow{u_p}.\nabla)\overrightarrow{u_p}\right)=\zeta_T\rho_p\emptyset(\overrightarrow{u_d}-\overrightarrow{u_p}). \tag{1.13}$$

Here $\zeta_T=\frac{6\pi r\,\mu_{md}}{m_p}$ is the volume transfer coefficient with an average mass of dust particle m_p, density ρ_p, velocity u_p, and radius r, $-\nabla p$ is the pressure term.

The heat transfer equation:

$$\rho_d c_d(1-\emptyset)\left(\frac{\partial T_d}{\partial t}+(\overrightarrow{u_d}.\nabla)T_d\right)=\begin{bmatrix}(1-\emptyset)\kappa_d\nabla^2T_d+(1-\emptyset)\mu_d\Phi\\ +\rho_p c_p\frac{\emptyset(T_d-T_p)}{\gamma_T}\\ +\zeta_T\rho_p\emptyset(\overrightarrow{u_p}-\overrightarrow{u_d})^2\end{bmatrix}. \tag{1.14}$$

$$\rho_p c_p\emptyset\left(\frac{\partial T_p}{\partial t}+(\overrightarrow{u_p}.\nabla)T_p\right)=-\rho_p c_p\frac{\emptyset(T_p-T_d)}{\gamma_T}. \tag{1.15}$$

Here c_d, κ_d are the specific heat capacity and thermal conductivity of the dusty fluid. Φ is the viscous dissipation term with u_d, v_d, w_d components of the dusty fluid velocity vector $\overrightarrow{u_d}$ in the direction of *x, y,* and *z,* respectively as:

$$\Phi=2\left[\left(\frac{\partial u_d}{\partial x}\right)^2+\left(\frac{\partial v_d}{\partial x}\right)^2+\left(\frac{\partial w_d}{\partial x}\right)^2\right]+\begin{bmatrix}\left(\frac{\partial u_d}{\partial y}+\frac{\partial v_d}{\partial x}\right)^2+\left(\frac{\partial v_d}{\partial z}+\frac{\partial w_d}{\partial y}\right)^2\\ +\left(\frac{\partial w_d}{\partial x}+\frac{\partial u_d}{\partial z}\right)^2\end{bmatrix}. \tag{1.16}$$

Most of the research cited above is limited to a single fluid, either micropolar, Newtonian, or dusty fluid flow analysis in the channel. However, several engineering issues exist, such as desalination procedures, petrochemical separation, X-ray crystallography, acid hydrolysis, applied hydrogeology, and thermo-hydraulics characterized by the immiscible multi-fluid flow. Interfacial inclusion in mathematical simulations of two immiscible liquids can improve the insight of transport processes and allow for more precise handling of changes in flow characteristics.

There are numerous approaches for modelling the interface between two immiscible fluids [75]. The moving grid [76], Lagrangian method, front tracking [77], boundary

integral [78], a level set technique [79], volume tracking, and volume of fluid (VOF) method [80] are all examples of interface tracking methods. The volume of fluid (VOF) approach is easy to expand in the three-dimensional instance and presents a convenient way of addressing deformations in the interface [81].

1.5 The volume of the fluid (VOF) model

The accurate evaluation of the complicated interface track between two immiscible liquids has been a significant concern in many of the above research. The interface might be significantly distorted or even collapse in extreme cases when it moves from one location to another.

Umavathi and Bég [82] deployed a finite difference code and special interfacial stress conditions to compute the influence of thermal conductivity ratio and viscosity ratio on interfacial heat and momentum transfer for two Newtonian immiscible fluids in a vertical duct with non-isothermal wall conditions. They showed that with different duct aspect ratios in the upper and lower duct regions, a marked movement of the interface is generated. Yih [83] observed that due to the viscosity drop from one fluid to another, the tangential velocity gradient also shifts, contributing to instability in the interface. As a result, in computational flow modelling, the interface between two immiscible fluids is critical, and it should be calculated as a critical feature of the solution.

DeBar [84] pioneered the volume of fluid (VOF) method, developing the first comprehensive numerical code for Eulerian hydrodynamics in the compressible non-viscous flow of several fluids in two-dimensional (axially symmetric) regions. Youngs [85] did some significant modifications to the volume of fluid (VOF) code by incorporating viscous and prominent interface deformation features. Kannan *et al.* [86] proposed a hybrid interface tracking simulation between two immiscible liquids. The geometric volume of the fluid method was employed to get the interface profile. Baniabedalruhman [87] implemented the level set method in the volume of fluid technique to achieve better accuracy in the interface track between two immiscible

liquids. The nonlinear behavior of a sheared immiscible fluid interface is studied by Tauber *et al.* [88]. Dong *et al*. [89] used a Lattice Boltzmann code to simulate two immiscible fluids displacement. This approach offers an apparent geometrical change in the interface. Li [90] studied the interface between two immiscible fluids with time by the VOF method. Zhao *et al.* [91] implemented the volume of fluid (VOF) method in the unstructured grid to study the time-dependent free surface flow. The interface tracking between two immiscible fluids was explored via various methods, including VOF by Gopala and van Wachem [92].

In the system of two immiscible liquids, the characteristics described by the momentum model are defined by the existence of each control volume. The average density and viscosity quantities are normalized by the following equations by Li and Renardy [81].

$$\rho^* = \rho_1 + C_s(\rho_2 - \rho_1), \tag{1.17}$$

$$\mu^* = \mu_1 + C_s(\mu_2 - \mu_1). \tag{1.18}$$

Here ρ_1, μ_1 be the density and viscosity of the one kind of fluid and ρ_2, μ_2 be the density and viscosity of others. The VOF-fraction function I is used to track the interface and transported by the mean velocity field $\overline{U^*}$.

$$\frac{\partial I}{\partial t} + \overline{U^*}.\nabla I = 0. \tag{1.19}$$

The incompressible flow velocity is driven by a single momentum equation, with the resultant velocity field shared between the transitions Li and Renardy [81].

$$\rho^* \left(\frac{\partial \overline{U^*}}{\partial t} + (\overline{U^*}.\nabla)\overline{U^*}\right) = -\nabla p + \mu^* \nabla^2 \overline{U^*} + F. \tag{1.20}$$

Here the body forces F is included with gravitational force and interfacial tension, and$-\nabla p$ is the applied pressure term.

When discretizing the advection equation (1.19) the VOF-fraction function I is also solved using the non-dimensionalized velocity U^* as the following equation [93]

$$\frac{\partial I}{\partial t} = -\nabla(U^* I). \tag{1.21}$$

1.6 Non-dimensional parameter

The importance of any fluid flow problem is proportional to its physical significance, and the dimensionless parameters in the fluid flow equation describe the strong physical relevance of the problems. These parameters are also employed to deduce the essential characteristics of a similar set of problems. The following subsections include a detailed overview of the non-dimensional parameters considered in this study.

1.6.1 Reynolds number

Reynolds number is a dimensional less number that describes the ratio of inertial to viscous forces. The Reynolds number controls whether a fluid flow pattern is laminar or turbulent as it flows through a channel. The following equation represents the Reynolds number.

$$Re = \frac{\rho U_0^2}{\mu U_0/k} = \frac{\rho U_0 k}{\mu}. \tag{1.22}$$

A higher value of Re in the one/two-fluid medium indicates lower viscous forces, which results in a growing pattern in fluid velocities.

1.6.2 Micropolar parameter

The ratio of two viscous forces (vortex and dynamic) is represented by the micropolar parameter, which is a dimensionally less quantity. When fluid flows through a duct, the micropolar parameter determines whether the flow pattern is irrotational. The micropolar parameter is represented by the equation below.

$$\eta_m = \frac{\kappa_m}{\mu_m}. \tag{1.23}$$

1.6.3 Capillary number

The capillary number *(Ca)* is a dimensionless number that depicts the proportional influence of viscous drag forces vs. surface tension forces operating across an immiscible liquid boundary. The capillary number *(Ca)* is defined as

$$Ca = \frac{\mu U_0}{\sigma}. \tag{1.24}$$

1.6.4 Froude number

The Froude number *(Fr)* is a dimensionless quantity defined as the flow inertia to extrinsic field (Gravitational acceleration) ratio and calculated as follows.

$$Fr = \frac{{U_0}^2}{gk}. \tag{1.25}$$

1.6.5 Particle concentration parameter

The concentration of dust particles is critical for enhancing the base fluid's thermal conductivity. By considering the volume fraction of the dust particles in the dusty fluid model, $R = \frac{K^* \rho_p k^2 \emptyset}{\mu_d m_p (1-\emptyset)}$ is particle concentration parameter and $K^* = 6\pi r \mu_d U_0$ is the Stokes drag coefficient. The dust particles are uniformly distributed in the fluid with $\frac{\emptyset}{(1-\emptyset)} = 1$.

1.6.6 Prandtl number

The Prandtl number *(Pr)* is a dimensionless number measured as the proportion of momentum diffusivity (kinematic viscosity) to thermal diffusivity, the Prandtl number *(Pr)* is calculated as follows:

$$Pr = \frac{{}^{\mu}/_{\rho}}{{}^{\kappa}/_{\rho c}} = \frac{\mu c}{\kappa}. \tag{1.26}$$

1.6.7 Eckert number

Eckert number*(Ec)* is a dimensionless number measured as the ratio of the kinetic energy to the flow's enthalpy difference (viscous dissipation). Although the value of the Eckert number for incompressible liquids is low, it plays a critical role in speedy flow, and it is defined as:

$$Ec = \frac{\rho U_0^2}{\rho c\, \Delta T} = \frac{U_0^2}{c\, \Delta T}. \tag{1.27}$$

1.6.8 Hartmann number

The Hartmann number expresses the ratio of the electromagnetic (Lorentz magnetic) drag force to the viscous hydrodynamic force. Since the Lorentz force exerts in the reverse direction of flow, an increase in the Hartmann number leads to a drop in flow velocity. It is defined as:

$$Ha = \frac{B_0^2 k^2 \sqrt{\sigma}}{\sqrt{\mu}}. \tag{1.28}$$

1.7 Differential quadrature method

Differential quadrature is one of the promising approaches for solving numerous linear and nonlinear system of partial differential equations that uses several forms of basis functions [94], [95]. This method was proposed by Bellman [96] to develop an efficient discretization strategy to achieve concise numerical solutions with significantly reduced grid stages. Quan and Chang [97] improved the DQM approach. Zhang and Wang [98] analyzed the elastoplastic bending characteristics of the thick slab using the differential quadrature (DQ) technique. Mittal and Rohila [99] observed that the differential quadrature method performs well for minor grid points. They considered the Fisher's and Burgers 'equation and used the Bernstein basis function in the differential quadrature method. Ding *et al.* [100] used the Lagrange and trigonometric basis function in the differential quadrature method to achieve strong stability in the

milling process. Various other test functions, namely, Lagrange interpolation polynomials, sink and spline, cubic and modified-cubic B-spline, are used in [101] to calculate the weighting coefficients in DQM. Because of the ease of the application and the convenience of the programming, this technique is prevalent. Korkmaz and Dag [102] employed it to derive the numerical solution to several engineering problems. Various other numerical studies using the differential quadrature method can be seen with different basis functions [103]–[107].

This thesis includes the modified cubic B-spline basis function to obtain the numerical solution for fluid flow problems of some immiscible fluids. In the horizontal duct, the different combinations of immiscible fluids, say micropolar, Newtonian, dusty, non-dusty, and micropolar-dusty fluids, are considered, and velocities, temperatures of respective fluids and particle phase, and interface tracking is analyzed.

In the different schemes of the horizontal channel, first, the domain $[a, b] \times [c, d]$ is uniformly discretized with phase length $y_{i+1} - y_i = h_1$ in the y-direction and $x_{i+1} - x_i = h_2$ in the *x*-direction. The nodes are expected to be spread equally.

$$\left.\begin{aligned} a = y_1 < y_2 < \cdots < y_{N-1} < y_N = b, \\ c = x_1 < x_2 < \cdots < x_{N-1} < x_N = d. \end{aligned}\right\} \tag{1.29}$$

Then the first and second-order derivatives of different unidirectional components of a particular fluid are approximated as follows.

The derivative coefficients of micropolar fluid velocity u_m as

$$\left.\begin{aligned} \frac{\partial u_m}{\partial y} &= \sum_{j=1}^{N} a_{ij}^{*} u_m(y_j, t), \\ \frac{\partial^2 u_m}{\partial y^2} &= \sum_{j=1}^{N} b_{ij}^{*} u_m(y_j, t), \quad for\ i = 1,2, \dots, N. \end{aligned}\right\} \tag{1.30}$$

The derivative coefficients of microrotation M_* of micropolar fluid as

$$\left.\begin{aligned} \frac{\partial M_*}{\partial y} &= \sum_{j=1}^{N} a_{ij}^{*} M_*(y_j, t), \\ \frac{\partial^2 M_*}{\partial y^2} &= \sum_{j=1}^{N} b_{ij}^{*} M_*(y_j, t), \quad for\ i = 1,2, \dots, N. \end{aligned}\right\} \tag{1.31}$$

The derivative coefficients of Newtonian fluid velocity u_n as

$$\left.\begin{aligned}\frac{\partial u_n}{\partial y} &= \sum_{j=1}^{N} a_{ij}^{*} u_n(y_j, t),\\ \frac{\partial^2 u_n}{\partial y^2} &= \sum_{j=1}^{N} b_{ij}^{*} u_n(y_j, t), \quad for\ i = 1,2, \dots, N.\end{aligned}\right\} \tag{1.32}$$

The derivative coefficients of dusty fluid velocity u_d as

$$\left.\begin{aligned}\frac{\partial u_d}{\partial y} &= \sum_{j=1}^{N} a_{ij}^{*} u_d(y_j, t),\\ \frac{\partial^2 u_d}{\partial y^2} &= \sum_{j=1}^{N} b_{ij}^{*} u_d(y_j, t), \quad for\ i = 1,2, \dots, N.\end{aligned}\right\} \tag{1.33}$$

The derivative coefficient of dust phase velocity u_p as

$$\left.\frac{\partial u_p}{\partial y} = \sum_{j=1}^{N} a_{ij}^{*} u_p(y_j, t), \ \ for\ i = 1,2, \dots, N.\right\} \tag{1.34}$$

The derivative coefficients of micropolar dusty fluid velocity u_{md} as

$$\left.\begin{aligned}\frac{\partial u_{md}}{\partial y} &= \sum_{j=1}^{N} a_{ij}^{*} u_{md}(y_j, t),\\ \frac{\partial^2 u_{md}}{\partial y^2} &= \sum_{j=1}^{N} b_{ij}^{*} u_{md}(y_j, t), \quad for\ i = 1,2, \dots, N.\end{aligned}\right\} \tag{1.35}$$

The derivative coefficients of micropolar dusty fluid temperature T_{md} as

$$\left.\begin{aligned}\frac{\partial T_{md}}{\partial y} &= \sum_{j=1}^{N} a_{ij}^{*} T_{md}(y_j, t),\\ \frac{\partial^2 T_{md}}{\partial y^2} &= \sum_{j=1}^{N} b_{ij}^{*} T_{md}(y_j, t), \quad for\ i = 1,2, \dots, N.\end{aligned}\right\} \tag{1.36}$$

The derivative coefficients of microrotation M_d of micropolar dusty fluid as

$$\left.\begin{aligned}\frac{\partial M_d}{\partial y} &= \sum_{j=1}^{N} a_{ij}^{*} M_d(y_j, t),\\ \frac{\partial^2 M_d}{\partial y^2} &= \sum_{j=1}^{N} b_{ij}^{*} M_d(y_j, t), \quad for\ i = 1,2, \dots, N.\end{aligned}\right\} \tag{1.37}$$

The derivative coefficients of Newtonian fluid temperature T_n as

$$\left.\begin{aligned}\frac{\partial T_n}{\partial y} &= \sum_{j=1}^{N} a_{ij}^{*} T_n(y_j, t),\\ \frac{\partial^2 T_n}{\partial y^2} &= \sum_{j=1}^{N} b_{ij}^{*} T_n(y_j, t), \quad for\ i = 1,2, \dots, N.\end{aligned}\right\} \tag{1.38}$$

The derivative coefficients of dusty fluid temperature T_d as

$$\left.\begin{aligned}\frac{\partial T_d}{\partial y} &= \sum_{j=1}^{N} a_{ij}^{*} T_d(y_j, t),\\ \frac{\partial^2 T_d}{\partial y^2} &= \sum_{j=1}^{N} b_{ij}^{*} T_d(y_j, t), \quad for\ i = 1,2, \dots, N.\end{aligned}\right\} \tag{1.39}$$

The derivative coefficient of dust phase temperature T_p as

$$\left.\frac{\partial T_p}{\partial y} = \sum_{j=1}^{N} a_{ij}^{*} T_p(y_j, t), \ \ for\ i = 1,2, \dots, N.\right\} \tag{1.40}$$

The derivative coefficients of an interface between two immiscible fluid C_i

$$\left.\begin{aligned}\frac{\partial C_i}{\partial y} &= \sum_{j=1}^{N} a_{ij}^{*} C_i(y_j, t),\\ \frac{\partial^2 C_i}{\partial y^2} &= \sum_{j=1}^{N} b_{ij}^{*} C_i(y_j, t), \quad for\ i = 1,2, \dots, N.\end{aligned}\right\} \tag{1.41}$$

The derivative coefficients of mean flow velocity $u^*$of two immiscible fluids

$$\left.\begin{aligned}\frac{\partial u^*}{\partial y} &= \sum_{j=1}^{N} a_{ij}^{*} u^*(y_j, t),\\ \frac{\partial^2 u^*}{\partial y^2} &= \sum_{j=1}^{N} b_{ij}^{*} u^*(y_j, t), \quad for\ i = 1,2, \dots, N.\end{aligned}\right\} \tag{1.42}$$

Similarly, first and second-order derivatives of two dimensional (spatial) interface $N_i(x, y, t)$ and fluid velocity $U^*(x, y, t), V^*(x, y, t)$ are approximated as follows.

$$\frac{\partial N_i}{\partial x} = \sum_{i=1}^{N} a_{ij} N_i(x_i, y, t), \text{ for } j = 1,2, \dots, N, \tag{1.43}$$

$$\frac{\partial N_i}{\partial y} = \sum_{j=1}^{N} a_{ij}^{*} N_i(x, y_j, t), \text{ for } i = 1,2, \dots, N, \tag{1.44}$$

$$\frac{\partial U^*}{\partial x} = \sum_{i=1}^{N} a_{ij} U^*(x_i, y, t), \text{ for } j = 1,2, \dots, N, \tag{1.45}$$

$$\frac{\partial U^*}{\partial y} = \sum_{j=1}^{N} a_{ij}^{*} U^*(x, y_j, t), \text{ for } i = 1,2, \dots, N, \tag{1.46}$$

$$\frac{\partial V^*}{\partial x} = \sum_{i=1}^{N} a_{ij} V^*(x_i, y, t), \text{ for } j = 1,2, \dots, N, \tag{1.47}$$

$$\frac{\partial V^*}{\partial y} = \sum_{j=1}^{N} a_{ij}^{*} V^*(x, y_j, t), \text{ for } i = 1,2, \dots, N, \tag{1.48}$$

$$\frac{\partial^2 N_i}{\partial x^2} = \sum_{i=1}^{N} b_{ij} N_i(x_i, y, t), \text{ for } j = 1,2, \dots, N, \tag{1.49}$$

$$\frac{\partial^2 N_i}{\partial y^2} = \sum_{j=1}^{N} b_{ij}^{*} N_i\left(x, y_j, t\right), \text{ for } i = 1,2, \dots, N, \tag{1.50}$$

$$\frac{\partial^2 U^*}{\partial x^2} = \sum_{i=1}^{N} b_{ij} U^*(x_i, y, t), \text{ for } j = 1,2, \dots, N, \tag{1.51}$$

$$\frac{\partial^2 U^*}{\partial y^2} = \sum_{j=1}^{N} b^*{}_{ij} U^*\left(x, y_j, t\right), \text{ for } i = 1,2, \dots, N, \tag{1.52}$$

$$\frac{\partial^2 V^*}{\partial x^2} = \sum_{i=1}^{N} b_{ij} V^*(x_i, y, t), \text{ for } j = 1,2, \dots, N, \tag{1.53}$$

$$\frac{\partial^2 V^*}{\partial y^2} = \sum_{j=1}^{N} b^*{}_{ij} V^*\left(x, y_j, t\right), \text{ for } i = 1,2, \dots, N. \tag{1.54}$$

Here $a_{ij}, a^*{}_{ij}, b_{ij}$, and $b^*{}_{ij}$are the weighting coefficients for the first and second-order derivatives of $u_m, u_n, M_*, C_i, u^*, u_d, u_p, T_d, T_p, T_n, u_{md}, M_d, T_m, T_{md}, N_i, U^*, V^*, U_p^*, V_p^*$, N_i, U^*, and V^* with respect to *x* and *y,* respectively.

The weighting coefficients are calculated using the following cubic B-spline basis function at knots $(y_1, y_2 \dots, y_n)$.

$$CB_j = \frac{1}{h^3} \begin{cases} \left(y - y_{j-2}\right)^3 & y\epsilon\ [y_{j-2}, y_{j-1}) \\ \left(y - y_{j-2}\right)^3 - 4\left(y - y_{j-1}\right)^3 & y\epsilon[y_{j-1}, y_j) \\ \left(y_{j+2} - y\right)^3 - 4\left(y_{j+1} - y\right)^3 & y\epsilon\ [y_j, y_{j+1}) \\ \left(y_{j+2} - y\right)^3 & y\epsilon[y_{j+1}, y_{j+2}) \\ 0 & otherwise\ . \end{cases} \tag{1.55}$$

CB_j with $j = 0,1,2 \dots, N+1$ forms a basis over the region [-1, 1].

The updated cubic B-spline functions are described in the nodes as follows.

$$\psi_1(y) = CB_1(y) + 2CB_0(y), \tag{1.56}$$

$$\psi_2(y) = CB_2(y) - CB_0(y), \tag{1.57}$$

$$\psi_j(y) = CB_j, for\ j = 3, \dots . N-2, \tag{1.58}$$

$$\psi_{N-1}(y) = CB_{N-1}(y) - CB_{N+1}(y), \tag{1.59}$$

$$\psi_N(y) = CB_N(y) + 2CB_{N+1}(y). \tag{1.60}$$

Where $\{\psi_1\psi_2, \dots, \psi_N\}$ forms a basis over the region $[-1,1]$. The weighting coefficients are determined as follows by the modified cubic B-spline function. The estimate of the first-order derivative is

$$\psi'_k(y_i) = \sum_{j=1}^{N} a^*{}_{ij} CB_k(y_j),\ for\ i = 1,2, \dots, N, k = 1,2, \dots, N. \tag{1.61}$$

The estimate can be provided for the first-knot point y_1.

$$\psi'_k(y_1) = \sum_{j=1}^{N} a^*{}_{1j} CB_k(y_j), for\ i = 1,2, \dots, N, k = 1,2, \dots, N. \tag{1.62}$$

Then for $a^*{}_{1j}$ the tri-diagonal system is established as

$$\begin{bmatrix} 6 & 4 & 0 & 0 & \dots & 0 & 0 \\ 0 & 4 & 1 & 0 & \dots & 0 & 0 \\ 0 & 1 & 4 & 1 & \dots & 0 & 0 \\ \vdots & \vdots & \vdots & \ddots & \ddots & \vdots & \vdots \\ 0 & 0 & \dots & 1 & 4 & 1 & 0 \\ 0 & 0 & \dots & 0 & 1 & 4 & 0 \\ 0 & 0 & \dots & 0 & 0 & 1 & 6 \end{bmatrix} \begin{bmatrix} a^*{}_{11} \\ a^*{}_{12} \\ a^*{}_{13} \\ \cdot \\ \cdot \\ \cdot \\ a^*{}_{N-3} \\ a^*{}_{N-2} \\ a^*{}_{N-1} \\ a^*{}_{N} \end{bmatrix} = \begin{bmatrix} -6/h \\ 6/h \\ 0 \\ \cdot \\ \cdot \\ \cdot \\ 0 \\ 0 \\ 0 \\ 0 \end{bmatrix}. \tag{1.63}$$

Similarly for the point, $y_2$we have,

$$\psi'_k(y_2) = \sum_{j=1}^{N} a^*{}_{2j} CB_k(y_j), for\ i = 1,2, \dots, N, k = 1,2, \dots, N. \tag{1.64}$$

Then again for $a^*{}_{2j}$,

$$\begin{bmatrix} 6 & 4 & 0 & 0 & \dots & 0 & 0 \\ 0 & 4 & 1 & 0 & \dots & 0 & 0 \\ 0 & 1 & 4 & 1 & \dots & 0 & 0 \\ \vdots & \vdots & \vdots & \ddots & \ddots & \vdots & \vdots \\ 0 & 0 & \dots & 1 & 4 & 1 & 0 \\ 0 & 0 & \dots & 0 & 1 & 4 & 0 \\ 0 & 0 & \dots & 0 & 0 & 1 & 6 \end{bmatrix} \begin{bmatrix} a^*{}_{21} \\ a^*{}_{22} \\ a^*{}_{23} \\ \cdot \\ \cdot \\ \cdot \\ a^*{}_{2N-3} \\ a^*{}_{2N-2} \\ a^*{}_{2N-1} \\ a^*{}_{2N} \end{bmatrix} = \begin{bmatrix} -3/h \\ 0 \\ 3/h \\ 0 \\ \cdot \\ \cdot \\ 0 \\ 0 \\ 0 \\ 0 \end{bmatrix}. \tag{1.65}$$

The three diagonal structures for the rest of the y_i are continued, and the system for ${a^*}_{NN}$ as follows.

$$\begin{bmatrix} 6 & 4 & 0 & 0 & \dots & 0 & 0 \\ 0 & 4 & 1 & 0 & \dots & 0 & 0 \\ 0 & 1 & 4 & 1 & \dots & 0 & 0 \\ \vdots & \vdots & \vdots & \ddots & \ddots & \vdots & \vdots \\ 0 & 0 & \dots & 1 & 4 & 1 & 0 \\ 0 & 0 & \dots & 0 & 1 & 4 & 0 \\ 0 & 0 & \dots & 0 & 0 & 1 & 6 \end{bmatrix} \begin{bmatrix} {a^*}_{N1} \\ {a^*}_{N2} \\ {a^*}_{N3} \\ . \\ . \\ . \\ {a^*}_{NN-3} \\ {a^*}_{NN-2} \\ {a^*}_{NN-1} \\ {a^*}_{NN} \end{bmatrix} = \begin{bmatrix} 0 \\ 0 \\ 0 \\ 0 \\ . \\ . \\ 0 \\ 0 \\ -6/h \\ 6/h \end{bmatrix}. \tag{1.66}$$

The above-mentioned systems have the coefficients-

${a^*}_{11}, {a^*}_{12} \dots, {a^*}_{1N}$, ${a^*}_{21}, {a^*}_{22} \dots, {a^*}_{2N} \dots, {a^*}_{N1}$, ${a^*}_{N2} \dots, {a^*}_{NN}$. Then the value of ${b^*}_{ij}$ for $i = 1,2,3 \dots, N$, and $j = 1,2,3 \dots, N$ is calculated as follows.

$${b^*}_{ij} = \begin{Bmatrix} 2{a^*}_{ij}\left({a^*}_{ij} - \frac{1}{y_i - y_j}\right) & for\ i \neq j \\ -\sum_{i=1, i\neq j}^{N} {b^*}_{ii} & i = j. \end{Bmatrix} \tag{1.67}$$

Similarly, one can calculate the weighting coefficients a_{ij} , b_{ij} for the first and second-order derivatives with respect to *x*.

According to the particular scheme flow, the fluid and particle velocity, microtation, temperature, and interface profile are obtained by putting derivative approximation in the coupled partial differential equation system. This system can be written as

$$I_t = I\left(u_m, u_n, M_*, C_i, u^*, u_d, u_p, T_d, T_p, T_n, u_{md}, M_d, T_m, T_{md}, N_i, U^*, V^*, U_p^*, V_p^*\right). \tag{1.68}$$

The following strong stability preserving scheme (SSP-RK43) is employed to get the final solution.

$$I^{(1)} = I^{(m)} + \frac{\Delta t}{2}.I\begin{pmatrix} u_m^{(m)}, u_n^{(m)}, M_*^{(m)}, C_i^{(m)}, {u^*}^{(m)}, u_d^{(m)}, u_p^{(m)}, T_d^{(m)}, \\ T_p^{(m)}, T_n^{(m)}, u_{md}^{(m)}, M_d^{(m)}, T_m^{(m)}, T_{md}^{(m)}, N_i^{(m)}, \\ {U^*}^{(m)}, {V^*}^{(m)}, {U_p^*}^{(m)}, {V_p^*}^{(m)} \end{pmatrix}, \tag{1.69}$$

$$I^{(2)} = I^{(1)} + \frac{\Delta t}{2} . I \begin{pmatrix} u_m^{(1)}, u_n^{(1)}, M_*^{(1)}, C_i^{(1)}, u^{*(1)}, u_d^{(1)}, u_p^{(1)}, T_d^{(1)}, T_p^{(1)}, T_n^{(1)}, \\ u_{md}^{(1)}, M_d^{(1)}, T_m^{(1)}, T_{md}^{(1)}, N_i^{(1)}, U^{*(1)}, V^{*(1)}, U_p^{*(1)}, V_p^{*(1)} \end{pmatrix}, \quad (1.70)$$

$$I^{(3)} = \frac{2}{3} I^{(m)} + \frac{I^{(2)}}{3} + \frac{\Delta t}{6} . I \begin{pmatrix} u_m^{(2)}, u_n^{(2)}, M_*^{(2)}, C_i^{(2)}, u^{*(2)}, u_d^{(2)}, u_p^{(2)}, T_d^{(2)}, \\ T_p^{(2)}, T_n^{(2)}, u_{md}^{(2)}, M_d^{(2)}, T_m^{(2)}, T_{md}^{(2)}, N_i^{(2)}, \\ U^{*(2)}, V^{*(2)}, U_p^{*(2)}, V_p^{*(2)} \end{pmatrix}, \quad (1.71)$$

$$I_{final} = I^{(3)} + \frac{\Delta t}{2} . I \begin{pmatrix} u_m^{(3)}, u_n^{(3)}, M_*^{(3)}, C_i^{(3)}, u^{*(3)}, u_d^{(3)}, u_p^{(3)}, T_d^{(3)}, T_p^{(3)}, T_n^{(3)}, \\ u_{md}^{(3)}, M_d^{(3)}, T_m^{(3)}, T_{md}^{(3)}, N_i^{(3)}, U^{*(3)}, V^{*(3)}, U_p^{*(3)}, V_p^{*(3)} \end{pmatrix}. \quad (1.72)$$

Chapter 2
A Numerical Study of The Unsteady Flow of Two Immiscible Micropolar and Newtonian Fluids Through a Horizontal Channel Using DQM With B-Spline Basis Function

2.1 Introduction

Many commercial and technology-driven fluids do not function as Newtonian fluids-they exhibit non-Newtonian characteristics. Therefore, various mathematical models have been developed to describe non-Newtonian fluids, including viscoelastic and polar (couple stress) fluids. The micropolar fluid model is an alternative and more elegant formulation, which has stimulated considerable interest in rheological modelling worldwide. Eringen pioneered the theory of micropolar fluids in the 1960s [108]. A remarkable aspect of the Eringen model is the competency to depict the fluid microstructure, including stresses neglected in the Newtonian (Navier-Stokes classical viscous flow) model and most rheological models. The microstructure is simulated via the microrotation vector, which is extraneous to the vorticity vector that creates unsymmetric stress. Microelements of the micropolar fluid can therefore sustain gyratory motions, i.e., spin. Therefore, micropolar fluid dynamics have been effectively used in various applications, including hemodynamic, nuclear reactor slurry flows, liquid crystals, lubricants, gels, greases, etc. Peddieson [109] explored the micropolar model for turbulent channel flow analysis. Thermal coating flows with micropolar fluids in the presence of cross-diffusion effects were studied numerically by Bég *et al*.

[110]. Micropolar blood flows were examined comprehensively by Kang and Eringen [111]. Devakar and Iyerger [112] studied the time-dependent flow of micropolar liquid in channels.

Apart from the micro-structured element, the efficiency of energy transfer in the fluid has been strengthened by the suspension of the nanoparticle. Using the magnetic field and nanofluid, Selimefendigil *et al*. [113] improved the thermal efficiency of the separated flow. The flow behavior of hybrid nanofluids was examined by Dogonchi *et al.* [114] in an embedded system comprising magnetic field effects. The problem of heat exchange among fluid and hot surfaces within a smooth air channel was addressed by Menni *et al.* [115]. Raza *et al.* [116] investigated the cumulative influence of heat radiation and a magneto force on molybdenum disulfide nanofluid in a conduit with shifting boundaries. The influence of Hall and ion slip on the MHD flow of nanofluids through the permeable rotating plate with a steady heat source was investigated by Krishna and Chamkha [117]. Hydrodynamic and thermal characterization of turbulent forced flows of pure water, pure ethylene glycol, and liquid glycol mixtures diffused by *Al2O3* microparticles were performed by Menni *et al*. [118]. Shashikumar *et al.* [119] discovered the influence of various alloy nanocrystals on magnetic materials' microchannel flow. Kumar *et al.* [120] examined The time-independent flow of an incompressible, optically thin fluid over a vertical plate using MHD convection flow. Menni *et al*. [121] described the findings of a computational investigation of forced-convection thermal expansion in heat exchanger ducts with various forms. Chamkha *et al.* [122] performed the simulation of unsteady conjugated natural convection of hybrid liquid emulsion of *Al2O3* and *Cu* nanocrystals (hybrid nanofluid), and the effects of important hydrodynamic parameters on flow character are identified. Parvin and Chamkha [123] evaluated naturally convective flow with heat exchange and thermal characteristics in an odd-shaped geometry. The complicated barriers inside solar structures with Newtonian fluid flow is studied by Menni *et al.* [124].Some further

important results on heat transfer with suspended particles and different geometry can perhaps be found in [125]–[132].

The above studies did not consider immiscible flows in which two fluids are separated by an interface and do not mix. Such flows arise in geo-hydrology, nuclear reactor thermo-hydraulics, slurry transport, coating dynamics, petrochemical separation techniques, desalination, and oil extraction systems. Many excellent studies of immiscible hydrodynamics and transport phenomena have therefore been communicated. Bir [133] reported on the laminar flow of two immiscible fluids in a channel. Umavathi *et al.* [134], [135]considered polar (couple stress) and Newtonian immiscible fluids in a channel. Kumar *et al.* [136] provided an analytical solution for two immiscible (micropolar and Newtonian) fluids in a composite porous medium inside a vertical channel. Srinivas and Murthy [137] considered immiscible flows of two couple stress fluids in porous layers. Srinivas *et al.* [138], [139] further investigated the influence of entropy generation in heat transfer of two couple stress immiscible fluids. Borrelli *et al.* [140] considered the hydromagnetic flow of two immiscible Newtonian fluids in a channel.

One of the primary problems in evaluating the behaviors of two immiscible liquid flows is the presence of an unusual interface in the area under consideration. Therefore, the interface of immiscible liquids is essential for the design of industrial systems, e.g., chemical separation devices, nuclear reactor transport, etc. Tauber *et al.* [88] addressed the deformations of a shearing immiscible fluid interface. Yih [83] found that when the viscosity of one fluid shifts to another, the tangential velocity slope, causes strife at the interface. DeBar [84] introduced the volume of fluid procedure, which was later improved by Youngs [85]. Li [90] investigated the VOF for interface development between two immiscible liquids. The VOF technique was used by Li and Renardy [81] to investigate the contact between two immiscible fluids. Vinay and Wachem [92] investigated the interface development of immiscible fluids, including volume of fluid (VOF).

Most of the above numerical approaches have proved to be generally reliable for simulating the interface dynamics accurately in immiscible flows. However, both artificial and normal conditions exist where the perspective of time dependence is intensely desirable. There are no actual circumstances in immiscible fluid dynamics that do not feature some instability. Consequently, the study of the time-dependent flow of immiscible liquids is critical for providing a deeper appreciation of the actual flow behavior of relevance to, for example, industrial processes. The time-dependent unstable fluid flow of two immiscible liquids has received relatively sparse attention in scientific works despite its actual existence. The unstable immiscible flow problem has been scrutinized by Tryggvason *et al.* [141] via the front tracking device. Riaz and Tchelepi [142] explored the volatility of the immiscible two-phase flow in porous media. Vajravelu *et al.* [143] investigated the magnetohydrodynamic (MHD) flow of immiscible Newtonian liquids in permeable layers. Thermo molded (heat and mass transfer) in immiscible viscous liquid channel flow was explored by Umavathi *et al.* [144].

A variety of linear and nonlinear fluid flow problems can be numerically solved using finite difference, finite element, and finite volume techniques. Devakar and Raje [1] numerically explored the time-dependent unsteady flow of two immiscible fluids by the Crank-Nicolson finite difference method. To achieve an acceptable degree of accuracy, the low-order approaches use several grid points to obtain specific outcomes at such defined points. The differential quadrature technique is easily applicable and efficient strategically, contributing to error reduction and simple to enforce, as described by Katta *et al*. [145]. Katta and Joshi [146] used the differential quadrature method(DQM) to numerically analyze the hydromagnetic flow of a viscoelastic Jeffrey fluid in a porous medium.

Motivated by the processing of non-Newtonian fluid, in the present chapter, an extensive computational model with the modified cubic B-spine-Differential Quadrature technique (MCB-DQM) is portrayed for the unsteady flow of two

immiscible fluids, the Newtonian and Eringen micropolar fluids through horizontal channels with two separate schemes.

This chapter has been echeloned into two sections. First, we consider a flat interface between the fluids in section-2.2. The differential quadrature method with cubic B-spline basis function is used to evaluate the velocity and micro-rotation of the unsteady flow of two immiscible, two immiscible micropolar, and Newtonian fluids through a horizontal channel. The analysis of fluid velocities and microrotation profile results is explained along with three cases for applied pressure gradient. The outcomes in volume flow rate across the channel for fluid velocities with different fluid parameters are addressed and analyzed along with Devakar and Raje [1].

Previous studies have been confined to examining the smooth and unstable movement of the micropolar fluid, the steady stream of two immiscible fluids, and interface monitoring through different modes. Further, section-2.3 extends the earlier studies to consider the unsteady flow of two immiscible Eringen micropolar and Newtonian fluids with a moving interface in the horizontal channel. The microrotation parameter affects the entire domain. First, the micro-rotation profile is computed, and then interface tracking with either constant, periodic, or decaying applied pressure gradients are obtained numerically by solving the coupled partial differential equations using the modified cubic B-spline differential quadrature method (MCB-DQM) to examine the effects of time, amplitude, wavenumber on the interface evolution and the velocity and micro-rotation velocity fields. The present work finds applications in chemical engineering flow control and separation processes [16].

2.2 Formulation for the immiscible flow of Newtonian and micropolar fluid with a stable interface

Consider two immiscible micropolar and Newtonian fluids in the horizontal channel, and the following assumptions are being made for fluid transportation.

i. Both fluids are incompressible and immiscible and are flowing in between two horizontal parallel plates, and the distance between these plates is *2k.* Both the plates that exist in the *X* and *Z* direction are shown in Figure 2.1.

ii. Eringen micropolar fluid occupies in the lower half-zone of the channel, i. e. zone-1 ($-k \leq y \leq 0$), and possesses the fluid velocity u_m, micro-rotation (angular velocity) M_*, density ρ_m, viscosity μ_m, vortex viscosity κ_m, gyration parameter τ, and gyro-viscosity ω_m.

iii. Newtonian fluid occupies in the upper half-space of the duct, zone-2 ($0 \leq y \leq k$), and possesses fluid velocity u_n, density ρ_n, viscosity μ_n.

iv. The transportation attributes are unchanged in both the zones and the common pressure gradients are applied from the horizontal (*X*) axial direction.

v. The flow of Newtonian fluid in zone -2 is governed by the equations (1.2) - (1.3), and the flow of micropolar fluid in zone -1 is governed by the equations (1.7) - (1.8).

vi. The fluid velocity vectors in both zones are $u_m(y,t)$, $u_n(y,t)$ and the micro-rotation vector $M_*(y,t)$ in the zone-1 are assumed to be $u_m = (u_m(y,t),0,0)$, $u_n = (u_n(y,t),0,0)$, and $(M = (0,0,M_*(y,t))$ respectively.

vii. The movement of fluids is incompressible unsteady, and driven by an applied pressure gradient in the *X*-axial direction; therefore, the velocity profile is unidirectional. The fluid layers are mechanically coupled through the mode of momentum exchange, and transferring momentum arises through consistency in velocity and shear stress over the interface.

viii. However, we assume that the flow rate and shear pressure are also stable at the interface between two liquids.

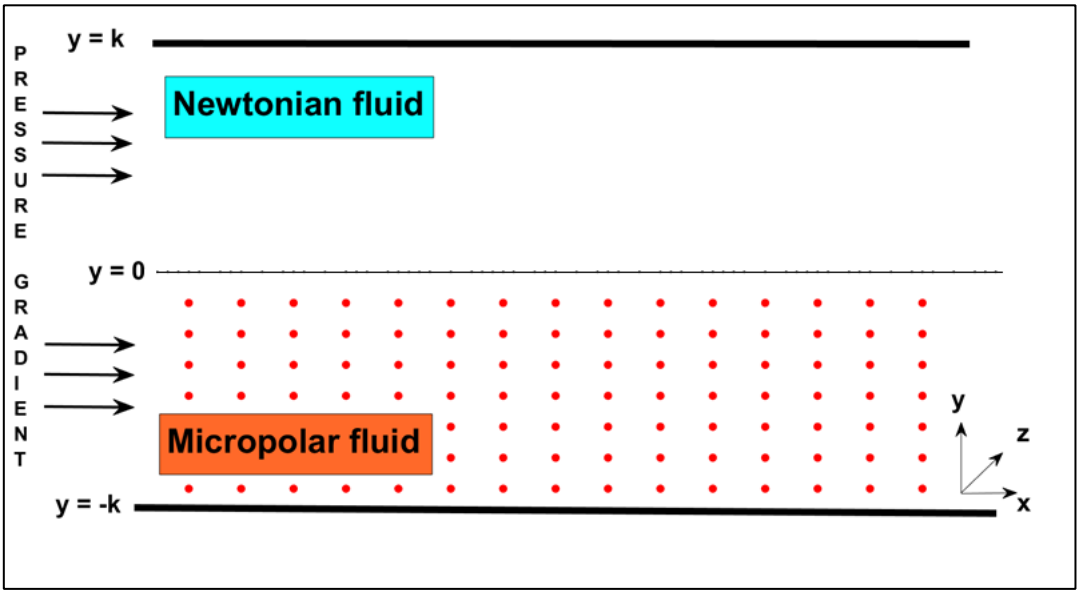

Figure 2.1: Geometry of immiscible micropolar and Newtonian (scheme-1a) fluids flow with a stable interface

Under the aforesaid assumed constraints, the Newtonian fluid flow equation (1.3) and micropolar fluid flow equations (1.7) - (1.8) for the unidirectional velocity and micro-rotation distribution take the form:

Zone-1 (micropolar fluid).

$$\rho_m \frac{\partial u_m}{dt} = -\nabla p + \kappa_m \frac{\partial M_*}{\partial y} + (\mu_m + \kappa_m) \frac{\partial^2 u_m}{\partial y^2}, \tag{2.1}$$

$$\rho_m \tau \frac{\partial M_*}{\partial t} = -2\kappa_m M_* - \kappa_m \frac{\partial u_m}{\partial y} + \omega_m \frac{\partial^2 M_*}{\partial y^2}. \tag{2.2}$$

Zone-2 (Newtonian fluid).

$$\rho_n \frac{\partial u_n}{\partial t} = -\nabla p + \mu_n \frac{\partial^2 u_n}{\partial y^2}. \tag{2.3}$$

Classical hyper-stick and no-slip boundary conditions are considered and can be numerical as.

Initial conditions: At $t \leq 0$,

$$u_m(y,t) = 0 \; for - k \leq y \leq 0, \tag{2.4}$$

$$M_*(y,t) = 0 \; for - k \leq y \leq 0, \tag{2.5}$$

$$u_n(y,t) = 0 \; for \; 0 \leq y \leq k. \tag{2.6}$$

Boundary and interface conditions: At $t > 0$,

$$u_m(-k,t) = 0, \tag{2.7}$$

$$u_n(k,t) = 0, \tag{2.8}$$

$$M_*(-k,t) = 0. \tag{2.9}$$

The fluid velocities and shear stress are both continuous at the liquid-liquid interface [1], [2], [147]. These constraints can be expressed mathematically as the equations (2.10), and (2.11).

$$u_m(0,t) = u_n(0,t), \tag{2.10}$$

$$\mu_n u_{n_y} = (\mu_m + \kappa_m) u_{m_y} + \kappa_m M_*, at \; y = 0. \tag{2.11}$$

As the microrotation is proportional to the couple stress at the boundary (At the interface), Hence the general form of the interfacial condition for angular velocity M_*especially for the droplet case can be considered as Niefer and Kaloni [148], Faltas and Saad [149], and Saad [150], but in the current study, we chose the interfacial condition for microrotation(spin–vorticity) [1], [147] over other existing conditions at *y=0* because it is realistic and consistent to apply at the interface between two immiscible fluids.

$$M_*(0,t) = -\frac{1}{2} u_{m_y}. \tag{2.12}$$

Introducing the non-dimensional parameters $\bar{x} = \frac{x}{k}, \bar{y} = \frac{y}{k}, \overline{u_m} = \frac{u_m}{U_0}, \overline{u_n} = \frac{u_n}{U_0}, \overline{u_p} = \frac{u_p}{U_0}$, $\bar{p} = \frac{p}{\rho_m {U_0}^2}, \bar{t} = \frac{tU_0}{k}$, $\omega_m = (\mu_m + \kappa_m/2)\tau$ with $\tau = k^2$ and $n_1 = \frac{\kappa_m}{\mu_m}$ and $Re = \frac{\rho_m U_0}{\mu_m}$ is the Reynolds number. $m_1 = \frac{\mu_n}{\mu_m}, r_n = \frac{\rho_n}{\rho_m}$ are the ratio of viscosity and density of the two liquids, respectively. $-\nabla p = -\partial p/\partial x = Ge(t)$ is the applied time-dependent pressure gradient in the *x*-axial direction with $t > 0$. Three distinct cases for $Ge(t)$ are considered in the numerical analysis:

Case-1:$Ge(t) = Ge$ (If the fluid flow is triggered by an applied constant pressure gradient).

Case-2:$Ge(t) = Ge * Sin(wt)$ (If the fluid flow is triggered by an applied periodic pressure gradient with oscillating parameter w).

Case-3:$Ge(t) = Ge * e^{-\lambda t}$ (If the fluid flow is triggered by a decaying pressure gradient with decaying parameter λ).

After dropping the bars and introducing the above non-dimensional parameters and appropriate initial, interfacial, and boundary conditions, according to the stable interface scheme, the equations (2.1) - (2.3) emerge as.

Zone-1 (micropolar liquid).

$$u_{m_t} = Ge(t) + \frac{n_1 M_{*_y}}{Re} + \frac{(n_1+1)u_{m_{yy}}}{Re}, \tag{2.13}$$

$$M_{*_t} = \frac{(2+n_1)M_{*_{yy}}}{2Re} - \frac{n_1\left(2M_* + u_{m_y}\right)}{Re}. \tag{2.14}$$

Zone-2 (Newtonian fluid).

$$u_{n_t} = \frac{Ge(t)}{r_n} + \frac{m_1}{r_n}\frac{u_{n_{yy}}}{Re}. \tag{2.15}$$

The equations (2.4) - (2.12) are considered as initial, interfacial, and boundary conditions with $k = 1$.

2.2.1 Computation of velocity and microrotation under scheme-1

To obtain the velocity and micro-rotation profiles for Newtonian and Eringen micropolar fluids in the respective zones under the flat interface scheme, one may replace the approximation of the spatial components as the equations (1.30), (1.31), and (1.32) of the I and II order unidirectional derivative. Hence the system of coupled partial equations (2.13) - (2.15) followed by the MCB-DQM scheme (1.69) - (1.72) numerically solved with the initial and boundary conditions (2.4) - (2.12), and the linear velocities and angular velocity component (microrotation) profiles of both fluids and are readily obtained. The equations (2.13) - (2.15) can be updated as follows.

Zone-1 (micropolar liquid).

$$u_{m_t}=Ge(t)+\frac{n_1}{Re}\left(\sum_{j=1}^{N} a^*{}_{ij}M_*(y_j,t)\right)+\frac{(n_1+1)}{Re}\left(\sum_{j=1}^{N} b^*{}_{ij}u_m(y_j,t)\right), \tag{2.16}$$

$$M_{*_t}=\frac{(n_1+2)}{2Re}\left(\sum_{j=1}^{N} b^*{}_{ij}M_*(y_j,t)\right)-\frac{n_1}{Re}\left(2M_*+\sum_{j=1}^{N} a^*{}_{ij}u_m(y_j,t)\right). \tag{2.17}$$

Zone-2 (Newtonian fluid).

$$u_{n_t}=\frac{Ge(t)}{r_n}+\frac{m_1}{r_n}\frac{\sum_{j=1}^{N} b^*{}_{ij}u_n(y_j,t)}{Re}. \tag{2.18}$$

Thus, equations are reduced into a system of ordinary differential equations in time, for *i=1, 2, 3…, N*, and the system is solved by the robust four-step third-order SSP-RK43 scheme (1.69) - (1.72). The velocities and microrotation in both zones are obtained as follows.

At first step, for *i=1,2,3…,N.*

Zone-1 (micropolar liquid).

$$u_{m_1} = u_{m_0} + \frac{\Delta t}{2}\begin{pmatrix} Ge(t) + \frac{n_1}{Re}\left(\sum_{j=1}^{N} a^*{}_{ij} M_{*_0}(y_j,t)\right) \\ + \frac{(n_1+1)}{Re}\left(\sum_{j=1}^{N} b^*{}_{ij} u_{m_0}(y_j,t)\right) \end{pmatrix}, \tag{2.19}$$

$$M_{*_1} = M_{*_0} + \frac{\Delta t}{2}\begin{pmatrix} \frac{(n_1+2)}{2Re}\left(\sum_{j=1}^{N} b^*{}_{ij} M_{*_0}(y_j,t)\right) - \\ \frac{n_1}{Re}\left(2M_{*_0} + \sum_{j=1}^{N} a^*{}_{ij} u_{m_0}(y_j,t)\right) \end{pmatrix}. \tag{2.20}$$

Zone-2 (Newtonian fluid).

$$u_{n_1} = u_{n_0} + \frac{\Delta t}{2}\left(\frac{Ge(t)}{r_n} + \frac{m_1}{r_n}\frac{\sum_{j=1}^{N} b^*{}_{ij} u_{n_0}(y_j,t)}{Re}\right). \tag{2.21}$$

In the first step of the method, the conditions (2.4) - (2.12) are applied favourably.

At the second step, for *i=1,2,3…,N.*

Zone-1 (micropolar liquid).

$$u_{m_2} = u_{m_1} + \frac{\Delta t}{2}\begin{pmatrix} Ge(t) + \frac{n_1}{Re}\left(\sum_{j=1}^{N} a^*{}_{ij} M_{*_1}(y_j,t)\right) \\ + \frac{(n_1+1)}{Re}\left(\sum_{j=1}^{N} b^*{}_{ij} u_{m_1}(y_j,t)\right) \end{pmatrix}, \tag{2.22}$$

$$M_{*_2} = M_{*_1} + \frac{\Delta t}{2}\begin{pmatrix} \frac{(n_1+2)}{2Re}\left(\sum_{j=1}^{N} b^*{}_{ij} M_{*_1}(y_j,t)\right) - \\ \frac{n_1}{Re}\left(2M_{*_1} + \sum_{j=1}^{N} a^*{}_{ij} u_{m_1}(y_j,t)\right) \end{pmatrix}. \tag{2.23}$$

Zone-2 (Newtonian fluid).

$$u_{n_2} = u_{n_1} + \frac{\Delta t}{2}\left(\frac{Ge(t)}{r_n} + \frac{m_1}{r_n}\frac{\sum_{j=1}^{N} b^*{}_{ij} u_{n_1}(y_j,t)}{Re}\right). \tag{2.24}$$

In the second step of the method, the conditions (2.4) - (2.12) are applied favourably.

At the third step, for *i=1,2,3…,N.*

Zone-1 (micropolar liquid).

$$u_{m_3} = \frac{2u_{m_0}}{3} + \frac{u_{m_2}}{3} + \frac{\Delta t}{6}\begin{pmatrix} Ge(t) + \frac{n_1}{Re}\left(\sum_{j=1}^{N} a^*{}_{ij} M_{*_2}(y_j,t)\right) \\ + \frac{(n_1+1)}{Re}\left(\sum_{j=1}^{N} b^*{}_{ij} u_{m_2}(y_j,t)\right) \end{pmatrix}, \tag{2.25}$$

$$M_{*_3} = \frac{2M_{*_0}}{3} + \frac{M_{*_2}}{3} + \frac{\Delta t}{6}\begin{pmatrix} \frac{(n_1+2)}{2Re}\left(\sum_{j=1}^{N} b^*{}_{ij} M_{*_2}(y_j,t)\right) - \\ \frac{n_1}{Re}\left(2M_{*_2} + \sum_{j=1}^{N} a^*{}_{ij} u_{\boldsymbol{m}_2}(y_j,t)\right) \end{pmatrix}. \tag{2.26}$$

Zone-2 (Newtonian fluid).

$$u_{n_3} = \frac{2u_{n_0}}{3} + \frac{u_{n_2}}{3} + \frac{\Delta t}{6}\left(\frac{Ge(t)}{r_n} + \frac{m_1}{r_n}\frac{\sum_{j=1}^{N} b^*{}_{ij} u_{n_2}(y_j,t)}{Re}\right). \tag{2.27}$$

In the third step of the method, the conditions (2.4) - (2.12) are once again applied favourably.

In the fourth step, for *i=1,2,3…, N.*

Zone-1 (micropolar liquid).

$$u_m = u_{m_3} + \frac{\Delta t}{2}\begin{pmatrix} Ge(t) + \frac{n_1}{Re}\left(\sum_{j=1}^{N} a^*{}_{ij} M_{*_3}(y_j,t)\right) \\ + \frac{(n_1+1)}{Re}\left(\sum_{j=1}^{N} b^*{}_{ij} u_{m_3}(y_j,t)\right) \end{pmatrix}, \tag{2.28}$$

$$M_* = M_{*_3} + \frac{\Delta t}{2}\begin{pmatrix} \frac{(n_1+2)}{2Re}\left(\sum_{j=1}^{N} b^*{}_{ij} M_{*_3}(y_j,t)\right) - \\ \frac{n_1}{Re}\left(2M_{*_3} + \sum_{j=1}^{N} a^*{}_{ij} u_{m_3}(y_j,t)\right) \end{pmatrix}. \tag{2.29}$$

Zone-2 Newtonian fluid.

$$u_n = u_{n_3} + \frac{\Delta t}{2}\left(\frac{Ge(t)}{r_n} + \frac{m_1}{r_n}\frac{\sum_{j=1}^{N} b^*{}_{ij} u_{n_3}(y_j,t)}{Re}\right). \tag{2.30}$$

In the fourth step of the method, the conditions (2.4) - (2.12) are also regarded favourably. Hence the fluid (linear) velocity and angular velocity (Eringen microrotation) profiles i. e. u_m, M_* of micropolar fluid in zone-1 and also the fluid velocity (linear) and particle velocity components i.e. u_n for Newtonian fluid in zone-

2 can be numerically obtained at the fourth step of MCB-DQM.In non-dimensional form, for both the fluid velocities, the volume flow rate across the duct is calculated as.

$$Q^* = \int_{-1}^{0} u_m(y_j, t)dy + \int_{0}^{1} u_n(y_j, t)dy. \quad (2.31)$$

2.2.2 Results and analysis for velocity and microrotation

The fluid velocity profiles for the constant pressure gradient at different times and different fluid parameters are demonstrated in Figure 2.2-Figure 2.6, and it is found to be of parabolic nature. It is spotted from Figure 2.2 and Figure 2.3 that fluid velocity rises in both regions with increasing time *t*, and Ge (pressure gradients) value furthermore; variations in the Newtonian region of fluid are higher in terms of magnitude than in the micropolar region of fluid.

The behavior of fluid velocity with Reynolds number *Re* can be seen in Figure 2.4. Enhancing the Re value reduced the viscous force, leading to an increase in the flow velocity. It is also noticed that the velocities in both the regions increase, the Reynolds number increases, and this attainment is reduced near the interface.

Figure 2.5 with varying micropolar parameter n_1 shows that, initially in the region-1, there is a very slight decrease in the velocity, and then this decrement rises a bit near to interface. A similar pattern in the velocity can be seen in the region-2 as the micropolar parameter grows and velocity reaches the steady-state at a higher value of n_1.

Figure 2.6 shows that the fluid velocity declines significantly in region-2 and declines slightly in region-1 with an increase in the viscous ratio m_1 .In region-2, the gain in velocity is reduced near the interface as the viscosity ratio increases; hence variations in the Newtonian region of fluid are higher in magnitude than in the micropolar region of fluid.

Like the velocity profile, similar behavior of the microrotation profile is observed for micropolar fluid in Figure 2.7, Figure 2.8, and Figure 2.11. The angular velocity

increases as the viscous ratio m_1, time t, and pressure Ge augments reach the steady-state at greater values.

Figure 2.9 with varying Reynolds number (Re) shows that initially there is a little decrease in the micro rotation for micropolar fluid, and then it rises significantly as the parameter Re grows.

Figure 2.10 demonstrated the microrotation profile for micropolar fluid with varying parameter n_1 and it can be seen that the micro-rotation decreases as the n_1 augments.

Figure 2.12 and Figure 2.13 show the velocity and micro-rotation profile when the periodic pressure gradient $Ge(t) = Ge * Sin(wt)$ is applied with differing time. It is observed that the fluid velocity oscillates in both the regions like it increases as $0 < wt \leq \pi$ and the velocity profile decreases after $wt > \pi$. Similarly, the micro-rotation also swings with variation in time. The fluid velocity and the micro-rotation profiles for the periodic pressure gradient with different fluid parameters like Reynolds number Re viscosity ratio m_1 and the micropolar parameter n_1 are also examined. It is found that in both regions the obtained results with varying values of Re, m_1, and n_1 are the same as the velocity and micro-rotation profiles for constant pressure gradient case, so these similar results are not presented.

The fluid velocity and micro rotation profiles are obtained for decaying pressure gradient $Ge(t)=Ge * e^{-\lambda t}$ with varying time and different fluid parameters like Reynolds number Re viscosity ratio m_1 and the micropolar parameter n_1. It is observed that all the results with varying values of Re, m_1, and n_1 are the same as the velocity and micro-rotation profiles for the constant pressure gradient case. It can be noticed from Figure 2.14 that initially, the fluid velocity increases in both the regions as $0 < t \leq 1$ and then it shows the significant declines after $t > 1$.The fluid velocity approaches zero in both regions for a high time value. Similarly, the micro-rotation profile for decaying pressure gradient in region-1 can be seen in Figure 2.15. It can be

noticed that initially, the micro-rotation increases in region-1 as $0 < t \leq 1$ and then it shows the significant declines after $t > 1$.

To study the volume flow rate for different fluid parameters like pressure gradient Ge , Reynolds number Re, viscosity ratio $m_1$and the micropolar parameter n_1 the fluid velocities $u_m(y_j, t)$, $u_n(y_j, t)$ for both regions are computed numerically with DQM using the B-Spline basis function, and then numerical integration using an equation (2.32) is obtained. It is also observed from Table 2.1 shows that pressure gradient Ge, Reynolds number Re have an increasing effect while viscosity ratio $m_1$and the micropolar parameter n_1, has a decreasing effect on volume flow rate. The qualitative nature of fluid flow in both regions is similar to [1] as in both the study, and the flow rate decreased with m_1, and n_1, and it increases with pressure and Reynolds number.

Table 2.1: The volume flow rate

CB-DQM $\Delta t = 10^3$		*Crank-Nicolson approach[1]*		*CB-DQM* $\Delta t = 10^3$		*Crank-Nicolson approach[1]*		*CB-DQM* $\Delta t = 10^3$		*Crank-Nicolson approach[1]*		*CB-DQM* $\Delta t = 10^3$		*Crank-Nicolson approach [1]*	
Ge	Q^*	Ge	Q^*	Re	Q^*	Re	Q^*	m_1	Q^*	m_1	Q^*	n_1	Q^*	n_1	Q^*
5	*2.124209*	*5*	*2.9526*	*2*	*4.260441*	*1*	*3.4248*	*0.15*	*4.7608*	*0.3*	*7.0797*	*0.1*	*1.28787*	*0.3*	*6.1146*
10	*4.248417*	*10*	*5.9052*	*3*	*4.572287*	*2*	*5.9052*	*0.30*	*4.4960*	*0.5*	*5.9052*	*0.2*	*1.27987*	*0.5*	*5.9052*
15	*6.372626*	*15*	*8.8577*	*4*	*4.763817*	*3*	*7.4472*	*0.45*	*4.3027*	*0.7*	*5.1970*	*0.3*	*1.27213*	*0.7*	*5.7176*
20	*8.496835*	*20*	*11.8103*	*5*	*4.895501*	*4*	*8.4637*	*0.60*	*4.1514*	*0.9*	*4.7401*	*0.4*	*1.26463*	*0.9*	*5.5490*

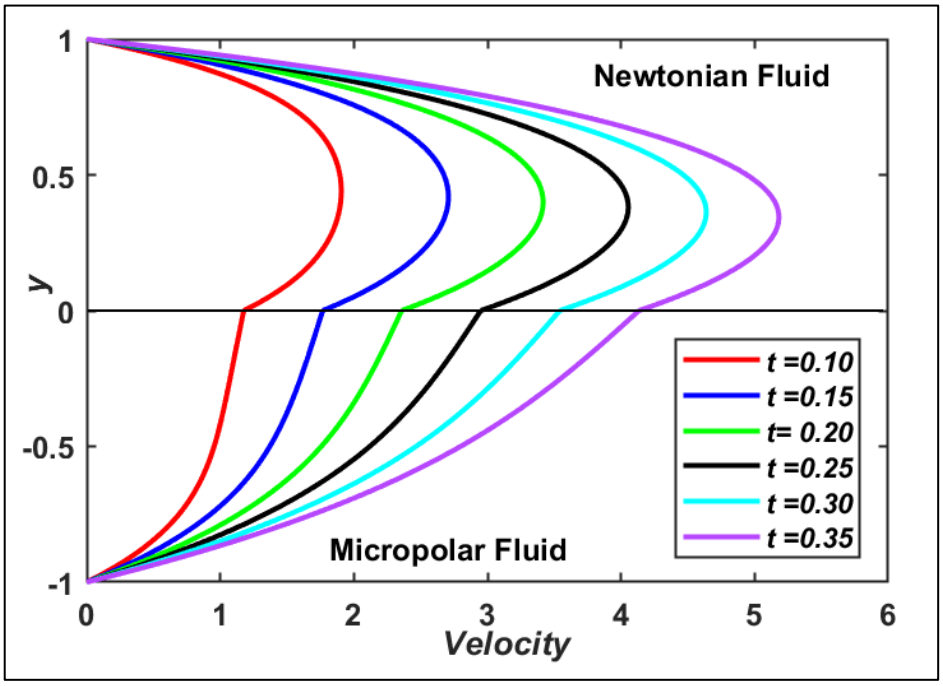

Figure 2.2:Velocity profile under scheme-1 with varying time

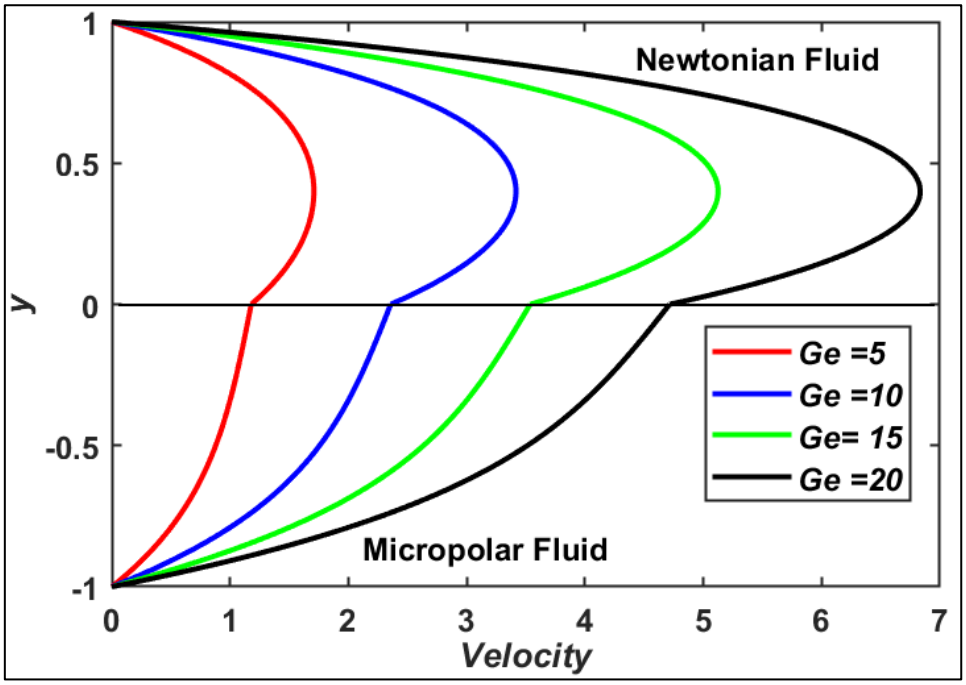

Figure 2.3: Velocity profile under scheme-1 with constant pressure gradient

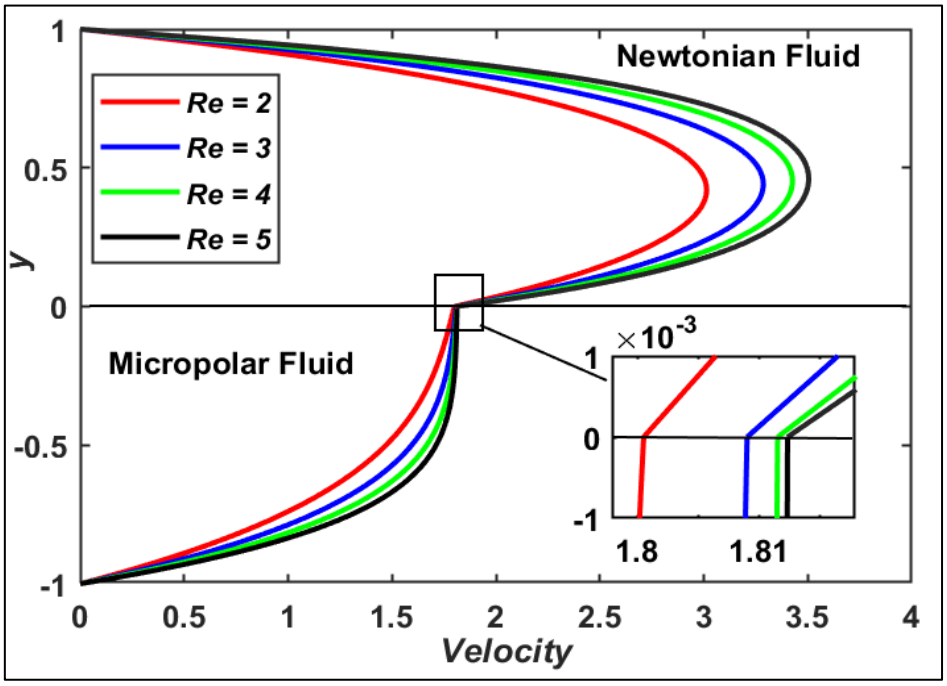

Figure 2.4: Velocity profile under scheme-1 with Reynolds number Re

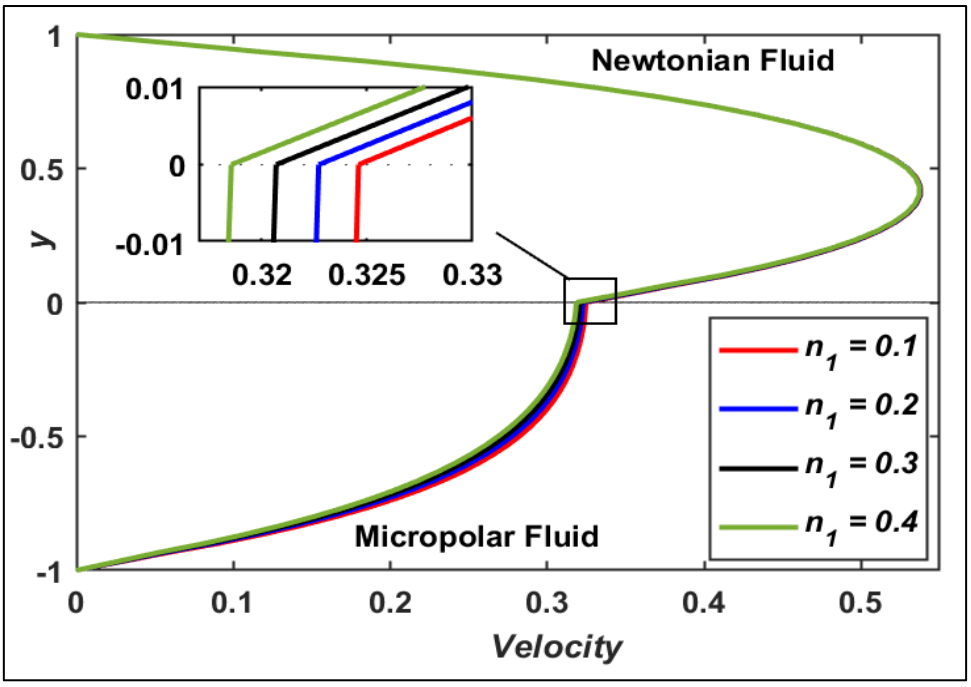

Figure 2.5: Velocity profile under scheme-1 with micropolar parameter

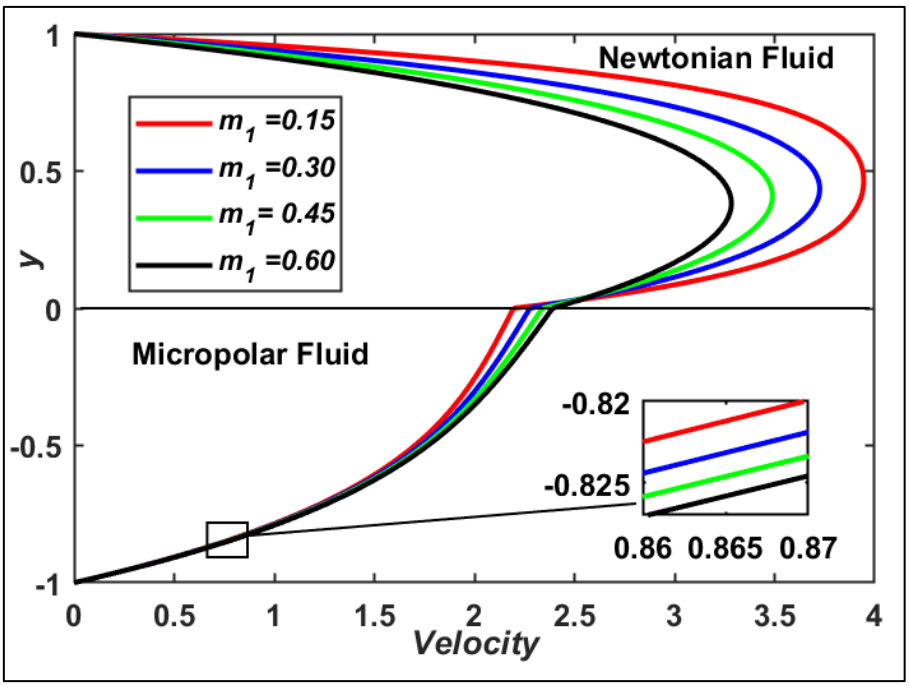

Figure 2.6:Velocity profile under the scheme-1with ratio of viscosity

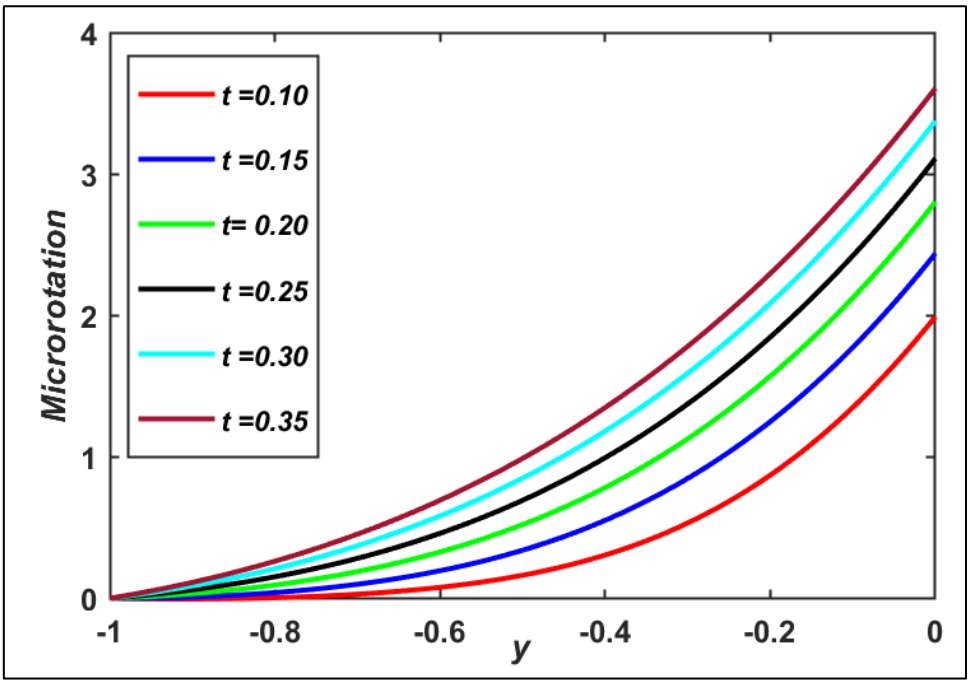

Figure 2.7:Microrotation profile with varying time

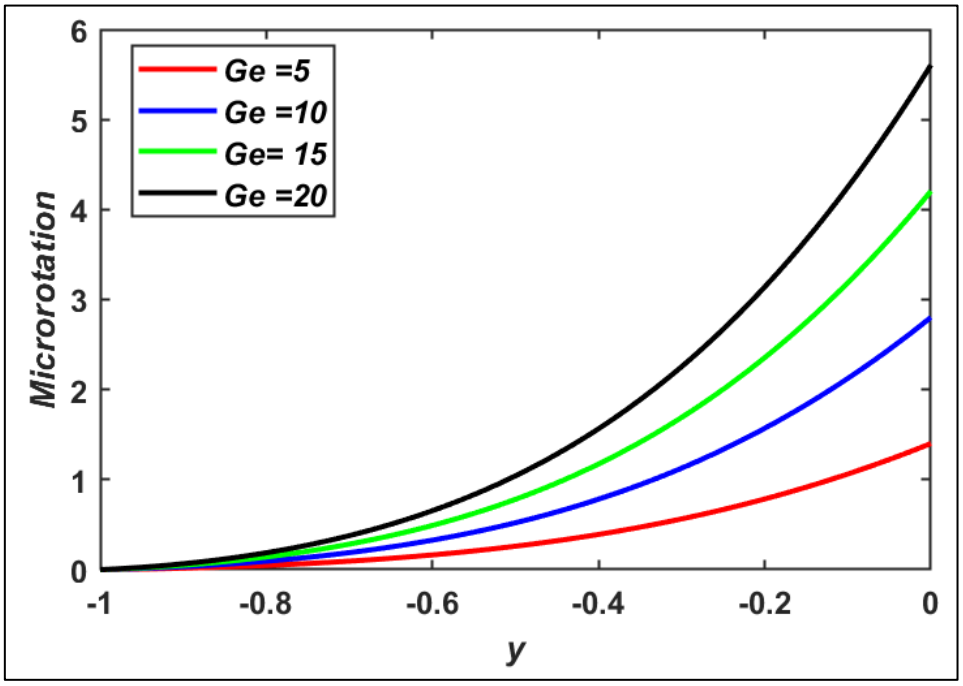

Figure 2.8: Microrotation under scheme-1 with constant pressure gradient

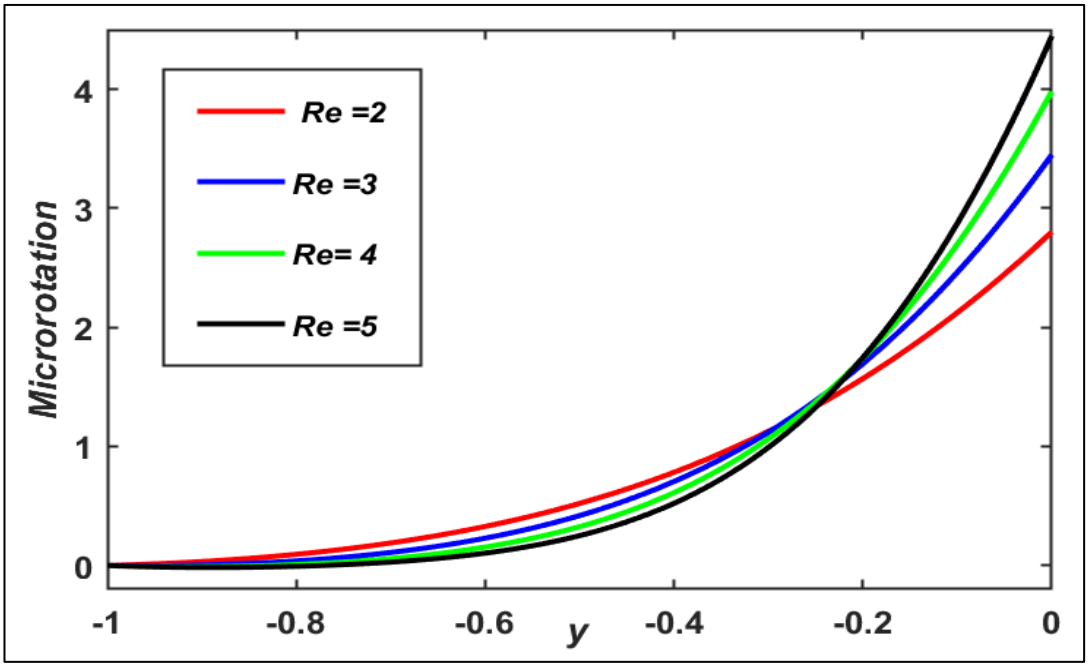

Figure 2.9: Microrotation under scheme-1with Reynolds number

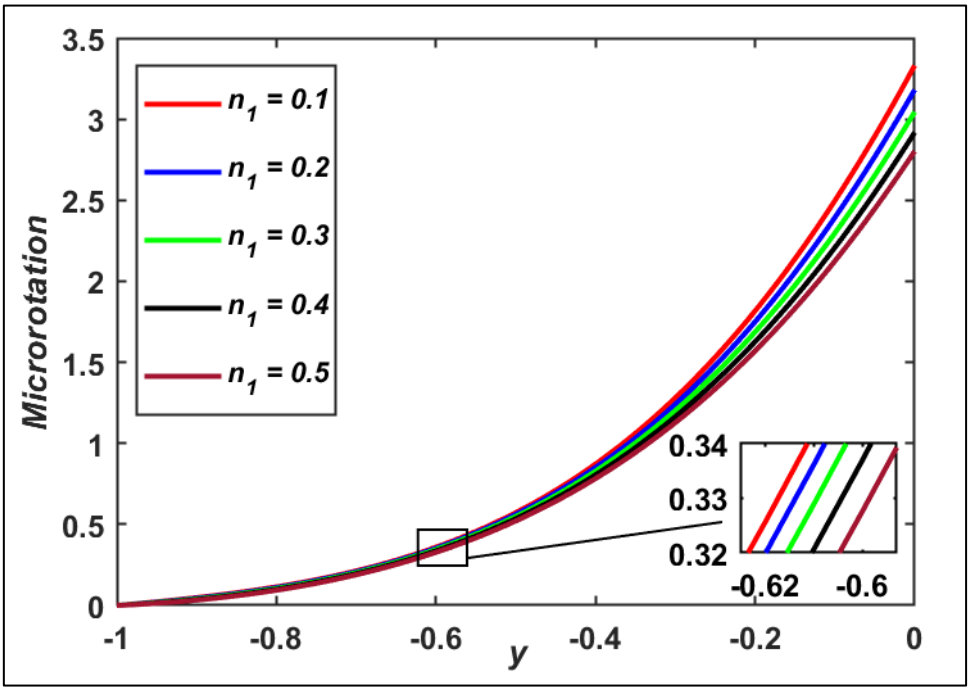

Figure 2.10: Microrotation under scheme-1 with micropolar parameter n_1

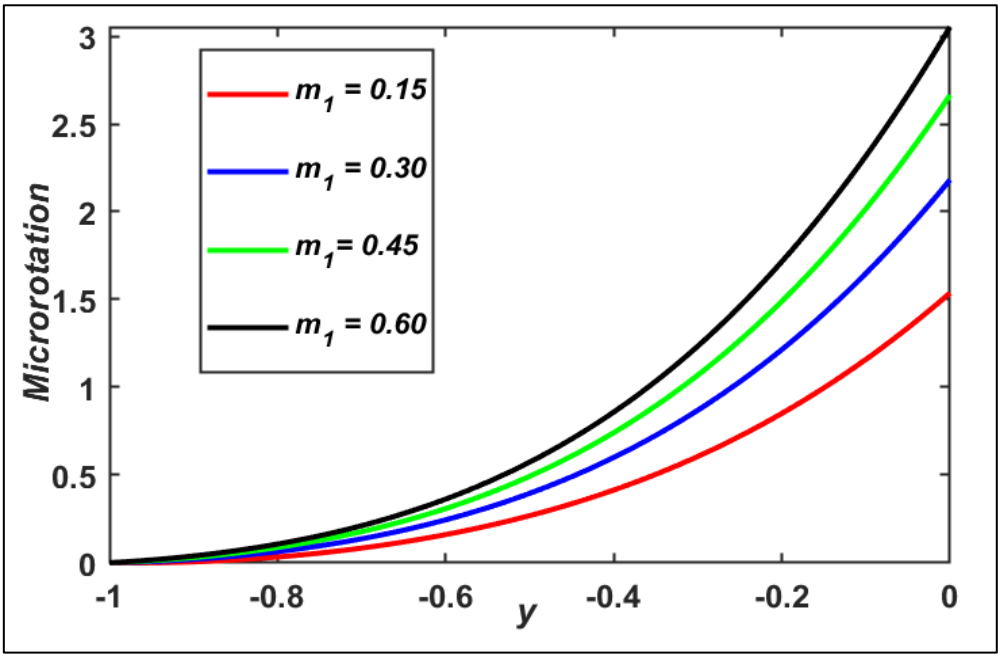

Figure 2.11: Microrotation under scheme-1 with the ratio of viscosity m_1

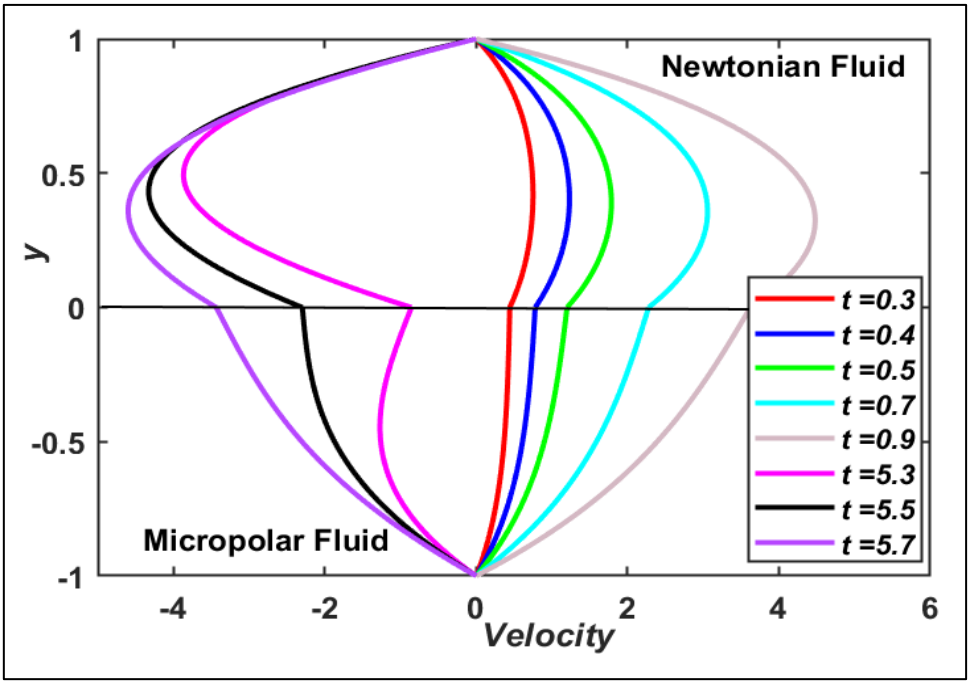

Figure 2.12: Velocity under scheme-1 for periodic pressure gradient with time

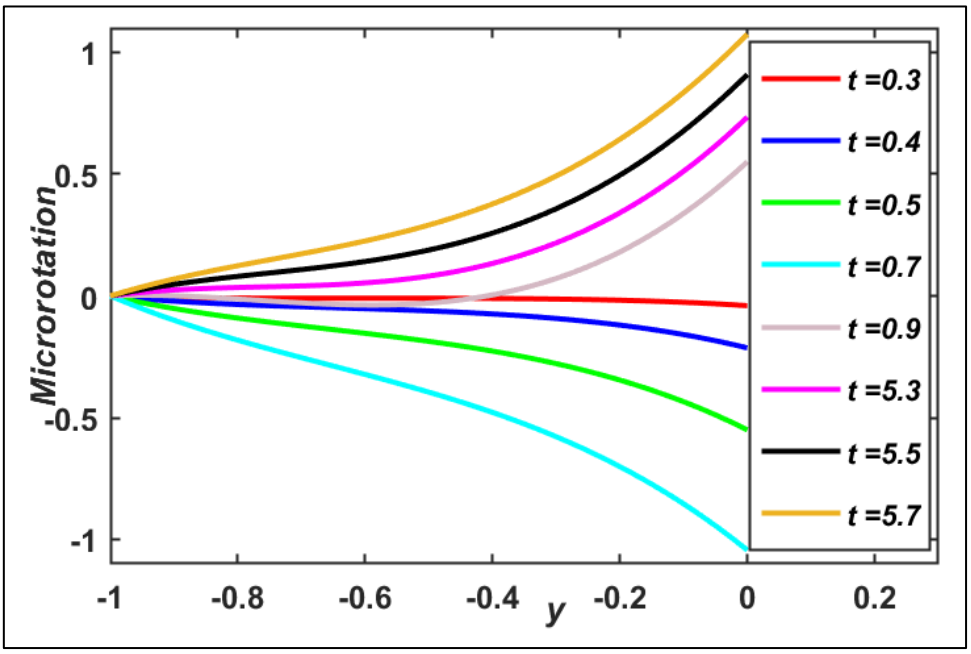

Figure 2.13: Microrotation under scheme-1 for periodic pressure gradient with time

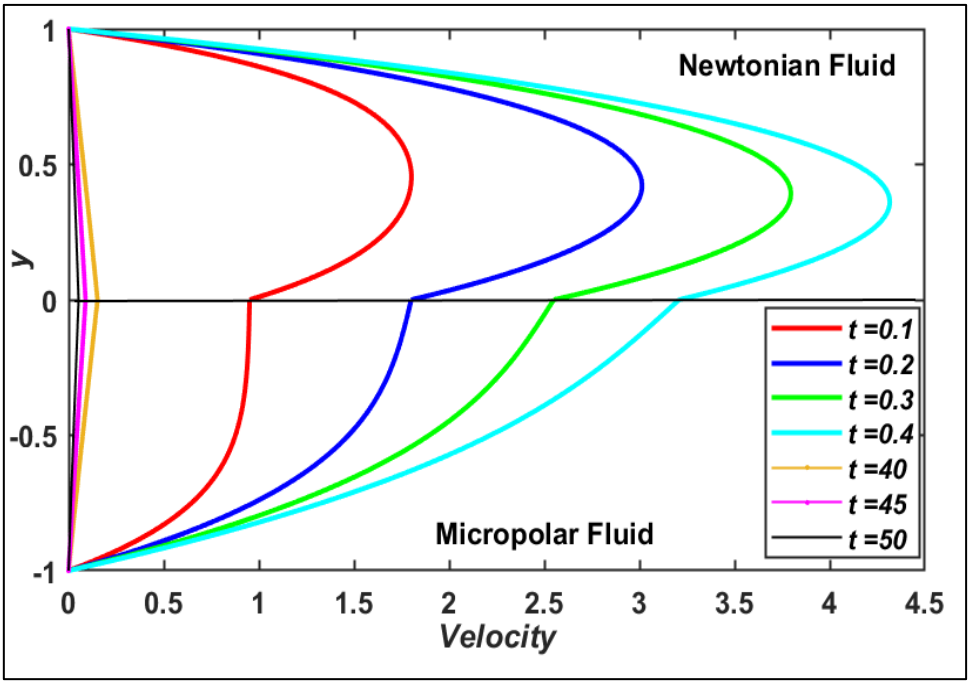

Figure 2.14: Velocity under scheme-1 for decaying pressure gradient with time

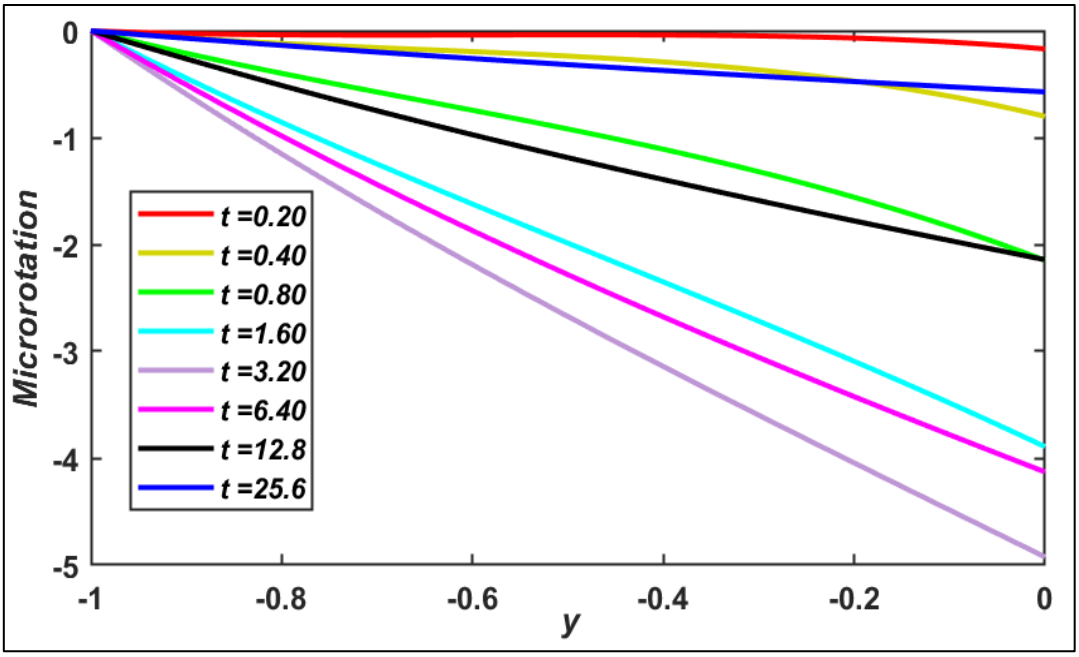

Figure 2.15: Microrotation under scheme-1 for decaying gradient with time

2.3 Formulation of two immiscible micropolar and Newtonian fluids with an unstable interface

Consider the unsteady, laminar, unidirectional, and pressure-driven flow of two immiscible, micropolar, and Newtonian fluids undergoing shearing motions. An interfacial instability occurs owing to a primary viscosity jump, so a moving interface is considered between these immiscible fluids. The following assumptions are being made for the flow transport.

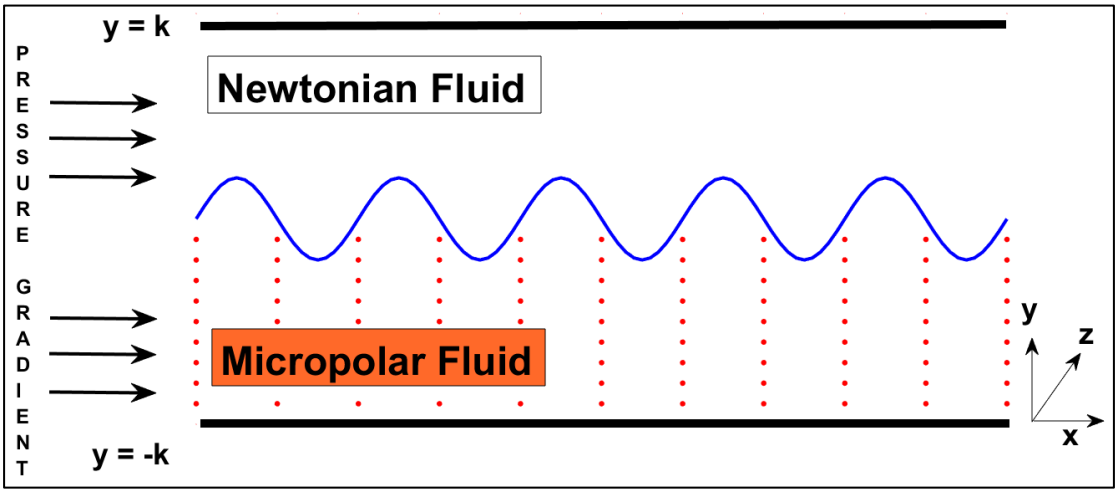

Figure 2.16: Geometrical configuration of two immiscible micropolar and Newtonian (scheme-1b) liquids with moving interface

i. Both the fluids are viscous and incompressible and move between two horizontal parallel non-porous plates. The plates are located in the *X*-*Z* plane, as depicted in Figure 2.16.

ii. Both plates are stable while the flow gets momentum by the uniform pressure gradient applied from the *x*-direction and the characteristic flow velocity is U_0.

iii. Let ρ_m, $\mu_m$be the density and viscosity of micropolar fluid which lies in ($-k \leq y \leq l_1$) and possesses a linear fluid velocity u_m, microrotation (angular velocity) M_1, vortex viscosity κ_m, gyro-viscosity ω_m, and gyration parameter τ.

iv. The Newtonian fluid has a density ρ_n, viscosity μ_n, velocity u_n and occupies the region ($l_1 \leq y \leq k$).

v. Due to a viscosity jump, interfacial instability occurs; the evolution of the interface is analyzed by using the horizontal attenuation in the initial interface phase.

vi. The flow of these immiscible fluids receives momentum in the x-direction via applied common pressure gradients with an average density given by $\rho^* = \rho_m + C_s(\rho_n - \rho_m)$ and the viscosity $\mu^* = \mu_m + C_s(\mu_n - \mu_m)$.

vii. The possibility of a jump across the interface is allowed, and the volume fraction function $C_{i=1}$ describes the interface movement between micropolar and Newtonian immiscible fluids of different densities and viscosities.

viii. Let the initial interface be $l_1 y_m + A_0 cos(B_0 y)$, where y_m is the average depth of interface, with the amplitude A_0, and wavenumber B_0.

ix. The mean flow velocity is driven by a single momentum equation (1.19), with the resultant velocity field shared between the transitions.

x. The volume fraction function $C_{i=1}$ is transported by the non-dimensionalized average velocity field u^* equation (1.19) Li and Renardy [81].

xi. The body force F, in the equation (1.20) is modelled as a surface tension force by the Continuum Surface Force model, and the surface tension is reconstructed as a volume force

$$F_s = \sigma\omega\nabla C_{i=1}. \tag{2.32}$$

where σ is the interfacial tension between two liquid phases and ω is the mean free surface curvature, given by-

$$\omega = -\frac{\nabla^2 C_{i=1}}{\|\nabla C_{i=1}\|} = -\frac{\frac{\partial^2 C_{i=1}}{\partial x^2}+\frac{\partial^2 C_{i=1}}{\partial y^2}}{\sqrt{\left(\frac{\partial C_{i=1}}{\partial x}\right)^2+\left(\frac{\partial C_{i=1}}{\partial y}\right)^2}}, \tag{2.33}$$

$$F_s = -\sigma \frac{\frac{\partial^2 C_{i=1}}{\partial x^2}+\frac{\partial^2 C_{i=1}}{\partial y^2}}{\sqrt{\left(\frac{\partial C_{i=1}}{\partial x}\right)^2+\left(\frac{\partial C_{i=1}}{\partial y}\right)^2}}\left(\frac{\partial C_{i=1}}{\partial x}+\frac{\partial C_{i=1}}{\partial y}\right). \tag{2.34}$$

As the flow is unidirectional so $\frac{\partial C_{i=1}}{\partial x} = \frac{\partial^2 C_{i=1}}{\partial x^2} = 0;\ F_s = -\sigma \frac{\partial^2 C_{i=1}}{\partial y^2}$. (2.35)

xii. The microrotation vector is available only in the zone –1 fluid, and it is assumed that the angular velocity of lower fluid also affects the interface between the immiscible fluids, so first, the microrotation profile is obtained by the governing equations of micropolar fluid flow.

$$\rho_m \frac{\partial u_m}{\partial t} = -\frac{\partial p}{\partial x} + \kappa_m \frac{\partial M_*}{\partial y} + (\mu_m + \kappa_m)\frac{\partial^2 u_m}{\partial y^2}, \tag{2.36}$$

$$\rho_m \tau \frac{\partial M_*}{\partial t} = \omega_m \frac{\partial^2 M_*}{\partial y^2} - \kappa_m (2M_* + \frac{\partial u_m}{\partial y}). \tag{2.37}$$

The governing equation for mean flow $u^*(y,t)$ and interface track $C_{i=1}$ in $(-k \le y \le k)$ under the aforesaid assumed constraints are

$$\frac{\partial C_i}{\partial t} + u^* \frac{\partial C_{i=1}}{\partial y} = 0 \tag{2.38}$$

$$\rho^* \frac{\partial u^*}{\partial t} = -\frac{\partial p}{\partial x} + (\mu^* + \kappa_m)\frac{\partial^2 u^*}{\partial y^2} + \kappa_m \frac{\partial M_*}{\partial y} + \rho^* g - \sigma \frac{\partial^2 C_{i=1}}{\partial y^2}. \tag{2.39}$$

The classical no-slip and hyper-stick conditions are considered at the boundaries. These conditions can be written as follows in numerical terms.

Initial conditions: At $t \le 0$,

$$\left.\begin{array}{ll} M_*(y,t) = 0 & for\ -k \le y \le l_1, \\ u^*(y,t) = 0 & for -k \le y \le k, \\ C_{i=1}(y,t) = A_0 cos(B_0 y) & for\ -k \le y \le k, \\ u_m(y,t) = 0 & for\ -k \le y \le l_1. \end{array}\right\} \tag{2.40}$$

Boundary conditions: At t > 0,

$$\left.\begin{array}{c} u_m(-k,t)=0, \\ M_*(-k,t)=\ 0, \\ u^*(-k,t)=0, \\ u^*(k,t)=\ 0, \\ u_m(\varepsilon,t)=\varepsilon\ , \\ M_*(\varepsilon,t)=\ -\frac{1}{2}\frac{\partial u_m}{\partial y}. \end{array}\right\} \tag{2.41}$$

Introducing the non-dimensional parameters

$$\left.\begin{array}{c} \bar{x}=\frac{x}{k},\bar{y}=\frac{y}{k},\overline{u^*}=\frac{u^*}{U_0},\bar{p}=\frac{p}{\rho^*{U_0}^2},\bar{t}=\frac{tU_0}{k},Ca=\frac{\mu^*U_0}{\sigma}, \\ \varepsilon\in[-1,1]\ s.t\ \sqrt{(u_m(\varepsilon,t)-C_{i=1})^2}=0,\ \omega_m=(\mu_m+\kappa_m/2)\tau, \\ \text{with } \tau=k^2,n_1=\frac{\kappa_m}{\mu_m},Re=\frac{\rho_m U_0}{\mu_m}\ ,r_m=\frac{\mu_n}{\mu_m},r_n=\frac{\rho_n}{\rho_m},Fr=\frac{{U_0}^2}{gk}. \end{array}\right\} \tag{2.42}$$

After dropping the bars and introducing the above non-dimensional parameters, appropriate initial, interfacial, and boundary conditions according to the scheme, the equations (2.36) - (2.39) can be revised as

(Micropolar liquid zone).

$$\frac{\partial u_m}{\partial t}=\ Ge(t)+\frac{n_1}{Re}\frac{\partial M_*}{\partial y}+\frac{(n_1+1)}{Re}\frac{\partial^2 u_m}{\partial y^2}, \tag{2.43}$$

$$\frac{\partial M_*}{\partial t}\ =\frac{\left(\frac{n_1}{2}+1\right)}{Re}\frac{\partial^2 M_*}{\partial y^2}-\frac{n_1\left(2M_*+\ \frac{\partial u_m}{\partial y}\right)}{Re}\ . \tag{2.44}$$

The Mean flow and interface track are governed as.

$$\frac{\partial C_i}{\partial t}+u^*\frac{\partial C_i}{\partial y}\ =0, \tag{2.45}$$

$$\frac{\partial u^*}{\partial t}=\left(\begin{array}{c} \frac{Ge(t)}{(\,1+C_s(r_n-1))}+\frac{(n_1+1)(1+C_s(r_m-1))}{Re(\,1+C_s(r_n-1))}\frac{\partial^2 u^*}{\partial y^2}+\frac{n_1(1+C_s(r_m-1))}{Re(\,1+C_s(r_n-1))}\frac{\partial M_*}{\partial y} \\ +\frac{1}{Fr}-\frac{1+C_s(r_m-1)}{Re*Ca(\,1+C_s(r_n-1)\,)}\frac{\partial^2 C_i}{\partial y^2} \end{array}\right). \tag{2.46}$$

Equations (2.40) - (2.42) are considered as initial and boundary conditions with $k=1$.

As the flow gets momentum by the *x*-directional time-dependent applied pressure gradient. Three different cases for $Ge(t)\ -\nabla p = -\partial p/\partial x$ with $t > 0$ are included in the analysis.

Case-I: $Ge(t) = Ge$.

Case-II: $Ge(t) = Ge * Sint$.

Case-III: $Ge(t) = Ge * e^{-t}$.

2.3.1 Computation of interface and flow velocity under scheme-1

To compute the interface tracking under the moving interface scheme flow, first, the microrotation profile is obtained in zone-1, and then the interface track is obtained by using the mean flow velocity. Hence the system of single momentum coupled partial differential equations (2.44) - (2.47) followed by the derivative approximation (1.30), (1.31), (1.41), and (1.41) are updated and solved numerically by the four-step third-order SSP-RK43 scheme (1.69) - (1.72).

(Micropolar liquid zone).

$$u_{m_t} = Ge(t) + \frac{n_1}{Re}\left(\sum_{j=1}^{N} a^*{}_{ij} M_*(y_j,t)\right) + \frac{(n_1+1)}{Re}\left(\sum_{j=1}^{N} b^*{}_{ij} u_m(y_j,t)\right), \tag{2.47}$$

$$M_{*_t} = \frac{(n_1+2)}{2Re}\left(\sum_{j=1}^{N} b^*{}_{ij} M_*(y_j,t)\right) - \frac{n_1}{Re}\left(2M_* + \sum_{j=1}^{N} a^*{}_{ij} u_m(y_j,t)\right). \tag{2.48}$$

(Micropolar fluid + Newtonian fluid zone).

$$\frac{\partial C_i}{\partial t} = -u^*(y_j,t)\left(\sum_{j=1}^{N} a^*{}_{ij} C_i(y_j,t)\right), \tag{2.49}$$

$$\frac{\partial u^*}{\partial t} = \frac{Ge(t)}{(1+C_s(r_n-1))} + \frac{(n_1+1)(1+C_s(r_m-1))}{Re(1+C_s(r_n-1))}\left(\sum_{j=1}^{N} b^*{}_{ij} u^*(y_j,t)\right) + \frac{1}{Fr} +$$
$$\frac{n_1(1+C_s(r_m-1))}{Re(1+C_s(r_n-1))}\left(\sum_{j=1}^{N} a^*{}_{ij} M_*(y_j,t)\right) - \frac{1+C_s(r_m-1)}{Re*Ca(1+C_s(r_n-1))}\left(\sum_{j=1}^{N} b^*{}_{ij} C_i(y_j,t)\right). \tag{2.50}$$

Thus, the equations are reduced into a system of ordinary differential equations in time, that is, for *i=1, 2, 3…, N*.

At the first step *for i=1,2,3…, N.*

(Micropolar liquid zone).

$$u_{m_1} = u_{m_0} + \frac{\Delta t}{2}\begin{bmatrix} Ge(t) + \frac{n_1}{Re}\left(\sum_{j=1}^{N} a^*{}_{ij} M_{*_0}(y_j,t)\right) \\ + \frac{(n_1+1)}{Re}\left(\sum_{j=1}^{N} b^*{}_{ij} u_{m_0}(y_j,t)\right) \end{bmatrix}, \tag{2.51}$$

$$M_{*_m} = M_{*_0} + \frac{\Delta t}{2}\frac{(n_1+2)}{2Re}\begin{bmatrix} \left(\sum_{j=1}^{N} b^*{}_{ij} M_{*_0}(y_j,t)\right) \\ -\frac{n_1}{Re}\left(2M_{*_0} + \sum_{j=1}^{N} a^*{}_{ij} u_{m_0}(y_j,t)\right) \end{bmatrix}. \tag{2.52}$$

(Micropolar fluid + Newtonian fluid zone).

$$C_{i_1} = C_{i_0} + \frac{\Delta t}{2}\left[-u^*{}_1(y_j,t)\left(\sum_{j=1}^{N} a^*{}_{ij} C_i(y_j,t)\right)\right], \tag{2.53}$$

$$u^*{}_1 = u^*{}_0 + \frac{\Delta t}{2}\begin{bmatrix} \frac{Ge(t)}{(1+C_s(r_n-1))} + \frac{(n_1+1)(1+C_s(r_m-1))}{Re(1+C_s(r_n-1))}\left(\sum_{j=1}^{N} b^*{}_{ij} u^*{}_0(y_j,t)\right) \\ + \frac{n_1(1+C_s(r_m-1))}{Re(1+C_s(r_n-1))}\left(\sum_{j=1}^{N} a^*{}_{ij} M_{*_0}(y_j,t)\right) + \frac{1}{Fr} \\ -\frac{1+C_s(r_m-1)}{Re*Ca(1+C_s(r_n-1))}\left(\sum_{j=1}^{N} b^*{}_{ij} C_{i_0}(y_j,t)\right) \end{bmatrix}. \tag{2.54}$$

In the second step *for i=1,2,3…, N.*

(Micropolar liquid zone).

$$u_{m_2} = u_{1_1} + \frac{\Delta t}{2}\begin{bmatrix} Ge(t) + \frac{n_1}{Re}\left(\sum_{j=1}^{N} a^*{}_{ij} M_{*_1}(y_j,t)\right) \\ + \frac{(n_1+1)}{Re}\left(\sum_{j=1}^{N} b^*{}_{ij} u_{m_1}(y_j,t)\right) \end{bmatrix}, \tag{2.55}$$

$$M_{*_2} = M_{*_1} + \frac{\Delta t}{2}\begin{bmatrix} \frac{(n_1+2)}{2Re}\left(\sum_{j=1}^{N} b^*{}_{ij} M_{*_1}(y_j,t)\right) \\ -\frac{n_1}{Re}\left(2M_{*_1} + \sum_{j=1}^{N} a^*{}_{ij} u_{m_1}(y_j,t)\right) \end{bmatrix}. \tag{2.56}$$

(Micropolar fluid + Newtonian fluid zone).

$$C_{i_2} = C_{i_1} + \frac{\Delta t}{2}\left(-u^*{}_2(y_j,t)\left(\sum_{j=1}^{N} a^*{}_{ij} C_{i_1}(y_j,t)\right)\right), \tag{2.57}$$

$$u^*_2 = u^*_1 + \frac{\Delta t}{2}\begin{bmatrix} \frac{Ge(t)}{(1+C_s(r_n-1))} + \frac{(n_1+1)(1+C_s(r_m-1))}{Re(1+C_s(r_n-1))}\left(\sum_{j=1}^{N} b^*_{ij}u^*_1(y_j,t)\right) \\ + \frac{n_1(1+C_s(r_m-1))}{Re(1+C_s(r_n-1))}\left(\sum_{j=1}^{N} a^*_{ij}M_{*_1}(y_j,t)\right) + \\ \frac{1}{Fr} - \frac{1+C_s(r_m-1)}{Re*Ca(1+C_s(r_n-1))}\left(\sum_{j=1}^{N} b^*_{ij}C_{i_1}(y_j,t)\right) \end{bmatrix}. \quad (2.58)$$

In the third step *for i=1,2,3…, N.*

(Micropolar liquid zone).

$$u_{m_3} = \frac{2u_{1_0}}{3} + \frac{u_{1_2}}{3} + \frac{\Delta t}{6}\begin{bmatrix} Ge(t) + \frac{n_1}{Re}\left(\sum_{j=1}^{N} a^*_{ij}M_{*_2}(y_j,t)\right) \\ + \frac{(n_1+1)}{Re}\left(\sum_{j=1}^{N} b^*_{ij}u_{m_2}(y_j,t)\right) \end{bmatrix}, \quad (2.59)$$

$$M_{*_3} = \frac{2M_{*_0}}{3} + \frac{M_{*_2}}{3} + \frac{\Delta t}{6}\begin{bmatrix} \frac{(n_1+2)}{2Re}\left(\sum_{j=1}^{N} b^*_{ij}M_{*_2}(y_j,t)\right) - \\ \frac{n_1}{Re}\left(2M_{*_2} + \sum_{j=1}^{N} a^*_{ij}u_{m_2}(y_j,t)\right) \end{bmatrix}. \quad (2.60)$$

(Micropolar fluid + Newtonian fluid zone).

$$C_{i_3} = \frac{2C_{i_0}}{3} + \frac{C_{i_2}}{3} + \frac{\Delta t}{6}\left[-u^*_3(y_j,t)\left(\sum_{j=1}^{N} a^*_{ij}C_{i_2}(y_j,t)\right)\right], \quad (2.61)$$

$$u^*_3 = \frac{2u^*_0}{3} + \frac{u^*_2}{3} + \frac{\Delta t}{6}\begin{bmatrix} \frac{(n_1+1)(1+C_s(r_m-1))}{Re(1+C_s(r_n-1))}\left(\sum_{j=1}^{N} b^*_{ij}u^*_2(y_j,t)\right) + \\ \frac{n_1(1+C_s(r_m-1))}{Re(1+C_s(r_n-1))}\left(\sum_{j=1}^{N} a^*_{ij}M_{*_2}(y_j,t)\right) + \\ \frac{1}{Fr} - \frac{1+C_s(r_m-1)}{Re*Ca(1+C_s(r_n-1))}\left(\sum_{j=1}^{N} b^*_{ij}C_{i_2}(y_j,t)\right) \end{bmatrix}. \quad (2.62)$$

At the fourth step *for i=1,2,3…, N.*

(Micropolar liquid zone).

$$u_m = u_{m_3} + \frac{\Delta t}{2}\begin{bmatrix} Ge(t) + \frac{n_1}{Re}\left(\sum_{j=1}^{N} a^*_{ij}M_{*_3}(y_j,t)\right) \\ + \frac{(n_1+1)}{Re}\left(\sum_{j=1}^{N} b^*_{ij}u_{m_3}(y_j,t)\right) \end{bmatrix}, \quad (2.63)$$

$$M_* = M_{*_3} + \frac{\Delta t}{2}\begin{bmatrix} \frac{(n_1+2)}{2Re}\left(\sum_{j=1}^{N} b^*_{ij}M_{*_3}(y_j,t)\right) - \\ \frac{n_1}{Re}\left(2M_{*_3} + \sum_{j=1}^{N} a^*_{ij}u_{m_3}(y_j,t)\right) \end{bmatrix}. \quad (2.64)$$

(Micropolar fluid + Newtonian fluid zone).

$$C_i = C_{i_3} + \frac{\Delta t}{6}\ \left[-u^*(y_j,t)\left(\sum_{j=1}^{N} a^*{}_{ij} C_{i_3}(y_j,t)\right)\right], \tag{2.65}$$

$$u^* = u^*{}_3 + \frac{\Delta t}{2}\begin{bmatrix} \frac{Ge(t)}{(1+C_s(r_n-1))} + \frac{(n_1+1)(1+C_s(r_m-1))}{Re(1+C_s(r_n-1))}\left(\sum_{j=1}^{N} b^*{}_{ij} u^*{}_3(y_j,t)\right) \\ + \frac{n_1(1+C_s(r_m-1))}{Re(1+C_s(r_n-1))}\left(\sum_{j=1}^{N} a^*{}_{ij} M_{*_3}(y_j,t)\right) + \\ \frac{1}{Fr} - \frac{1+C_s(r_m-1)}{Re*Ca(1+C_s(r_n-1))}\left(\sum_{j=1}^{N} b^*{}_{ij} C_{i_3}(y_j,t)\right) \end{bmatrix}. \tag{2.66}$$

In every stage, the initial and boundary conditions are taken as equations (2.41) - (2.42) with $k = 1$.

2.3.2 Results and discussion

The unstable flow of two immiscible micropolar and Newtonian fluids with mutual momentum transfer and viscosity jump across the interface is considered according to the time-dependent pressure gradient. The traditional no-slip and hyper-stick conditions on the channel's boundaries were presumed to describe the solution. Single mean flow problems with moving interface have been addressed, and MCB-DQM has acquired the interface tracking profiles. The ratio of viscous drag forces and surface tension forces acting at an interface between two immiscible fluids is known as the capillary number$\left(Ca = \frac{\mu^* U_0}{\sigma}\right)$. The current numerical technique is validated by comparing the approximated numerical result for a single non-micropolar Newtonian fluid($r_m = 1, r_n = 1, n_1 = 0$)with the exact solution. Note that if $r_m = r_n = 1$, then the interfacial force $\sigma = 0$, and hence $\frac{1}{Ca} = 0, \frac{1}{Fr} = 0$. Figure 2.17-Figure 2.18 shows the comparative analysis of calculated and exact solutions for velocity profiles at different times and discretized nodes. It is noticed that the applied numerical technique results in achieving perfect corroboration with the exact solution. The root means square error between

analytical and calculated results is significantly less and decreases with time and discretized node value.

Figure 2.18-Figure 2.27 shows the evolution of the interface between two liquids with varying time, amplitude, and wavenumber under the applied constant, periodic, and decaying pressure gradient. It is evident from Figure 2.19-Figure 2.22 that, in the case of applied constant pressure gradients, initially, the vertical elongation of the interface is large, and then the shape of the interface evolves with time; hence the undulating sequence occurs faster for a more considerable time, and the interface becomes stable for high time. Note that the top fluid is even less viscous than the bottom fluid. It is also noticed that the qualitative characteristics of this flow shall be maintained. As expected, the interface starts to shift vertically if the amplitude and wavenumber are enhanced (see Figure 2.23 and Figure 2.24). The two liquids do not penetrate each other in the same way. The evolution of the interface profile for decaying pressure gradient cases is qualitatively similar. However, a greater elapse of time is required for it to become stable, and the crest of the waves is smaller than the constant pressure case see Figure 2.25. It is also worth mentioning that the evolution of the interface profile for the periodic pressure gradient case is qualitatively similar to other cases; however, it takes more time to stabilize, and the crest of the waves is large compared to the constant and decaying pressure case (see Figure 2.26). The interface is characterized by the flow velocity, and as the externally applied pressure gradient changes periodically, the mean flow velocity also has a fluctuating nature, so the interface takes a long time to become stable. It is also noticed from Figure 2.27 that the interface becomes stable quickly with time as the micropolar parameter is reduced, i.e., weaker micropolar fluids encourage faster stabilization of the interface. The reduction in the micropolar parameter reduces the vortex viscosity and increases the dynamic viscosity, so the lower region fluid has a small vertical shift over time which leads to stability in the interface.

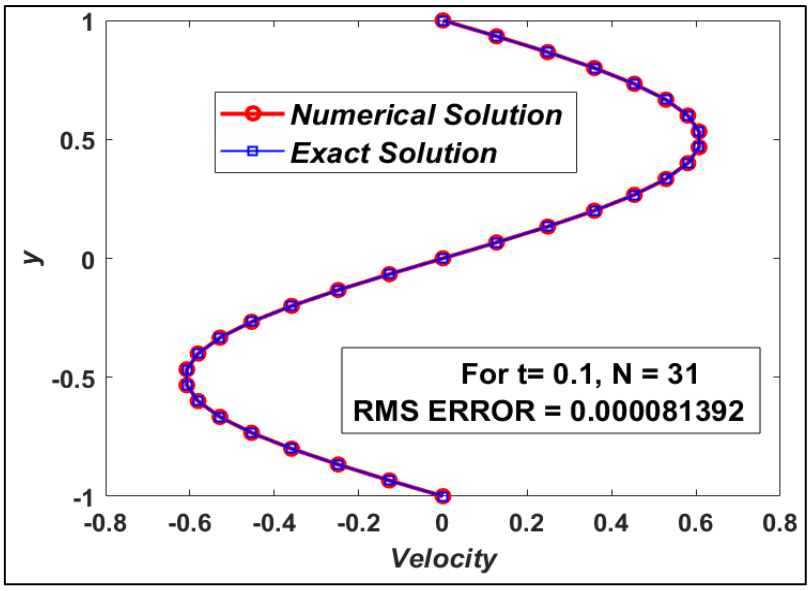

Figure 2.17: The velocity profile comparison at time *t=0.1* and *N=31*.

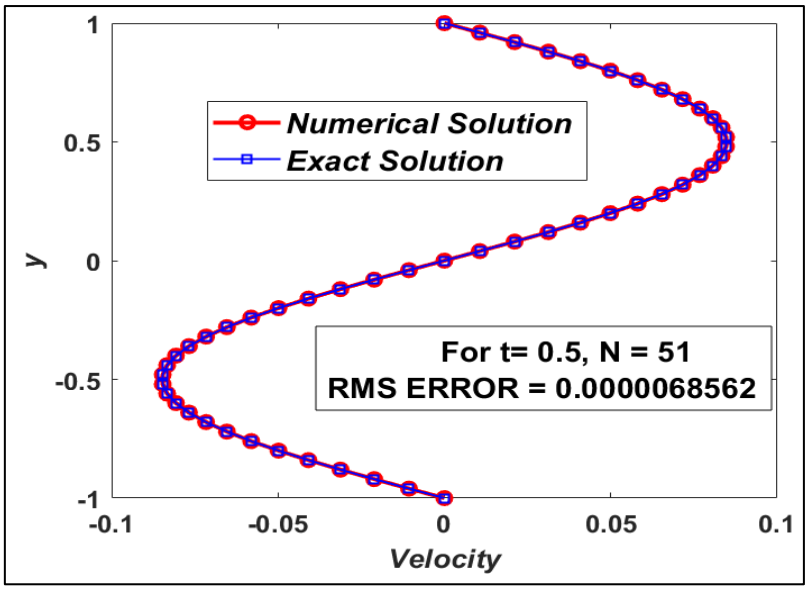

Figure 2.18: The velocity profile comparison at time *t=0.5* and *N=51*.

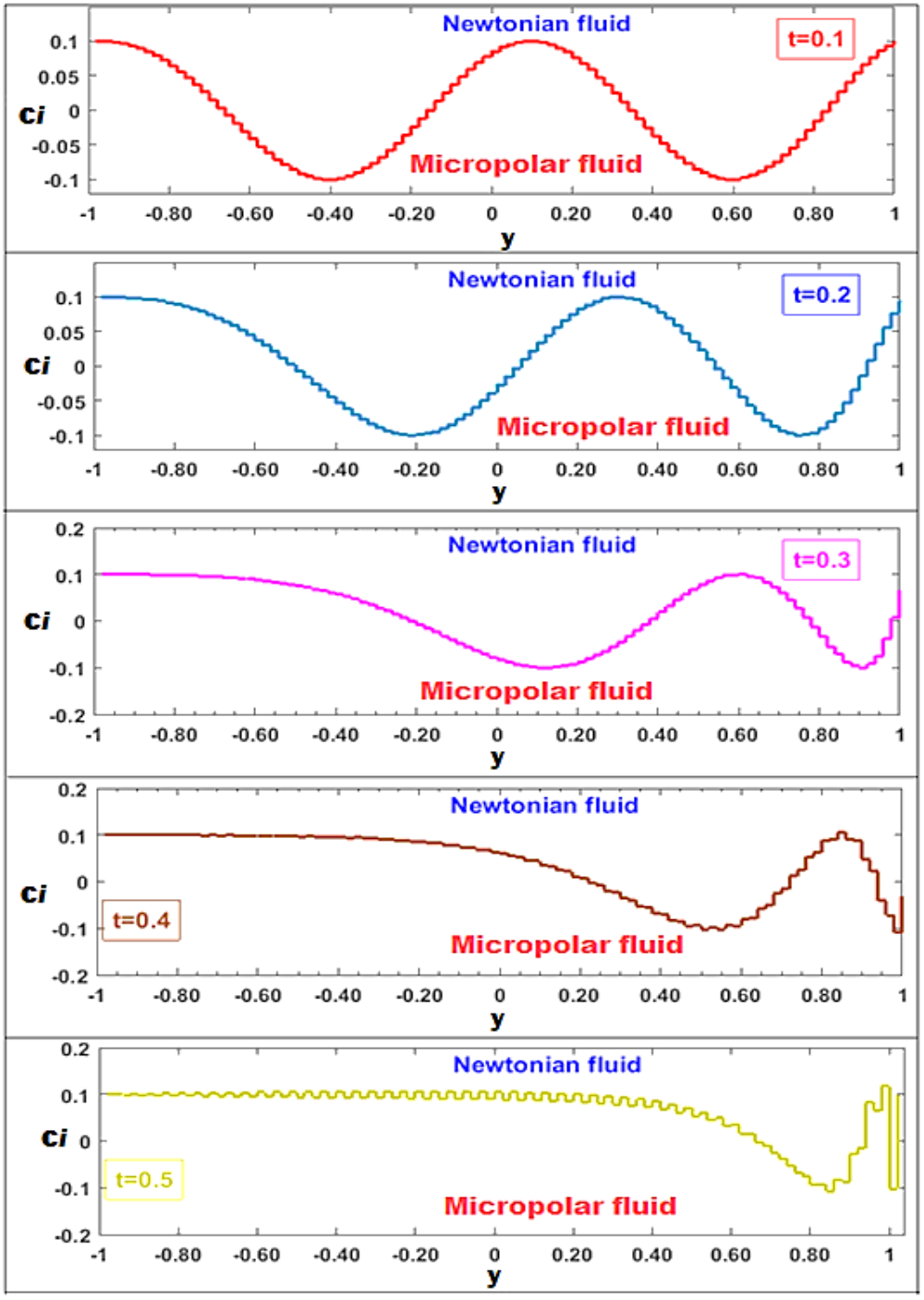

Figure 2.19:Interface tracking with varying small time when *Ge=10*, *Re*=2, r_1=0.5, r_2=0.5, C_s=0.5, Ca=0.5, $Fr = 2, n_1 = 0.5$.

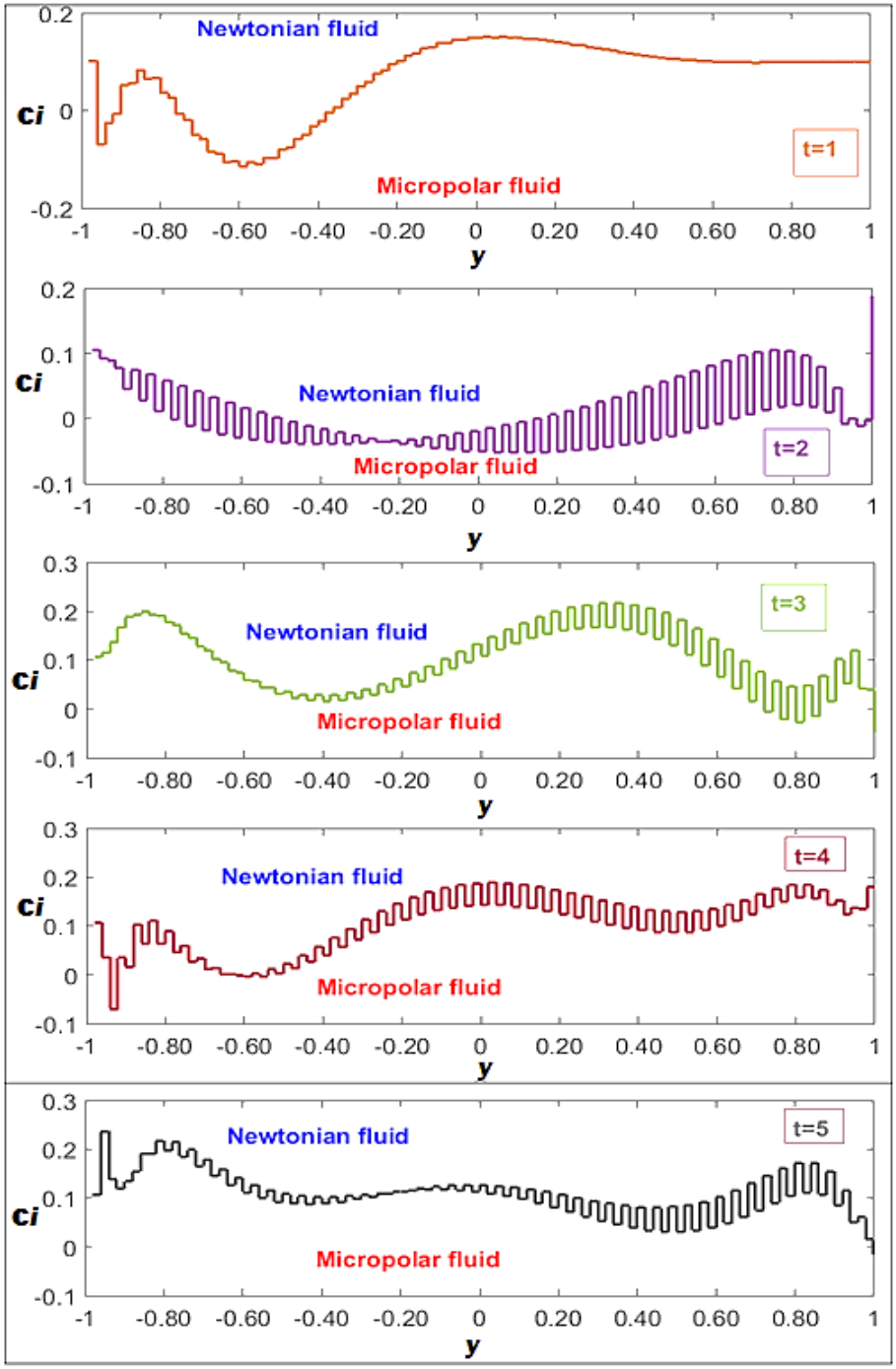

Figure 2.20:Interface tracking with varying times when *Ge=10, Re=2,* r_1*=0.5,* r_2*=0.5,* C_s*=0.5,* Ca*=0.5,* $Fr = 2, n_1 = 0.5$.

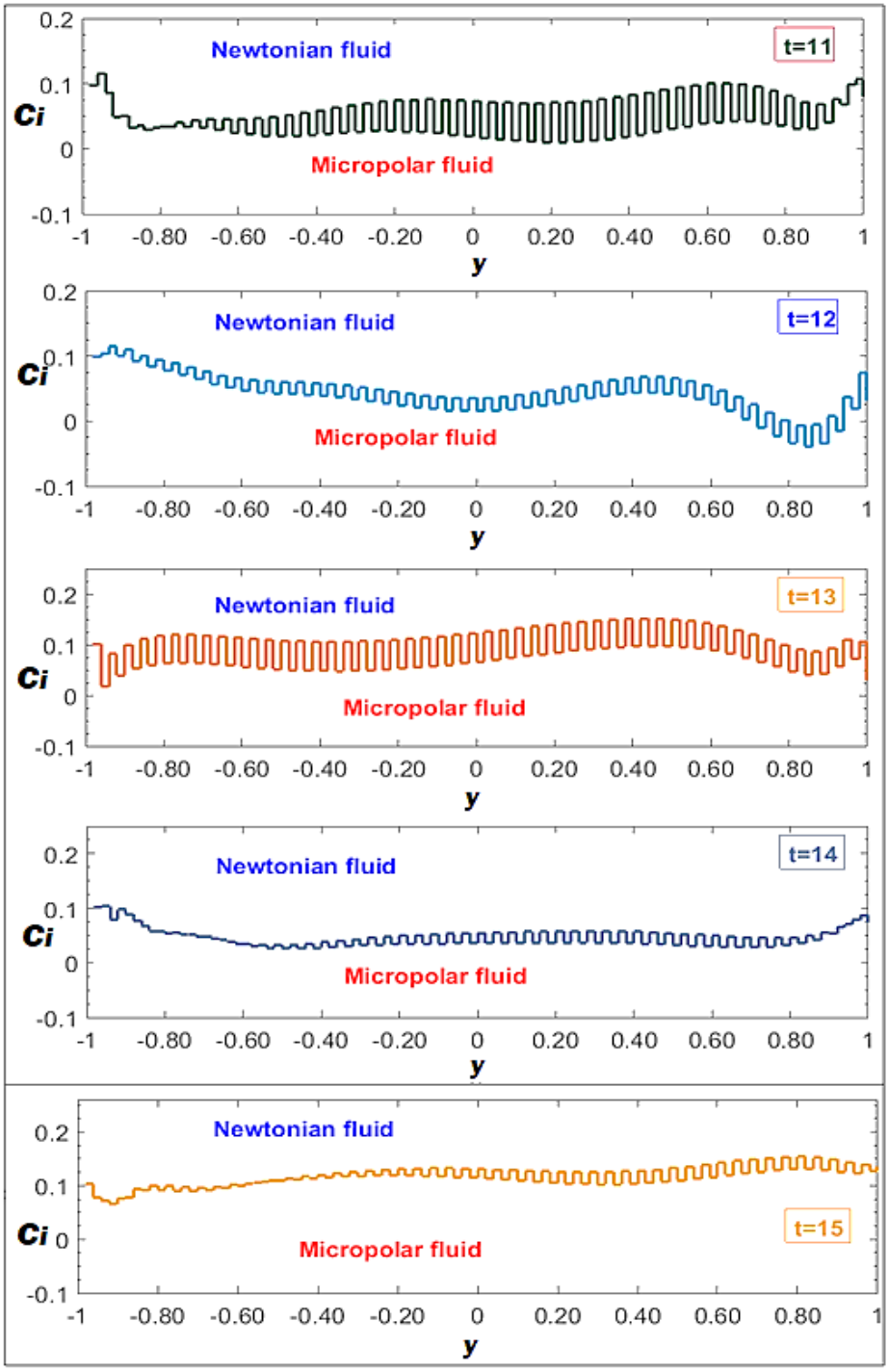

Figure 2.21: Interface tracking with varying high times when *Ge=10, Re=2,* r_1*=0.5,* r_2*=0.5,* C_s*=0.5,* Ca*=0.5,* $Fr = 2, n_1 = 0.5$.

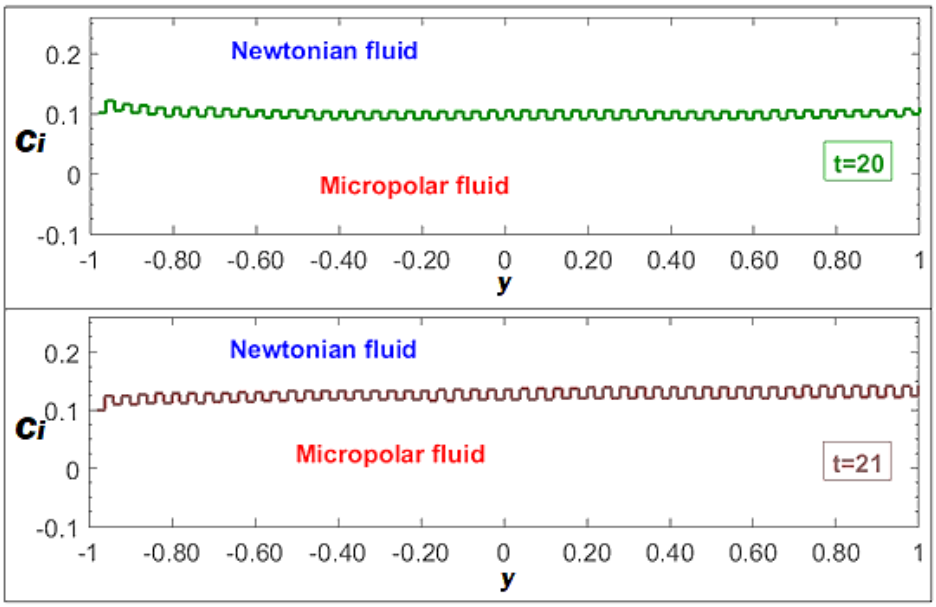

Figure 2.22: Interface tracking with varying high times when *Ge=10, Re=2,* r_1*=0.5,* r_2*=0.5,* C_s*=0.5,* Ca*=0.5,* $Fr = 2, n_1 = 0.5$

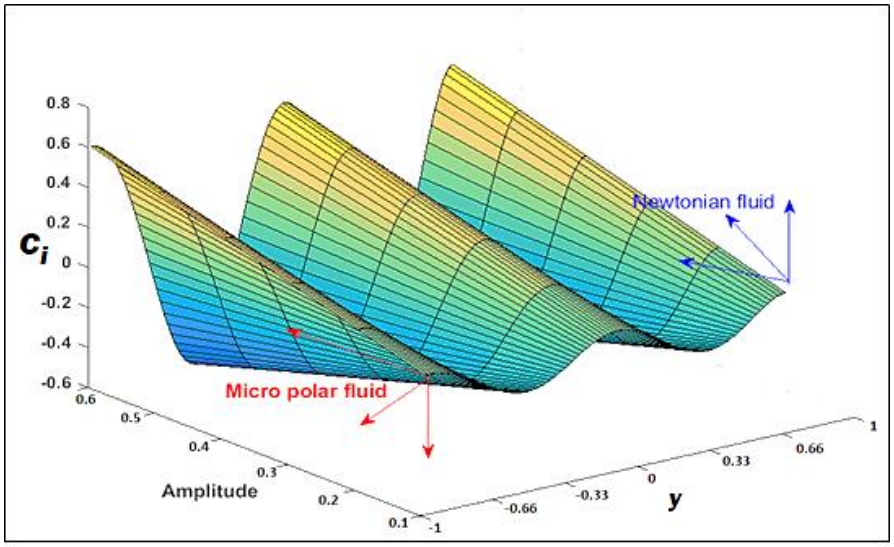

Figure 2.23: 3D evolution of an interface between micropolar and Newtonian fluids with amplitude.

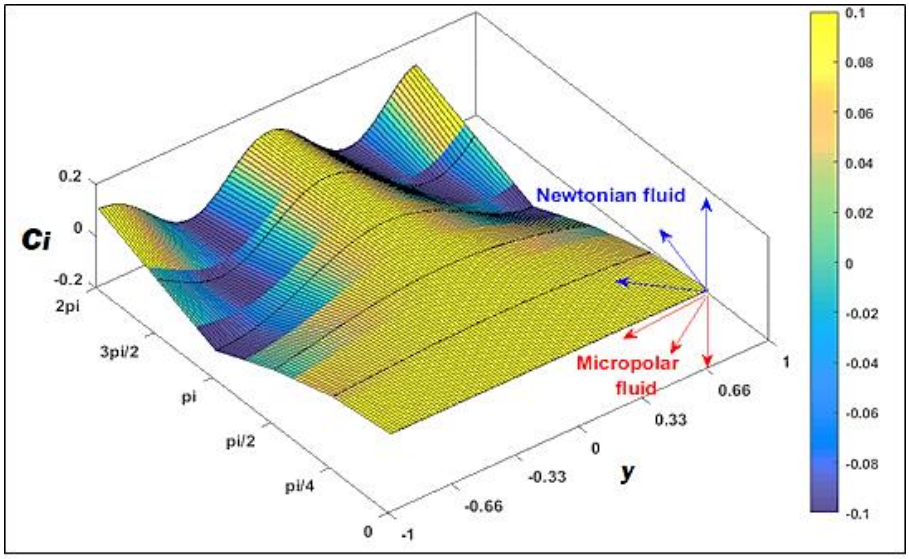

Figure 2.24:3D evolution of an interface between micropolar and Newtonian fluids with varying wavenumber.

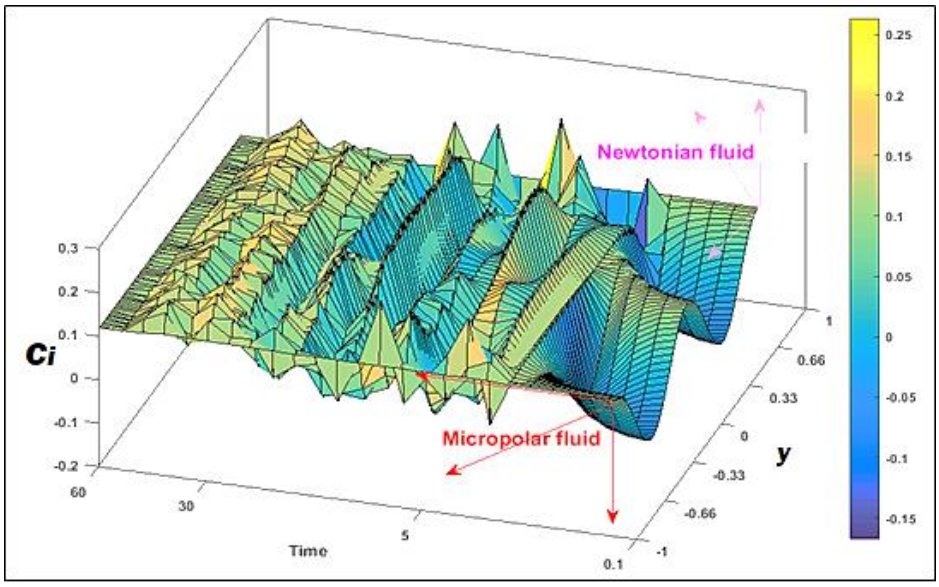

Figure 2.25: Interface tracking with varying time when the flow is carried by periodic pressure gradient $Ge = 10 * Sin(wt)$.

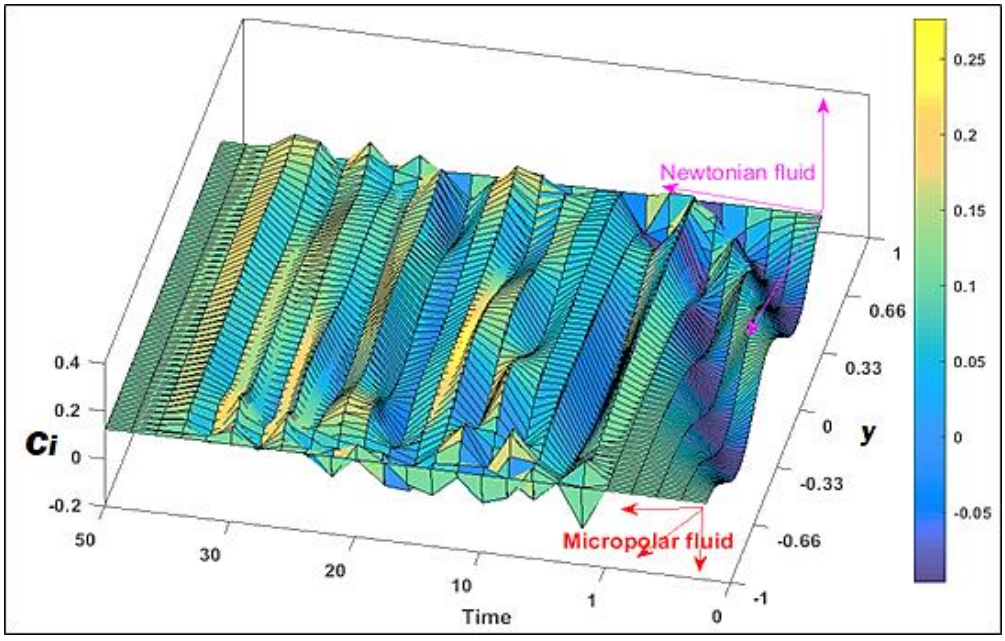

Figure 2.26: Interface tracking with varying time when the flow is carried by decaying pressure gradient $Ge = 10 * e^{-\lambda t}$

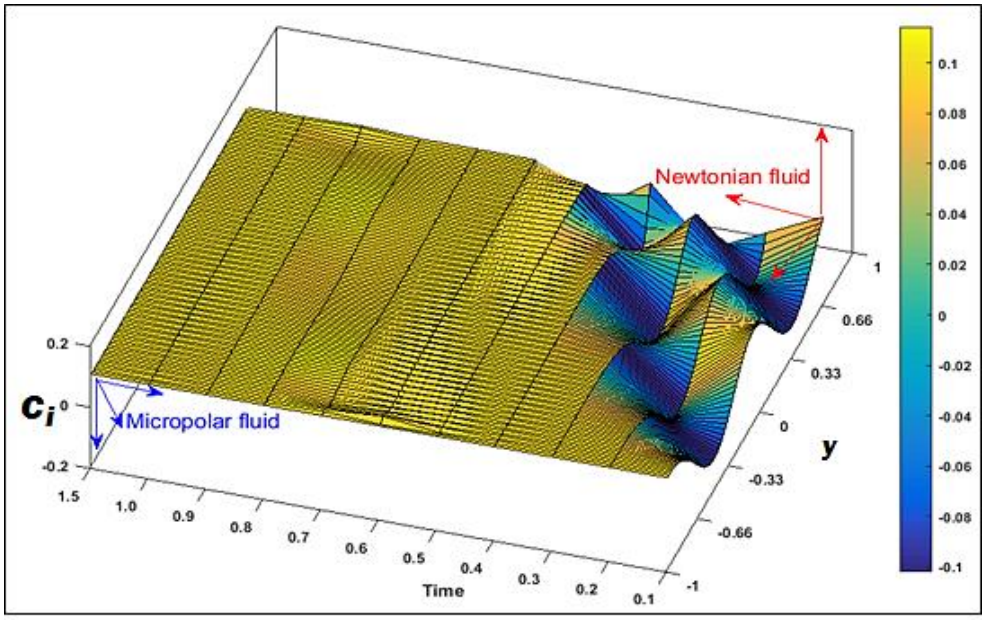

Figure 2.27: Interface tracking with varying time when micropolar parameter curtailed as $n_1 = 0.005$

2.4 Conclusions

The unsteady flow of two immiscible (micropolar and Newtonian) fluids through a horizontal channel under a stable and moving interface scheme has been analyzed numerically using the modified Cubic B-Spline Differential Quadrature method. The effects of critical parameters such as time, amplitudes, Reynolds number, viscosity ratio, wave number, and micropolar parameter on velocity, microrotation, and interface evolution have been addressed with three different applied pressure gradients. The core findings of the present article can be summarized in the following points:

-The Eringen micropolar parameter is only present in the micropolar fluid only, but it affects the velocity of Newtonian fluid a little. Enhancing the micropolar parameter increases the vortex viscosity in lower region fluid, reducing the fluid velocity and microrotation. As the shear stress is continuous across the interface, the upper region fluid velocity also gets reduced under the stable interface scheme.

-Under the stable interface scheme, the linear and angular velocity shows the accelerating, oscillating and decelerating pattern with externally applied constant, periodic, and decaying pressure gradients.

- Initially, the vertical stretching of the interface is enormous, and afterward, its shape advances with time; subsequently, the undulating succession occurs quicker, and the interface becomes steady for a higher time when a constant pressure gradient is applied in the moving interface scheme.

- The development of the interface profile for decaying pressure gradient cases in the moving interface scheme is subjectively comparative; however, it requires more time to achieve the steady state, and the peak of the waves resembles the constant pressure gradient case. The interface profile for periodic pressure gradient cases is qualitatively similar to the other cases; however, it takes more time to stabilize, and the crest of the waves is large compared to the constant and decaying pressure case.

-The interface becomes stable quickly with time as the micropolar parameter is curtailed when a constant pressure gradient induces the flow.

The present computations have shown that MCB-DQM is a robust numerical approach for simulating complex interfacial immiscible flows of Newtonian and non-Newtonian fluids. However, the present study may be extended to consider nanofluids and porous media [151] and more complex geometries [152], e.g., microchannels, and efforts in these directions are currently underway.

Chapter 3
Numerical Study of Unsteady Flow of Immiscible Saffman Dusty (Fluid-Particle Suspension) and Eringen Micropolar Fluids in a Duct with Modified Cubic B-Spline Differential Quadrature Method

3.1 Introduction

It is challenging to isolate pure liquids in many industrial problems, including separating complex petrochemical liquids, petroleum filtration, polymer technology, and slurry dynamics. Industrial fluent media often contain impurities such as dust particles and other suspended contaminants. Such fluids are "dusty" or "fluid-particle suspensions" and require multiphase models for accurate simulation. Thus, in functional applications such as petroleum production, crude oil purification, biochemical separation techniques, etc., the study of two-phase flows is significant where solid spherical objects are distributed in a sterile fluid. Many excellent investigations of the transport phenomena associated with the passage of dusty fluids through conduits (ducts, pipes, channels, etc.) have been reported, primarily motivated by a desire to explain the fundamental aspects of dust particle and fluid phase interaction in petroleum, biochemical, nuclear, geothermal and also aerospace (fuel) systems. In his pioneering work, Saffman [50] proposed a dusty fluid dynamics framework considering the impact of suspended particles on laminar flow stability, assuming a homogenous distribution of identical particles in a dusty gas. Michael and Miller [153] derived analytical solutions for a moving dusty gas, which is dispersed

uniformly over a rigid plane, considering phase change and oscillatory wave decay as functions of the mass concentration of the dust and that the dusty density greatly exceeds the gas density. Later Peddieson [154] examined boundary-layer characteristics of a quintet of unsteady parallel flows of particulate (dusty) suspensions using the Marble dusty gas model. Mitra and Bhattacharyya [155]–[157] discussed the unstable gas flow between two parallel plates for a variety of boundary conditions (oscillatory and stationary walls) and in magnetic fields. Chamkha [73] used a finite difference algorithm to compute solutions for dusty heat transfer in a porous walled channel with heat transfer. Attia *et al.* [74], [158], [159] explored the dusty fluid flow, hydromagnetic dusty Couette flow with heat transfer, and dusty flows in porous media under transpiration wall effects using analytical methods. Attia and Ewis [160] further investigated the movement of dust particles in non-Newtonian Darcy flow under a magnetic field. To analyze the effects of various fluid parameters on dusty phase mass transfer, Singh and Singh [161] examined the unstable flow between two oscillating walls in a hydromagnetic channel for viscous, dusty fluid.

Although several studies described earlier have considered non-Newtonian fluid characteristics (viscoelastic, viscoelastic, etc.), they have neglected microstructural effects. Suspended particles may spin independently of the suspension fluid medium in natural, industrial, and geophysical systems. This rotation at the microscopic level cannot be simulated with conventional rheological models. Particles in atmospheric flows also exhibit such behavior. The diversion from the direct relationship between pressure and tension of a liquid also contributes to non-Newtonian liquid characteristics. A more complex framework is required to simulate the influence of microstructural characteristics on global hydrodynamic behavior. The micropolar theory offers such a framework by extending the conventional linear momentum conservation to include angular momentum conservation of the microelements ("micro-rotation") in complex fluent media. Physically micropolar fluids represent fluids consisting of rigid, randomly oriented (or spherical) particles suspended in a viscous

medium, where the deformation of fluid particles is ignored. Therefore, the micropolar theory features gyratory motions of microelements via the inclusion of an appropriate micro-rotation vector field that permits analysis of different rotational degrees of freedom. Animal, blood, polyurethane solution, liquids with admixtures, rheological slurries, synovial fluid, crude oil, and multiphase geothermal liquids are just some examples of complex media which can be simulated via micropolar fluid dynamics.

Eringen [108] introduced micropolar fluid dynamics in his monumental paper as a particular case of his more general micromorphic ("simple microfluid") theory in the mid-1960s. A remarkable aspect of the Eringen formulation is the elegance of simpler models e. g. The Newtonian fluid formulation can be extracted as special cases. The microstructure is simulated with the microrotation vector, extraneous to the vorticity vector, creating unsymmetric stress. The theory is more comprehensive than the Stokes polar (couple stress) model since it includes separate balance equations for micro-rotation, providing a more comprehensive picture of microstructural behavior. Micropolar fluid mechanics has been embraced extensively in the engineering and scientific community and has been deployed successfully to investigate an astonishing range of applications spanning hemodynamics, grease tribology, bearing design, orthopaedics, drug delivery (pharmacodynamics), sediment transport in river hydraulics, nuclear reactor flows, seeded magnetohydrodynamic energy generator fluid dynamics, ocular biomechanics, vestibular flows, geothermic, biomagnetic peristatic flows, etc. The application of micropolar fluid dynamics for simulation and predicting the flow behavior in microchannels, primarily on the flow field's topology, was provided by Kucaba-Pięta[l] [162]. Many of these areas have been reviewed by Bég *et al.* [163]. One of the earliest studies of micropolar boundary layer flows was communicated by Peddieson [109], who considered plane or axisymmetric stagnation-point flow of a micropolar fluid over a flat plate and turbulent shear flows providing a solid base for future modifications to multi-physics. Apparao *et al.* [164] studied orthopedic lubrication performance with micropolar theory, confirming the superior

load-carrying characteristics achieved relative to conventional Newtonian viscous liquids. The microstructural influence on blood rheology characteristics was reported by Kang and Eringen [111]. Devakar and Iyerger [112] investigated the dynamics of micropolar liquids in channels.

There are many applications in engineering sciences and geophysics in which multiple fluids arise which do not mix. These immiscible fluids feature oil slicks, river contamination, crystal growth, sedimentary reservoir systems, desalination processes, liquid metal fabrication, multiphase oil pipeline transport, ice accretion on aircraft wings, biopolymeric interfaces, etc. Therefore, the analysis of immiscible fluid flows has stimulated significant interest in applied mathematics and engineering computation in parallel with experimental studies. Sherief *et al.* [165] considered the minor deformed interface between two immiscible liquids where one of the fluids is micropolar in the channel. Then the Stokes flow generated by a spherical shape particle migrating orthogonal to a planar interface separating two semi-infinite immiscible fluid regimes is explored using an analytical and numerical technique based on collocation approximation. An excellent appraisal of the viscous Newtonian flow of two immiscible fluids in channel flow has been documented in the classical treatise by Bird [133]. Some extensive studies of immiscible fluid duct (channel) flows are found in [134], [166]–[168] Umavathi *et al.* [135] provided an analytical solution for the free convective flow of two immiscible fluids (Stokes' polar and viscous Newtonian) in a composite porous medium vertical channel for fully developed laminar conditions. Kumar *et al.* [136] later extended the analysis to micropolar and Newtonian liquids. Srinivas and Ramana Murthy [137] studied the dynamics of two homogeneous, permeable beds saturated with different density immiscible couple stress (polar) fluids with carefully constructed interfacial boundary conditions. Srinivas *et al.* [138] extended the hydrodynamic model to consider heat transfer effects with entropy generation minimization for a horizontal channel. Mittal and Rana [169] further generalized the studies in the broader range of thermal boundary conditions. Borrelli *et*

al. [140] considered two immiscible Newtonian fluids in a vertical channel under a transverse magnetic field, examining buoyancy effects in detail and computing reversed flow phenomena. Srinivas *et al.* [170] extended the studies above for couple stress flows in ducts to consider nonlinear thermal radiative effects with an algebraic flux model and homotopy method. Chandrawat *et al.* [171] explored the two immiscible dusty and non-dusty fluids in the horizontal channel with different geometry. Most of the studies mentioned above neglected time effects, i. e., were confined to steady-state analysis. However, numerous interfacial duct flows feature transient effects.

Time inclusion in mathematical models can provide a deeper insight into the transport phenomena, and flow characteristics can be addressed more accurately. Despite significant relevance to modern industry, relatively little work has been conducted regarding the time-dependent unstable flow of two immiscible liquids. The unsteady multiphase flow problem has been rigorously explored via the front tracking method by Tryggvason *et al.* [141]. Riaz and Tchelepi [142] studied the instability of immiscible two-phase flow in porous media. The unstable hydromagnetic flow of immiscible liquids was numerically studied by Vajravelu *et al.* [143], with different permeability of two permeable beds. The unstable oscillatory flow problem with heat transfer of two viscous immiscible fluids through a horizontal channel is studied by Umavathi *et al.* [144]. A study of the coupling effect of heat and mass convection in time-dependent incompressible immiscible viscous fluid flow was presented by Umavathi *et al.* [172].

One of the most challenging aspects of evaluating two immiscible fluid flows is a complicated interface in the concerned region. The interface moves from one place to another and might be twisted and even collapse in extreme situations (related to the adjustment of surface pressure and flexible strengths). Subsequently, the interface between two immiscible liquids plays an imperative part in controlling the flow characteristics and should be identified as an essential setup component. Tauber *et al.* [88] investigated the dynamic behavior of a sheared immiscible fluid at the interfacial contact. To simulate the complex interfacial stress effects in hydromagnetic

regulation of slick oil behavior under periodic (wave) effects for double porosity media, Bég *et al.* [173] used a variationally finite element technique with a forward time centered space (FTCS) finite difference method. Yih [83] discovered that when the viscosity jumps from one fluid to another, the tangential velocity gradient alters, resulting in turbulence at the interface of immiscible fluids. Recently, Umavathi and Bég [82] used an intrinsic finite-difference logic with successive over-relaxation (SOR) to approximate the interfacial composition in two-fluid duct convection flow more precisely, finding that various feature ratios in the upper and lower areas of the channel cause significant interface movement. Many computational methods have been developed in recent years to analyze immiscible flows. Dong *et al.* [89] described an optimized Lattice Boltzmann method for simulation of immiscible fluids displacement. Norouzi *et al.* [174], [175] deployed COMSOL finite element software to study viscous dissipation and anisotropic permeability effects in immiscible displacement flow in porous media, also computing the linear hydrodynamic stability of such flows with an Eigenvalue solver in MATLAB.

Front tracking (FT), moving grid (MG), level set (LS), and volume of fluid (VOF) approach are some kinds of interface monitoring techniques. In immiscible hydrodynamics, the volume of fluid (VOF) method provides a clear and easy mechanism for handling geometrical changes at the interface. DeBar and Roger [176] invented the volume of the fluid (VOF) technique. Youngs [85]made substantial improvements to the DeVar-Roger technique. VOF simulations for interface tracking between two immiscible liquids for a variety of situations have been well-explained in [90], [177]–[181]. Under modest inertial forces, the VOF technique was used by Li and Renardy [81] to investigate the contact between two immiscible fluids. Vinay and Wachem [92] used the VOF technique to investigate the surveillance of the interface between two immiscible fluids for free surface fluid mechanics.

The extensive spectrum of industrial linear and nonlinear fluid flow problems can be numerically resolved using finite difference, finite element, and finite volume

techniques. Devakar *et al.* [147] numerically explored the time-dependent unsteady flow of two immiscible fluids with an explicit Crank-Nicolson finite difference method. The low-order approaches do use several grid points to achieve an acceptable degree of accuracy to obtain specific outcomes at such defined points. The differential quadrature method (DQM) was initially proposed by the celebrated Princeton applied mathematician Richard Bellman [96] to search for an efficient discretization strategy to achieve concise numerical solutions with significantly reduced grid steps. DQM was further improved by Quan and Chang [97], [182]. Various test functions, namely, Lagrange interpolation polynomials, sink, and spline, cubic, and modified cubic B-spline functions, have been implemented successfully in numerous recent studies, including [94], [101], [183]–[187] for the calculation of weighting coefficients in DQM. This technique is also convenient and computationally efficient with reduced data complexity, leading to error mitigation and easy implementation. Using the DQM, Katta and Joshi [146] analyzed the behavior of incomprehensible viscoelastic magnetohydrodynamic flow in a porous medium channel. Katta *et al.* [145] again numerically explored the unsteady fluid flow of two immiscible fluids by DQM. Chandrawat *et al.* [188], [189] investigate the numerical solution of two immiscible fluid problems using the cubic B-spline differential quadrature method.

A close inspection of the scientific literature has shown that no attempt has been made thus far to study the unsteady flow of two immiscible (dusty and micropolar fluids) with a stable and moving interface to the authors' best knowledge. The focus of this chapter is that the velocity, microrotation, and interface navigation between two different viscous-dense micropolar and particle suspension led dusty fluids is proposed in the horizontal channel. A horizontal channel considers two different schemes of stable and moving interfaces. This study might assist systems such as transient two-phase transport in enhanced geothermal ducts [190], hemodynamic flow separation [191], [192], and biological pump layouts [193]. Motivated by applications in non-Newtonian duct processing, in the present chapter, a comprehensive mathematical

model and computational simulation with the modified cubic B-spine-Differential Quadrature method (MCB-DQM) is described for the unsteady flow of two immiscible fluids- dusty (fluid-particle suspension) and Eringen micropolar fluids- through horizontal channels with two separate schemes.

This chapter has two sections. In section-3.2, the flow is modelled with the stable interface between the two immiscible fluids for the velocity profiles of both fluids, micro-rotation (angular velocity) profile of micropolar fluid through the non-porous plates. The effects of various fluid parameters on the fluids and particle velocity and microrotation have been identified by solving coupled partial differential equations using the modified cubic B-spline differential quadrature method. The moving liquid-liquid interface is considered between two immiscible fluids in section-3.3. It is assumed that the interface travels from one position to another, which may even be seriously deformed; hence the single momentum equation by the volume of fluid (VOF) method is combined with the continuum surface approach model, and an interface tracking is proposed. An interface tracking under consideration of various fluid parameters has been obtained numerically by solving the transformed coupled partial differential equations using the modified cubic B-spline differential quadrature method.

3.2 Formulation of dusty and Micropolar fluid flow under the stable interface scheme

Consider the unsteady, fully developed, laminar, unidirectional, immiscible, incompressible viscous flow of Eringen micropolar and Saffman dusty fluids. Some assumptions are invoked under the stable interface scheme.

a. Both fluids move between two horizontal parallel non-porous plates, which are electrically non-conductive. The plates are located in the *X*-*Z* plane, as depicted in Figure 3.1.
b. Eringen micropolar fluid occupies the lower channel half-space (zone-1), i. e. $(-k \leq y \leq 0)$, and possesses the fluid velocity u_m, density ρ_m, viscosity μ_m, microrotation (angular velocity) M_*, vortex viscosity κ_m, gyro-viscosity ω_m, and gyration parameter τ.
c. Saffman dusty fluid occupies the upper half-space (zone-2), i. e. $(0 \leq y \leq k)$, and possesses fluid velocity u_d, density ρ_d, viscosity μ_d.In the dusty fluid, the dust particles have particle velocity u_p, and density ρ_p.
d. The transportation attributes are unchanged in both the zones and the common pressure gradients are applied from the horizontal (*X*) axial direction. The flow of dusty fluid in zone-2 is governed by the equations (1.10) - (1.13), and the flow of micropolar fluid in zone-1 is governed by the equations (1.7) - (1.8).
e. The fluid velocity vectors in both zones are $u_m(y,t)$, $u_d(y,t)$ and the micro-rotation vector $M_*(y,t)$ in the zone-1(lower) are assumed to be $(u_m(y,t),0,0)$, $(u_d(y,t),0,0)$ and $(M = (0,0,M_*(y,t))$ respectively.
f. The movement of fluids is incompressible unsteady, and driven by an applied pressure gradient in the *X*-axial direction; therefore, the velocity profile is unidirectional.
g. The fluid layers are mechanically coupled through the mode of momentum exchange. Transferring momentum arises through consistency in velocity and

shear stress over the interface. However, we assume that the flow rate and shear pressure are also stable at the interface between two liquids.

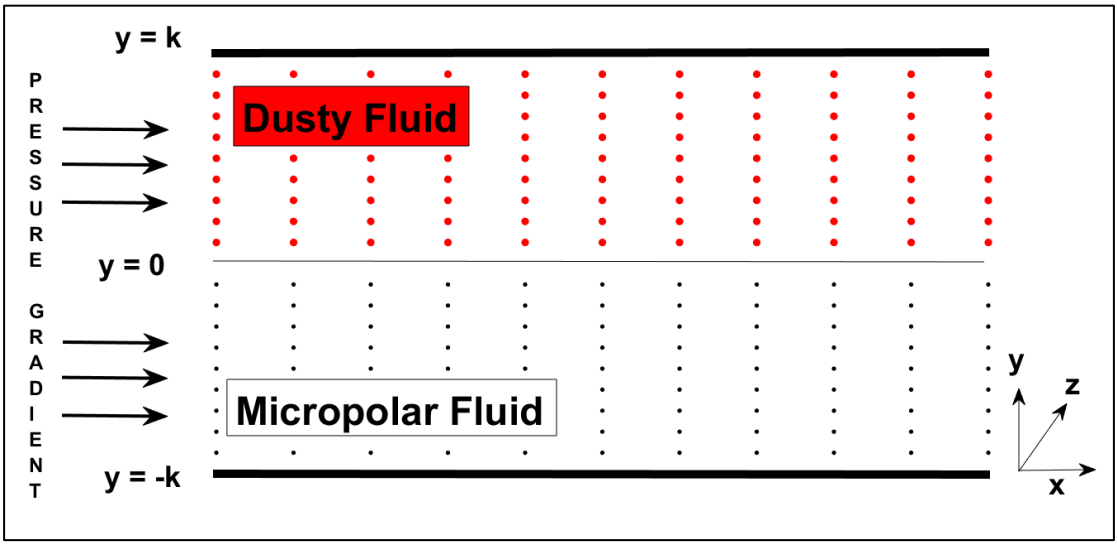

Figure 3.1: Geometry of immiscible micropolar and dusty (scheme-2a) fluids flow with a stable interface

The micropolar fluid flow equations (1.7) - (1.8) and dusty fluid flow equation (1.12)-(1.13) have transformed into equations (3.1) - (3.4) as unidirectional fluid flow velocity and micro-rotation distribution under the aforesaid assumed constraints.

Zone-1 (Micropolar fluid).

$$\rho_m \frac{\partial u_m}{dt} = -\nabla p + \kappa_m \frac{\partial M_*}{\partial y} + (\mu_m + \kappa_m) \frac{\partial^2 u_m}{\partial y^2}, \tag{3.1}$$

$$\rho_m \tau \frac{\partial M_*}{\partial t} = -2\kappa_m M_* - \kappa_m \frac{\partial u_m}{\partial y} + \omega_m \frac{\partial^2 M_*}{\partial y^2}. \tag{3.2}$$

Zone-2 (Dusty fluid).

$$\rho_d \frac{\partial u_d}{\partial t} = -\nabla p + \mu_d \frac{\partial^2 u_d}{\partial y^2} - \zeta_T \rho_p \emptyset \frac{(u_d - u_p)}{(1-\emptyset)}, \tag{3.3}$$

$$\frac{\partial u_p}{\partial t} = \zeta_T (u_d - u_p). \tag{3.4}$$

Classical hyper-stick and no-slip boundary conditions are considered and can be numerical as follows.

Initial conditions: At $t \leq 0$,

$$u_m(y,t) = 0 \; for - k \leq y \leq 0, \tag{3.5}$$

$$M_*(y,t) = 0 \; for - k \leq y \leq 0, \tag{3.6}$$

$$u_d(y,t) = 0 \; for \; 0 \leq y \leq k, \tag{3.7}$$

$$u_p(y,t) = 0 \; for \; 0 \leq y \leq k. \tag{3.8}$$

Boundary and interface conditions: At $t > 0$,

$$u_m(-k,t) = 0, \tag{3.9}$$

$$u_d(k,t) = 0, \tag{3.10}$$

$$u_p(k,t) = 0, \tag{3.11}$$

$$M_*(-k,t) = 0. \tag{3.12}$$

The fluid velocities and shear stress are both continuous at the liquid-liquid interface [1], [2], [147]. These constraints can be expressed mathematically as (3.13) and (3.15).

$$u_m(0,t) = u_d(0,t). \tag{3.13}$$

As the microrotation is proportional to the couple stress at the boundary (At the interface), Hence the general form of the interfacial condition for angular velocity M_* especially for the droplet case can be considered as Niefer and Kaloni [148], Faltas and Saad [149], and Saad [150], but in the current study, we chose the interfacial condition for microrotation(spin–vorticity) [1], [147] over other existing conditions at *y=0* because it is realistic and consistent to apply at the interface between two immiscible fluids.

$$M_*(0,t) = -\frac{1}{2}u_{m_y}, \tag{3.14}$$

$$\mu_d u_{d_y} = (\mu_m + \kappa_m) u_{m_y} + \kappa_m M_* \ \ at\ y = 0. \tag{3.15}$$

Introducing the non-dimensional parameters $\bar{x} = \frac{x}{k}, \bar{y} = \frac{y}{k}, \overline{u_m} = \frac{u_m}{U_0}, \overline{u_d} = \frac{u_d}{U_0}, \overline{u_p} = \frac{u_p}{U_0}, \bar{p} = \frac{p}{\rho_m {U_0}^2}, \bar{t} = \frac{tU_0}{k}, \omega_m = (\mu_m + \kappa_m/2)\tau$ with $\tau = k^2$ and $n_1 = \frac{\kappa_m}{\mu_m}$ and $\zeta_T = \frac{6\pi r \mu_d}{m_p}$ is the volume transfer coefficient with an average mass of dust particle m_p and radius r. Hence the last term of equation (3.3) $\zeta_T \rho_p \emptyset \frac{(u_d - u_p)}{(1-\emptyset)}$ can be written as $\frac{R * r_1}{Re * r_2}(u_d - u_p)$ where $R = \frac{K^* \rho_p k^2}{\mu_d m_p}$ is particle concentration parameter, and $K^* = 6\pi r \mu_d U_0$ is the Stokes drag coefficient, and $Re = \frac{\rho_m U_0}{\mu_m}$ is the Reynolds number. $r_1 = \frac{\mu_d}{\mu_m}, r_2 = \frac{\rho_d}{\rho_m}$ are the ratio of viscosity and density of the two liquids, respectively. Hence the last term of equation (3.4) is updated accordingly where $r_3 = \frac{\rho_d}{\rho_p}$ denotes the ratio of the density of the fluid to the density of dust particles in zone-2. $-\nabla p = -\partial p/\partial x = Ge(t)$ is the applied time-dependent pressure gradient in the *x*-axial direction with $t > 0$. Three distinct cases for $Ge(t)$ are considered in the numerical analysis:

Case-I: $Ge(t) = Ge$. (If the fluid flow is triggered by an applied constant pressure gradient).

Case-II: $Ge(t) = Ge * Sin(wt)$. (If the fluid flow is triggered by an applied periodic pressure gradient with oscillating parameter w).

Case-III: $Ge(t) = Ge * e^{-\lambda t}$. (If the fluid flow is triggered by a decaying pressure gradient with decaying parameterλ).

According to the stable interface scheme, the equations (3.1) - (3.4) emerge as below equations (3.16) - (3.19) with dropping the bars and introducing the above non-dimensional parameters and appropriate initial, interfacial, and boundary conditions.

Micropolar liquid zone.

$$u_{m_t} = Ge(t) + \frac{n_1 M_{*y}}{Re} + \frac{(n_1+1) u_{m_{yy}}}{Re}, \tag{3.16}$$

$$M_{*t} = \frac{(2+n_1)M_{*yy}}{2Re} - \frac{n_1\left(2M_* + u_{m_y}\right)}{Re}. \quad (3.17)$$

Saffman dusty fluid zone.

$$u_{d_t} = \frac{Ge(t)}{r_2} + \frac{r_1}{r_2}\frac{u_{d_{yy}}}{Re} - \frac{R*r_1}{r_2}\frac{(u_d - u_p)}{Re}, \quad (3.18)$$

$$u_{p_t} = \frac{R*r_3*r_1}{r_2}\frac{(u_d - u_p)}{Re}. \quad (3.19)$$

Equations (3.5) - (3.15) are considered as initial, interfacial, and boundary conditions with $k = 1$.

3.2.1 Computation of velocity and microrotation under scheme-2

To obtain the velocity (fluids and particle phase) and micro-rotation profiles for Saffman dusty and Eringen micropolar fluids in the respective zones under the flat interface scheme, replace the approximation of the spatial components of the I and II order unidirectional derivative as the equations (1.30), (1.31), and (1.33), (1.34). Hence the system of coupled partial equations (3.16) - (3.19) followed by the MCB-DQM scheme solved with the initial and boundary conditions (3.5) - (3.15), and the linear velocities and angular velocity component (microrotation) profiles of both fluids and particles are readily obtained. The equations (3.16) -(3.19) can be updated as follows.

Micropolar liquid zone.

$$u_{m_t} = Ge(t) + \frac{n_1}{Re}\left(\sum_{j=1}^{N} a^*_{ij} M_*(y_j, t)\right) + \frac{(n_1+1)}{Re}\left(\sum_{j=1}^{N} b^*_{ij} u_m(y_j, t)\right), \quad (3.20)$$

$$M_{*t} = \frac{(n_1+2)}{2Re}\left(\sum_{j=1}^{N} b^*_{ij} M_*(y_j, t)\right) - \frac{n_1}{Re}\left(2M_* + \sum_{j=1}^{N} a^*_{ij} u_m(y_j, t)\right). \quad (3.21)$$

Saffman dusty fluid zone.

$$u_{d_t} = \frac{Ge(t)}{r_2} + \frac{r_1}{r_2}\frac{\sum_{j=1}^{N} b^*_{ij} u_d(y_j, t)}{Re} - \frac{R*r_1}{r_2}\frac{\left(u_d(y_j,t) - u_p(y_j,t)\right)}{Re}, \quad (3.22)$$

$$u_{p_t} = \frac{R*r_3*r_1}{r_2}\frac{\left(u_d(y_j,t) - u_p(y_j,t)\right)}{Re}. \quad (3.23)$$

Thus, equations (3.20) - (3.23) are reduced into a system of ordinary differential equations in time, for *i=1, 2, 3…, N*, and the system is solved by the robust four-step third-order SSP-RK43 scheme (1.69) - (1.72). The velocities and microrotation in both zones are obtained as follows.

At first- the step for *i=1,2,3…, N*.

Micropolar liquid zone.

$$u_{m_1} = u_{1_0} + \frac{\Delta t}{2}\begin{pmatrix} Ge(t) + \frac{n_1}{Re}\left(\sum_{j=1}^{N} a^*{}_{ij} M_{*_0}(y_j,t)\right) \\ + \frac{(n_1+1)}{Re}\left(\sum_{j=1}^{N} b^*{}_{ij} u_{m_0}(y_j,t)\right) \end{pmatrix}, \tag{3.24}$$

$$M_{*_1} = M_{*_0} + \frac{\Delta t}{2}\begin{pmatrix} \frac{(n_1+2)}{2Re}\left(\sum_{j=1}^{N} b^*{}_{ij} M_{*_0}(y_j,t)\right) - \\ \frac{n_1}{Re}\left(2M_{*_0} + \sum_{j=1}^{N} a^*{}_{ij} u_{m_0}(y_j,t)\right) \end{pmatrix}. \tag{3.25}$$

Saffman dusty fluid zone.

$$u_{d_1} = u_{d_0} + \frac{\Delta t}{2}\left(\frac{Ge(t)}{r_2} + \frac{r_1}{r_2}\frac{\sum_{j=1}^{N} b^*{}_{ij} u_{d_0}(y_j,t)}{Re} - \frac{R*r_1}{r_2}\frac{\left(u_{d_0}(y_j,t) - u_{p_0}(y_j,t)\right)}{Re}\right), \tag{3.26}$$

$$u_{p_1} = u_{p_0} + \frac{\Delta t}{2}\left(\frac{R*r_3*r_1}{r_2}\frac{\left(u_{d_0}(y_j,t) - u_{p_0}(y_j,t)\right)}{Re}\right). \tag{3.27}$$

At the first step of the method, the conditions (3.5) - (3.15) are regarded favourably.

In the second step for *i=1,2,3…, N*.

Micropolar liquid zone.

$$u_{m_2} = u_{m_1} + \frac{\Delta t}{2}\begin{pmatrix} Ge(t) + \frac{n_1}{Re}\left(\sum_{j=1}^{N} a^*{}_{ij} M_{*_1}(y_j,t)\right) \\ + \frac{(n_1+1)}{Re}\left(\sum_{j=1}^{N} b^*{}_{ij} u_{m_1}(y_j,t)\right) \end{pmatrix}, \tag{3.28}$$

$$M_{*_2} = M_{*_1} + \frac{\Delta t}{2}\begin{pmatrix} \frac{(n_1+2)}{2Re}\left(\sum_{j=1}^{N} b^*{}_{ij} M_{*_1}(y_j,t)\right) - \\ \frac{n_1}{Re}\left(2M_{*_1} + \sum_{j=1}^{N} a^*{}_{ij} u_{m_1}(y_j,t)\right) \end{pmatrix}. \tag{3.29}$$

Saffman dusty fluid zone.

$$u_{d_2} = u_{d_1} + \frac{\Delta t}{2}\left(\frac{Ge(t)}{r_2} + \frac{r_1}{r_2}\frac{\sum_{j=1}^{N} b^*_{ij} u_{d_1}(y_j,t)}{Re} - \frac{R*r_1}{r_2}\frac{\left(u_{d_1}(y_j,t) - u_{p_1}(y_j,t)\right)}{Re}\right), \tag{3.30}$$

$$u_{p_2} = u_{p_1} + \frac{\Delta t}{2}\left(\frac{R*r_3*r_1}{r_2}\frac{\left(u_{d_1}(y_j,t) - u_{p_1}(y_j,t)\right)}{Re}\right). \tag{3.31}$$

In the second step of the method, the conditions (3.5) - (3.15) are regarded favourably.

In the third step for *i=1,2,3…, N.*

Micropolar liquid zone.

$$u_{m_3} = \frac{2u_{m_0}}{3} + \frac{u_{m_2}}{3} + \frac{\Delta t}{6}\begin{pmatrix} Ge(t) + \frac{n_1}{Re}\left(\sum_{j=1}^{N} a^*_{ij} M_{*_2}(y_j,t)\right) \\ + \frac{(n_1+1)}{Re}\left(\sum_{j=1}^{N} b^*_{ij} u_{m_2}(y_j,t)\right) \end{pmatrix}, \tag{3.32}$$

$$M_{*3} = \frac{2M_{*_0}}{3} + \frac{M_{*_2}}{3} + \frac{\Delta t}{6}\begin{pmatrix} \frac{(n_1+2)}{2Re}\left(\sum_{j=1}^{N} b^*_{ij} M_{*_2}(y_j,t)\right) - \\ \frac{n_1}{Re}\left(2M_{*_2} + \sum_{j=1}^{N} a^*_{ij} u_{m_2}(y_j,t)\right) \end{pmatrix}. \tag{3.33}$$

Saffman dusty fluid zone.

$$u_{d_3} = \frac{2u_{d_0}}{3} + \frac{u_{d_2}}{3} + \frac{\Delta t}{6}\left(\frac{Ge(t)}{r_2} + \frac{r_1}{r_2}\frac{\sum_{j=1}^{N} b^*_{ij} u_{d_2}(y_j,t)}{Re} - \frac{R*r_1}{r_2}\frac{\left(u_{d_2}(y_j,t) - u_{p_2}(y_j,t)\right)}{Re}\right), \tag{3.34}$$

$$u_{p_3} = \frac{2u_{p_0}}{3} + \frac{u_{p_2}}{3} + \frac{\Delta t}{6}\left(\frac{R*r_3*r_1}{r_2}\frac{\left(u_{d_2}(y_j,t) - u_{p_2}(y_j,t)\right)}{Re}\right). \tag{3.35}$$

In the third step of the method, the conditions (3.5) - (3.15) are once again regarded favourably.

At the fourth step for *i=1,2,3…, N.*

Micropolar liquid zone.

$$u_m = u_{m_3} + \frac{\Delta t}{2}\begin{pmatrix} Ge(t) + \frac{n_1}{Re}\left(\sum_{j=1}^{N} a^*_{ij} M_{*_3}(y_j,t)\right) \\ + \frac{(n_1+1)}{Re}\left(\sum_{j=1}^{N} b^*_{ij} u_{m_3}(y_j,t)\right) \end{pmatrix}, \tag{3.36}$$

$$M_* = M_{*_3} + \frac{\Delta t}{2}\begin{pmatrix} \frac{(n_1+2)}{2Re}\left(\sum_{j=1}^{N} b^*{}_{ij} M_{*_3}(y_j,t)\right) - \\ \frac{n_1}{Re}\left(2M_{*_3} + \sum_{j=1}^{N} a^*{}_{ij} u_{m_3}(y_j,t)\right) \end{pmatrix}. \quad (3.37)$$

Saffman dusty fluid zone.

$$u_d = u_{d_3} + \frac{\Delta t}{2}\left(\frac{Ge(t)}{r_2} + \frac{r_1}{r_2}\frac{\sum_{j=1}^{N} b^*{}_{ij} u_{d_3}(y_j,t)}{Re} - \frac{R*r_1}{r_2}\frac{\left(u_{d_3}(y_j,t) - u_{p_3}(y_j,t)\right)}{Re}\right), \quad (3.38)$$

$$u_p = u_{p_3} + \frac{\Delta t}{2}\left(\frac{R*r_3*r_1}{r_2}\frac{\left(u_{d_3}(y_j,t) - u_{p_2}(y_j,t)\right)}{Re}\right). \quad (3.39)$$

In the fourth step of the method, the conditions (3.5) - (3.15) are also regarded favourably. Hence the fluid (linear) velocity and angular velocity (Eringen microrotation) profiles i. e. u_m, M_* of micropolar fluid in zone-1 and also the fluid velocity (linear) and particle velocity components, i.e., u_d, u_p for Saffman dusty fluid in zone-2 can be numerically obtained at the fourth step of MCB-DQM.

3.2.2 Results and Interpretation with stable interface scheme

Under the stable interface flow schemes, the unidirectional unstable flow of two immiscible (i. e. Saffman dusty and Eringen micropolar fluids) attributable to the time-dependent pressure gradient has been simulated with a novel MCB-DQM algorithm. Traditional no-slip and hyper-stick conditions are assumed at the boundaries to obtain robust solutions. The two-fluid flow coupled problem in the corresponding zones with stable interfaces has been numerically solved, and velocity, micro-rotation, and dust phase profiles of the respective fluids and dust particles have been obtained. The results are discussed as follows. The following value of parameters are considered to simulate a system of coupled partial differential equation *Re=2, R=0.5,* r_1*=0.5,* r_2*=0.5,* r_3 *=300,* and η_1*=0.5.*

Figure 3.2-Figure 3.21 visualize the evolution in fluid and dust particle-phase velocities and micro-rotation (angular velocity) distributions in the respective dusty and

micropolar zones with variation in key control parameters featured in the mathematical model, i. e. Reynolds number, particulate concentration parameter, applied pressure gradients, density ratio, viscosity ratio, and time. It is evident that the linear velocity profiles for the dust (zone-1) and fluid phase in both zones are parabolic, and the curvature of micropolar angular velocity (microrotation) is lower than the dusty one. Furthermore, the curvature of velocity and micro-rotation profiles for the periodic pressure gradient case is smaller than the decaying pressure gradient. The curvature for the constant pressure gradient is more significant than that computed for the decaying pressure gradient case.

Figure 3.2 and Figure 3.12 exhibit the change in fluid and particle velocities and micro-rotation with varying times when a constant pressure gradient is applied. It is noted that, with rising time, the velocities are growing in both zones, and micro-rotation profile magnitude is accentuated in the micropolar liquid zone.

Figure 3.3 and Figure 3.13 show that the dust particle, dusty fluid, micropolar linear velocities, and microrotation (angular velocity) are pulsating since the flow is induced by the periodic pressure gradient and never achieves the steady-state. Hence the velocities increase when $0 < t \leq \pi/2$, decrease when $\pi/2 < t \leq 3\pi/2$ and further increase with $3\pi/2 < t \leq 5\pi/2$.

Figure 3.4 and Figure 3.14 reveal that the fluid and particle velocities and micro-rotation increase initially in the respective zones, then decrease with greater elapse in time and eventually approach zero as time is enhanced when the applied periodic pressure gradient generates the flow.

It can be noted from Figure 3.11 and Figure 3.21 that the linear velocity (micropolar fluid, dusty fluid, and dust particle) and micro-rotation profiles increase with increment in the pressure gradient.

It may be observed from Figure 3.5 and Figure 3.15 that elevation in Reynolds number enhances both the fluids and particle velocities and micro-rotation magnitudes, owing to the increase in inertial force contribution (relative to viscous force) for all three pressure gradient cases-i.e., applied constant, periodic, and decaying pressure gradients. However, the variations in the velocities are more extensive in magnitude in the dusty fluid zone than in the micropolar liquid zone, indicating the greater sensitivity of Saffman dusty fluid to inertial effects.

Increasing the micropolar parameter reduces the velocity profiles for fluid and dust particles (via coupling in the conservation equations) in both zones. Also, it suppresses microrotation profiles in the lower zone for all three applied pressure gradients (see Figure 3.6 and Figure 3.16). Therefore, the stronger micro polarity of the micropolar liquid achieves a notable damping effect in both zones. It is worth mentioning that the micropolar parameter, while unique to micropolar fluid in the lower zone, exerts a significant (no-trivial) influence on the upper zone (Saffman dusty fluid) via the appropriate coupling terms in the angular momentum (micro-rotation) conservation equation. This markedly modifies the velocity of dust particles and dusty fluid, although there is no fluid mechanical framework in Saffman's model for simulating microstructural spin. The elegance of Eringen's theory is again emphasized since it generalizes Navier-Stokes (Newtonian) viscous hydrodynamics and provides a coupling mechanism to other fluid models via the inclusion of mixed derivative coupling terms in the differential balance equations. Micropolar theory features an additional Eringen vortex viscosity and allows the relative effect of rotation to linear motion to be simulated through the gyratory motions in the micro-rotation vector. The micropolar effect is also removable by prescribing vanishing values to the micropolar parameter, another advantage of micropolar fluid mechanics.

It is noted in Figure 3.7 and Figure 3.17 that dust particle velocity increases significantly with the enhancement of particle concentration parameters. A slight increase in dusty fluid velocity and micro-rotation component (Eringen angular velocity

of micro-elements) is observed for constant and decaying applied pressure gradients. Hence, the particle concentration parameter does not substantially affect micropolar fluid velocity. It is also judicious to note that dusty fluid velocity and micro-rotation decrease marginally when a periodic pressure gradient is applied.

An increase in the viscosity ratio r_1 and density ratio r_2 manifests in an increase in the viscosity and density of the dusty fluid zone. Because of this, for all three applied pressure gradients, a significant decline in dust particle and fluid velocity (zone-2) is computed, whereas there is no tangible alteration in the micropolar fluid velocity (zone-1) with an increase in r_1 and r_2 (see Figure 3.8 and Figure 3.9).

It is also observed from Figure 3.18 and Figure 3.19 for all three applied pressure gradients that as the ratio r_1 enhances, the micro-rotation profile increases significantly; however, when r_2 rises, the micro-rotation profile decreases significantly. Acceleration in gyratory motions of microelements is therefore elevated with a boost in viscosity ratio. In contrast, deceleration is generated in the spin of microelements with an increment in density ratio (owing to the inhibiting effect of a greater mass per unit volume on microstructural motions).

It is noted from Figure 3.10 and Figure 3.20 for all three applied pressure gradients the dust particle velocity climbs significantly, and fluid phase velocity also ascends slightly in zone-2; however, the micropolar fluid (linear) velocity is not displaced, whereas the microrotation component (angular velocity) is weakly elevated in zone-1 with an increase in the ratio r_3.

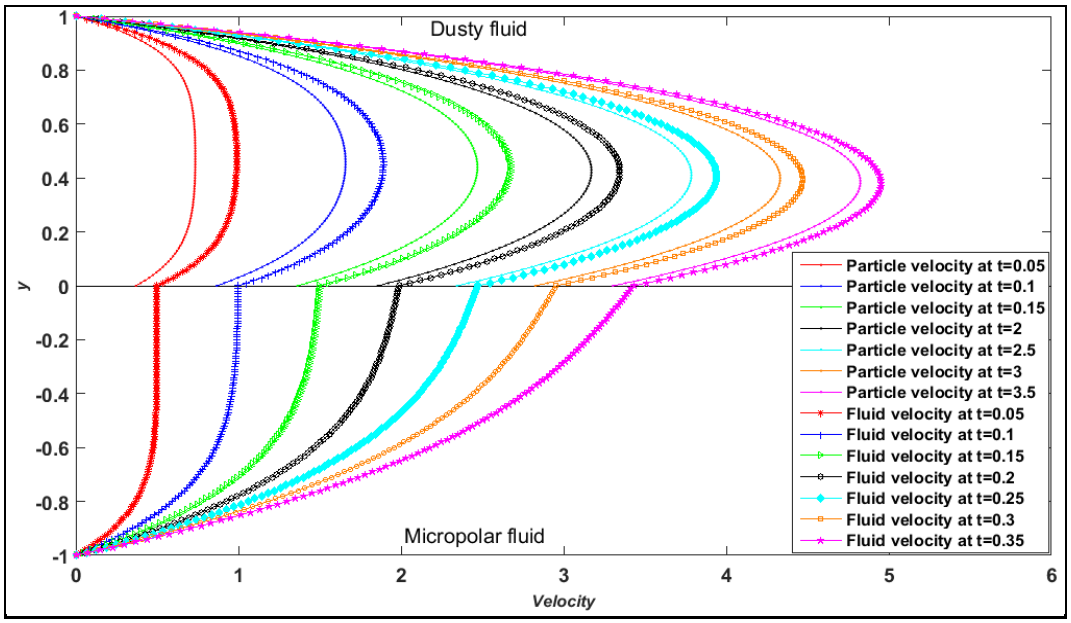

Figure 3.2 Velocity under the scheme-2 with time for constant pressure gradient *Ge=10*

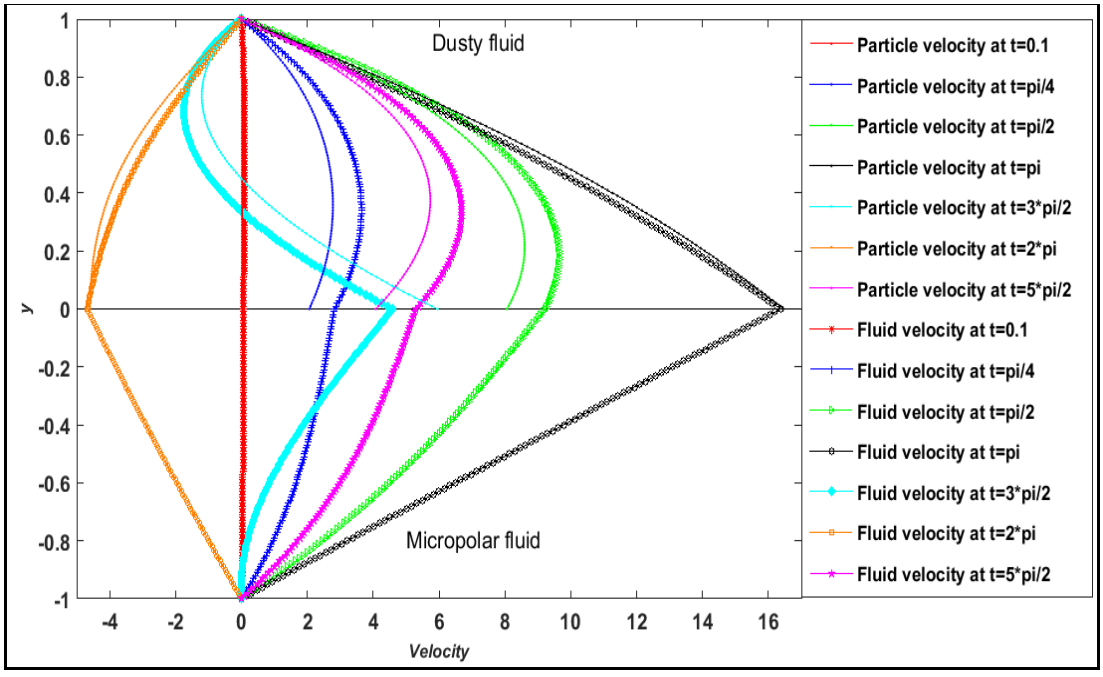

Figure 3.3:Velocity profiles under the scheme-2 with time for periodic pressure gradient

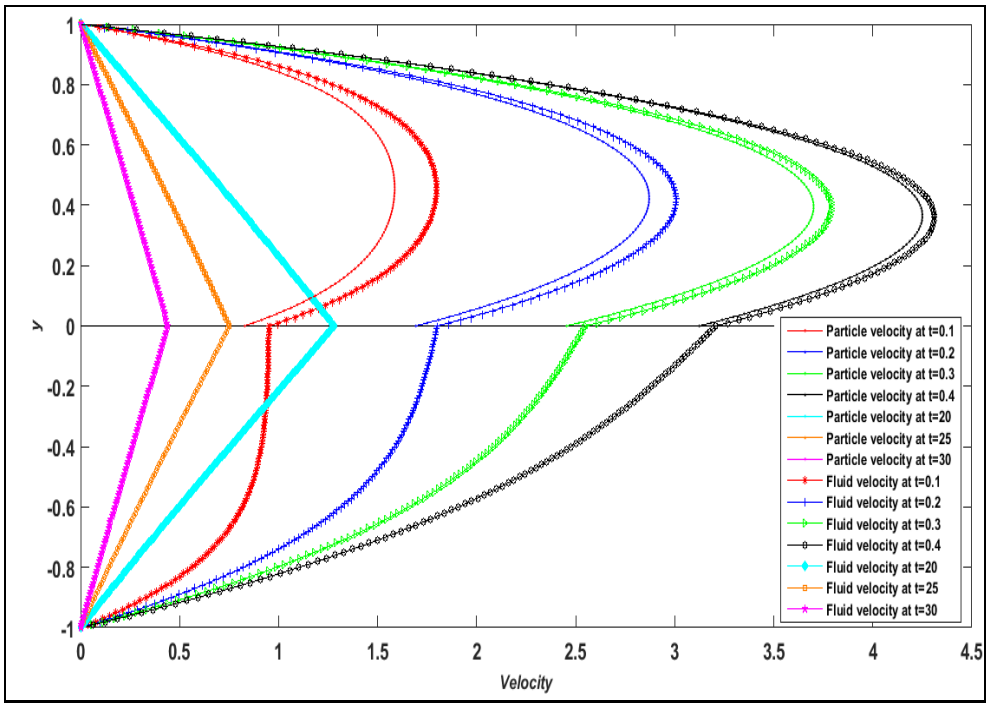

Figure 3.4: Velocity profiles under the scheme-2 with time for decaying pressure gradient

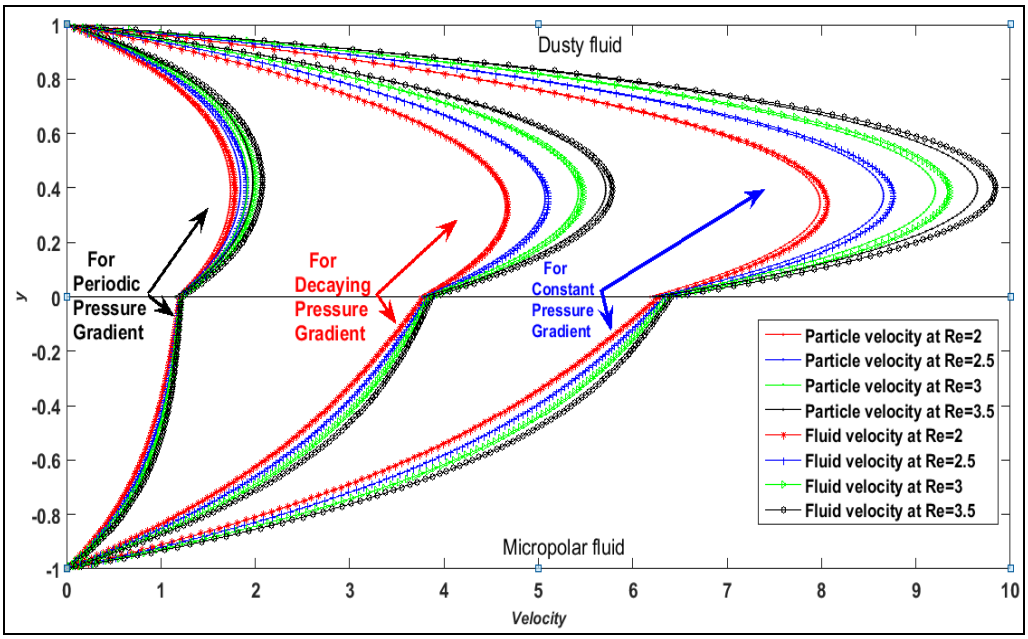

Figure 3.5:Velocity profiles under scheme-2 with Reynolds number.

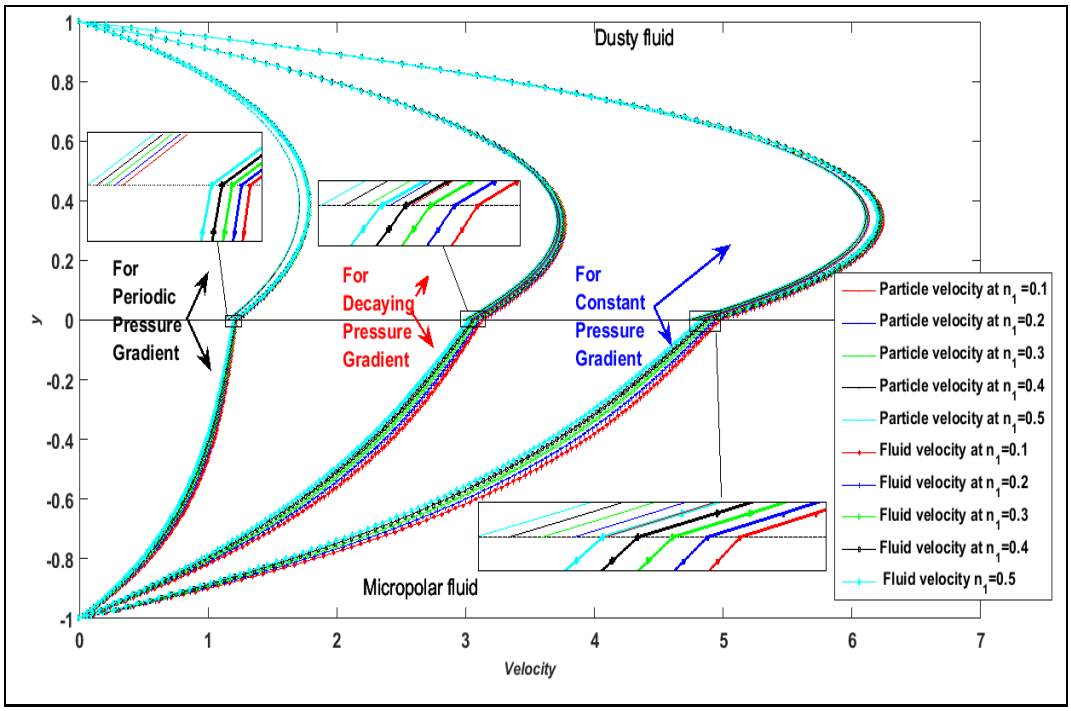

Figure 3.6: Velocity profiles under the scheme-2 with micropolar parameters n_1

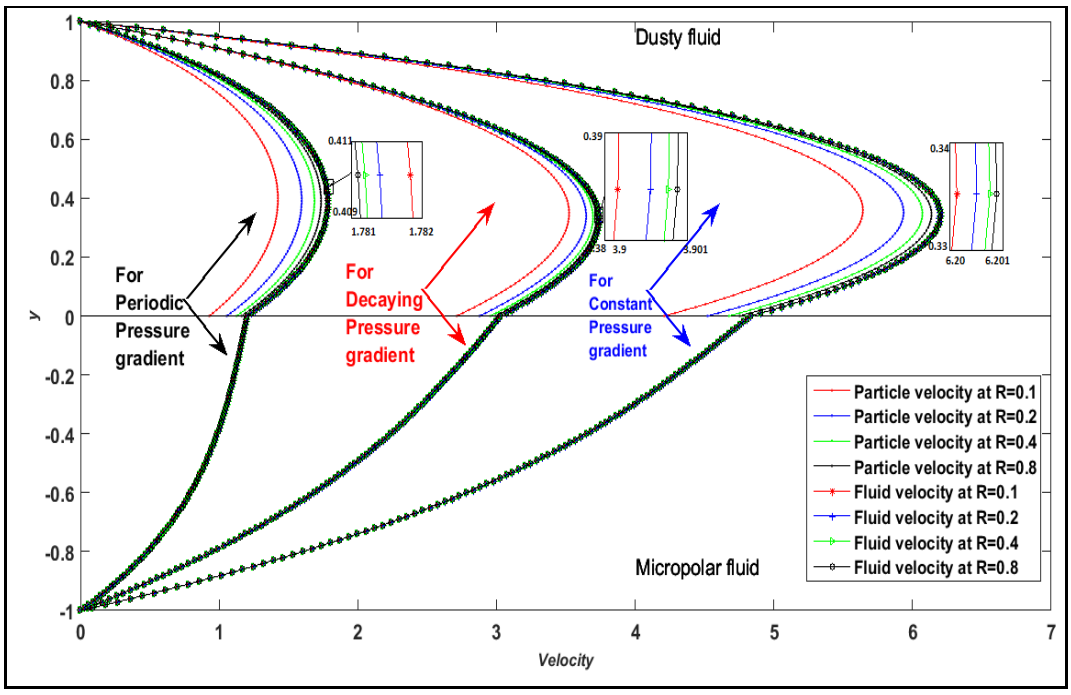

Figure 3.7: Velocity profiles under the scheme-2 with particle concentration parameter

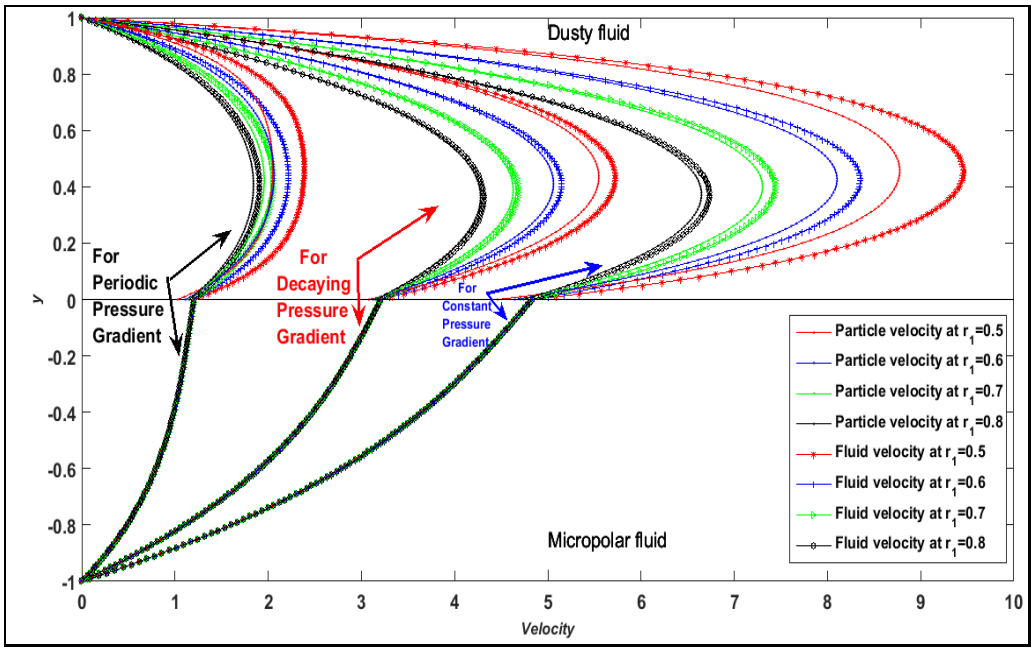

Figure 3.8: Velocity profiles under the scheme-2 with ratios of viscosities

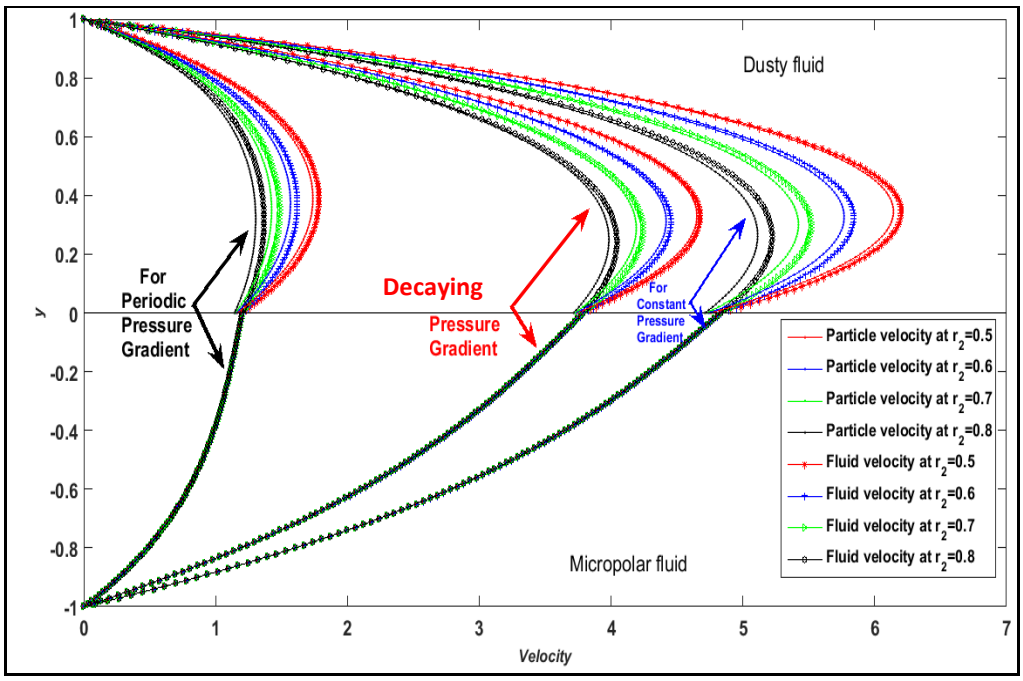

Figure 3.9:Velocity under the scheme-2 with varying ratios of densities

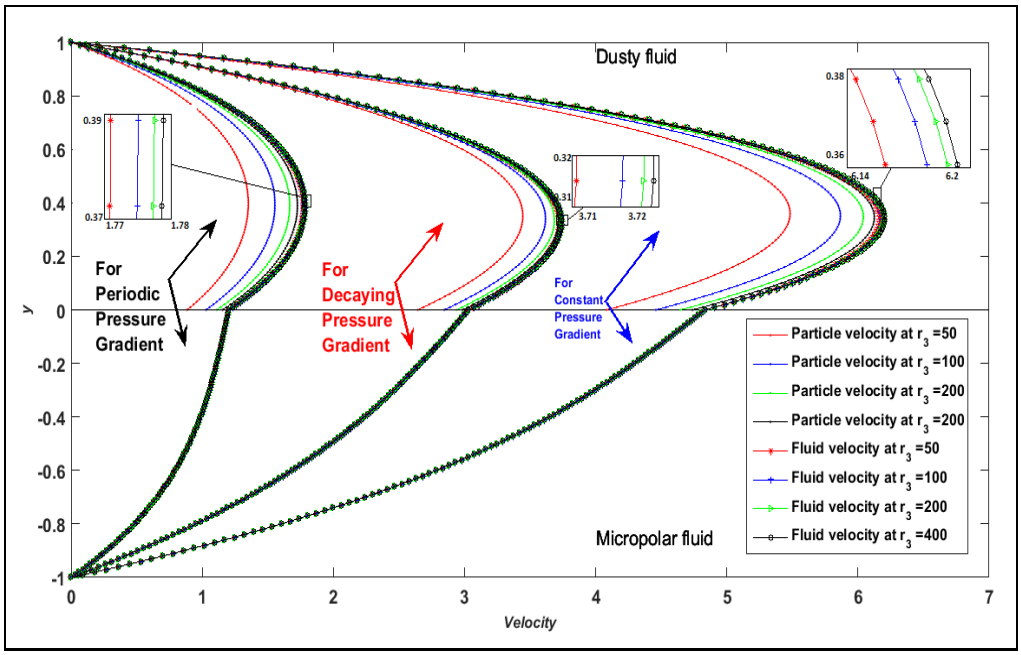

Figure 3.10: Velocity under the scheme-2 with varying r_3

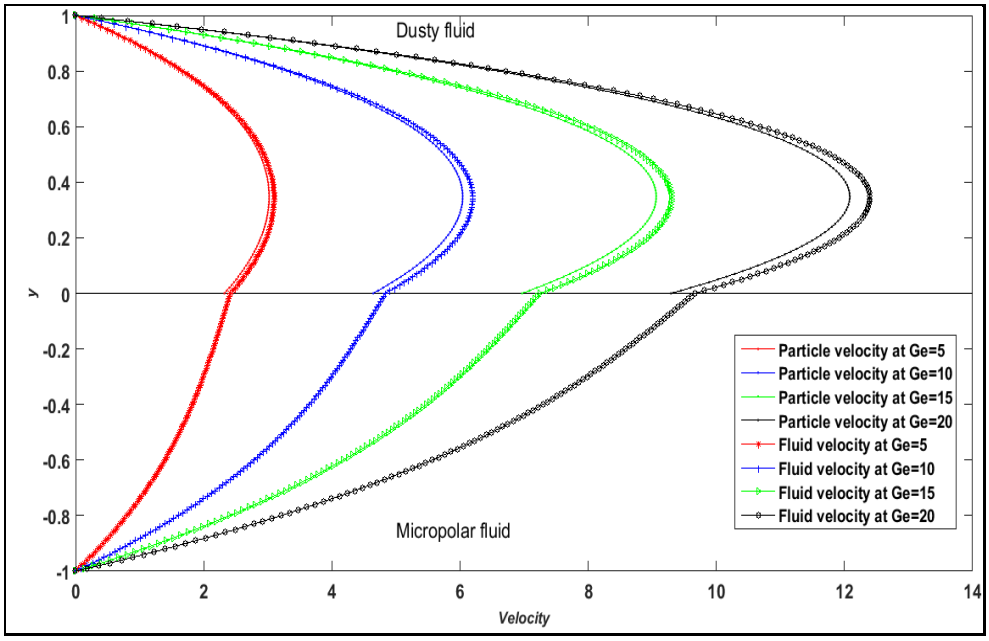

Figure 3.11:Velocity under the scheme-2 with constant pressure gradient

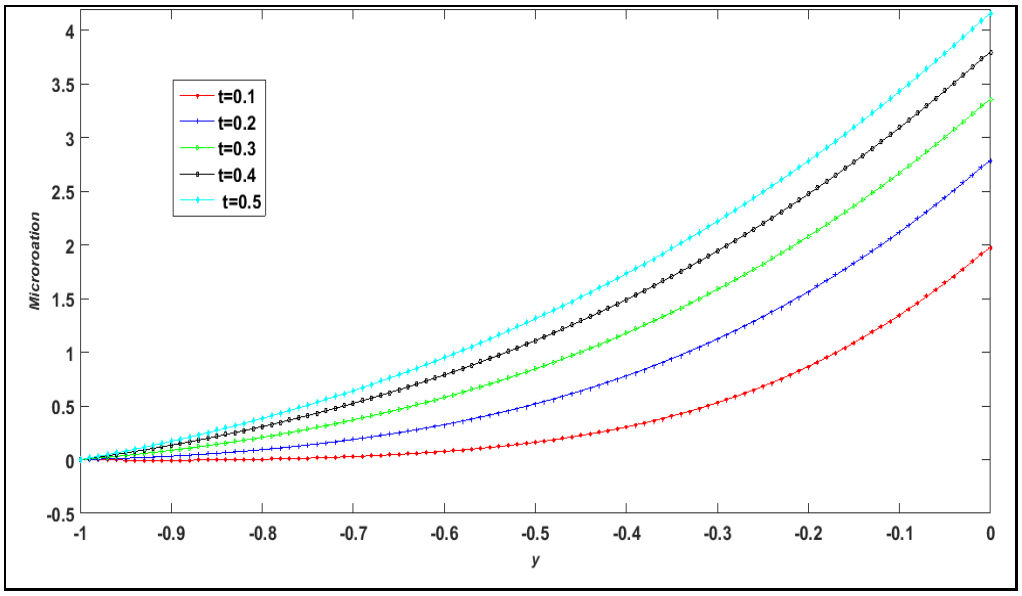

Figure 3.12: Micro-rotation of micropolar fluid under the scheme-2 with varying time

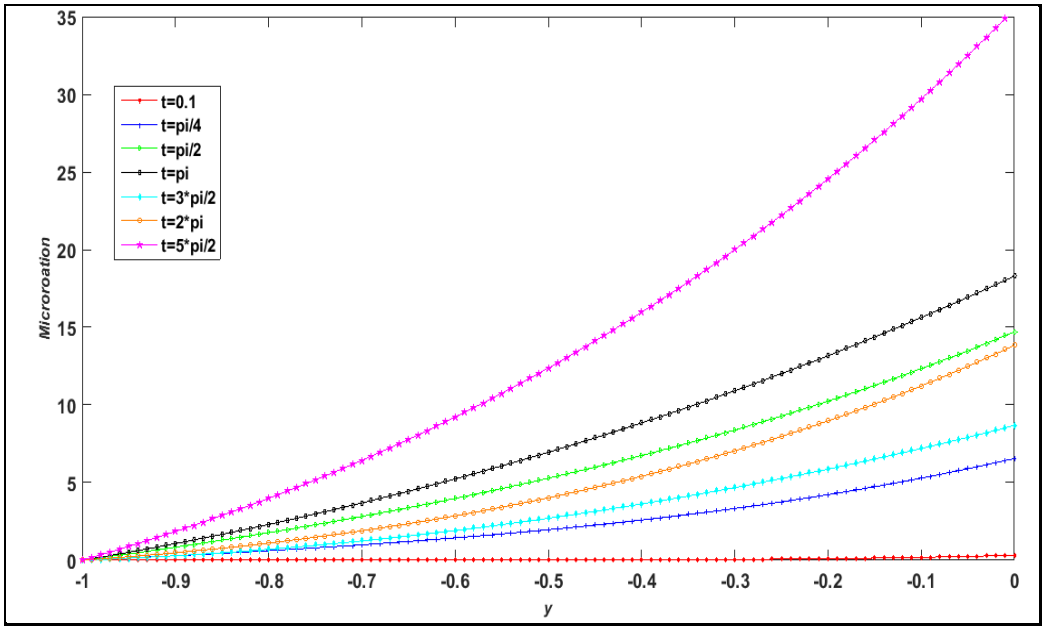

Figure 3.13: Micro-rotation under the scheme-2 with time and periodic pressure gradient

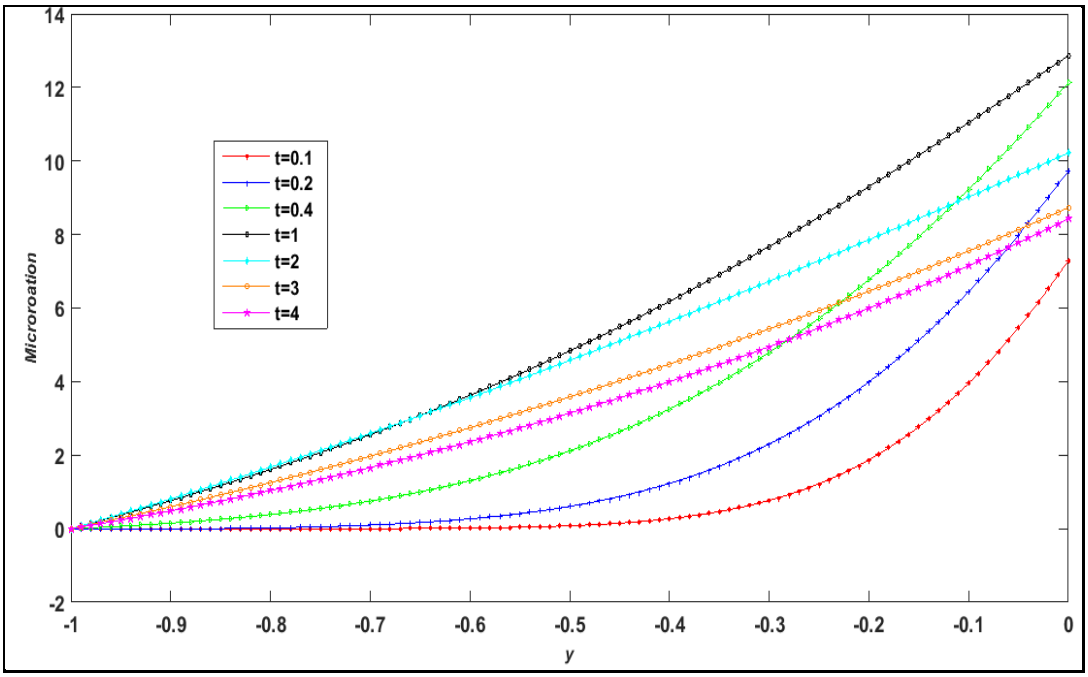

Figure 3.14: Micro-rotation under the scheme-2 with time and periodic pressure gradient

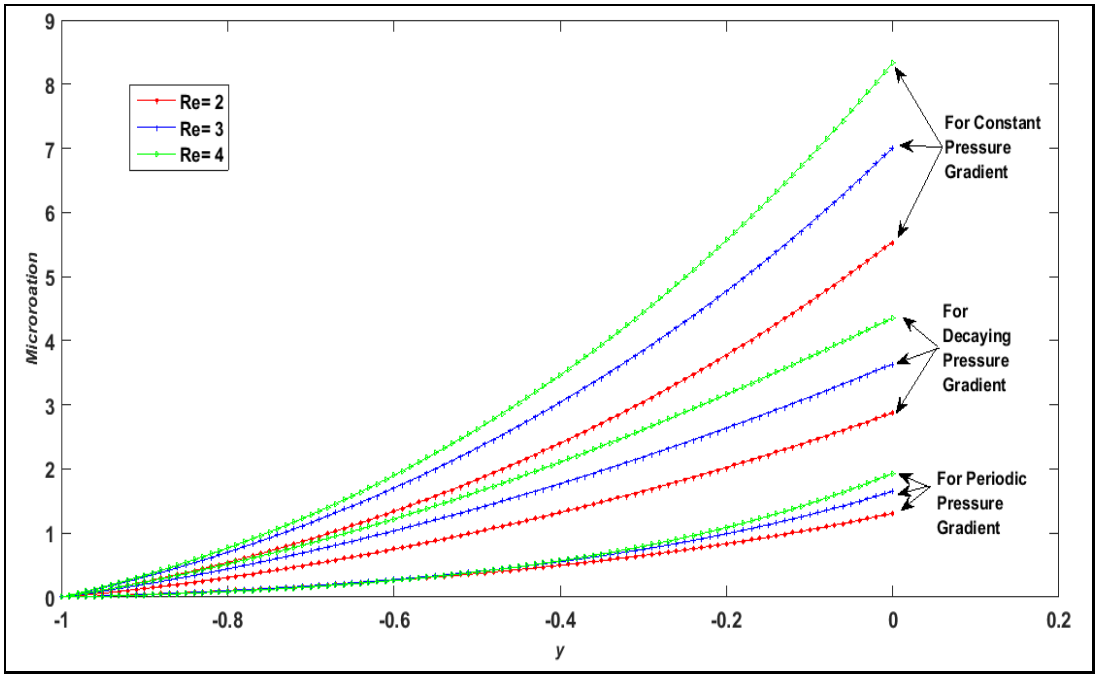

Figure 3.15: Micro-rotation under the scheme-2 with varying Reynolds number

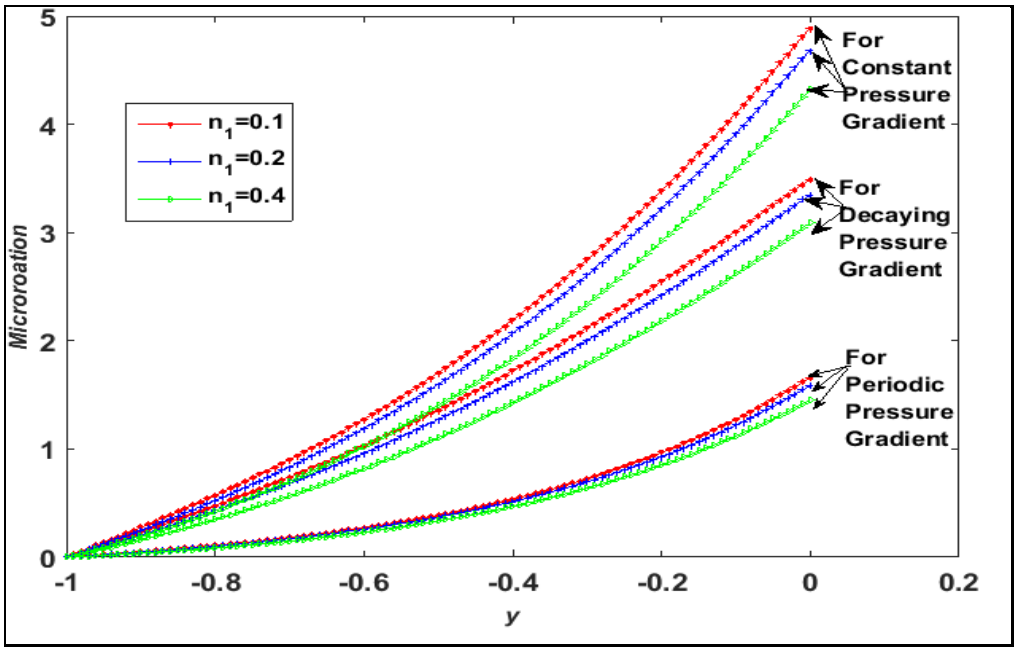

Figure 3.16: Micro-rotation under the scheme-2 with micropolar parameter (n_1)

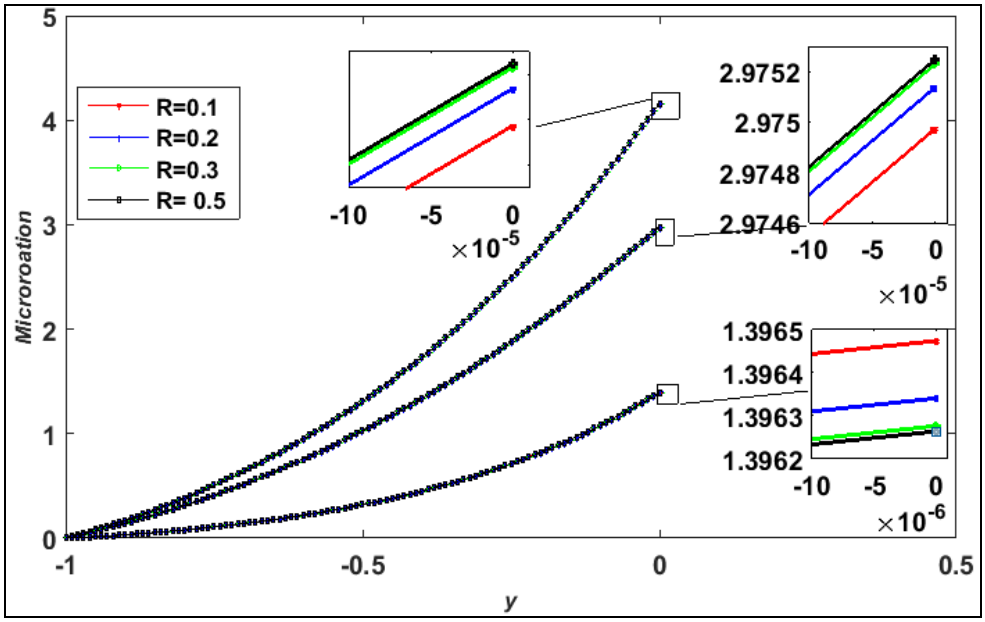

Figure 3.17: Micro-rotation under the scheme-2 with particle concentration parameter (R)

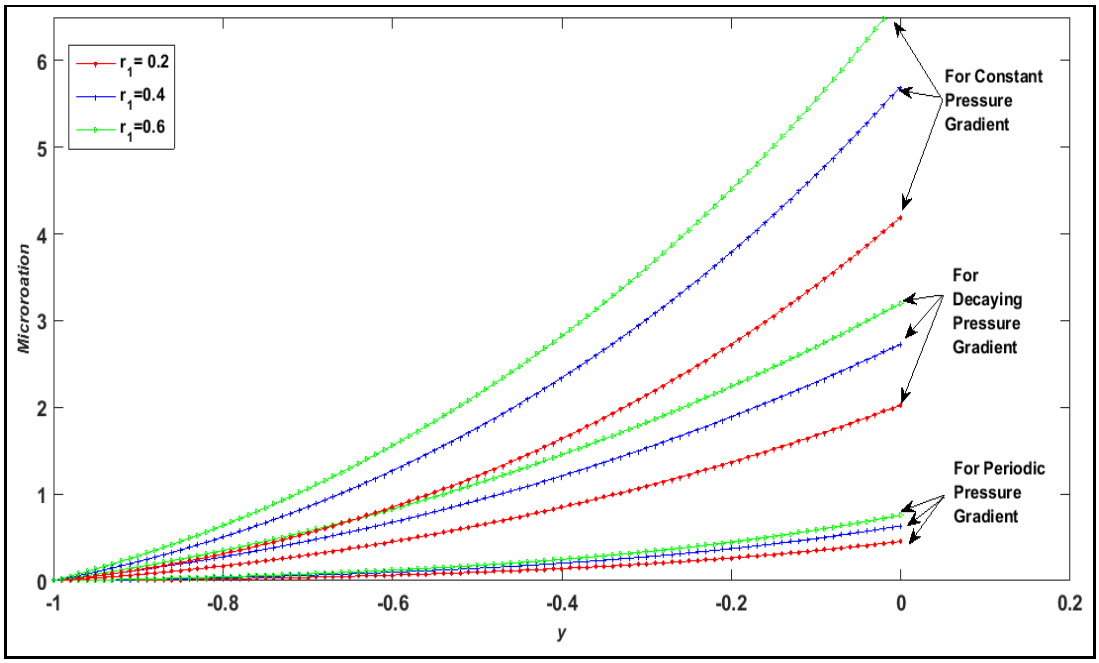

Figure 3.18: Micro-rotation under the scheme-2 with a ratio of viscosities

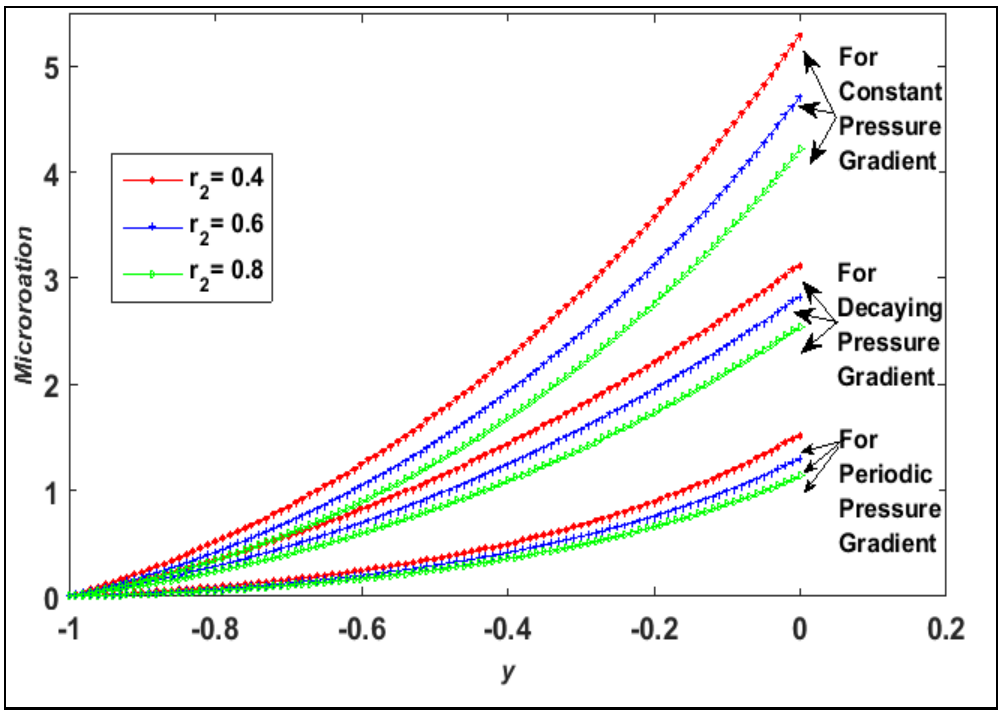

Figure 3.19: Micro-rotation profiles under the scheme-2 with a ratio of densities (r_2)

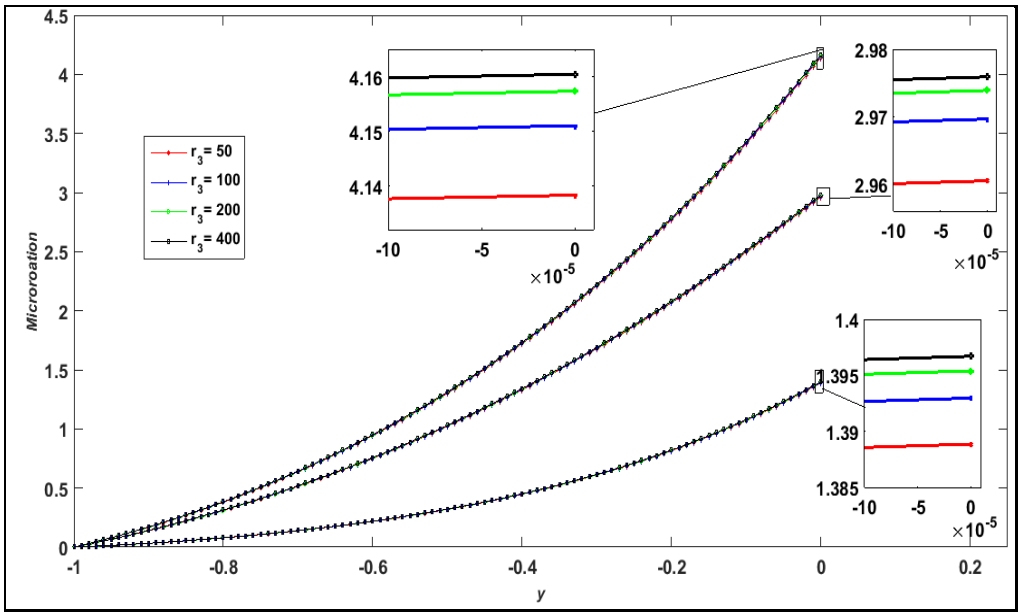

Figure 3.20: Micro-rotation profiles under the scheme-2 with varying ratios (r_3)

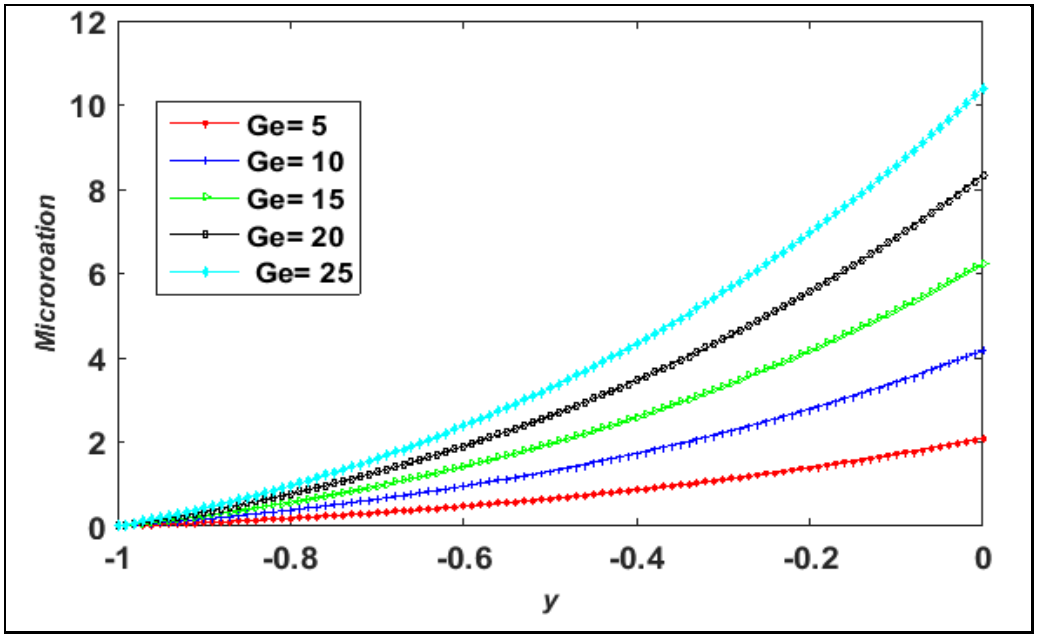

Figure 3.21: Micro-rotation under the scheme-2 with constant pressure gradient

3.3 Formulation of two immiscible micropolar and dusty fluids with an unstable interface

Consider the unsteady, laminar, and unidirectional flow of two immiscible-micropolar and dusty fluids- undergoing shearing motions. The following assumptions are being made for the momentum of the flow

a. Both fluids are viscous and incompressible move between two horizontal parallel non-porous plates.
b. Both plates are believed to be electrically non-conductive. The plates are located in the *X*-*Z* plane, as depicted in Figure 3.22.
c. Both plates are stable while the flow gets momentum by the uniform pressure gradient applied from *x*-direction and maximum flow velocity is U_0.
d. Let ρ_m, μ_m be the density and viscosity of micropolar fluid which lies in ($-k \leq y \leq l_m$) and possesses a linear fluid velocity u_m, microrotation (angular velocity) M_*, vortex viscosity κ_m, gyro-viscosity ω_m , and gyration parameter τ.
e. The dusty fluid has a density ρ_d and viscosity μ_d and occupies the region ($l_m \leq y \leq k$).
f. The dusty (upper region) fluid contains suspended dust particles of equal size and mass, non-deformable, and homogeneously distributed throughout the liquid.
g. In the dusty fluid, the dust particles have particle velocity u_p, density ρ_pAnd possess the average mass $m_p$with a particle volume fraction function $\emptyset$.
h. Owing to a viscosity jump primarily, interfacial instability occurs; the evolution of the interface is analyzed by using the horizontal attenuation in the initial interface phase

i. The flow of these immiscible fluids receives momentum in the x-direction via applied common pressure gradients with an average density given by $\rho^* = \rho_m + C_s(\rho_d - \rho_m)$ and the viscosity $\mu^* = \mu_m + C_s(\mu_d - \mu_m)$.

j. We do allow for the possibility of a jump across the interface. The volume fraction function $C_{i=2}$ describes the interface movement of immiscible fluids of various densities and viscosities.

k. Let the initial interface be $l_m y_m + A_0 cos(B_0 y)$ where y_m is the average depth of interface and A_0, B_0 are the amplitude and wavenumber

l. The volume fraction function $C_{i=2}$ is transported by the average velocity field u^* equation (1.19) Li and Renardy [81]:

m. The mean flow velocity is driven by a single momentum equation, with the resultant velocity field shared between the transitions:

n. The body force F, in the equation (1.20) is modelled as a surface tension force by the Continuum Surface Force model, and the surface tension is reconstructed as a volume force

$$F_s = \sigma\omega\nabla C_i. \tag{3.40}$$

where σ is the interfacial tension between two liquid phases and ω is the mean free surface curvature, given by

$$\omega = -\frac{\nabla^2 C_{i=2}}{\|\nabla C_{i=2}\|} = -\frac{\frac{\partial^2 C_{i=2}}{\partial x^2}+\frac{\partial^2 C_{i=2}}{\partial y^2}}{\sqrt{\left(\frac{\partial C_{i=2}}{\partial x}\right)^2+\left(\frac{\partial C_{i=2}}{\partial y}\right)^2}}, \tag{3.41}$$

$$F_s = -\sigma\frac{\frac{\partial^2 C_{i=2}}{\partial x^2}+\frac{\partial^2 C_{i=2}}{\partial y^2}}{\sqrt{\left(\frac{\partial C_{i=2}}{\partial x}\right)^2+\left(\frac{\partial C_{i=2}}{\partial y}\right)^2}}\left(\frac{\partial C_{i=2}}{\partial x}+\frac{\partial C_{i=2}}{\partial y}\right), \tag{3.42}$$

As the flow is unidirectional so-

$$\frac{\partial C_{i=2}}{\partial x} = \frac{\partial^2 C_{i=2}}{\partial x^2} = 0; \text{Hence } F_s = -\sigma\frac{\partial^2 C_{i=2}}{\partial y^2}. \tag{3.43}$$

o. It is also assumed that the particle phase is sufficiently dilute such that the interactions between any two particles are ignored. The dust particle size (radius *r*)

is also relatively tiny in scale. Hence the net dust effect on the fluid particles is equivalent to the following additional force per unit volume [24], [74]:

$$D_f = \zeta_T \rho_p (u^* - u_p) \tag{3.44}$$

Here $\zeta_T = \frac{6\pi r \mu^*}{m_p}$ is the volume transfer coefficient with an average mass of dust particle m_p, density ρ_p and radius r

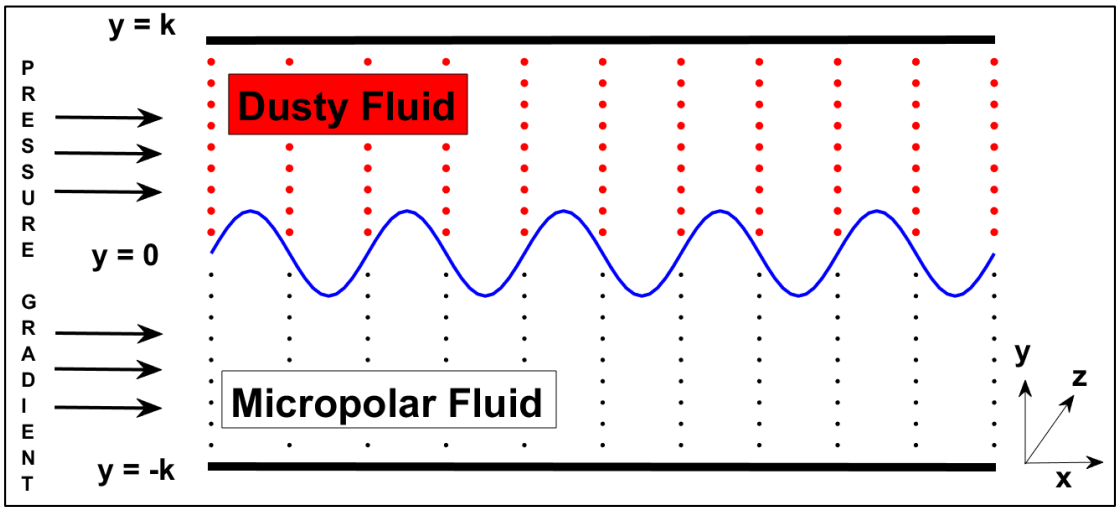

Figure 3.22:Geometrical configuration of two immiscible micropolar and dusty (scheme-2b) liquids with moving interface

The microrotation vector is available only in the zone-1 fluid, so first, the microrotation profile is obtained by the governing equations of micropolar fluid flow

The following convention is adopted for the micropolar fluid velocity $u_m = (u_m(y,t), 0, 0)$, micro-structural rotation vector $M = (0, 0, M_*(y,t))$ in zone-1.

Region-1 for Micropolar fluid $(-k \le y \le l_m)$.

$$\rho_m \frac{\partial u_m}{\partial t} = -\frac{\partial p}{\partial x} + \kappa_m \frac{\partial M_*}{\partial y} + (\mu_m + \kappa_m) \frac{\partial^2 u_m}{\partial y^2}, \tag{3.45}$$

$$\rho_m \tau \frac{\partial M_*}{\partial t} = \omega_m \frac{\partial^2 M_*}{\partial y^2} - \kappa_m (2M_* + \frac{\partial u_m}{\partial y}). \tag{3.46}$$

The governing equation for mean flow $u^*(y,t)$ and interface track $C_{i=2}$ in $(-k \le y \le k)$ under the aforesaid assumed constraints are

$$\frac{\partial C_{i=2}}{\partial t} + u^* \frac{\partial C_{i=2}}{\partial y} = 0, \tag{3.47}$$

$$\rho^* \frac{\partial u^*}{\partial t} = \begin{pmatrix} -\frac{\partial p}{\partial x} + (\mu^* + \kappa_m)\frac{\partial^2 u^*}{\partial y^2} + \kappa_m \frac{\partial M_*}{\partial y} \\ -\zeta_T \rho_p (u^* - u_p) + \rho^* g - \sigma \frac{\partial^2 C_{i=2}}{\partial y^2} \end{pmatrix}, \tag{3.48}$$

$$\frac{\partial u_p}{\partial t} = \zeta_T (u^* - u_p). \tag{3.49}$$

The classical no-slip and hyper-stick conditions are considered at the boundaries. These conditions can be written as follows in numerical terms.

Initial conditions: At $t \le 0$,

$$\left.\begin{array}{l} u_m(y,t) = 0 \quad for \ -k \le y \le l_m, \\ M_*(y,t) = 0 \quad for \ -k \le y \le l_m, \\ u^*(y,t) = 0 \quad for -k \le y \le k, \\ C_j(y,t) = A_0 cos(B_0 y) \ for \ -k \le y \le k, \\ u_p(y,t) = 0 \quad for \ l_m \le y \le k. \end{array}\right\} \tag{3.50}$$

Boundary conditions: At $t > 0$,

$$\left.\begin{array}{l} u_m(-k,t) = 0, \\ M_*(-k,t) = 0, \\ u^*(-k,t) = 0, \\ u^*(k,t) = 0, \\ u_m(\varepsilon,t) = \varepsilon, \\ M_*(\varepsilon,t) = -1/2 \ \frac{\partial u_m}{\partial y}. \end{array}\right\} \tag{3.51}$$

Introducing the non-dimensional parameters-

$$\left.\begin{array}{c} \bar{x}=\frac{x}{k},\bar{y}=\frac{y}{k},\overline{u^*}=\frac{u^*}{U_0},\overline{u_p}=\frac{u_p}{U_0},\bar{p}=\frac{p}{\rho^* {U_0}^2},\bar{t}=\frac{tU_0}{k},Ca=\frac{\mu^* U_0}{\sigma}, \\ \varepsilon\in[-1,1]\, s.t\,\sqrt{(u_m(\varepsilon,t)-C_{i=2})^2}=0, R=\frac{Kk^2\rho_p}{\mu_d m_p}, \\ \omega_m=(\mu_m+\kappa_m/2)\tau\ with\ \tau=k^2, n_1=\frac{\kappa_m}{\mu_m}, K=6\pi r\mu_d U_0, \\ Re=\frac{\rho_m U_0}{\mu_m}, r_1=\frac{\mu_d}{\mu_m}, r_2=\frac{\rho_d}{\rho_m}, r_3=\frac{\rho_m+\rho_d}{\rho_p}, Fr=\frac{{U_0}^2}{gk}. \end{array}\right\} \quad (3.52)$$

After dropping the bars and introducing the above non-dimensional parameters, appropriate initial, interfacial, and boundary conditions according to the scheme, the equations (3.45) – (3.49) can be revised as

(Micropolar liquid zone: $-k \le y \le 0$),

$$\frac{\partial u_m}{\partial t} = Ge(t) + \frac{n_1}{Re}\frac{\partial M_*}{\partial y} + \frac{(n_1+1)}{Re}\frac{\partial^2 u_m}{\partial y^2}, \quad (3.53)$$

$$\frac{\partial M_*}{\partial t} = \frac{\left(\frac{n_1}{2}+1\right)}{Re}\frac{\partial^2 M_*}{\partial y^2} - \frac{n_1\left(2M_* + \frac{\partial u_m}{\partial y}\right)}{Re}. \quad (3.54)$$

The Mean flow and interface track *($-k \le y \le k$)* is governed as

$$\frac{\partial C_i}{\partial t} + u^*\frac{\partial C_i}{\partial y} = 0, \quad (3.55)$$

$$\frac{\partial u^*}{\partial t} = \begin{pmatrix} \frac{Ge(t)}{(1+C_s(r_2-1))} + \frac{(n_1+1)(1+C_s(r_1-1))}{Re(1+C_s(r_2-1))}\frac{\partial^2 u^*}{\partial y^2} + \frac{n_1(1+C_s(r_1-1))}{Re(1+C_s(r_2-1))}\frac{\partial M_*}{\partial y} \\ -\frac{R(1+C_s(r_1-1))}{Re(1+C_s(r_2-1))}(u^*-u_p) + \frac{1}{Fr} - \frac{1+C_s(r_1-1)}{Re*Ca(1+C_s(r_2-1))}\frac{\partial^2 C_i}{\partial y^2} \end{pmatrix}, \quad (3.56)$$

$$\frac{\partial u_p}{\partial t} = \frac{Rr_3(1+C_s(r_1-1))}{Re(1+r_2)}(u^*-u_p). \quad (3.57)$$

equations (3.50) - (3.51) are considered as initial and boundary conditions with $k = 1$

As the flow gets momentum by the *x*-directional time-dependent applied pressure gradient, three different cases for $Ge(t)$ $-\nabla p = -\partial p/\partial x$ with $t > 0$ are included in the analysis.

Case-*I*: $Ge(t) = Ge$.

Case-*II*: $Ge(t) = Ge * Sint.$

Case-*III*: $Ge(t) = Ge * e^{-t}$.

3.3.1 Computation of interface and flow velocity under scheme-2

To compute the interface tracking under the moving interface scheme flow, first, the microrotation profile is obtained in zone-1, and then the interface track is obtained by using the mean flow velocity. Hence the system of single momentum coupled partial differential equations (3.53) - (3.57) followed by the approximation of the spatial components of order I and order II are updated and solved numerically, and the fluid and particle velocities profiles are obtained.

Micropolar fluid zone ($-k \leq y \leq 0$):

$$u_{m_t} = Ge(t) + \frac{n_1}{Re}\left(\sum_{i=1}^{N} a^*{}_{ij} M_*(y_j,t)\right) + \frac{(n_1+1)}{Re}\left(\sum_{j=1}^{N} b^*{}_{ij} u_m(y_j,t)\right), \quad (3.58)$$

$$M_{*_t} = \frac{(n_1+2)}{2Re}\left(\sum_{j=1}^{N} b^*{}_{ij} M_*(y_j,t)\right) - \frac{n_1}{Re}\left(2M_* + \sum_{j=1}^{N} a^*{}_{ij} u_m(y_j,t)\right). \quad (3.59)$$

Micropolar fluid + dusty fluid zone ($-l \leq y \leq l$):

$$\frac{\partial C_i}{\partial t} = -u^*(y_j,t)\left(\sum_{j=1}^{N} a^*{}_{ij} C_i(y_j,t)\right), \quad (3.60)$$

$$\frac{\partial u^*}{\partial t} = \frac{Ge(t)}{(1+C_s(r_2-1))} + \frac{(n_1+1)(1+C_s(r_1-1))}{Re(1+C_s(r_2-1))}\left(\sum_{j=1}^{N} b^*{}_{ij} u^*(y_j,t)\right) + \frac{1}{Fr} +$$
$$\frac{n_1(1+C_s(r_1-1))}{Re(1+C_s(r_2-1))}\left(\sum_{j=1}^{N} a^*{}_{ij} M_*(y_j,t)\right) - \frac{R(1+C_s(r_1-1))}{Re(1+C_s(r_2-1))}\left(u^*(y_j,t) - u_p(y_j,t)\right) -$$
$$\frac{1+C_s(r_1-1)}{Re*Ca(1+C_s(r_2-1))}\left(\sum_{j=1}^{N} b^*{}_{ij} C_i(y_j,t)\right), \quad (3.61)$$

$$\frac{\partial u_p}{\partial t} = \frac{Rr_3\,(1+C_s(r_1-1))}{Re(1+r_2)}\left(u^*(y_j,t) - u_p(y_j,t)\right). \quad (3.62)$$

Thus, the equations are reduced into a system of ordinary differential equations in time, that is, for *i=1, 2, 3…, N*, and the system is again solved by the four-step third-order SSP-RK43 scheme (1.69) - (1.72).

At the first step for *i=1,2,3…, N.*

Micropolar fluid zone *($-1 \le y \le 0$):*

$$u_{m_1} = u_{m_0} + \frac{\Delta t}{2}\begin{bmatrix} Ge(t) + \frac{n_1}{Re}\left(\sum_{j=1}^{N} a^*{}_{ij} M_{*_0}(y_j,t)\right) \\ + \frac{(n_1+1)}{Re}\left(\sum_{j=1}^{N} b^*{}_{ij} u_{m_0}(y_j,t)\right) \end{bmatrix}, \tag{3.63}$$

$$M_{*m} = M_{*0} + \frac{\Delta t}{2}\frac{(n_1+2)}{2Re}\begin{bmatrix} \left(\sum_{j=1}^{N} b^*{}_{ij} M_{*_0}(y_j,t)\right) \\ -\frac{n_1}{Re}\left(2M_{*_0} + \sum_{j=1}^{N} a^*{}_{ij} u_{m_0}(y_j,t)\right) \end{bmatrix}. \tag{3.64}$$

Micropolar fluid + dusty fluid zone ($-1 \le y \le 1$):

$$C_{i_1} = C_{i_0} + \frac{\Delta t}{2}\left[-u^*{}_1(y_j,t)\left(\sum_{j=1}^{N} a^*{}_{ij} C_i(y_j,t)\right)\right], \tag{3.65}$$

$$u^*{}_1 = u^*{}_0 + \frac{\Delta t}{2}\left[\frac{Ge(t)}{(1+C_s(r_2-1))} + \frac{(n_1+1)(1+C_s(r_1-1))}{Re(1+C_s(r_2-1))}\left(\sum_{j=1}^{N} b^*{}_{ij} u^*{}_0(y_j,t)\right) + \right.$$
$$\frac{n_1(1+C_s(r_1-1))}{Re(1+C_s(r_2-1))}\left(\sum_{j=1}^{N} a^*{}_{ij} M_{*_0}(y_j,t)\right) - \frac{R(1+C_s(r_1-1))}{Re(1+C_s(r_2-1))}\left(u^*{}_0(y_j,t) - u_{p_0}(y_j,t)\right) +$$
$$\left. \frac{1}{Fr} - \frac{1+C_s(r_1-1)}{Re*Ca(1+C_s(r_2-1))}\left(\sum_{j=1}^{N} b^*{}_{ij} C_{i_0}(y_j,t)\right)\right], \tag{3.66}$$

$$u_{p_1} = u_{p_0} + \frac{\Delta t}{2}\left[\left(\frac{Rr_3(1+C_s(r_1-1))}{Re(1+r_2)}\right) u^*{}_0(y_j,t) - u_{p_0}(y_j,t)\right]. \tag{3.67}$$

In the first step of the method, similar to earlier, the conditions (3.50) - (3.51) are applied favourably.

At the second step *for i=1,2,3…,N.*

Micropolar fluid zone ($-1 \le y \le 0$):

$$u_{m_2} = u_{1_1} + \frac{\Delta t}{2}\begin{bmatrix} Ge(t) + \frac{n_1}{Re}\left(\sum_{j=1}^{N} a^*{}_{ij} M_{*_1}(y_j,t)\right) \\ + \frac{(n_1+1)}{Re}\left(\sum_{j=1}^{N} b^*{}_{ij} u_{m_1}(y_j,t)\right) \end{bmatrix}, \tag{3.68}$$

$$M_{*2} = M_{*1} + \frac{\Delta t}{2}\begin{bmatrix} \frac{(n_1+2)}{2Re}\left(\sum_{j=1}^{N} b^*{}_{ij} M_{*_1}(y_j,t)\right) \\ -\frac{n_1}{Re}\left(2M_{*_1} + \sum_{j=1}^{N} a^*{}_{ij} u_{m_1}(y_j,t)\right) \end{bmatrix}. \tag{3.69}$$

Micropolar fluid + dusty fluid zone ($-1 \le y \le 1$):

$$C_{i_2} = C_{i_1} + \frac{\Delta t}{2}\left(-u^*{}_2(y_j,t)\left(\sum_{j=1}^{N} a^*{}_{ij} C_{i_1}(y_j,t)\right)\right), \tag{3.70}$$

$$u^*{}_2 = u^*{}_1 + \frac{\Delta t}{2}\left[\frac{Ge(t)}{\left(1+C_s(r_2-1)\right)} + \frac{(n_1+1)\left(1+C_s(r_1-1)\right)}{Re\left(1+C_s(r_2-1)\right)}\left(\sum_{j=1}^{N} b^*{}_{ij} u^*{}_1(y_j,t)\right) + \right.$$
$$\frac{n_1\left(1+C_s(r_1-1)\right)}{Re\left(1+C_s(r_2-1)\right)}\left(\sum_{j=1}^{N} a^*{}_{ij} M_{*_1}(y_j,t)\right) - \frac{R\left(1+C_s(r_1-1)\right)}{Re\left(1+C_s(r_2-1)\right)}\left(u^*{}_1(y_j,t) - u_{p_1}(y_j,t)\right) +$$
$$\left.\frac{1}{Fr} - \frac{1+C_s(r_1-1)}{Re*Ca\left(1+C_s(r_2-1)\right)}\left(\sum_{j=1}^{N} b^*{}_{ij} C_{i_1}(y_j,t)\right)\right], \tag{3.71}$$

$$u_{p_2} = u_{p_1} + \frac{\Delta t}{2}\left[\frac{Rr_3\left(1+C_s(r_1-1)\right)}{Re(1+r_2)}\left(u^*{}_1(y_j,t) - u_{p_1}(y_j,t)\right)\right]. \tag{3.72}$$

In the second step of the method, the conditions (3.50) - (3.51) are implemented again.

In the third step for *i=1,2,3…,N*.

Micropolar fluid zone ($-1 \le y \le 0$):

$$u_{m_3} = \frac{2u_{1_0}}{3} + \frac{u_{1_2}}{3} + \frac{\Delta t}{6}\left[\begin{matrix} Ge(t) + \frac{n_1}{Re}\left(\sum_{j=1}^{N} a^*{}_{ij} M_{*_2}(y_j,t)\right) \\ + \frac{(n_1+1)}{Re}\left(\sum_{j=1}^{N} b^*{}_{ij} u_{m_2}(y_j,t)\right) \end{matrix}\right], \tag{3.73}$$

$$M_{*_3} = \frac{2M_{*_0}}{3} + \frac{M_{*_2}}{3} + \frac{\Delta t}{6}\left[\begin{matrix} \frac{(n_1+2)}{2Re}\left(\sum_{j=1}^{N} b^*{}_{ij} M_{*_2}(y_j,t)\right) - \\ \frac{n_1}{Re}\left(2M_{*_2} + \sum_{j=1}^{N} a^*{}_{ij} u_{m_2}(y_j,t)\right) \end{matrix}\right]. \tag{3.74}$$

Micropolar fluid + dusty fluid zone ($-1 \le y \le 1$):

$$C_{i_3} = \frac{2C_{i_0}}{3} + \frac{C_{i_2}}{3} + \frac{\Delta t}{6}\left[-u^*{}_3(y_j,t)\left(\sum_{j=1}^{N} a^*{}_{ij} C_{i_2}(y_j,t)\right)\right], \tag{3.75}$$

$$u^*{}_3 = \frac{2u^*{}_0}{3} + \frac{u^*{}_2}{3} + \frac{\Delta t}{6}\left[\frac{(n_1+1)\left(1+C_s(r_1-1)\right)}{Re\left(1+C_s(r_2-1)\right)}\left(\sum_{j=1}^{N} b^*{}_{ij} u^*{}_2(y_j,t)\right) + \right.$$
$$\frac{n_1\left(1+C_s(r_1-1)\right)}{Re\left(1+C_s(r_2-1)\right)}\left(\sum_{j=1}^{N} a^*{}_{ij} M_{*_2}(y_j,t)\right) - \frac{R\left(1+C_s(r_1-1)\right)}{Re\left(1+C_s(r_2-1)\right)}\left(u^*{}_2(y_j,t) - u_{p_2}(y_j,t)\right) +$$
$$\left.\frac{1}{Fr} - \frac{1+C_s(r_1-1)}{Re*Ca\left(1+C_s(r_2-1)\right)}\left(\sum_{j=1}^{N} b^*{}_{ij} C_{i_2}(y_j,t)\right)\right], \tag{3.76}$$

$$u_{p_3} = \frac{2u_{p_0}}{3} + \frac{u_{p_2}}{3} + \frac{\Delta t}{6}\left[\frac{Rr_3\left(1+C_s(r_1-1)\right)}{Re(1+r_2)}\frac{\left(u^*{}_2(y_j,t) - u_{p_2}(y_j,t)\right)}{Re}\right]. \tag{3.77}$$

At the third step of the method, the conditions equations (3.50) - (3.51) are again invoked.

At the fourth step for *i=1,2,3…,N.*

Micropolar fluid zone ($-k \le y \le 0$):

$$u_m = u_{m_3} + \frac{\Delta t}{2}\left[\begin{matrix} Ge(t) + \frac{n_1}{Re}\left(\sum_{j=1}^{N} a^*{}_{ij} M_{*_3}(y_j,t)\right) \\ + \frac{(n_1+1)}{Re}\left(\sum_{j=1}^{N} b^*{}_{ij} u_{m_3}(y_j,t)\right) \end{matrix}\right], \tag{3.78}$$

$$M_* = M_{*_3} + \frac{\Delta t}{2}\left[\begin{matrix} \frac{(n_1+2)}{2Re}\left(\sum_{j=1}^{N} b^*{}_{ij} M_{*_3}(y_j,t)\right) - \\ \frac{n_1}{Re}\left(2M_{*_3} + \sum_{j=1}^{N} a^*{}_{ij} u_{m_3}(y_j,t)\right) \end{matrix}\right]. \tag{3.79}$$

Micropolar fluid + dusty fluid zone ($-1 \le y \le 1$):

$$C_i = C_{i_3} + \frac{\Delta t}{6}\left[-u^*(y_j,t)\left(\sum_{j=1}^{N} a^*{}_{ij} C_{i_3}(y_j,t)\right)\right], \tag{3.80}$$

$$\begin{aligned} u^* = u^*{}_3 + \frac{\Delta t}{2}\Bigg[& \frac{Ge(t)}{(1+C_s(r_2-1))} + \frac{(n_1+1)(1+C_s(r_1-1))}{Re(1+C_s(r_2-1))}\left(\sum_{j=1}^{N} b^*{}_{ij} u^*{}_3(y_j,t)\right) + \\ & \frac{n_1(1+C_s(r_1-1))}{Re(1+C_s(r_2-1))}\left(\sum_{j=1}^{N} a^*{}_{ij} M_{*_3}(y_j,t)\right) - \frac{R(1+C_s(r_1-1))}{Re(1+C_s(r_2-1))}\left(u^*{}_3(y_j,t) - u_{p_3}(y_j,t)\right) + \\ & \frac{1}{Fr} - \frac{1+C_s(r_1-1)}{Re*Ca(1+C_s(r_2-1))}\left(\sum_{j=1}^{N} b^*{}_{ij} C_{i_3}(y_j,t)\right)\Bigg], \end{aligned} \tag{3.81}$$

$$u_p = u_{p_3} + \frac{\Delta t}{2}\left[\frac{R*r_3*r_1}{r_2}\frac{\left(u^*{}_3(y_j,t) - u_{p_3}(y_j,t)\right)}{Re}\right]. \tag{3.82}$$

At the fourth step of the method, the conditions (3.50) - (3.51) are again deployed. Hence the interface profile is eventually computed at the fourth step of MCB-DQM simulation.

3.3.2 Result and analysis for an interface track

The MCB-DQM results for interface tracking between two immiscible micropolar and dusty fluids are observed by the following value of parameters $r_1 = 0.5, Re = 10, R = 0.5, r_2 = 0.5, r_3 = 300, \eta_1 = 0.5, Cs = 0.5, Ca = 0.5, Fr = 2 \; and \; Ge = 10$

Figure 3.23-Figure 3.31 shows the evolution of the interface between two liquids with numerous fluid parameters, including the Reynolds number, time, amplitude, wave number, particulate concentration parameter, density ratio, viscosity ratio, and applied pressure gradients.

It is apparent from Figure 3.23 that initially, the vertical elongation of the interface is large, and then the shape of the interface (topology) evolves; hence the undulating sequence occurs faster for a more considerable time and eventually becomes stable. It can be concluded that initially, with small-time, the large sinusoidal interface is observed, and later, the wave's peak moves forward quickly as time increases.

The top fluid (dusty Saffman liquid) is even less viscous than the bottom fluid (Eringen micropolar fluid). It is also noticed that the qualitative characteristics of this flow are sustained, and as expected, the interface starts to shift vertically if the amplitude is enhanced (see Figure 3.24).

It is observed from Figure 3.25 that for a small value of wave number, the interface is stable, and the vertical undulation is cited with a greater weight of B_0.The sinusoidal undulation occurs faster with a constant pressure gradient, and the interface does not become stable (see Figure 3.26).

Figure 3.27-Figure 3.30 indicates that a tiny shift in the sinusoidal interface is observed with an increment in Reynolds number, density ratio, Froude number, capillary number, and the two liquids do not penetrate each other in the same fashion. It is noteworthy also that Froude number (Fr) is generally constrained as values from 2 to 10; inertial force is double the gravity force or a maximum of ten times that of the gravity force in

all simulations. This range of values is practicable for many industrial immiscible two-fluid duct systems. Additionally, the capillary number *Ca*, the dimensionless number expressing the ratio of viscous force and the surface tension acting across the interface between the two immiscible liquids is the prescribed ratio of viscous drag force to surface tension force across the interface, is defined by values from 0.1 to 2, with the default value of 0.5. In other words, for the minimal *Ca* case, the viscous force is 10% of the surface tension force (*Ca = 0.1*), whereas for the maximum *Ca* case, the viscous force is double the surface tension force at the interface (*Ca = 2*).

Figure 3.31 shows the sequence of the interface evolution with all three applied pressure gradients at a specific time (*t=1*), also showing the impact of capillary number, *Ca*; it is observed that initially at the crest of the wave is high, and then the displacement is gradually decelerated as the interface moves horizontally when decaying pressure gradient is applied. The interface's vertical elongation is also tiny compared to either the constant or periodic pressure gradient cases.

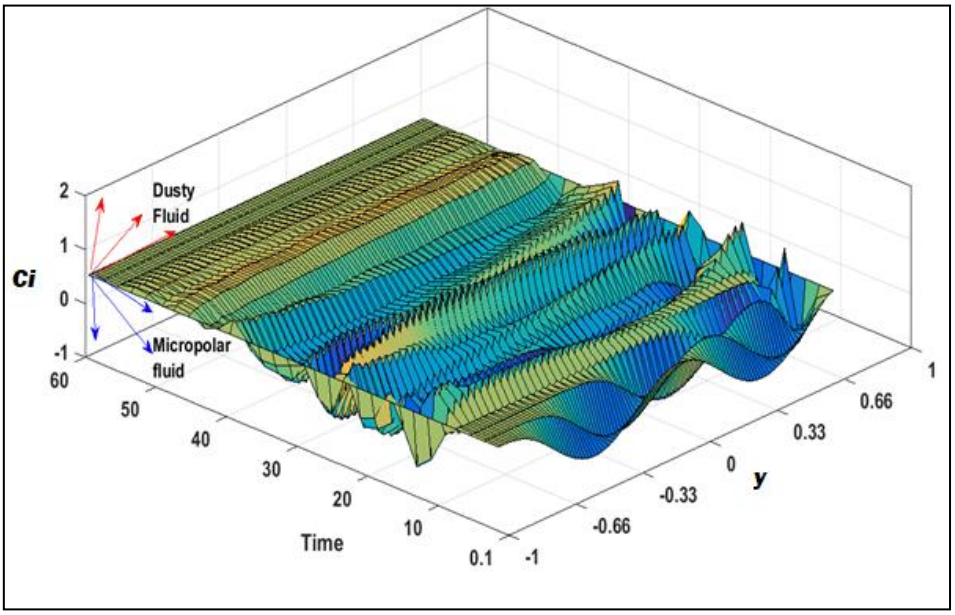

Figure 3.23:: Interface tracking between micropolar and dusty fluid with time

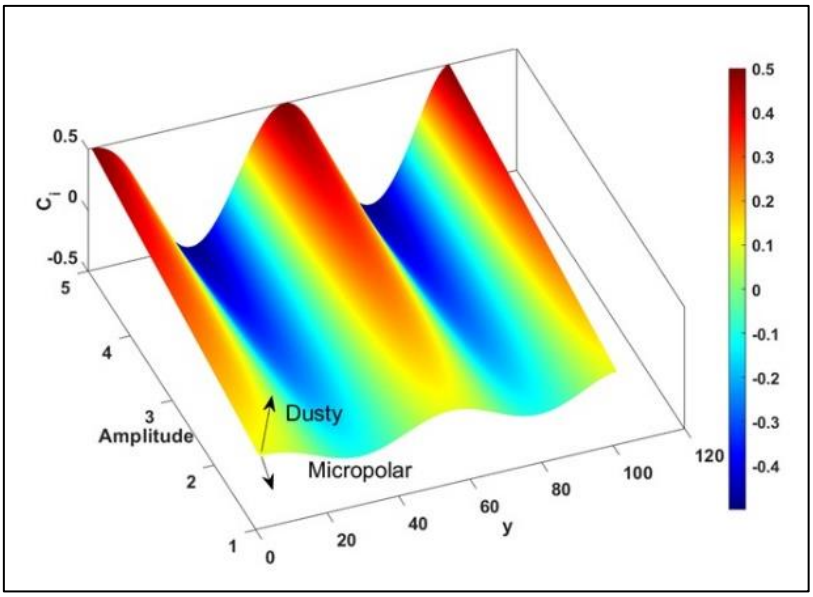

Figure 3.24: Interface tracking between micropolar and dusty fluid with amplitude

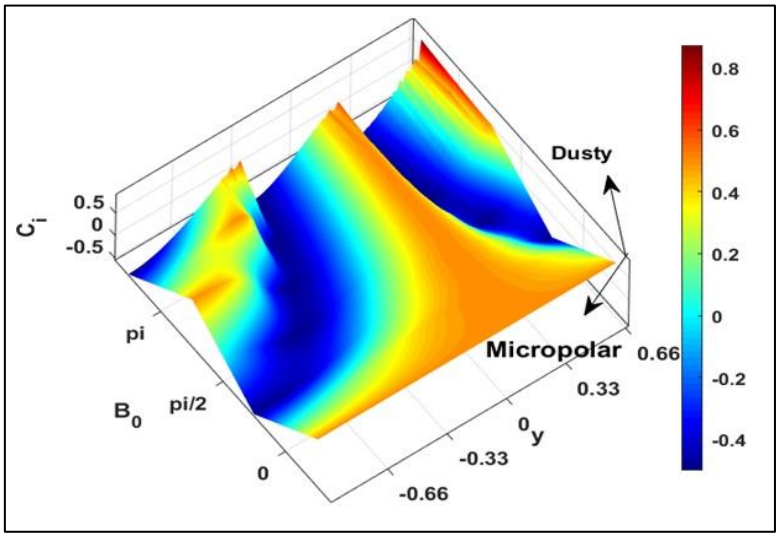

Figure 3.25: Interface tracking between micropolar and dusty fluid with wavenumber

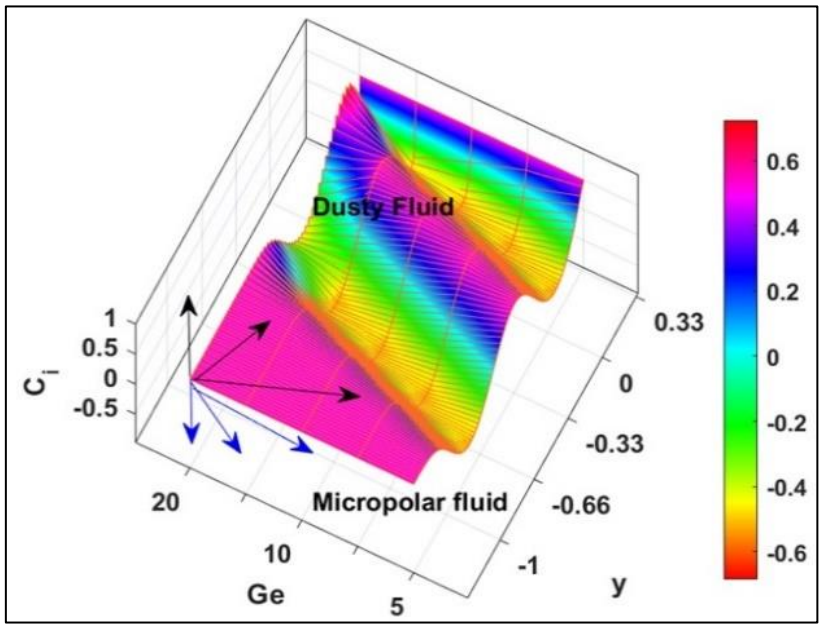

Figure 3.26: Interface tracking between micropolar and dusty fluid with *Ge*

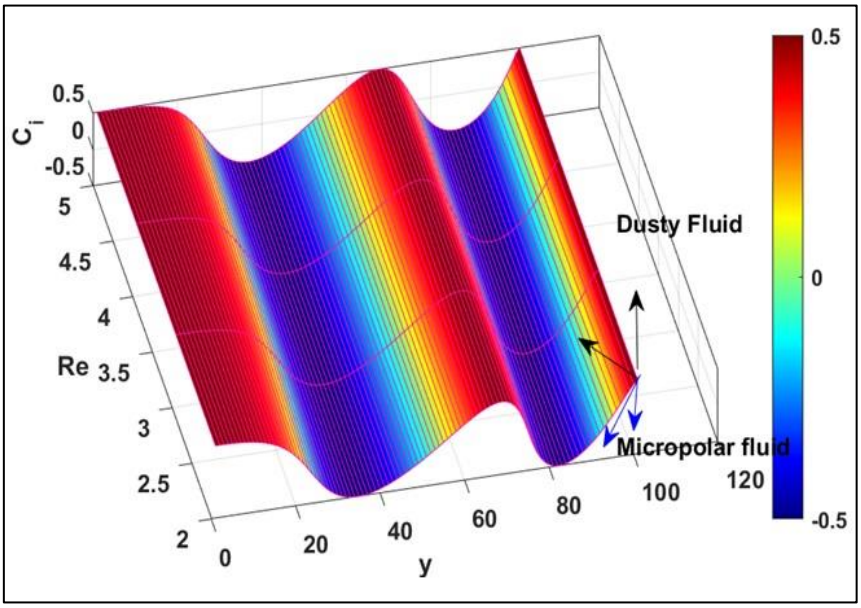

Figure 3.27: Interface tracking between micropolar and dusty fluid with Reynolds number

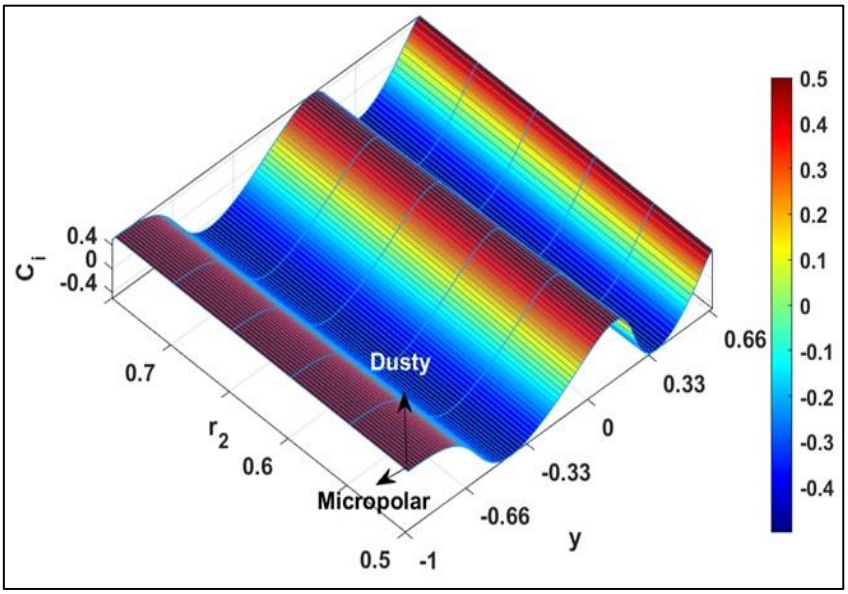

Figure 3.28: Interface tracking between micropolar and dusty fluid with the ratio of densities

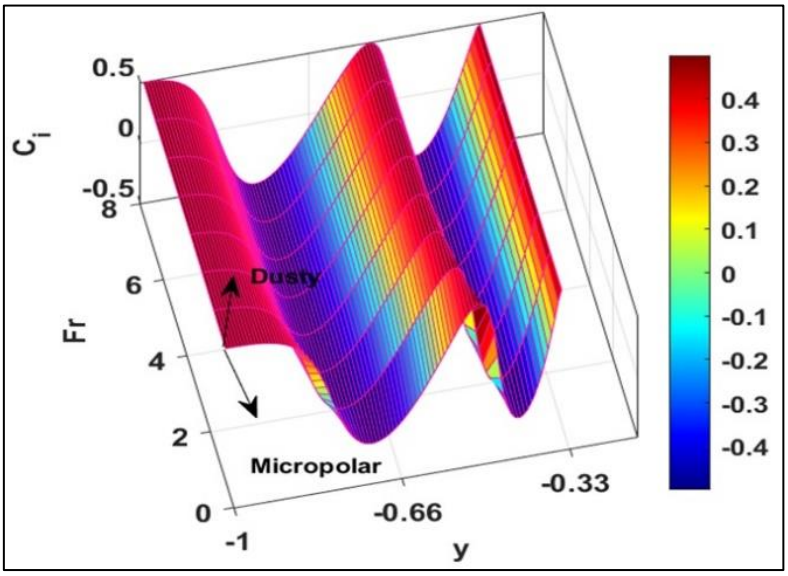

Figure 3.29: Interface tracking between micropolar and dusty fluid with Froude number

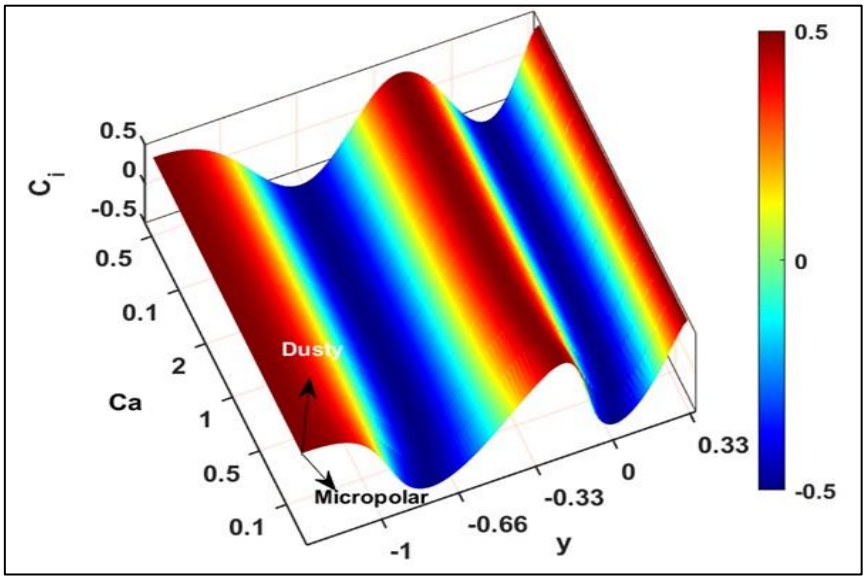

Figure 3.30: Interface tracking between micropolar and dusty fluid with Capillary number

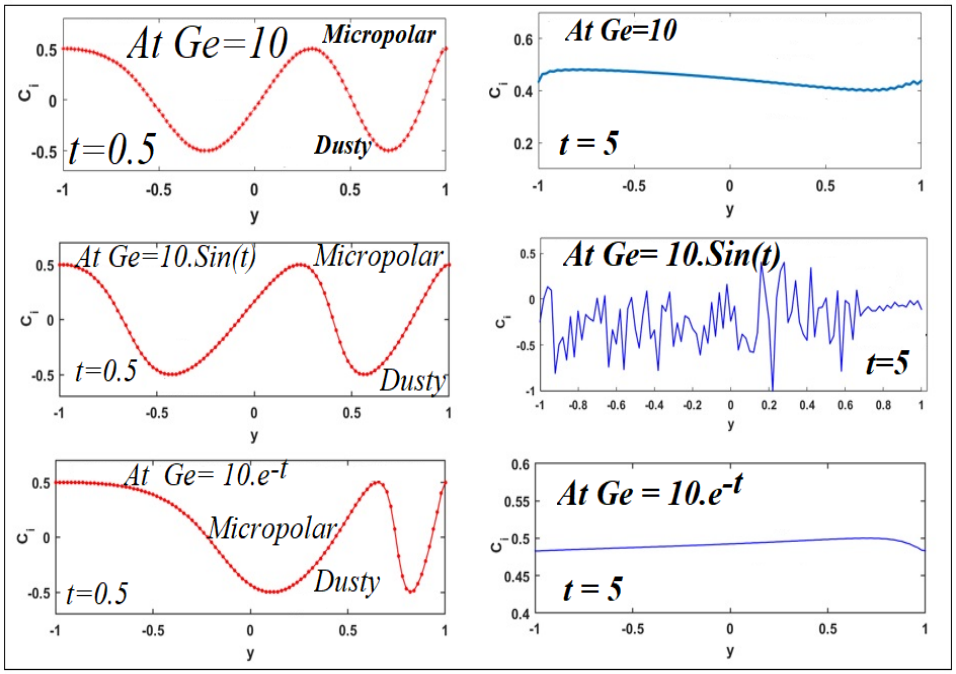

Figure 3.31: Interface tracking between micropolar and dusty fluid with applied pressure gradient

3.4 Conclusion

The unsteady flow of two immiscible Saffman dusty and Eringen micropolar fluids through a horizontal channel with a stable and unstable interface has been analyzed numerically using a novel modified cubic B-spine differential quadrature method (MCB-DQM) with distinct computational schemes for the different zones. Extensive details of the discretization procedures in the MCB-DQM algorithm have been provided. The effects of the emerging hydrodynamic control procedures for both regions have been elaborated, and four steps are necessary for the interface tracking computation. The impact of critical hydrodynamic parameters i. e. Reynolds number, Froude number, particle concentration parameter, Eringen micropolar material parameter, volume fraction parameter, pressure gradient, time, viscosity ratio, and density ratio on fluid and particle velocities, microrotation (angular velocity

component), and interface evolution have been computed and visualized graphically. The stability and fast convergence of the MCB-DQM algorithm have been confirmed. The core findings of the present analysis can be summarized in the following points:

-Under the horizontal channel scheme flow, accelerating, oscillating and decelerating behavior in the fluids and particle velocities and micro-rotation profile with time is observed in respective zones depending on whether the hydrodynamics is triggered by constant, periodic, or decaying pressure gradients, respectively.

-As anticipated, magnitudes of the fluid and particle velocities and micro-rotation components are enhanced with an increment in the pressure gradient.

-Increasing the Reynolds number produces a marked enhancement in fluids and particle velocities and micro-rotation profile for all applied constant, periodic, and decaying pressure gradient cases.

-Increasing the micropolar parameter affects the dust particle velocity and fluid velocity in the upper zone even though the micropolar fluid is restricted to the lower zone. Hence increment in the parameter flow leads to a diminution in both fluid and particle linear velocities and micro-rotation magnitudes (i.e., deceleration in the angular spin of the micro-elements in the micropolar fluid) with applied constant, periodic, or decaying pressure gradient.

-Elevation in dusty particle concentration parameter increase the velocities of dust particle significantly for all three applied pressure gradient cases. This parameter is, of course, associated with Saffman dusty fluid, which is present only in upper zone fluid; however, as noted in the discussion, the coupling of the dusty fluid momentum balance to the angular momentum balance of the micropolar liquid results in a delicate interplay between linear and angular velocity fields. This affects the microrotation profile for the lower zone fluid- hence the upper zone Saffman fluid velocity and lower zone micro-rotation profiles both slightly increase when the particle concentration parameter is

enhanced for constant and periodic pressure gradient cases and slightly decrease for the decaying pressure case.

-A significant decline in dust particles and fluid velocities in the dusty fluid zone (upper) is observed. In contrast, there is no substantial change in micropolar fluid velocity (lower zone) noted with an increase in the ratio of viscosity and density for all three applied pressure gradients. Micro-rotation increases significantly with an increment in the ratio of viscosities but considerably decreases with elevation in the ratio of densities.

-It is emphasized that initially, the vertical elongation of the interface is significant, and after that, the shape evolves with time. Hence the undulating sequence occurs faster for a longer duration of time

-The qualitative features of this flow are retained with variation in Reynolds number, time, amplitude, wave number, particulate concentration parameter, viscosity ratio, and applied pressure gradients.

The current study has demonstrated the excellent accuracy characteristics of the modified cubic B-spine differential quadrature method (MCB-DQM) in numerical simulations of interfacial two-fluid (dusty-micropolar) duct flows. However, heat transfer and electromagnetic effects [191], [192] have been neglected. These may be considered in future studies and are relevant in biomedical and materials processing systems.

Chapter 4

Computation of unsteady generalized Couette flow and heat transfer in immiscible dusty and non-dusty fluids with viscous heating and wall suction effects using a modified cubic B-spine differential quadrature method

4.1 Introduction

In the fields of power generation, microelectronics, and fluid transportation, significant effort has been concentrated on minimizing the size of equipment and processes in the past few years. Experts are looking at techniques to enhance heat transmission in such devices to reduce operational expenses in the manufacturing processes. Thermal conductivity is primarily essential for a fluid's capacity to transport heat. Compared to solid substances, the thermal conductivities of the fluids often used in heat-transfer devices are relatively low. The suspension of tiny-sized particles in the base fluid can enhance the thermal conductivity; such fluids are known as fluids with particle suspension.

Isolating pure fluids is difficult in many industrial complexities, such as extracting complicated petrochemical liquids, hydrocarbon filtering, and thermoplastic technology. Industrial fluent media frequently include contaminants such as particulate matter and other persistent pollutants, and these fluids are referred to as "dusty" or

"fluid-particle suspensions," which need multiphase models. Analyzing two-phase flows where solid spherical objects are dispersed in a sterile fluid is essential in practical applications such as the petroleum industry, crude oil purification, and biochemical flows.

Dusty fluids or fluid-particle suspensions are multiphase and can be simulated with the Saffman model [50], which provides a promising approach for analyzing the influence of suspended particles on laminar flows when there is a homogenous distribution of identical particles in the dusty fluid Ibrahim and Gamachu [194] investigated the effect of various thermo-hydrodynamical parameters on dusty nanofluids. Reddy and Ferdows [195] explored the micropolar dusty fluid with heat transfer. The convection of energy in dusty turbulent flow is analyzed by Ahmed *et al.* [196]. The heat transfer and magnetic effect on dusty Casson fluid are reviewed by Gireesha *et al.* [197]. Tariq and Khan [198] identified the impact of low Reynolds number on dusty Peristaltic flow.

Many flow configurations arising in industrial materials processing, nuclear engineering, and petrochemical systems feature two-fluid flows. These relate to the presence of two viscous liquids that do not mix, which are immiscible. Comprehensive discussions on such flows have been given by Meyer and Garder [199] and Briscoe *et al.* [200]for geological and chemical engineering colloidal applications, respectively. As noted, immiscible or stratified flows are also critical in nuclear engineering, specifically in the late in-vessel stage of core melt severe accidents of a nuclear reactor [201]. These flows are also relevant to liquid polymer layers on a solid substrate [202]. Therefore, many theoretical and numerical studies of two-fluid flow transport phenomena have been communicated. Stamenković *et al.* [203] studied theoretically the thermal convection of electrically conducting immiscible Newtonian fluids in channel flow under an oblique magnetic field. Mori *et al.* [204] used a moving finite element method to compute the transient two-phase free sharp interface problem arising in the flow of two immiscible fluids (slag and molten metal) in a blast furnace with an implicit time-stepping scheme. Tang and Wrobel [205] employed a volume-of-fluid

(VOF) method interface tracking method for modelling the flow of immiscible metallic liquids in mixing processes, noting that the mixing of immiscible metallic liquids is significantly impacted by the viscosity of the system, shear forces, and turbulence. Wan *et al.* [206] deployed an implicit hybrid finite element/volume (FE/FV) solver to flows involving two immiscible fluids, using a segregated pressure correction or projection method on staggered unstructured hybrid meshes. They captured the fluid interface by solving an advection equation for the volume fraction of one of the fluids, which improved the interface sharpening strategy by reducing the smearing of the interface over time. Than *et al.* [207] investigated the hydrodynamic stability of plane Poiseuille flow of two immiscible liquids of different viscosities and equal densities, noting the sensitivity of results to the viscosity and volume ratio. They identified that high viscosity fluid centrally located achieves good stability, whereas centrally located layers of less viscous liquid (fingering zones) are consistently unstable. Yagodnitsyna *et al.* [208] simulated the flow patterns of immiscible liquid-liquid flow in a rectangular microchannel with a T-junction for three liquid-liquid flow systems (kerosene-water, paraffin oil-water, and castor oil-paraffin oil) and included a variety of analyses for parallel flow, slug flow, plug flow, dispersed (droplet) flow, and rivulet flow at different velocity ratios for other Weber and Ohnesorge numbers. Anwar Bég *et al.* [173] analyzed the unsteady hydromagnetic flow of two immiscible Newtonian fluids in a rigid horizontal channel containing two non-Darcian porous media with oscillating lateral wall mass flux under a sinusoidal pressure gradient. They deployed forward time/central space (FT/CS) finite-difference and Galerkin finite-element methods, observing a solid modification in velocity components with inertial and magnetic field effects. Zhou *et al.* [209] implemented a meshless Local Petrov–Galerkin method with Rankine source solution (MLPG_R method) to compute two-fluid Newtonian flows with both low density and very high-density ratios. Further investigations include McLean *et al.* [210] and Pelipenko *et al.* [211] (on primary cement displacement immiscible flows in oil well systems) and Tang *et al.* [212] (on two- and three-dimensional piecewise linear (PLIC) VOF Eulerian grid computation of immiscible

twin-screw extruder interfacial flows). Borrelli *et al.* [140] considered two immiscible Newtonian fluids in a vertical channel and studied the magneto-convection parameter effects on flow behavior.

The investigation of a dielectric viscous fluid flowing via channels under the presence of an external magnetic field is not only intriguing conceptually, but also has implications in the mathematical modelling of a variety of industrial and biological systems. The homotopy perturbation technique is applied to find the solutions to the system of modelled differential equations for Williamson nanofluid flow with external magnetic effect Bhatti *et al.* [213]. The results of applied magnetic field on hybrid bio-nanofluid flow in a peristaltic duct are investigated by Elkhair *et al.* [214], and Hsiao [215] studied an electrical MHD ohmic dissipation energy release on Carreau-Nanofluid. Bibi *et al.* [216],[217] did the numerical analysis of magnetohydrodynamics effect on Williamson and hyperbolic tangent fluid. Some more studies on MHD flow can be seen in References [218]–[220].

Another critical aspect of interfacial two-fluid dynamics is the effect of time. Despite its essential importance, relatively little work has been conducted regarding the time-dependent unstable flow of two immiscible liquids. However, the unsteady multiphase flow problem has been explored via the front tracking method by Tryggvason *et al.* [141]. Riaz and Tchelepi [142] studied the instability of immiscible two-phase flow in porous media. In addition to VOF methods, other numerical algorithms have also been deployed in interfacial flows. These include spectral, alternating direction implicit (ADI) finite difference, finite element, and meshless smoothed particle hydrodynamics (SPH). Devakar and Raje [1] numerically explored the time-dependent unsteady flow of two immiscible fluids by the Crank–Nicolson finite difference method. The low-order approaches do use several grid points to achieve an acceptable degree of accuracy to obtain specific outcomes at such defined points. The differential quadrature method (DQM) approach for linear and nonlinear partial differential equations was proposed by Bellman *et al.* [96]. Motivated by chemical engineering applications, DQM was

again enhanced with a modified discretization strategy [182]. A detailed literature regarding the various test functions in the differential quadrature method was presented in [183]–[187]. The above chapter 1 (section 1.7), chapter 2 (section 2.1), and chapter 3 (section 3.1) also present the numerical solution of various linear and nonliar partial differential equations using with good accuracy and stability.

To the authors' best knowledge, no attempt has been made to study the unsteady flow of two immiscible dusty and non-dusty fluids with heat transfer and interface evolution. This flow regime has essential applications in nuclear reactor designs and thermal duct systems in petrochemical engineering. The computational approach adopted in this paper is a modified cubic B-spine Differential Quadrature Method. Generalized Couette flow of two immiscible dusty (fluid-particle suspension) and pure (Newtonian) fluids are considered through rigid horizontal channels for three separate schemes: first for nonporous plates with heat transfer, second for porous plates with uniform suction and injection and heat transfer, and third for nonporous plates with interface evolution. A detailed appraisal of the physics is included. Validation is also conducted through skin friction coefficient and Nusselt number. The advection and reconstruction/tracking of the interface for the third scheme is also explored. MCB-DQM is shown to achieve exceptional stability and accuracy and offers significant promise in simulating interfacial duct flows in nuclear and geothermal energy, petrochemical transport, and materials processing systems. Three different pressure gradients are studied, viz applied constant, decaying, and periodic pressure gradients. The fluid and particle velocities, temperatures, and interface tracking are computed by solving coupled partial differential equations. Detailed graphical visualizations are included, and the physical implications are provided with comprehensive elaboration.

4.2 Formulation of dusty and pure fluids flow with non-porous plates

Consider the unsteady, fully developed, laminar, and unidirectional Generalized Couette flow of two immiscible dusty (fluid-particle suspension) and pure (non-dusty Newtonian) fluids shown in Figure 4.1.

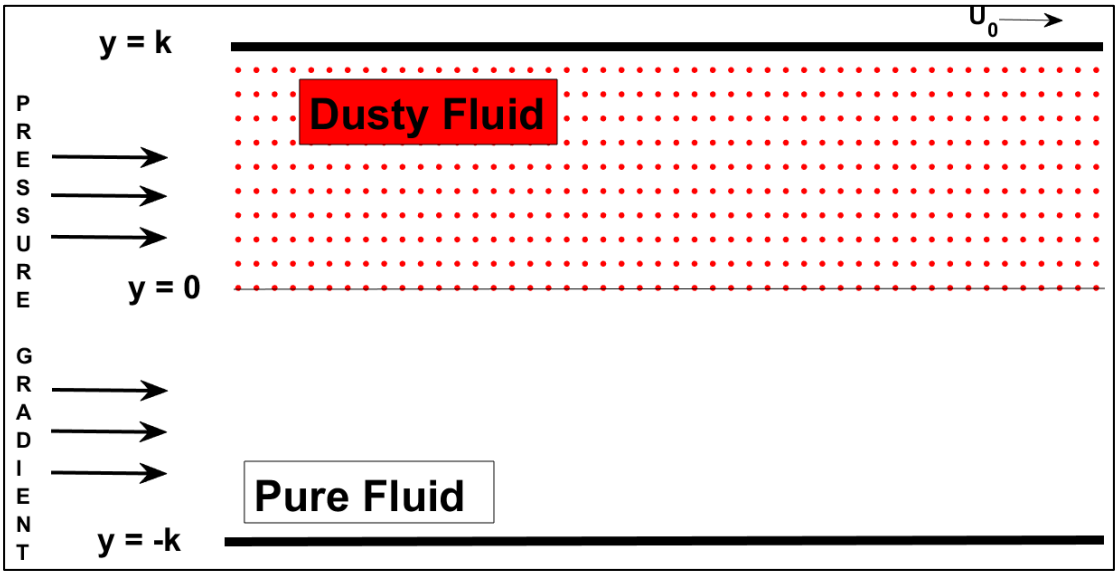

Figure 4.1: Geometry of generalized Couette immiscible dusty and pure (scheme-3a) fluids flow with a stable interface

Some assumptions are being made under scheme-3a.

i. Both fluids are immiscible, viscous, and incompressible.
ii. The fluids move between two horizontal parallel non-porous plates (two-dimensional channel).
iii. Both plates are electrically non-conductive with zero polarization voltage.
iv. The plates oppose each other and occupy the *x*-*z* plane, as depicted in Figure 4.1.

v. The lower plate is stationary and has a steady temperature of t_1, while the upper plate travels at a fixed velocity of U_0 in the *x*-(axial) direction at a constant temperature of t_2, here $t_2 > t_1$.

vi. Pure non-dusty Newtonian fluid occupies the bottom region-1 ($-k \leq y \leq 0$) and has a fluid velocity u_n, density ρ_n, viscosity μ_n, specific heat capacity $c_n$of fluid at constant volume, temperature $T_n$and thermal conductivity κ_n.

vii. Dusty fluid occupies the upper region-2 ($0 \leq y \leq k$) and has a fluid velocity u_d, density ρ_d, viscosity μ_d, specific heat capacity c_d of fluid at constant volume, temperature T_d, thermal conductivity κ_d.

viii. In the dusty fluid, the dust particles possess a particle velocity u_p, density ρ_p, specific heat capacity $c_p$of a particle at constant volume, temperature T_p and thermal conductivity κ_p.

ix. The transportation attributes are unchanged in both the regions and common pressure gradients are applied from the horizontal *x*-direction.

x. The flow of dusty fluid in the region –II is governed by the equations (1.12)-(1.15). In the absence of dust particles in the region I, the pure fluid flow (Newtonian, i.e., non-dusty) is governed by equations (1.3) - (1.5).

xi. The fluid velocity vectors in both zones are $u_n(y,t)$, $u_d(y,t)$ and the dust particle velocity $u_p(y,t)$ in the zone II (upper) is assumed to be ($u_n(y,t)$,0,0) , ($u_d(y,t)$,0,0), and ($u_p(y,t)$,0,0) respectively.

xii. The fluid temperature in both zones are $T_n(y,t)$, $T_d(y,t)$ and the dust particle temperature $T_p(y,t)$ in the zone II (upper) is assumed to be ($T_n(y,t)$,0,0) , ($T_d(y,t)$,0,0) and ($T_p(y,t)$,0,0) respectively.

xiii. The fluid layers are mechanically coupled through the model of momentum exchange. Transferring momentum arises through consistency in velocity and shear stress over the interface.

xiv. However, we assume that the flow rate and shear-induced pressure are also stable at the interface between two liquids.

Given the above constraints, the fluid flow and temperature distribution governed by the equations (1.3) - (1.5) and (1.12)- (1.15) are presumed by the following equations:

Region-1 (Pure fluid).

$$\rho_n.\frac{\partial u_n}{\partial t} = -\nabla P + \mu_n \nabla^2 u_n, \tag{4.1}$$

$$\rho_n c_n.\frac{\partial T_n}{\partial t} = \kappa_n \nabla^2 T_n - \mu_n (\nabla u_n)^2. \tag{4.2}$$

Region-2 (Dusty fluid).

$$\rho_d.\frac{\partial u_d}{\partial t} = -\nabla P + \mu_d \nabla^2 u_d - \zeta_T \rho_p \emptyset \frac{(u_d - u_p)}{(1-\emptyset)}, \tag{4.3}$$

$$\frac{\partial u_p}{\partial t} = \zeta_T (u_d - u_p), \tag{4.4}$$

$$\rho_d c_d.\frac{\partial T_d}{\partial t} = \kappa_d \nabla^2 T_d - \mu_d (\nabla u_d)^2 - \frac{\rho_p c_p \emptyset (T_d - T_p)}{\gamma_T (1-\emptyset)} + \zeta_T \rho_p \emptyset \frac{(u_d - u_p)^2}{(1-\emptyset)}, \tag{4.5}$$

$$\frac{\partial T_p}{\partial t} = -\frac{(T_p - T_2)}{\gamma_T}. \tag{4.6}$$

The hydrodynamic motion is driven by an applied pressure gradient in the *x*-axial direction; therefore, the velocity profile is unidirectional. Thus,

$$\left.\begin{aligned} \nabla u_n &= u_{n_y}, \\ \nabla^2 u_n &= u_{n_{yy}}, \\ \nabla u_d &= u_{d_y}, \\ \nabla^2 u_d &= u_{d_{yy}}, \\ \nabla u_p &= u_{p_y}, \\ \nabla T_n &= T_{n_y}, \\ \nabla^2 T_n &= T_{n_{yy}}, \\ \nabla T_d &= T_{d_y}, \\ \nabla^2 T_d &= T_{d_{yy}}, \\ \nabla T_p &= T_{p_y}. \end{aligned}\right\} \tag{4.7}$$

Classical hyper-stick and no-slip boundary conditions are considered and can be numerically prescribed:

Initial conditions: At $t \leq 0$,

$$\left.\begin{array}{c} u_n(y,t) = T_n(y,t) = 0, for -k \leq y \leq 0, \\ u_d(y,t) = u_p(y,t) = 0 \; and \; T_d(y,t) = T_p(y,t) = 0, for \; 0 \leq y \leq k. \end{array}\right\} \quad (4.8)$$

Boundary and interface conditions: At $t > 0$,

$$\left.\begin{array}{c} u_n(-k,t) = 0, u_d(k,t) = u_p(k,t) = U_0, \\ T_n(-k,t) = t_1, \; T_d(k,t) = T_p(k,t) = t_2, \\ u_n(0,t) = u_d(0,t), T_n(0,t) = T_d(0,t), \\ and \;\; at \; y = 0, \;\; \mu_n u_{n_y} = \mu_d u_{d_y}, \kappa_n T_{n_y} = \kappa_d T_{d_y}. \end{array}\right\} \quad (4.9)$$

Introducing the non-dimensional parameters:

$$\left.\begin{array}{c} \bar{x} = \frac{x}{k}, \bar{y} = \frac{y}{k}, , \overline{u_n} = \frac{u_n}{U_0}, \overline{u_d} = \frac{u_d}{U_0}, \overline{u_p} = \frac{u_p}{U_0}, \\ \bar{p} = \frac{p}{\rho_n {U_0}^2}, \bar{t} = \frac{tU_0}{k}, \overline{T_n} = \frac{T_n - t_1}{t_2 - t_1}, \overline{T_d} = \frac{T_d - t_2}{t_2 - t_1}, \overline{T_p} = \frac{T_p - t_2}{t_2 - t_1}. \end{array}\right\} \quad (4.10)$$

Where $\zeta_T = \frac{6\pi r \mu_d}{m_p}$ is the volume transfer coefficient with an average mass of dust particle m_p, and radius r. Hence the last term of equation (4.3) $\zeta_T \rho_p \emptyset \frac{(u_2 - u_p)}{(1-\emptyset)}$ can be written as $\frac{R * r_1}{Re * r_2}(u_d - u_p)$. Here $R = \frac{K^* \rho_p k^2}{\mu_d m_p}$ is particle concentration parameter and $K^* = 6\pi r \mu_d U_0$ is the Stokes drag coefficient, and $Re = \frac{\rho_n U_0}{\mu_n}$ is the Reynolds number. $r_2 = \frac{\mu_d}{\mu_n}, r_1 = \frac{\rho_d}{\rho_n}$ are the viscosity and density ratios for the two immiscible fluids in zones I and II, respectively. Hence the last term of equation (4.4) is updated accordingly where $r_3 = \frac{\rho_d}{\rho_p}$ is the ratio of the density of fluid and dust particles in region II. In equations (4.5) and (4.6) $\gamma_T = \frac{3}{2}\frac{\rho_p . c_p . \mu_d}{K^* N . \kappa_d}$ is the temperature relaxation time where N is the number density of dust particles in per unit volume. Prandtl number (ratio of momentum and thermal diffusivity) is $pr = \frac{c_n * \mu_n}{\kappa_n}$. $Ec = \frac{U_0}{c_n(t_2 - t_1)}$ is the Eckert number

which is the ratio of the kinetic energy of the flow to the enthalpy difference (viscous dissipation). $k_r = \frac{\kappa_d}{\kappa_n}$ is the ratio of thermal conductivity. $C_r = \frac{c_d}{c_n}$ is the ratio of specific heat. $C_{r_r} = \frac{c_d}{c_p}$ is the ratio of specific heat of fluid and dust particles in region II. $-\nabla p = -\partial p/\partial x = Ge(t)$ is the applied time-dependent pressure gradient in the *x*-axial direction with $t > 0$. Three distinct cases for $Ge(t)$ are considered to analyze the numerical results:

Case-*1*: $Ge(t) = Ge$ (when the flow is induced by applied constant pressure gradient).

Case-*2*: $Ge(t) = Ge * Sin(wt)$ (when the flow is induced by applied periodic pressure gradient with oscillating parameter w).

Case-*3*: $Ge(t) = Ge * e^{-\lambda t}$ (when the flow is induced by a decaying pressure gradient with the decaying parameter, λ).

After dropping the bars and introducing the above non-dimensional parameters, appropriate initial, interfacial, and boundary conditions according to the scheme-3a, the equations (4.1) - (4.6) can be modified as follows:

Region-1 ($-k \leq y \leq 0$) (Pure Newtonian fluid region):

$$u_{n_t} = Ge(t) + \frac{u_{n_{yy}}}{Re}, \tag{4.11}$$

$$T_{n_t} = \frac{T_{n_{yy}}}{Re*pr} + \frac{Ec}{Re}\left(u_{n_y}\right)^2, \tag{4.12}$$

Region-2 *(0 ≤ y ≤ k)* (Dusty fluid):

$$u_{2_t} = \frac{Ge(t)}{r_1} + \frac{r_2}{r_1}\frac{u_{d_{yy}}}{Re} - \frac{R*r_2}{r_1}\frac{(u_d - u_p)}{Re}, \tag{4.13}$$

$$u_{p_t} = \frac{R*r_3*r_2}{r_1}\frac{(u_d - u_p)}{Re}, \tag{4.14}$$

$$T_{d_t} = \frac{\boldsymbol{k_r}*T_{d_{yy}}}{\boldsymbol{C_r}*r_1*Re*pr} + \frac{r_2}{\boldsymbol{C_r}*r_1}\frac{Ec}{Re}\left(u_{d_y}\right)^2 + \frac{2}{3}\frac{R*\boldsymbol{k_r}}{\boldsymbol{C_r}*r_1*pr}\frac{(T_p - T_d)}{Re} + \frac{R*Ec*r_2}{r_1\,\boldsymbol{C_r}}\frac{(u_d - u_p)^2}{Re}, \tag{4.15}$$

$$T_{p_t} = \frac{2}{3}\frac{R*\boldsymbol{k_r}*\boldsymbol{C_{r_r}}*r_3}{\boldsymbol{C_r}*r_1*pr}\frac{(T_d - T_p)}{Re}. \tag{4.16}$$

Initial, boundary and interfacial conditions are considered as equations (4.8) - (4.9) with *k=1*, $U_0 = 1, t_1 = 0, t_2 = 1$.

4.2.1 Numerical solution of immiscible dusty and pure fluids flow under scheme-3a.

To get the velocity and temperature profile of dusty and pure fluid flow under scheme-3a, replace the approximation of the spatial components of the first and second-order obtained by using MCB-DQM. Hence the system of coupled partial equations (4.11) - (4.16) followed by scheme-3a, numerically solved with the initial and boundary conditions equations (4.8) - (4.9), and the velocities temperature profiles of both region fluids and particles are obtained. Using the approximations (1.32) - (1.34), and (1.38) - (1.40), the equations (4.11) - (4.16) can be updated as follows.

Region-1 (Pure fluid region: $-k \le y \le 0$):

$$u_{n_t} = Ge(t) + \frac{\sum_{j=1}^{N} b^*{}_{ij} u_n(y_j,t)}{Re}, \tag{4.17}$$

$$T_{n_t} = \frac{\sum_{j=1}^{N} b^*{}_{ij} T_n(y_j,t)}{Re*Pr} + \frac{Ec}{Re}\left(\sum_{j=1}^{N} a^*{}_{ij} u_n(y_j,t)\right)^2, \tag{4.18}$$

Region-2 (Dusty fluid: $0 \le y \le k$):

$$u_{d_t} = \frac{Ge(t)}{r_2} + \frac{r_2}{r_1}\frac{\sum_{j=1}^{N} b^*{}_{ij} u_d(y_j,t)}{Re} - \frac{R*r_2}{r_1}\frac{\left(u_d(y_j,t) - u_p(y_j,t)\right)}{Re}, \tag{4.19}$$

$$u_{p_t} = \frac{R*r_3*r_2}{r_1}\frac{\left(u_d(y_j,t) - u_p(y_j,t)\right)}{Re}, \tag{4.20}$$

$$T_{d_t} = \frac{\boldsymbol{k_r}*\sum_{j=1}^{N} b^*{}_{ij} T_d(y_j,t)}{\boldsymbol{C_r}*r_1*Re*Pr} + \frac{r_2}{\boldsymbol{C_r}*r_1}\frac{Ec}{Re}\left(\sum_{j=1}^{N} a^*{}_{ij} u_d(y_j,t)\right)^2 + \frac{2}{3}\frac{R*\boldsymbol{k_r}}{\boldsymbol{C_r}*r_2*pr}\frac{\left(T_p(y_j,t) - T_d(y_j,t)\right)}{Re}$$
$$+ \frac{R*Ec*r_2}{r_1\,\boldsymbol{C_r}}\frac{\left(u_d(y_j,t) - u_p(y_j,t)\right)^2}{Re}, \tag{4.21}$$

$$T_{p_t} = \frac{2}{3}\frac{R*\boldsymbol{k_r}*\boldsymbol{C_{r_r}}*r_3}{\boldsymbol{C_r}*r_2*pr}\frac{\left(T_d(y_j,t)-T_p(y_j,t)\right)}{Re}. \tag{4.22}$$

Thus, equations (4.17) - (4.22) are reduced into a system of ordinary differential equations in time, that is, for *i=1, 2, 3…, N*, and the system is solved by four-stage order three SSP RK43 scheme (1.69) - (1.72). The velocities and temperature in both regions are obtained as follows:

At the first stage *for i=1,2,3…, N*:

Region-1 ($-k \le y \le 0$) (Pure fluid region):

$$u_{n_1} = u_{n_0} + \frac{\Delta t}{2}\left(Ge(t) + \frac{\sum_{j=1}^{N} b^*_{ij} u_{n_0}(y_j,t)}{Re}\right), \tag{4.23}$$

$$T_{n_1} = T_{n_0} + \frac{\Delta t}{2}\left(\frac{\sum_{j=1}^{N} b^*_{ij} T_{n_0}(y_j,t)}{Re*Pr} + \frac{Ec}{Re}\left(\sum_{j=1}^{N} a^*_{ij} u_{n_0}(y_j,t)\right)^2\right). \tag{4.24}$$

Region-2 (*0* $\le y \le k$) (Dusty fluid):

$$u_{d_1} = u_{d_0} + \frac{\Delta t}{2}\left(\frac{Ge(t)}{r_1} + \frac{r_2}{r_1}\frac{\sum_{j=1}^{N} b^*_{ij} u_{d_0}(y_j,t)}{Re} - \frac{R*r_2}{r_1}\frac{\left(u_{d_0}(y_j,t)-u_{p_0}(y_j,t)\right)}{Re}\right), \tag{4.25}$$

$$u_{p_1} = u_{P_0} + \frac{\Delta t}{2}\left(\frac{R*r_3*r_2}{r_1}\frac{\left(u_{d_0}(y_j,t)-u_{p_0}(y_j,t)\right)}{Re}\right), \tag{4.26}$$

$$T_{d_1} = T_{d_0} + \frac{\Delta t}{2}\left(\begin{array}{l}\frac{\boldsymbol{k_r}*\sum_{j=1}^{N} b^*_{ij} T_{d_0}(y_j,t)}{\boldsymbol{C_r}*r_1*Re*Pr} + \frac{r_2}{\boldsymbol{C_r}*r_1}\frac{Ec}{Re}\left(\sum_{j=1}^{N} a^*_{ij} u_{d_0}(y_j,t)\right)^2 + \\ \frac{2}{3}\frac{R*\boldsymbol{k_r}}{\boldsymbol{C_r}*r_2*pr}\frac{\left(T_{p_0}(y_j,t)-T_{d_0}(y_j,t)\right)}{Re} + \frac{R*Ec*r_2}{r_1\,\boldsymbol{C_r}}\frac{\left(u_{d_0}(y_j,t)-u_{p_0}(y_j,t)\right)^2}{Re}\end{array}\right), \tag{4.27}$$

$$T_{p_1} = T_{p_0} + \frac{\Delta t}{2}\left(\frac{2}{3}\frac{R*\boldsymbol{k_r}*\boldsymbol{C_{r_r}}*r_3}{\boldsymbol{C_r}*r_1*pr}\frac{\left(T_{p_0}(y_j,t)-T_{p_0}(y_j,t)\right)}{Re}\right). \tag{4.28}$$

At the first stage of the scheme, the initial and boundary conditions (4.8) - (4.9) are considered accordingly.

At the second stage *for i=1,2,3…, N:*

Region-1 ($-k \le y \le 0$) (Pure fluid region):

$$u_{n_2} = u_{n_1} + \frac{\Delta t}{2}\left(Ge(t) + \frac{\sum_{j=1}^{N} b^*_{ij} u_{n_1}(y_j,t)}{Re}\right), \tag{4.29}$$

$$T_{n_2} = T_{n_1} + \frac{\Delta t}{2}\left(\frac{\sum_{j=1}^{N} b^*_{ij} T_{n_1}(y_j,t)}{Re*Pr} + \frac{Ec}{Re}\left(\sum_{j=1}^{N} a^*_{ij} u_{n_1}(y_j,t)\right)^2\right). \tag{4.30}$$

Region-2 ($0 \le y \le k$) (Dusty fluid):

$$u_{d_2} = u_{d_1} + \frac{\Delta t}{2}\left(\frac{Ge(t)}{r_2} + \frac{r_2}{r_1}\frac{\sum_{j=1}^{N} b^*_{ij} u_{d_1}(y_j,t)}{Re} - \frac{R*r_2}{r_1}\frac{\left(u_{d_1}(y_j,t) - u_{p_1}(y_j,t)\right)}{Re}\right), \tag{4.31}$$

$$u_{p_2} = u_{p_1} + \frac{\Delta t}{2}\left(\frac{R*r_3*r_2}{r_1}\frac{\left(u_{d_1}(y_j,t) - u_{p_1}(y_j,t)\right)}{Re}\right), \tag{4.32}$$

$$T_{d_2} = T_{d_1} + \frac{\Delta t}{2}\left(\begin{array}{l} \frac{\boldsymbol{k_r}*\sum_{j=1}^{N} b^*_{ij} T_{d_1}(y_j,t)}{\boldsymbol{C_r}*r_1*Re*Pr} + \frac{r_2}{\boldsymbol{C_r}*r_1}\frac{Ec}{Re}\left(\sum_{j=1}^{N} a^*_{ij} u_{d_1}(y_j,t)\right)^2 + \\ \frac{2}{3}\frac{R*\boldsymbol{k_r}}{\boldsymbol{C_r}*r_2*pr}\frac{\left(T_{p_1}(y_j,t) - T_{d_1}(y_j,t)\right)}{Re} + \frac{R*Ec*r_2}{r_1\,\boldsymbol{C_r}}\frac{\left(u_{d_1}(y_j,t) - u_{p_1}(y_j,t)\right)^2}{Re} \end{array}\right), \tag{4.33}$$

$$T_{p_2} = T_{p_1} + \frac{\Delta t}{2}\left(\frac{2}{3}\frac{R*\boldsymbol{k_r}*\boldsymbol{C_{r_r}}*r_3}{\boldsymbol{C_r}*r_2*pr}\frac{\left(T_{p_1}(y_j,t) - T_{p_1}(y_j,t)\right)}{Re}\right). \tag{4.34}$$

At the second stage of the scheme, the initial and boundary conditions (4.8) - (4.9) are considered accordingly.

At the third stage *for i=1,2,3…,N:*

Region-1 ($-k \le y \le 0$) (Pure fluid region):

$$u_{n_3} = \frac{2u_{n_0}}{3} + \frac{u_{n_2}}{3} + \frac{\Delta t}{6}\left(Ge(t) + \frac{\sum_{j=1}^{N} b^*_{ij} u_{n_2}(y_j,t)}{Re}\right), \tag{4.35}$$

$$T_{n_3} = \frac{2T_{n_0}}{3} + \frac{T_{n_2}}{3} + \frac{\Delta t}{6}\left(\frac{\sum_{j=1}^{N} b^*_{ij} T_{n_2}(y_j,t)}{Re*Pr} + \frac{Ec}{Re}\left(\sum_{j=1}^{N} a^*_{ij} u_{n_2}(y_j,t)\right)^2\right). \tag{4.36}$$

Region-2 ($0 \le y \le k$) (Dusty fluid):

$$u_{d_3} = \frac{2u_{d_0}}{3} + \frac{u_{d_2}}{3} + \frac{\Delta t}{6}\left(\frac{Ge(t)}{r_1} + \frac{r_2}{r_1}\frac{\sum_{j=1}^{N} b^*_{ij} u_{d_2}(y_j,t)}{Re} - \frac{R*r_2}{r_1}\frac{\left(u_{d_2}(y_j,t) - u_{d_2}(y_j,t)\right)}{Re}\right), \quad (4.37)$$

$$u_{p_3} = \frac{2u_{p_0}}{3} + \frac{u_{p_2}}{3} + \frac{\Delta t}{6}\left(\frac{R*r_3*r_2}{r_1}\frac{\left(u_{d_2}(y_j,t) - u_{p_2}(y_j,t)\right)}{Re}\right), \quad (4.38)$$

$$T_{d_3} = \frac{2T_{d_0}}{3} + \frac{T_{d_2}}{3} + \frac{\Delta t}{6}\left(\begin{array}{c}\frac{\boldsymbol{k_r}*\sum_{j=1}^{N} b^*_{ij} T_{d_2}(y_j,t)}{\boldsymbol{C_r}*r_2*Re*Pr} + \frac{r_2}{\boldsymbol{C_r}*r_1}\frac{Ec}{Re}\left(\sum_{j=1}^{N} a^*_{ij} u_{d_2}(y_j,t)\right)^2 \\ + \frac{2}{3}\frac{R*\boldsymbol{k_r}}{\boldsymbol{C_r}*r_2*pr}\frac{\left(T_{p_2}(y_j,t) - T_{d_2}(y_j,t)\right)}{Re} + \\ \frac{R*Ec*r_2}{r_1\,\boldsymbol{C_r}}\frac{\left(u_{d_2}(y_j,t) - u_{p_2}(y_j,t)\right)^2}{Re}\end{array}\right), \quad (4.39)$$

$$T_{p_3} = \frac{2T_{p_0}}{3} + \frac{T_{p_2}}{3} + \frac{\Delta t}{6}\left(\frac{2}{3}\frac{R*\boldsymbol{k_r}*\boldsymbol{C_{r_r}}*r_3}{\boldsymbol{C_r}*r_2*pr}\frac{\left(T_{d_2}(y_j,t) - p_2(y_j,t)\right)}{Re}\right). \quad (4.40)$$

At the third stage of the scheme, the initial and boundary conditions (4.8) - (4.9) are considered accordingly.

At the fourth stage *for i=1,2,3…,N:*

Region-1 ($-k \le y \le 0$) (Pure fluid region):

$$u_n = u_{n_3} + \frac{\Delta t}{2}\left(Ge(t) + \frac{\sum_{j=1}^{N} b^*_{ij} u_{n_3}(y_j,t)}{Re}\right), \quad (4.41)$$

$$T_n = T_{n_3} + \frac{\Delta t}{2}\left(\frac{\sum_{j=1}^{N} b^*_{ij} T_{n_3}(y_j,t)}{Re*Pr} + \frac{Ec}{Re}\left(\sum_{j=1}^{N} a^*_{ij} u_{n_3}(y_j,t)\right)^2\right). \quad (4.42)$$

Region-2 for Dusty fluid ($0 \le y \le k$):

$$u_d = u_{d_3} + \frac{\Delta t}{2}\left(\frac{Ge(t)}{r_2} + \frac{r_2}{r_1}\frac{\sum_{j=1}^{N} b^*_{ij} u_{d_3}(y_j,t)}{Re} - \frac{R*r_2}{r_1}\frac{\left(u_{d_3}(y_j,t) - u_{p_3}(y_j,t)\right)}{Re}\right), \quad (4.43)$$

$$u_p = u_{p_3} + \frac{\Delta t}{2}\left(\frac{R*r_3*r_2}{r_1}\frac{\left(u_{d_3}(y_j,t) - u_{p_3}(y_j,t)\right)}{Re}\right), \quad (4.44)$$

$$T_d = T_{d_3} + \frac{\Delta t}{2}\left(\begin{array}{l} \frac{\boldsymbol{k_r}*\sum_{j=1}^{N} b^*{}_{ij} T_{d_3}(y_j,t)}{\boldsymbol{C_r}*r_2*Re*Pr} + \frac{r_2}{\boldsymbol{C_r}*r_1}\frac{Ec}{Re}\left(\sum_{j=1}^{N} a^*{}_{ij} u_{d_3}(y_j,t)\right)^2 + \\ \frac{2}{3}\frac{R*\boldsymbol{k_r}}{\boldsymbol{C_r}*r_2*pr}\frac{\left(T_{p_3}(y_j,t)-T_{d_3}(y_j,t)\right)}{Re} + \frac{R*Ec*r_2}{r_1\,\boldsymbol{C_r}}\frac{\left(u_{d_3}(y_j,t)-u_{p_3}(y_j,t)\right)^2}{Re} \end{array}\right), \quad (4.45)$$

$$T_p = T_{p_3} + \frac{\Delta t}{2}\left(\frac{2}{3}\frac{R*\boldsymbol{k_r}*\boldsymbol{C}_{r_r}*r_3}{\boldsymbol{C_r}*r_2*pr}\frac{\left(T_{d_3}(y_j,t)-T_{p_3}(y_j,t)\right)}{Re}\right). \quad (4.46)$$

At the fourth stage of the scheme, the initial and boundary conditions (4.8) - (4.9) are considered accordingly. Hence the fluid velocity, temperature profiles u_n, T_n of pure fluid in the region-1 and fluid, particle velocity, and temperature profiles u_d, u_p, T_d, T_P of dusty fluid in region-2 have been numerically obtained in the fourth stage of MCB-DQM.

4.3 The Nusselt number and skin friction coefficients

When the fluid flows over the plates, it exerts a frictional effect on the plates' surfaces, obstructing forward motion and causing skin friction drift on the surface. The skin-friction coefficient is used to quantify this effect.

The expression of Nusselt number and skin friction coefficients at both plates are calculated as

$$\left.\begin{array}{l} (N_u)_{y=-1} = \left(-T_{n_y}\right)_{y=-1}, (N_u)_{y=1} = \left(-T_{d_y}\right)_{y=1}, \\ \left(C_f\right)_{y=-1} = \left(\frac{2u_{n_y}}{Re}\right)_{y=-1}, \left(C_f\right)_{y=1} = \left(\frac{2r_2 u_{d_y}}{r_1 Re}\right)_{y=1}. \end{array}\right\} \quad (4.47)$$

4.4 Formulation of dusty and pure fluid flow under the scheme-3b

Consider again the unsteady, fully developed, laminar, and unidirectional Generalized Couette flow of pure and dusty fluids in a horizontal channel shown in Figure 4.2.

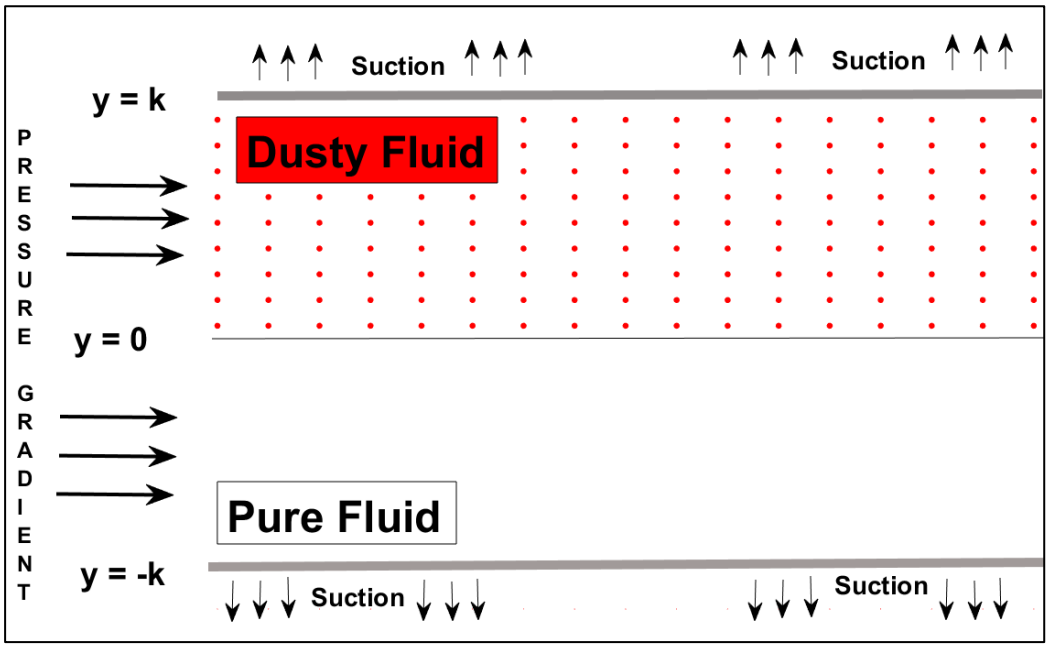

Figure 4.2: Geometry of generalized Couette flow of immiscible dusty and Pure fluids with the sight of suction and stable interface

Let $U = u_i\ (y,t)i + u_0{}^*j + u_k k.$ be the velocity vector of fluids. Both plates have long length, say L_∞ and $S^*{}_i (i = 1 - nondusty, 2 - dusty)$ is the volume of fluid sucked per unit length of the lower and upper plate, respectively (the plates are porous, and wall transpiration is possible). Hence $S^*{}_i * L_\infty$ is the total volume of fluid sucked by the respective plate, and the same amount of fluid is mechanically injected. A uniform suction from the upper and a uniform injection is applied to the dusty fluid in region 2; similarly, a uniform suction from the lower and a uniform injection in the *y*-direction are applied to the pure Newtonian fluid in region 1. The size, mass, and radius of dust

particles and other fluids credentials are similar to the scheme-3a flow except for the uniform suction and injection effect [72] $S_1 = S_2 = \frac{u_0{}^*}{U_0}$.

After dropping the bars and introducing the non-dimensional parameters, initial, interfacial, and boundary conditions according to the scheme-3b flow the governing equations for fluids and particle-phase equations (1.3) - (1.5) and (1.12)- (1.15) in both the regions of scheme-3b flow emerge as follows.

Region-1 ($-k \leq y \leq 0$) (Pure fluid region):

$$u_{n_t} = Ge(t) + \frac{u_{n_{yy}}}{Re} - S_1 u_{n_y}, \tag{4.48}$$

$$T_{n_t} = \frac{T_{n_{yy}}}{Re*pr} - S_1 T_{n_y} + \frac{Ec}{Re}\left(u_{n_y}\right)^2, \tag{4.49}$$

Region-2 *for* Dusty fluid ($0 \leq y \leq k$):

$$u_{d_t} = \frac{Ge(t)}{r_1} + \frac{r_2}{r_1}\frac{u_{d_{yy}}}{Re} - \frac{R*r_2}{r_1}\frac{(u_d - u_p)}{Re} - S_2 u_{d_y}, \tag{4.50}$$

$$u_{p_t} = \frac{R*r_3*r_2}{r_1}\frac{(u_d - u_p)}{Re}. \tag{4.51}$$

$$T_{d_t} = \frac{\boldsymbol{k_r}*T_{d_{yy}}}{\boldsymbol{C_r}*r_1*Re*pr} - S_2 T_{d_y} + \frac{r_2}{\boldsymbol{C_r}*r_1}\frac{Ec}{Re}\left(u_{d_y}\right)^2 + \frac{2}{3}\frac{R*r_2*\boldsymbol{k_r}}{\boldsymbol{C_r}*r_1*pr}\frac{(T_p - T_d)}{Re} + \frac{R*Ec*r_2}{r_1\,\boldsymbol{C_r}}\frac{(u_d - u_p)^2}{Re}, \tag{4.52}$$

$$T_{p_t} = \frac{2}{3}\frac{R*\boldsymbol{k_r}*\boldsymbol{C}_{r_r}*r_3}{\boldsymbol{C_r}*r_1*pr}\frac{(T_d - T_p)}{Re}. \tag{4.53}$$

Initial, boundary and interfacial conditions are considered as equations (4.8) - (4.9) with $k=1$, $U_0 = 1, t_1 = 0, t_2 = 1$.

4.4.1 Numerical solution of immiscible dusty and pure fluids flow under scheme-3b.

To get the velocity and temperature profile of dusty and pure fluid flow under scheme-3b, replace the approximation of the spatial components of the first and second-order

obtained by using MCB-DQM. Hence the system of coupled partial equations (4.48) - (4.53) followed by scheme-3b is updated as equations (4.54) - (4.59) then solved numerically, and the velocity and temperature profiles of both fluids and particles are obtained.

Region-1 ($-k \le y \le 0$) (Pure fluid region):

$$u_{n_t} = Ge(t) + \frac{\sum_{j=1}^{N} b^*_{ij} u_n(y_j,t)}{Re} - S_1\left(\sum_{j=1}^{N} a^*_{ij} u_n(y_j,t)\right), \tag{4.54}$$

$$T_{n_t} = \frac{\sum_{j=1}^{N} b^*_{ij} T_n(y_j,t)}{Re*Pr} + \frac{Ec}{Re}\left(\sum_{j=1}^{N} a^*_{ij} u_n(y_j,t)\right)^2 - S_1\left(\sum_{j=1}^{N} a^*_{ij} T_n(y_j,t)\right). \tag{4.55}$$

Region-2 ($0 \le y \le k$) (Dusty fluid):

$$u_{d_t} = \frac{Ge(t)}{r_2} + \frac{r_2}{r_1}\frac{\sum_{j=1}^{N} b^*_{ij} u_d(y_j,t)}{Re} - \frac{R*r_2}{r_1}\frac{\left(u_d(y_j,t) - u_p(y_j,t)\right)}{Re} - S_2\left(\sum_{j=1}^{N} a^*_{ij} u_d(y_j,t)\right), \tag{4.56}$$

$$u_{p_t} = \frac{R*r_3*r_2}{r_1}\frac{\left(u_2(y_j,t) - u_p(y_j,t)\right)}{Re}, \tag{4.57}$$

$$T_{d_t} = \frac{\boldsymbol{k_r}*\sum_{j=1}^{N} b^*_{ij} T_d(y_j,t)}{\boldsymbol{C_r}*r_1*Re*Pr} + \frac{r_2}{\boldsymbol{C_r}*r_1}\frac{Ec}{Re}\left(\sum_{j=1}^{N} a^*_{ij} u_d(y_j,t)\right)^2 + \frac{2}{3}\frac{R*\boldsymbol{k_r}}{\boldsymbol{C_r}*r_2*pr}\frac{\left(T_p(y_j,t) - T_d(y_j,t)\right)}{Re}$$

$$+ \frac{R*Ec*r_2}{r_1\,\boldsymbol{C_r}}\frac{\left(u_d(y_j,t) - u_p(y_j,t)\right)^2}{Re} - S_2\left(\sum_{j=1}^{N} a^*_{ij} T_d(y_j,t)\right), \tag{4.58}$$

$$T_{p_t} = \frac{2}{3}\frac{R*\boldsymbol{k_r}*\boldsymbol{C_{r_r}}*r_3}{\boldsymbol{C_r}*r_2*pr}\frac{\left(T_2(y_j,t) - T_p(y_j,t)\right)}{Re}. \tag{4.59}$$

Thus, the reduced system of ordinary differential equations in time, that is, for *i=1, 2, 3…, N*, and the system is solved by the above-mentioned four-stage order three SSP-RK43 scheme (1.69) - (1.72). At each stage of the scheme, the initial and boundary condition equations (4.8) - (4.9) are considered accordingly. Hence the fluid velocity, temperature profiles u_n, T_n of pure fluid in the region-1 and fluid, particle velocity, and temperature profiles u_d, u_P, T_d, $T_P$of dusty fluid in region-2 have been numerically obtained in the fourth stage of MCB-DQM.

4.5 Formulation of interface reconstruction and averaged flow of dusty and pure fluids under the scheme-3c

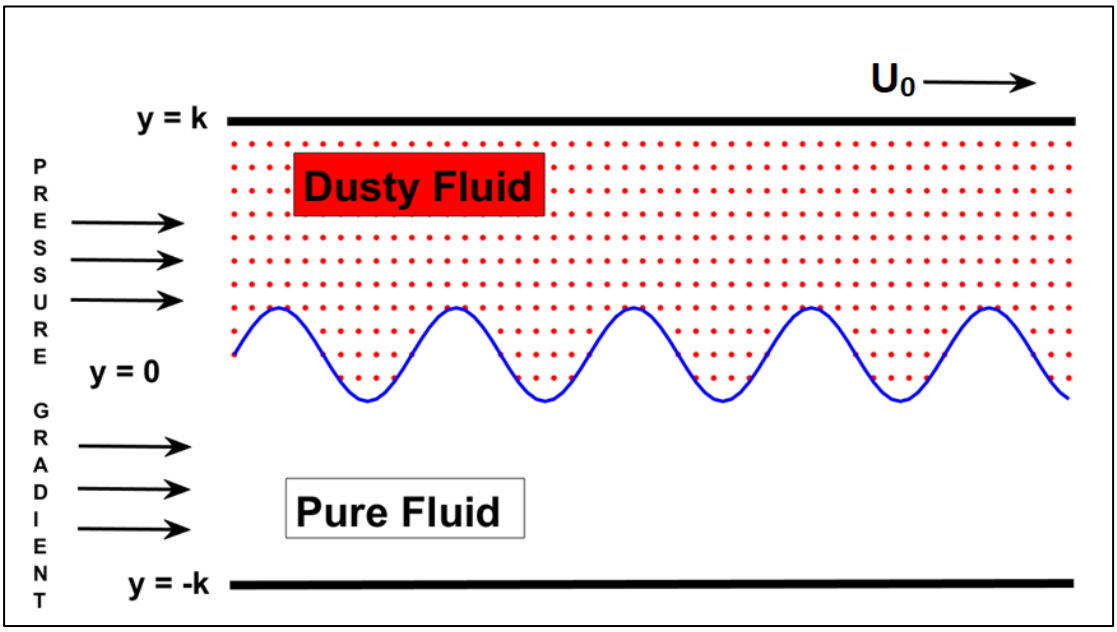

Figure 4.3: Geometry of generalized Couette immiscible dusty and pure fluids flow with a moving interface

In this third scenario, again, we study the Generalized Couette flow of two immiscible, pure, and dusty fluids undergoing shearing motions; however, we assumed that owing to a viscosity jump, interfacial instability occurs. All other assumptions are as in schemes-3a and 3b. Scheme-3c is visualized in Figure 4.3. The lower plate is stationary while the upper plate travels at a fixed velocity of U_0 in the x-axial direction. Let ρ_n, μ_n be the density and viscosity of pure fluid which lies in the region $(-k \leq y \leq l_1)$ with the interface height from the lower plate, l_1. The dusty fluid has the density ρ_d and the viscosityμ_d occupies in $(l_1 \leq y \leq k)$. The evolution of the interface is analyzed by using horizontal attenuation in the initial interface phase. Let the initial interface be an Eigen-mode, say $l_1 y_m + A_0 cos(B_0 y)$ where y_m is the average depth of interface and A_0, B_0 are the amplitude and wavenumber. The dust particles have the same size and a

circular shape, mass, and un-deformable electro-free form. They are evenly spread across the fluid in the region with density ρ_p. The particle phase is sufficiently distilled so that the interactions between any two dust particles are ignored, and the dust particle size is also relatively tiny in scale but affects the mean flow velocity U^*. The flow of these immiscible fluids acquires momentum due to the common pressure gradient, which is applied in the direction of the x-axis with an average density $\rho^* = \rho_n + C_s(\rho_d - \rho_n)$ and viscosity $\mu^* = \mu_n + C_s(\mu_d - \mu_n)$.The flow velocity u^*, particle velocity u_p and interface track C_i vectors are presumed as u^*= $(u^*(y,t)$,0,0), u_p=$(U_p(y,t)$,0,0) and (C_i=$(C_i(y,t)$,0,0), respectively. The movement of fluids is incompressible unsteady and is driven by an applied pressure gradient in the *x*-axial direction; therefore, the velocity profile is unidirectional. Thus,$\nabla u^* = \frac{\partial u^*}{\partial y}, \nabla^2 u^* = \frac{\partial^2 u^*}{\partial y^2}, \nabla C_k = \frac{\partial C_k}{\partial y}, \nabla^2 C_k = \frac{\partial^2 C_k}{\partial y^2}$. The fluid layers are mechanically coupled through the model of momentum exchange. The movement of the interface between two immiscible fluids of distinct density and viscosity is described by the local value of the concentration parameter as the volume fraction between two immiscible liquids C_s, and the interface is characterized by the following constraints.

$$C_s = \begin{cases} 0 & outside\ the\ s^{th}\ fluid \\ > 0, < 1 & at\ the\ s^{th}\ fluid\ interface \\ 1 & inside\ the\ s^{th}\ fluid \end{cases} \tag{4.60}$$

Depending on the local value of C_s, the necessary attributes and variables are allocated to each control volume inside the domain. Hence by using the equations (1.12) (1.13), (1.19), and (1.20), the averaged flow is governed as ($-k \le y \le k$).

$$\frac{\partial C_i}{\partial t} + U^* \frac{\partial C_i}{\partial y} = 0, \tag{4.61}$$

$$\rho^* \frac{\partial u^*}{\partial t} = -\nabla P + \mu^* \frac{\partial^2 u^*}{\partial y^2} - \zeta_T \rho_p \left(u^* - u_p\right) + F, \tag{4.62}$$

$$\frac{\partial u_p}{\partial t} = \zeta_T \left(u^* - u_p\right). \tag{4.63}$$

Again, classical hyper-stick and no-slip boundary conditions are considered. The relevant initial and boundary conditions take the form:

Initial conditions: At $t \leq 0$,

$$u^*(y,t) = u_p(y,t) = 0,\ C_i(y,t) = A_0 cos(B_0 y). \tag{4.64}$$

Boundary conditions: At $t > 0$,

$$u^*(-k,t) = u_p(-k,t) = 0,\ u^*(k,t) = u_p(k,t) = u_0. \tag{4.65}$$

Again, introducing the non-dimensional parameters:

$\bar{x} = \frac{x}{k}, \bar{y} = \frac{y}{k}, \overline{u^*} = \frac{u^*}{U_0}, \overline{u_p} = \frac{u_p}{U_0}, \bar{p} = \frac{p}{\rho^* {U_0}^2}, \bar{t} = \frac{tU_0}{k}$ allows the normalization of the model. Here $\zeta_T = \frac{6\pi r \mu^*}{m_p}$ is the volume transfer coefficient with an average mass of dust particle m_p and radius r. Hence the term $\zeta_T \rho_p \frac{(u^* - u_p)}{\rho^*}$ of equation (4.62) can be written as $\frac{R\,(1+C_s(r_1-1))}{Re(\,1+C_s(r_2-1)\,)}(u^* - u_p)$. Furthermore $R = \frac{K^* k^2 \rho_p}{\mu_d m_p}$ is particle concentration parameter and $K^* = 6\pi r \mu_d U_0$ is the Stokes drag coefficient, and $Re = \frac{\rho_n U_0}{\mu_n}$ is the Reynolds number, $r_2 = \frac{\mu_d}{\mu_n}$ is the ratio of viscosity, $r_1 = \frac{\rho_d}{\rho_n}$ is the ratio density, and $r_{nd} = \frac{\rho_d + \rho_n}{\rho_p}$ is the ratio of the density of fluid and dust particles. The body force $F = (\rho^* g + F_s)$ is modeled as gravitation force and interfacial tension by the continuum surface force model, and the surface tension is reconstructed as a volume force $F_s = \sigma \omega \nabla C_i$ where σ is the interfacial tension between two liquid phases and ω is the mean free surface curvature, given by $\omega = -\frac{\nabla^2 C_k}{\|\nabla C_k\|}$ and $Ca = \frac{\mu^* U_0}{\sigma}$ is the capillary number. $Fr = \frac{{U_0}^2}{gk}$ is the Froude number. The time-dependent pressure gradient is applied in the direction of the x-axis for momentum in the averaged flow. As before in schemes 3a and 3b, three separate cases for $Ge(t)$ are considered in the computational simulations described later:

Case-I: $Ge(t) = Ge$ (when the flow is induced by applied constant pressure gradient).

Case-II: $Ge(t) = Ge * Sin(wt)$ (when the flow is induced by applied periodic pressure gradient with oscillating parameter w).

Case-III: $Ge(t) = Ge * e^{-\lambda t}$ (when the flow is induced by a decaying pressure gradient with the decaying parameter, λ).

After dropping the bars and introducing the non-dimensional parameters, initial, interfacial, and boundary conditions (4.64) - (4.65) according to the scheme-3c flow, the governing equations for fluids and particle-phase equations in the region ($-k \leq y \leq k$) emerge as:

$$\frac{\partial C_i}{\partial t} + u^* \frac{\partial C_i}{\partial y} = 0, \tag{4.66}$$

$$\frac{\partial u^*}{\partial t} = \left[\begin{array}{c} \frac{Ge(t)}{1+C_s(r_1-1)} + \frac{(1+C_s(r_2-1))}{Re(1+C_s(r_1-1))} \frac{\partial^2 u^*}{\partial y^2} - \frac{R(1+C_s(r_2-1))}{Re(1+C_s(r_1-1))}(u^* - u_p) \\ + \frac{1}{Fr} - \frac{1+C_s(r_2-1)}{Re*Ca(1+C_s(r_1-1))} \frac{\partial^2 C_i}{\partial y^2} \end{array} \right], \tag{4.67}$$

$$\frac{\partial u_p}{\partial t} = \frac{Rr_{nd}(1+C_s(r_2-1))}{Re(1+r_1)}(u^* - u_p). \tag{4.68}$$

Initial and boundary conditions are considered as the equations (4.64) - (4.65) with *k=1*, $A_0 = 0.05, B_0 = 2\pi$.

4.5.1 Numerical solution of immiscible dusty and pure fluids flow under scheme-3c.

To get the averaged flow velocity, reconstructed interface, and dust and particle velocity profiles under scheme-3c, replace the approximation of the spatial components of the first and second-order obtained by using MCB-DQM. Hence the system of single momentum coupled partial differential equations (4.66) - (4.68) followed by scheme-3c are updated as equations then solved numerically, and the fluid and particle velocities profiles are obtained.

As ($-1 \leq y \leq 1$):

$$\frac{\partial C_i}{\partial t} = -u^*(y_j,t)\left(\sum_{j=1}^{N} a^*{}_{ij} C_i(y_j,t)\right), \tag{4.69}$$

$$\frac{\partial u^*}{\partial t} = \frac{Ge(t)}{1+C_s(r_2-1)} + \frac{(1+C_s(r_2-1))}{Re(\,1+C_s(r_1-1)\,)}\left(\sum_{j=1}^{N} b^*{}_{ij} u^*(y_j,t)\right) - \frac{R\,(1+C_s(r_2-1))}{Re(\,1+C_s(r_1-1))}\Big(u^*(y_j,t) - u_p(y_j,t)\Big) + \frac{1}{Fr} - \frac{1+C_s(r_2-1)}{Re*Ca(\,1+C_s(r_1-1))}\left(\sum_{j=1}^{N} b^*{}_{ij} C_i(y_j,t)\,\right), \tag{4.70}$$

$$\frac{\partial u_p}{\partial t} = \frac{Rr_{nd}\,(1+C_s(r_2-1))}{Re(1+r_1)}\Big(u^*(y_j,t) - u_p(y_j,t)\Big). \tag{4.71}$$

Thus, the reduced system of ordinary differential equations in time, that is, *for i=1, 2, 3…, N*, and the system is solved as above by a four-stage order-three SSP-RK43 scheme (1.69) - (1.72). At each stage of the scheme, the initial and boundary conditions (4.64) -(4.65) are considered accordingly. Hence the averaged flow, particle velocity profiles u^*, u_p and interface profile C_i have been obtained in the fourth stage of MCB-DQM.

4.6 MCB-DQM Results and Analysis

Under three separate flow schemes, the unidirectional unstable Generalized Couette flow of two immiscible dusty and pure fluids attributable to the time-dependent pressure gradient is examined. To pursue the solutions, traditional no-slip and hyper-stick conditions are assumed at the boundaries. First, the obtained numerical results are validated for the velocity profile of a single non-dusty Newtonian fluid flow (Here in the absence of dust particles, the Stokes drag coefficient $K^* = 0$, and particle concentration parameter ($R = 0$ *and* r_1*=1,* r_2*=1*) by comparing them with the exact solutions of Poiseuille flow (*Ge=10*) through a horizontal channel. It is observed from Table 4.1-Table 4.3 that a good agreement is seen as the maximum absolute error and root mean square error is very less between the calculated numerical solution and the exact solution. As the number of discretizing nodes ($N = 31 - 201$) and time ($t = 0.1 - 2$) is increasing the errors are also reducing so it can be noticed that the applied

modified cubic B-spline differential quadrature method is suitable for the current system of fluid flow.

The two-fluid flow coupled problem in the corresponding regions with stable interfaces through separate schemes-3a scheme-3b have been numerically solved, and velocity, temperature profiles of fluids, and dust particles have been obtained. Single mean flow problems with inconsistent interfaces under scheme-3c have also been addressed, and the interface reconstruction profiles have been acquired along with the mean flow and dust particles velocity profiles. The results are discussed in the following set of fixed values of all parameters, *Ge*=10, *Re*=2, *R*=0.5, r_1=0.5, r_2=0.5, r_{nd}=200, C_s=0.5, Ca=0.5, $Fr = 2, \lambda = 1, w = 2$.

4.6.1 Results and analysis of immiscible dusty and pure fluid flow under the scheme-3a

Figure 4.4 *(A-H)* shows the velocity profiles in dusty and pure fluid areas, and Figure 4.4 *(I-O)* exhibits the dust particle velocity with Reynolds numbers, particulate concentration parameters, applied pressure gradients, density ratio, viscosity ratio, and time. It is found that the velocity profiles for dust particles and fluids in both regions are parabolic and because the lower fluid is more viscous and denser than the upper one (r_1=0.5, r_2=0.5), the curvature of pure fluid velocity is lower than the dusty fluid profile. Figure 4.4 *(A)* exhibits the change in fluid velocities, and Figure 4.4 *(H)* shows the particle velocities with varying times when a constant pressure gradient is applied. It is noted that, with rising time, the fluids and particle velocities are growing in respective regions, and at a higher time, it may become stable. The fluid velocities in Figure 4.4 *(B)* and dust particle velocity in Figure 4.4 *(I)* are pulsating, wherein the flow is caused by the periodic pressure gradient and never attains the steady-state. Hence the velocities increase when $0 < \omega t \leq \frac{\pi}{2}$, decrease when $\frac{\pi}{2} < \omega t \leq \frac{3\pi}{2}$ and further increase with $\frac{3\pi}{2} < \omega t \leq \frac{5\pi}{2}$. Figure 4.4 *(I and J)* reveals that the fluid velocities in

both the regions and particle velocity in the upper region decrease with time and eventually attain a steady-state as time is enhanced, for the case where periodic pressure gradient induces the flow. It is also worth mentioning that, owing to the upper plate movement (the generalized Couette flow), the velocities do not approach zero with time. It may be observed from Figure 4.4 $(D - for\ fluid\ velocity)$ and Figure 4.4 $(N - particle\ velocity)$ that the increase in Reynolds number enhances the fluids and particle velocities for all three cases of applied constant, periodic, and decaying pressure gradients, which is due to the elevation in inertial (momentum) force relative to viscous hydrodynamic force. However, the variations are larger in magnitude in the dusty fluid region than in the pure fluid (Newtonian) region indicating a greater sensitivity in the velocity of the particles compared to the Newtonian fluid. It can be noted in Figure 4.4 $(G\ and\ O)$ that the velocity magnitudes of fluid and particle are accentuated with an increment of the pressure gradient. An increase in the ratios of viscosities r_2 and densities r_1 corresponds to an increase in the viscosity and density of the dusty fluid region relative to the pure Newtonian fluid region. Because of this for all three applied pressure gradients, a significant decline in dust particle and fluid velocity is observed in region-2, whereas no tangible change in the pure fluid velocity in region-1 is witnessed with an increase in the ratio r_2 and r_1 see Figure 4.4$(E\ and\ F)$ for fluid velocities and Figure 4.4 $(K\ and\ L)$ for particle velocities. Figure 4.4 *(M)* indicates that the dust particle velocity increases with an enhancement of the particle concentration parameter, and no variation in fluid velocities is observed for all three pressure gradients; hence the figures are not mentioned.

Table 4.1: Numerical vs Exact solution for *N = 31, t = 0.1*

Exact	*Numerical*	*Error*	*Exact*	*Numerical*	*Error*	*Exact*	*Numerical*	*Error*
1	*1*	*0*	*0.54631*	*0.54751*	*0.0012*	*1.60715*	*1.6078*	*0.00064*
0.87307	*0.8733*	*0.00023*	*0.64116*	*0.64232*	*0.00116*	*1.60715*	*1.60776*	*0.00061*
0.75169	*0.75215*	*0.00047*	*0.75169*	*0.7528*	*0.00112*	*1.58062*	*1.5812*	*0.00058*
0.64116	*0.64181*	*0.00065*	*0.87307*	*0.87413*	*0.00106*	*1.52871*	*1.52925*	*0.00055*
0.54631	*0.54713*	*0.00082*	*1*	*1.001*	*0.001*	*1.45369*	*1.4542*	*0.00051*
0.47129	*0.47226*	*0.00096*	*1.12693*	*1.12786*	*0.00093*	*1.35884*	*1.35931*	*0.00047*

0.41938	0.42046	0.00107	1.24831	1.24919	0.00087	1.24831	1.24872	0.00041
0.39285	0.394	0.00115	1.35884	1.35966	0.00082	1.12693	1.12731	0.00038
0.39285	0.39405	0.0012	1.45369	1.45445	0.00076	1	1	0
0.41938	0.42061	0.00123	1.52871	1.52942	0.00072	Maximum Error =0.0012		
0.47129	0.47252	0.00122	1.58062	1.5813	0.00068	RMSE=0.00083205		

Table 4.2: Numerical vs Exact solution for $N = 62,\ t = 0.5$

Exact	Numerical	Error	Exact	Numerical	Error	Exact	Numerical	Error
5	5	0	4.92964	4.93036	0.00073	5.07856	5.07914	0.00058
4.99128	4.99156	0.00028	4.93488	4.93561	0.00073	5.08143	5.08198	0.00056
4.98265	4.98296	0.00031	4.94081	4.94155	0.00074	5.08343	5.08397	0.00054
4.97421	4.97455	0.00034	4.94737	4.94811	0.00075	5.08455	5.08507	0.00052
4.96604	4.96641	0.00037	4.95449	4.95523	0.00075	5.08478	5.08527	0.00049
4.95823	4.95863	0.0004	4.96208	4.96283	0.00075	5.0841	5.08457	0.00047
4.95086	4.95129	0.00043	4.97008	4.97083	0.00075	5.08254	5.08298	0.00044
4.94402	4.94447	0.00045	4.9784	4.97915	0.00075	5.0801	5.08052	0.00042
4.93776	4.93824	0.00048	4.98695	4.98769	0.00075	5.07681	5.0772	0.00039
4.93217	4.93268	0.00051	4.99563	4.99637	0.00074	5.0727	5.07307	0.00037
4.9273	4.92783	0.00053	5.00437	5.0051	0.00073	5.06783	5.06817	0.00034
4.92319	4.92375	0.00056	5.01305	5.01378	0.00073	5.06224	5.06255	0.00031
4.9199	4.92048	0.00058	5.0216	5.02231	0.00072	5.05598	5.05627	0.00029
4.91746	4.91806	0.0006	5.02992	5.03062	0.00071	5.04914	5.0494	0.00026
4.9159	4.91652	0.00062	5.03792	5.03861	0.0007	5.04177	5.042	0.00023
4.91522	4.91587	0.00064	5.04551	5.0462	0.00068	5.03396	5.03416	0.0002
4.91545	4.91611	0.00066	5.05263	5.0533	0.00067	5.02579	5.02596	0.00017
4.91657	4.91725	0.00068	5.05919	5.05984	0.00065	5.01735	5.01749	0.00014
4.91857	4.91927	0.00069	5.06512	5.06576	0.00064	5.00872	5.00884	0.00012
4.92144	4.92215	0.0007	5.07036	5.07098	0.00062	5	5	0
4.92514	4.92586	0.00072	5.07486	5.07545	0.0006	Max Error = 0.00075, RMSE= 0.00055		

Table 4.3: Error with time and discretizing points

	For N=51, t=0.5	For N=101, t=1	For N=151, t=1.5	For N=201, t=2
MAX ERROR	0.000749	0.000481	0.000341	0.000320
RMSE	0.000557	0.000377	0.000280	0.000229

Table 4.4: Skin friction Coefficient with varying parameter

T	*Lower plate*	*Upper plate*	*Re*	*Lower plate*	*Upper plate*	*R*	*Lower plate*	*Upper plate*
0.1	*4.955721*	*-7.36259*	*2*	*4.955721*	*-7.36259*	*0.3*	*4.955721*	*-7.36354*
0.2	*7.046197*	*-12.1264*	*3*	*6.057319*	*-8.99958*	*0.5*	*4.955721*	*-7.36259*
0.3	*8.651487*	*-15.2324*	*4*	*6.980517*	*-10.3652*	*1*	*4.955721*	*-7.36219*
0.4	*10.01278*	*-17.4958*	*5*	*7.789845*	*-11.5605*	*2*	*4.955721*	*-7.362*
r1	*Lower plate*	*Upper plate*	*r2*	*Lower plate*	*Upper plate*	*r3*	*Lower plate*	*Upper plate*
0.3	*4.955721*	*-11.5605*	*0.5*	*4.955721*	*-7.36259*	*50*	*4.955721*	*-7.30038*
0.5	*4.955721*	*-9.47826*	*0.6*	*4.955721*	*-6.25616*	*100*	*4.955721*	*-7.3294*
0.8	*4.955721*	*-8.22539*	*0.7*	*4.955721*	*-5.35892*	*200*	*4.955721*	*-7.35322*
1	*4.955721*	*-7.36259*	*0.8*	*4.955721*	*-4.60702*	*400*	*4.955721*	*-7.37042*

Table 4.5: Nusselt number with varying parameter

Re	*Lower plt*	*Upper plt*	*t*	*Lower plt*	*Upper plt*	*Kr*	*Lower plt*	*Upper plt*	*r2*	*Lower plt*	*Upper plt*
2	*-0.00231*	*2.913626*	*0.1*	*-0.00231*	*5.827251*	*0.1*	*-0.00231*	*11.85818*	*0.5*	*-0.00231*	*5.827251*
3	*-1.19E-05*	*6.171196*	*0.2*	*-0.89595*	*11.55846*	*0.3*	*-0.00231*	*7.680487*	*0.6*	*-0.00243*	*9.352168*
4	*-2.25E-06*	*7.261058*	*0.3*	*-8.06006*	*29.57051*	*0.5*	*-0.00231*	*2.913626*	*0.7*	*-0.00254*	*11.56419*
5	*-2.22E-06*	*7.671225*	*0.4*	*-26.5908*	*62.88988*	*0.7*	*-0.00231*	*-1.80442*	*0.8*	*-0.00263*	*12.97823*
Pr	*Lower plt*	*Upper plt*	*Ec*	*Lower plt*	*Upper plt*	*r1*	*Lower plt*	*Upper plt*			
2	*-0.00231*	*5.827251*	*0.25*	*-0.00116*	*1.392961*	*0.25*	*-0.00069*	*0.951823*			
3	*-1.67E-05*	*20.68563*	*0.5*	*-0.00231*	*5.827251*	*0.5*	*-0.00231*	*5.827251*			
4	*-5.28E-06*	*35.045*	*0.75*	*-0.00347*	*10.26154*	*0.75*	*-0.00459*	*12.10357*			
5	*-6.60E-06*	*49.13418*	*1*	*-0.00462*	*14.69583*	*1*	*-0.00724*	*37.73138*			

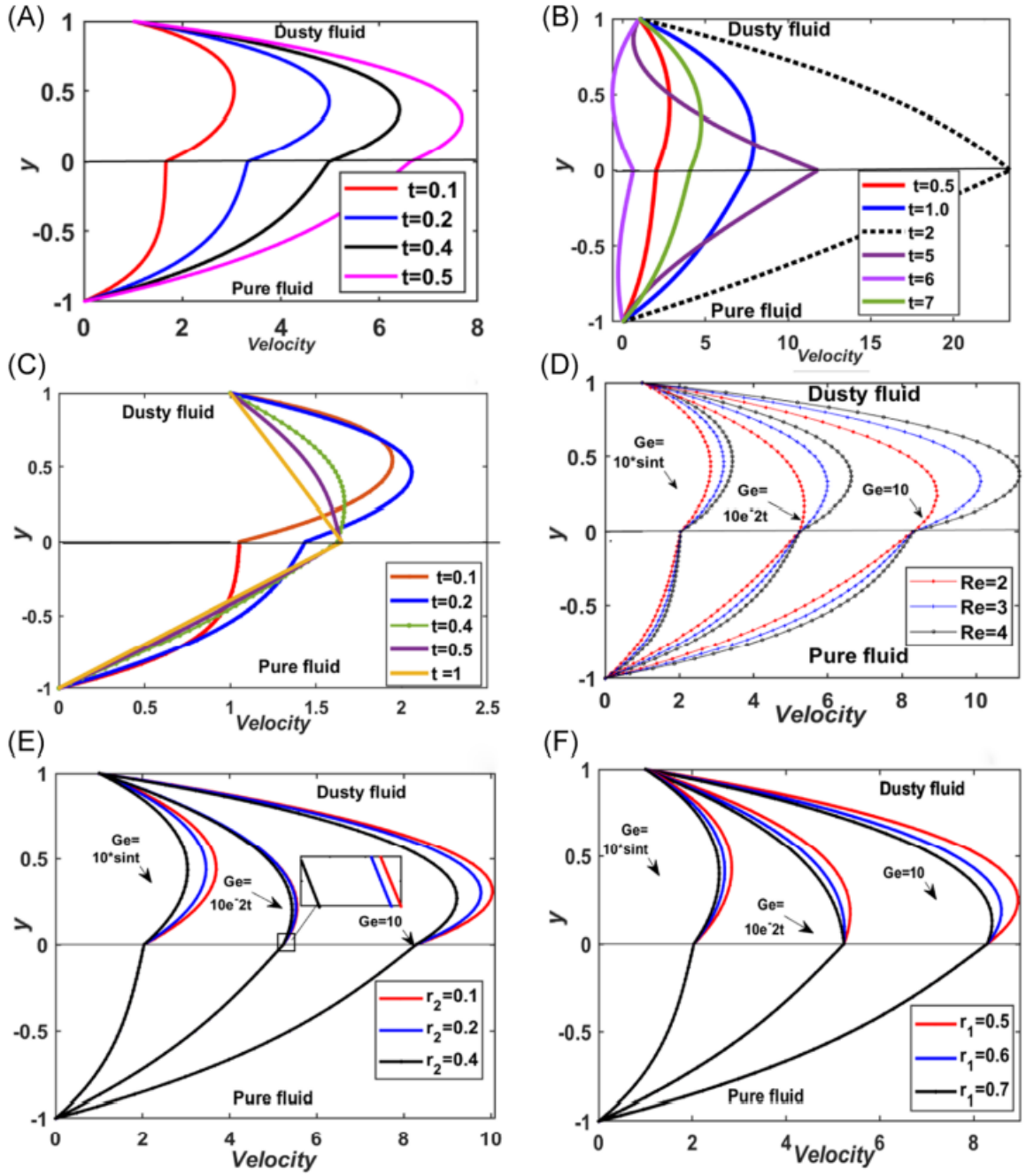
(A)
Dusty fluid
Pure fluid
t=0.1
t=0.2
t=0.4
t=0.5
y
Velocity
(B)
Dusty fluid
Pure fluid
t=0.5
t=1.0
t=2
t=5
t=6
t=7
y
Velocity
(C)
Dusty fluid
Pure fluid
t=0.1
t=0.2
t=0.4
t=0.5
t =1
y
Velocity
(D)
Dusty fluid
Ge= 10*sint
Ge= 10e^2t
Ge=10
Re=2
Re=3
Re=4
Pure fluid
y
Velocity
(E)
Dusty fluid
Ge= 10*sint
Ge= 10e^2t
Ge=10
r2=0.1
r2=0.2
r2=0.4
Pure fluid
y
Velocity
(F)
Dusty fluid
Ge= 10*sint
Ge= 10e^2t
Ge=10
r1=0.5
r1=0.6
r1=0.7
Pure fluid
y
Velocity

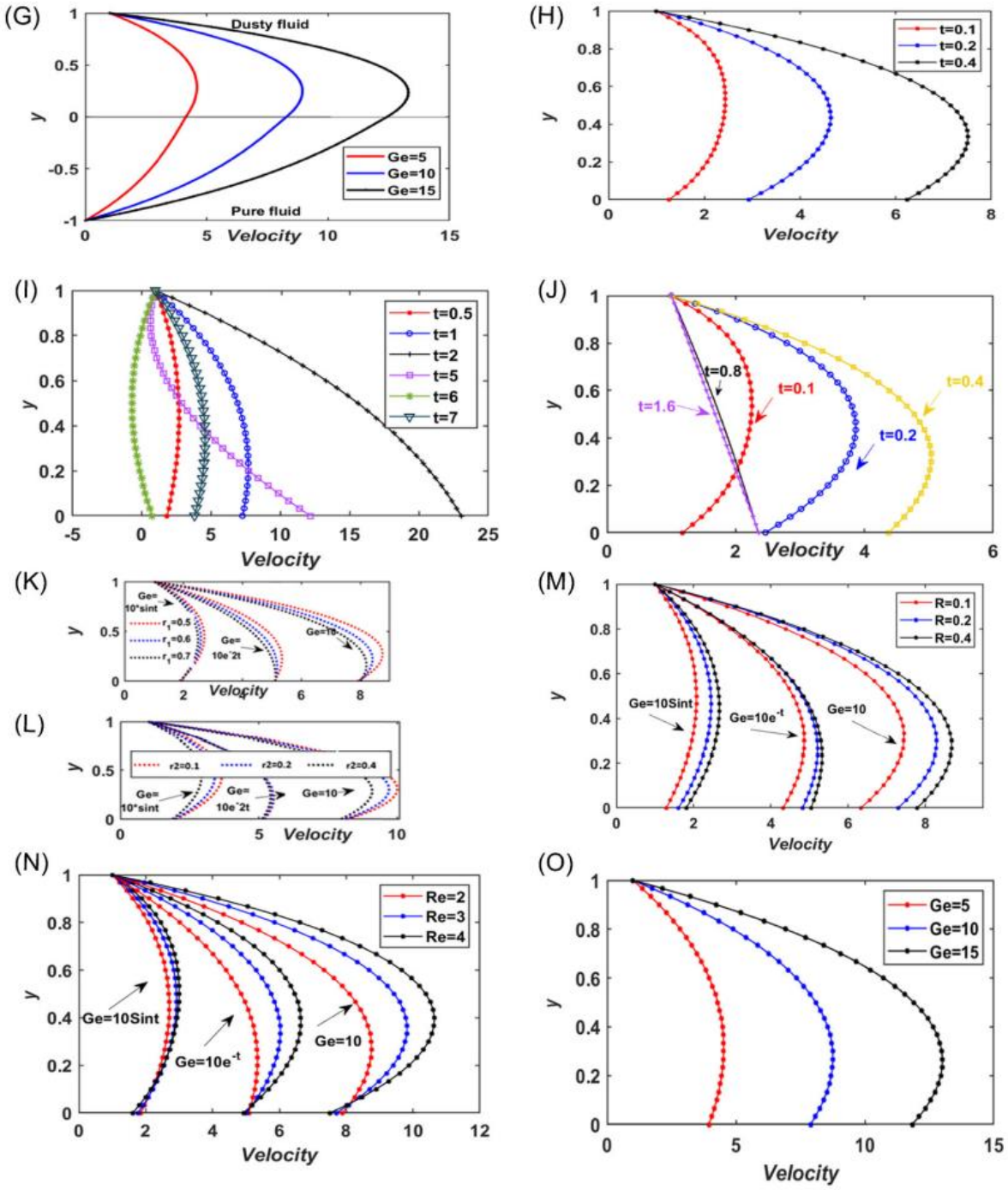

Figure 4.4: Fluid and particle velocity with varying parameters under scheme 3a-

(A) fluids and *(H)* particle with time and constant pressure, *(B)* fluids and *(I)* particle with time and periodic pressure, *(C)* fluids and *(J)* particle with time and decaying pressure, *(D)* fluids and *(N)* particle with Reynolds number and pressures, *(E)* fluids and *(L)* particle with the ratio of viscosities and pressures, *(F)* fluids and *(K)* particles with ratio of densities and pressures, *(G)* fluids and *(O)* particle with constant pressure, *(M)* particle with concentration parameter.

Figure 4.5*(A-H)* illustrates the evolution in the fluid and dust particle temperature distributions in the respective dusty and pure fluid regions with numerous thermophysical parameters. Figure 4.5*(A-C)* demonstrates that the dust particles and fluid temperatures in respective regions increase with progression in time and elevation in Eckert number Ec and the ratio of viscosities r_2. Clearly, a greater proportion of kinetic energy is converted to thermal energy via internal friction with an increment in Eckert number- this boosts the temperature magnitudes. A decrement in temperature magnitudes is observed with an increase in Reynolds number Re and Prandtl number p_r – clearly greater inertial effect and smaller thermal diffusivity (and thermal conductivity) manifest in suppression in thermal diffusion in the regime, and lower temperatures are computed see Figure 4.5 *(D-E).* However, owing to the momentum transfer near the interface, the profiles show the opposite trend since temperature apparently is elevated weakly in both the regions. It can be deduced from Figure 4.5 *(F-G)* that the pure fluids do not display any notable displacement in the temperature profiles with an increase in the parameter K_r and C_r in region-1. Conversely, the temperatures are significantly increased in region II as a parameter K_r increases whereas a significant decline are computed as parameter C_r increases for both dust particles and fluid. Similarly, the variation in the temperature profiles is only observed in region II (See Figure 4.5 *(H)* with an increase in the particle concentration parameter *R.* A slight decrease in the dusty fluid and a significant increase in the particle temperature profiles can be seen. This means the increasing presence of dust particles, therefore, also weakly inhibits thermal diffusion in the dual fluid regime.

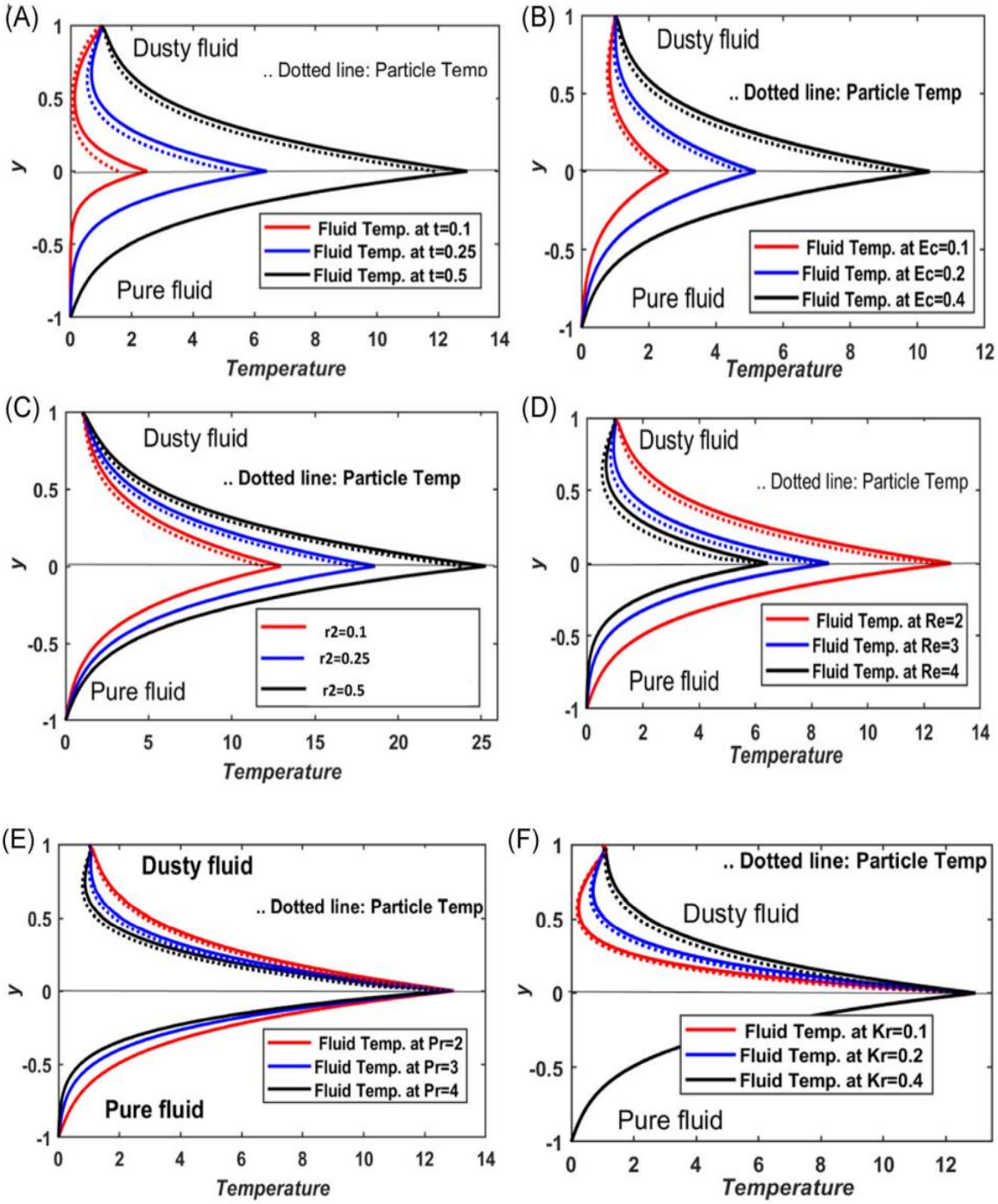
(A)
Dusty fluid
.. Dotted line: Particle Temp
Fluid Temp. at t=0.1
Fluid Temp. at t=0.25
Fluid Temp. at t=0.5
Pure fluid
Temperature
y
(B)
Dusty fluid
.. Dotted line: Particle Temp
Fluid Temp. at Ec=0.1
Fluid Temp. at Ec=0.2
Fluid Temp. at Ec=0.4
Pure fluid
Temperature
y
(C)
Dusty fluid
.. Dotted line: Particle Temp
r2=0.1
r2=0.25
r2=0.5
Pure fluid
Temperature
y
(D)
Dusty fluid
.. Dotted line: Particle Temp
Fluid Temp. at Re=2
Fluid Temp. at Re=3
Fluid Temp. at Re=4
Pure fluid
Temperature
y
(E)
Dusty fluid
.. Dotted line: Particle Temp
Fluid Temp. at Pr=2
Fluid Temp. at Pr=3
Fluid Temp. at Pr=4
Pure fluid
Temperature
y
(F)
.. Dotted line: Particle Temp
Dusty fluid
Fluid Temp. at Kr=0.1
Fluid Temp. at Kr=0.2
Fluid Temp. at Kr=0.4
Pure fluid
Temperature
y

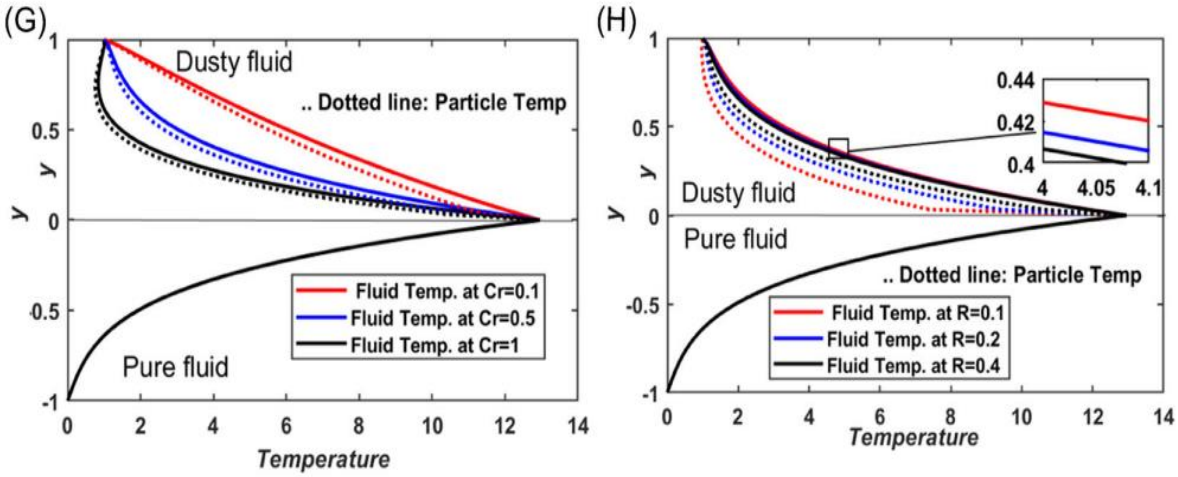

Figure 4.5: Temperature profiles with varying parameters under scheme 3a- *(A)* time, *(B)* Eckert number, *(C)* ratio of viscosities, *(D)* Reynolds number, *(E)* Prandtl number, *(F)* ratio of thermal conductivity, *(G)* ratio of specific heat, *(H)* particle concentration parameter

The skin friction coefficient is a dimensionless quantity that describes the amount of resistance provided to an object moving through a fluid and causing skin friction drift on the surface. Table 4.4 shows that skin friction increases with time and Reynolds number at the lower plate of the channel but remains constant with increasing values of particle concertation parameter, the ratio of viscosities and densities ($R, r_2, r_1, and\ r_3$). On the upper plate, the decrease in skin friction co-efficient is induced by rising values of time, $Re, and\ r_3$. When r_1, r_2 is increased, the co-efficient improves, and it does not change with *R*.

The Nusselt number (Nu) is the ratio of convective heat transfer to conductive heat transfer at the boundary. Table 4.5 shows that the Nusselt number increases at the upper plate and decreases at the lower plate with time, Reynolds number, particle concertation parameter R, ratio of viscosities and densities ($r_1, r_2, and\ r_3$).

4.6.2 Results and analysis of immiscible dusty and pure fluid flow under the scheme-3b

Figure 4.6 *(A-F)* visualize the response in fluid and dust particle velocities under scheme-3b with selected thermophysical parameters. In both regions generally, it is apparent that owing to the uniform suction effect, the velocity profiles of dust and fluids are not parabolic, and the curvature of pure fluid velocity is markedly different from the dusty fluid velocity topology. It is also observed that under scheme-3b, the flow profiles are elongated as compared to the flow profiles under scheme-3a. Figure 4.6 (*A*) exhibits the change in fluid and particle velocities with varying times when a constant pressure gradient is applied. It is noted that, with rising time, the fluid velocity is clearly increasing in both regions, i. e. a substantial acceleration is induced. However, the magnitude of velocity profiles computed by periodic pressure is lower than decaying, and constant pressure gradients see Figure 4.6*(C).* It can be noted from Figure 4.6 *(B)* that the velocity profiles increase with the increment of the pressure gradient again owing to the imparting of momentum to the channel flow regime. It is observed from Figure 4.6*(D)* that augmentation in the Reynolds number enhances the fluids and particle velocities for all three cases of applied constant, periodic, and decaying pressure gradients. However, the variations are more extensive in magnitude in the dusty fluid region compared to the pure fluid region. Figure 4.6*(E)* shows that owing to the suction effect (removal of material via the boundary) for all three applied pressure gradient cases, the dust particle and fluids velocities climb significantly in region-2 and decline slightly in the region-1 with an increase in the density ratio r_1. A weak decline in the pure fluid region for fluid velocity profiles can be seen in Figure 4.6*(F)*, and the profiles exhibit an increasing nature in the pure fluid region but only near the interface in the dusty fluid region. The qualitative properties of fluids and particle temperature profiles under scheme-3a and 3b are equivalent, and therefore these results are not presented for brevity.

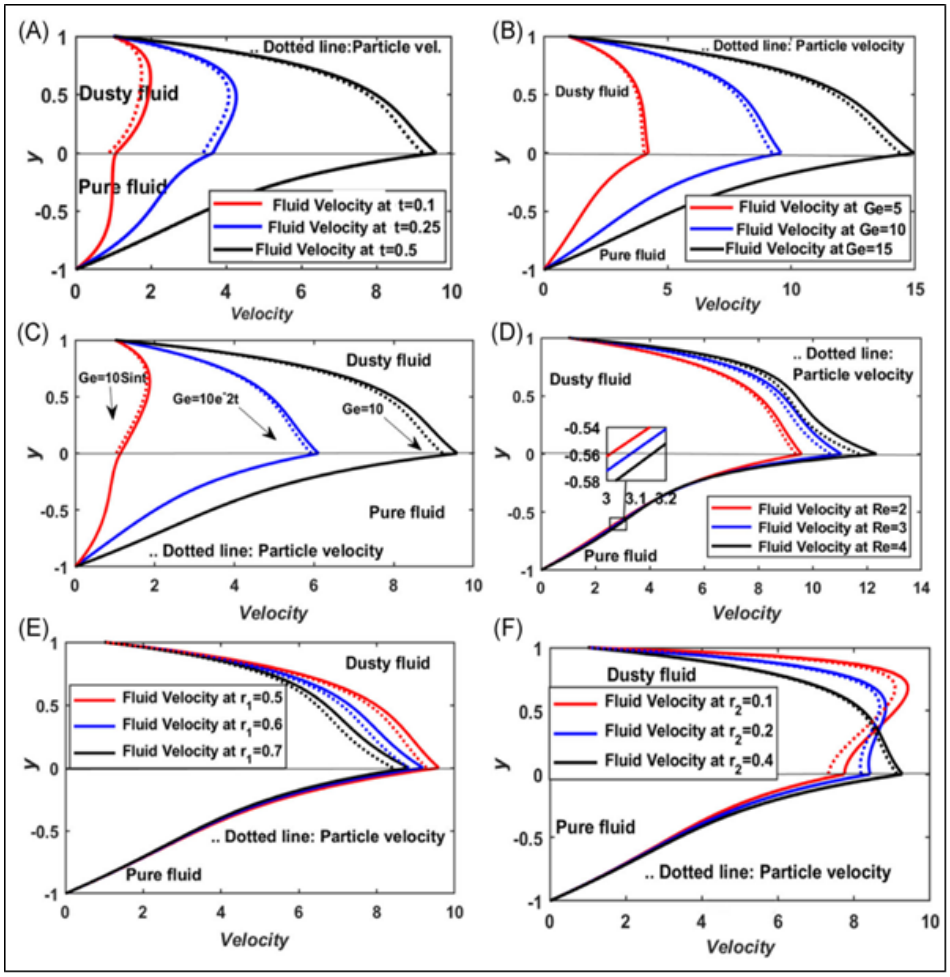

Figure 4.6: Fluid and particle velocity with varying parameters under scheme-3b, *(A)* time, *(B)* constant pressure, *(C)* constant periodic and decaying pressure, *(D)* Reynolds number, *(E)* ratio of densities, *(F)* ratio of viscosities

4.6.3 Interface tracking under scheme-3c

Figure 5 shows the evolution of the interface between the two liquid zones with varying time and amplitude under scheme 3c when the constant pressure gradient is present, and a vertical shift can be seen in the interface. It is also observed that initially, the vertical elongation of the interface is large, and thereafter the shape of the interface evolves progressively over time; hence the undulating sequence occurs faster for a more

considerable time. It is also judicious to note that the top fluid is less viscous than the bottom fluid. It is also noticed that the qualitative characteristics of this flow shall be maintained, and as expected, the interface starts to shift vertically if the amplitude is enhanced. The two liquids do not penetrate each other in the same way. Hence it can be concluded that initially, at small times, a large sinusoidal interface is observed, and later, the peak of the wave progresses rapidly as time increases. It is also worth mentioning that the evolution of the interface profile for periodic and decaying pressure gradient cases is qualitatively similar to that computed for the constant pressure gradient case, although magnitudes are different (for brevity, these simulations are not visualized).

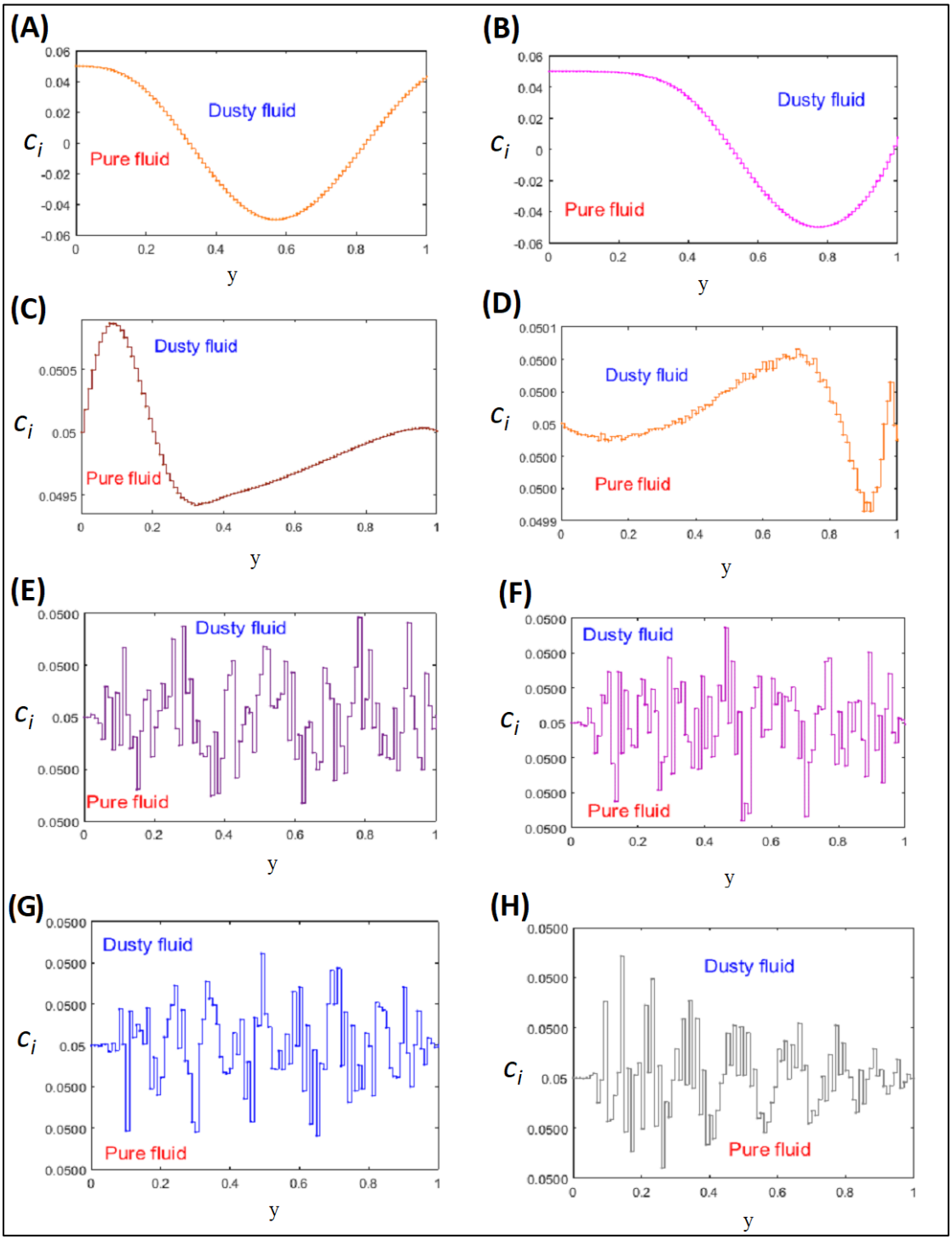
(A)
Dusty fluid
Pure fluid
c_i
y
(B)
Dusty fluid
Pure fluid
c_i
y
(C)
Dusty fluid
Pure fluid
c_i
y
(D)
Dusty fluid
Pure fluid
c_i
y
(E)
Dusty fluid
Pure fluid
c_i
y
(F)
Dusty fluid
Pure fluid
c_i
y
(G)
Dusty fluid
Pure fluid
c_i
y
(H)
Dusty fluid
Pure fluid
c_i
y

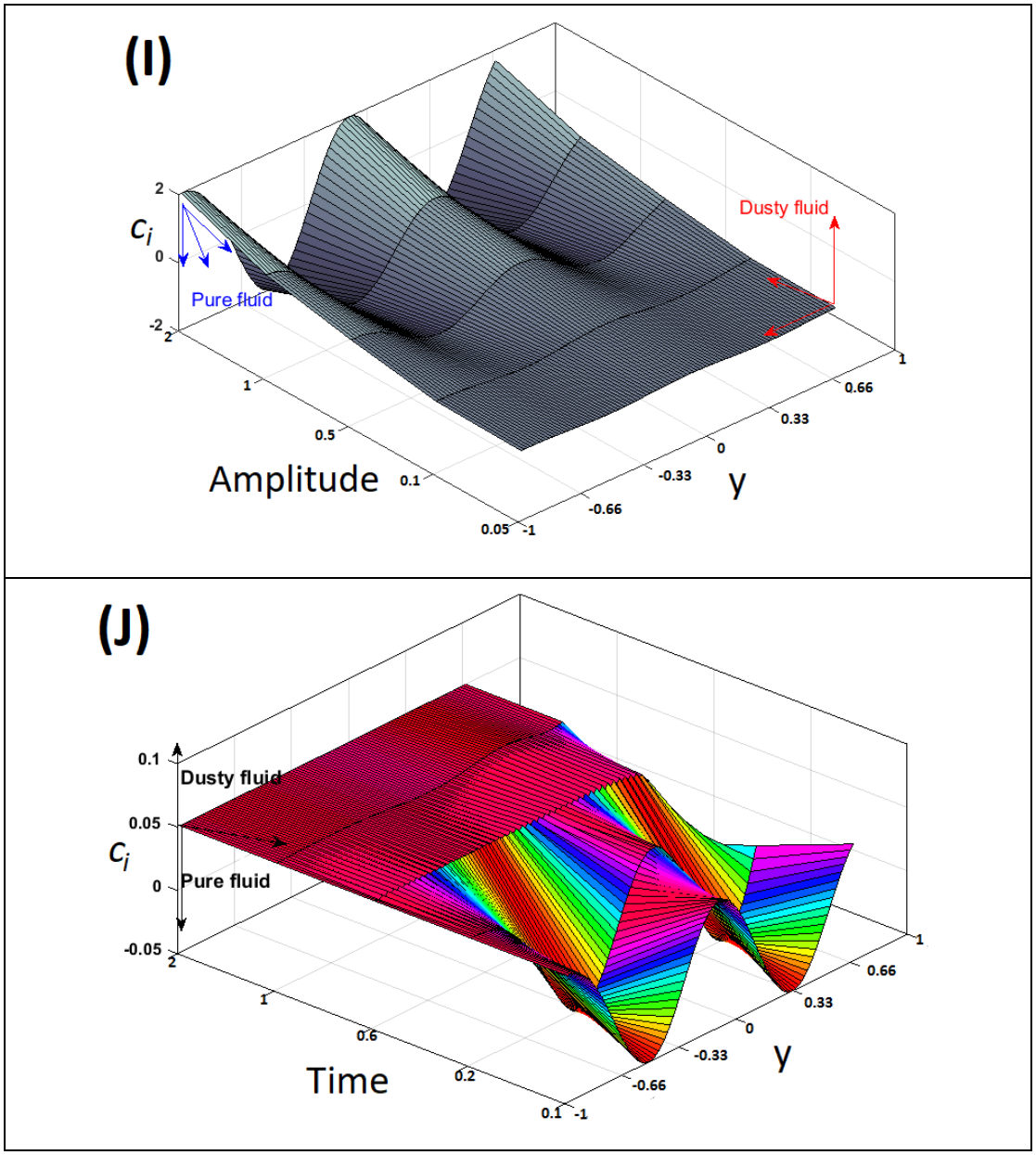

Figure 4.7: Sequence of interface position with varying time and amplitude under the scheme-3c,*(A)* interface track at t = 0.1, *(B)* interface track at t = 0.2, *(C)* interface track at t = 0.6, *(D)* interface track at t = 1, *(E)* interface track at t = 2, *(F)* interface track at t= 5, *(G)* interface track at t = 10, *(H)* interface track at t = 20, *(I)* interface track with amplitude, *(J)* 3D track of interface with time

4.7 Conclusions

The unsteady Generalized Couette flow of two immiscible dusty and pure fluids through a horizontal channel under three distinct scenarios with a stable and unstable interface has been analyzed numerically using the modified Cubic B-Spine Differential Quadrature method (MCB-DQM). The effects of the emerging thermophysical and hydrodynamic parameters on fluid and particle velocity, flow velocity, temperature, and interface evolution have been addressed. The core findings of the present analysis can be summarized in the following points:

1. For the flow under schemes 3a and 3b, an increasingly oscillatory and decreasing behavior in the fluid's velocities and particle velocity with time is computed in regions I and II when the flow is induced by constant, periodic, and decaying pressure gradients, respectively.
2. As anticipated in the stable interface schemes flow, values of the fluids and particle-phase velocities are enhanced with increments in the pressure gradient.
3. Increasing the Reynolds number in the stable interface schemes generates a marked enhancement in the fluid and particle-phase velocities for all three applied constant, periodic, and decaying pressure gradient cases. However, in the case of periodic gradient under scheme-3b, the velocities are observed to be decreasing near the interface.
4. Elevation in the particle concentration parameter increases the velocities of dust particles with all three applied pressure gradient scenarios in the stable interface schemes.
5. In the case of all three applied pressure gradients, an increment in the ratio of densities is found to significantly damp the velocities in the dusty fluid regions for scheme-3a scheme-3b. Furthermore, elevation in density ratio depresses velocities slightly for scheme-3b but does not tangibly modify the velocities in scheme-3a flow in the pure (Newtonian) fluid region.

6. Under scheme-3a (Dusty and non-dusty fluid through porous plates), a significant decline in dust particle and fluid velocities in the dusty liquid region and a negligible decline in the pure fluid velocity are noted with an increase in the ratio of viscosities for all three applied pressure gradients.
7. Under the scheme-3b (Dusty and non-dusty fluid through non-porous plates) flow, the behavior of fluids and particle velocities for the periodic pressure gradient differs from the constant and decaying pressure gradient case with an increment in the ratio of viscosities. The velocity profiles decline in both regions when the periodic pressure gradient is applied. At the same time, the pure fluid velocity increases weakly for both constant and decaying applied pressure gradients. Additionally, the dusty fluid and particle velocity alter from decreasing to growing trends near the interface. The dissimilar behavior observed may be owing to the suction effect and coupling nature of fluids.
8. The qualitative features of fluids and particle temperature profiles under scheme-3a and 3b are similar to all control parameters. Hence the critical output for temperature can be summarized as follows:
9. Dust particle and fluid temperatures in respective regions increase with an enhancement in time, Eckert number, and the ratio of viscosities (i.e., heating of the channeling regime). In contrast, they decrease with Reynolds and Prandtl numbers (i.e., cooling of the channeling regimes). Temperatures decline slightly in both regions with an increase in particle concentration parameters.
10. A rise in the ratio of densities results in a substantial decline in dust particle and fluid temperature in region-2, and pure fluid temperature decreases slightly in region-1; however, owing to the momentum transfer near the interface, the profiles show the converse response and temperatures are somewhat enhanced in both regions.
11. Elevation in the ratio of thermal conductivities produces a notable enhancement in temperature magnitudes of both dust particles and fluid in region-2. However, the pure fluids do not exhibit any shift in the temperature.

12. A boost in the ratio of specific heat of both fluids induces a significant reduction in the temperature magnitudes of both dust particles and fluid in region II. Nevertheless, the pure fluids do not demonstrate any displacement in the temperature.
13. Under scheme-3c, tracking the interface between the two immiscible liquids is also simulated with varying times. It is noticed that initially, the vertical elongation of the interface is significant, and subsequently, the topology evolves with time. Therefore, the undulating sequence occurs faster for a more considerable time, and the qualitative features of this flow are retained with high time and amplitude.
14. The MCB-DQM algorithm described offers excellent capabilities in interfacial fluid dynamics. Of course, the present study has neglected electrically conducting properties of either dusty or Newtonian fluids, which give rise to magnetohydrodynamic behavior, which may be assessed in future work.

Chapter 5

Ion-Slip and Hall Effects on Generalized/Plane Time-Dependent Hydromagnetic Couette Flow of Immiscible Micropolar and Dusty Micropolar Fluids with Heat Transfer and Dissipation: A Numerical Study

5.1 Introduction

Micropolar fluid dynamics has emerged as a significant branch of modern non-Newtonian fluid mechanics and has been deployed successfully in an impressive range of applications, including hemodynamics, geothermic, pharmacodynamics, turbulent shear flows, sensors, liquid crystals, and lubrication systems. Micropolar liquids are non-Newtonian liquids comprising rigid non-deformable particles that can spin, i.e., possess gyratory degrees of freedom. The Navier-Stokes equations cannot sufficiently describe the properties of non-Newtonian fluids. Eringen developed the fundamental model of micropolar fluids [108] as a simplification of his earlier theory of micro-morphic liquids ("simple microfluidics"). Kang and Eringen [111] applied the micropolar model to blood flow, demonstrating its superiority to many other rheological models. Fakour *et al.* [221] investigated micropolar fluids with heat transfer. The interaction between non-deformable spheroids rotating through a micropolar fluid was analyzed using a collocation scheme by Sherief *et al.* [222].

The integration of micro-sized crystals (dust particles) in hybrid nanofluids is commonly used to improve the thermal conductivity of the base fluid, also known as dusty fluid. It has a variety of implementations, covering combustion, crude oil filtration, and electrostatic precipitation. Menni *et al.* [151] provide a comprehensive

analysis of numerous scholars' computational and experimental studies to improve convection in porous environments with nanofluids. Reddy and Ferdows [195] identified the heat and mass transportations for micropolar dusty boundary layer flow. The intrinsic configuration of the channel for thermal and kinetic study with Newtonian and turbulent fluid has been extensively examined by Menni *et al.* [124], and the integration of dynamic objects into solar channels has been investigated.

Micropolar dusty fluids are increasingly used in engineering applications such as polymeric processing, metal spinning, synovial lubrication, artificial fabrics, cardio-vascular flows, glass-fiber processing, paper production, peristaltic transfer, drug distribution, emulsion suspensions, and colloidal fluids. Menni *et al.* [115] provided a systematic analysis of the different heat transfer techniques utilized to increase the efficiency of the smoother air duct.

Immiscible flows arise in nuclear engineering power systems, the pharmaceutical industry, and the extraction and purification of crude oil in petroleum engineering. These applications have stimulated interest in mathematical modelling, and some studies on the flow of immiscible transport phenomena have been communicated. Devakar and Iyengar [112] determined the effect of various fluid parameters featuring only one immiscible fluid and the resulting velocity and temperature distributions in the other immiscible fluid. Srinivas *et al*. [139], [223], [224] explored the dynamics of dual immiscible fluid flows in various configurations and with multiple thermodynamics magnetic and time-dependent effects. There is little more research on the movement of immiscible fluids between two plates for Newtonian and non-Newtonian fluids can be seen by Umavathi *et al*. [135], [144], [172].

The magnetic characteristics and nature of electromagnetic conducting fluids are applicable in various scientific fields such as plasma confinement, molten metals, power generation, drug targeting, and microfluidics. Because of its relevance and uses in different areas such as magnetic drug monitoring, astronautics, and astrophysics,

researchers are studying magnetohydrodynamic flows rapidly around the world. Attia *et al*. [74], [160] extensively studied various magneto-thermodynamics flow parameters on dusty fluids. The effect of externally transverse applied uniform magnetic field on unsteady MHD flow has been discovered by Krishna *et al.* [225]. Krishna [226] investigated the thermal and magnetic factors on unsteady rotating MHD flow of Jeffery fluid. In the presence of electromagnetic energy, the analytical solutions of an unsteady-MHD Boussinesq fluid, including heat and mass transport properties, are proposed by Krishna *et al.* [227] across a vertical undulating plate enclosed in a Darcian permeable medium. The power-law stream with heat transfer and the magnetohydrodynamic impact was examined by Prasad *et al*. [228]. Some more remarkable studies on Ion slip and the Hall effect on MHD flow can be seen in [117], [229]–[231].

Many computational approaches are available to analyze a system of partial differential equations. Menni *et al.* [232] performed a numerical analysis of heat transfer for fluid flow using flat rectangular and V-upstream geometries. A numerical simulation for unsteady-MHD flow was carried out by Krishna *et al.* [233] using the B-spline collocation method. The effects of specific baffle forms on the radiant aerodynamic efficiency were investigated by Menni *et al.* [234] using turbulent forced-convection fluid flow models. Some more fascinating fluid flow simulations with different shapes and geometry can be seen in [118], [235]–[237].

The differential quadrature method (DQM) is one of the most prominent methods for dealing with unsteadiness and nonlinear terms in the coupled partial differential equation. Arora and Joshi [238] solved the nonlinear Burgers equation for higher dimensions. Katta and Joshi [146] solved the time-dependent flow of Jeffery fluid between two porous plates using the trigonometric B-spline differential quadrature method. Two immiscible micropolar and Newtonian fluids were considered in the horizontal channel, and the system of partial differential equations was solved by the modified cubic B-Spline differential quadrature method [145].

Researchers have presented multiple studies on the steady and unsteady flow of single and immiscible combinations of micropolar, Newtonian fluids via different shapes and numerical simulation, resulting in various effects. To the best of the authors' awareness, no effort has been made to investigate the unsteady flow of two immiscible magnetohydrodynamic micropolar and micropolar dusty (fluid-particle suspension) fluids.

In light of this, the current study investigates theoretically and computationally the combined effects of ion slip, viscous dissipation, Joule heating, and Hall-current effect on unsteady generalized and plane Couette flow of two immiscible non-Newtonian incompressible magnetohydrodynamic micropolar and micropolar dusty (fluid-particle suspension) fluids through a horizontal channel. The novelty is embodied in the simultaneous inclusion of multiple magnetic effects, a sophisticated mesomorphic non-Newtonian model, and an alternative computational algorithm (modified cubic B-Spline differential quadrature method) which has never been considered collectively in previous studies. Ion-slip and Hall's current effects have been extensively studied by Bég and co-workers [239]–[242] in the context of nuclear reactor transport modelling and magnetohydrodynamic energy generators (MHD). These studies have confirmed the substantial modification in velocity and temperature distributions produced with Hall current and ion slip which are relevant to, for example, seeded potassium interfacial flows in Hall and Faraday generator systems [39], [41], [243], [244] and also hydromagnetic pumps and channel flow control in nuclear reactors [245], [246] In the present study, the inclusion of such effects is therefore justified. The mathematical model is formulated as a coupled partial differential equations system, and suitable transformations are implemented to render the boundary value problem as non-dimensional. Robust numerical results are obtained for velocity, microrotation, and temperature profiles under the effect of various important fluid parameters. Detailed interpretation is included for both scheme flows.

5.2 Mathematical Formulation

First, the generalized Couette flow of two immiscible, micropolar and micropolar dusty fluids is considered through a horizontal duct, and then plane Couette flow is analyzed.

5.2.1 Generalized Couette flow of two immiscible, micropolar and micropolar dusty fluids through a horizontal duct ($-1 \leq y \leq 1$)

The following assumptions are made for time-dependent, generalized Couette flow of two immiscible, micropolar and micropolar dusty fluids through a horizontal duct (channel).

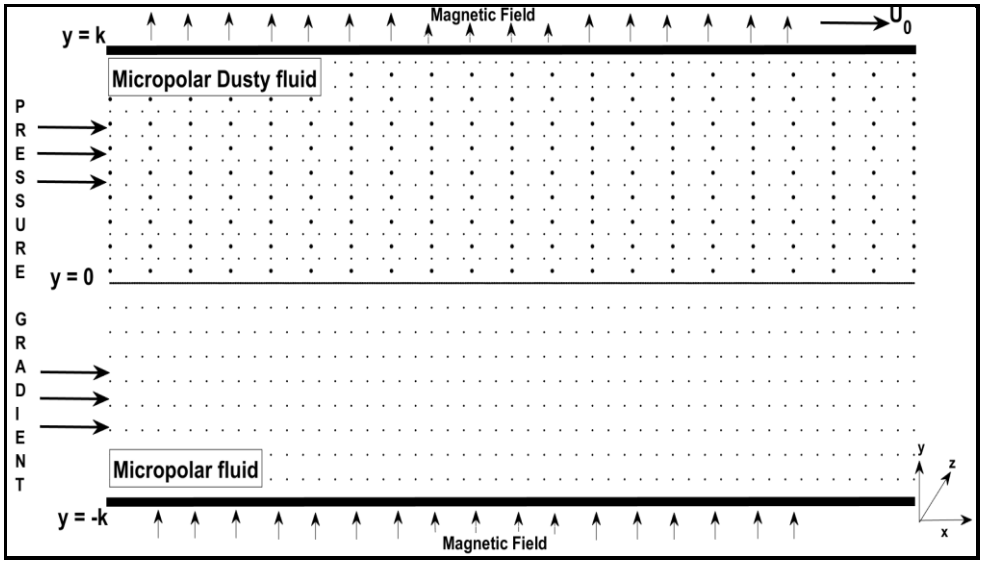

Figure 5.1: Geometry of generalized Couette flow of two immiscible, micropolar and micropolar dusty fluids

i. Both fluids are electrically conducting, incompressible, unidirectional, and occupied in a horizontal channel comprised of two parallel upper and lower plates, as depicted in Figure 5.1

ii. A distance of 2k separates the walls of the channel. The lower wall is fixed and situated at $y=-k$, with a constant temperature T_{w1} while the upper wall moves with constant velocity U_0 at $y=k$, has a temperature T_{w2}.

iii. The flow is induced by the upper plate movement and a constant pressure gradient $\left(-\frac{\partial p}{\partial x}\right)$ which is applied in the *x*-direction of the channel.

iv. Both duct walls are electrically non-conductive and are located in the *X*-*Z* plane, and both fluids are assumed to have electrical conductivity, σ.

v. An external uniform static magnetic field B_0 is imposed on the fluids in the *y*-direction.

vi. The effect of an applied transverse magnetic field on both fluids generates resistance to fluid movement through the Lorentz force, which is orthogonal to the applied magnetic field and produces the following body force acting on both fluids [74]:

$$J \times B_0 = \frac{\sigma {B_0}^2 (1+Bi.Be) u_i}{(1+Bi.Be)^2+Be^2}. \tag{5.1}$$

Here J is the current density, B_0 is the external magnetic field, σ is the electric conductivity, Bi is the ion slip parameter, Be is the Hall parameter.

vii. As the fluids are immiscible, the micropolar fluid occupies the lower region of the channel, i. e. zone I ($-k \leq y \leq 0$), and possesses a linear fluid velocity u_m, microrotation (angular velocity) M_*, density ρ_m, viscosity μ_m, vortex viscosity κ_m, gyro-viscosities $\omega_m \; and \; \beta_m$, gyration parameter j_m, thermal conductivity K_m, specific heat capacity $C_{m.}$

viii. Micropolar dusty fluid occupies the upper region of the channel, i. e. zone II ($0 \leq y \leq k$), and possesses linear fluid velocity u_{md}, microrotation (angular velocity) M_d density ρ_{md}, viscosity μ_{md}, vortex viscosity κ_{md}, gyro-viscosities $\omega_{md} \; and \; \beta_{md}$, gyration parameter j_{md}, thermal conductivity K_{md} and specific heat capacity C_{md}.

ix. The micropolar dusty (upper region) fluid contains suspended dust particles that have the same size and mass, are non-deformable, and are homogeneously distributed throughout the liquid.

x. In the dusty fluid, the dust particles have particle velocity u_p, density ρ_p, and possess the average mass m_p with a particle volume fraction function $\emptyset$.

xi. It is also assumed that the particle phase is sufficiently dilute such that the interactions between any two particles are ignored. The dust particle size (radius r) is also relatively tiny in scale. Hence the net dust effect on the fluid particles is equivalent to the following additional force per unit volume [24], [74]:

$$D_f = \zeta_T \rho_p \left(u_{md} - u_p\right) \tag{5.2}$$

Here $\zeta_T = \frac{6\pi r\, \mu_{md}}{m_p}$ is the volume transfer coefficient with an average mass of dust particle m_p , density ρ_p , velocity u_p, and radius r.

xii. Dust particles acquire heat from the fluid by thermal conduction through their surface. Designating c_p as for the specific heat capacity of the particles, the heat conduction between the fluid and particles depends on the temperature relaxation parameter γ_T.We are adopting the approach in [24], [74] may be stated as. $\gamma_T = \frac{3}{2}\frac{\rho_p . c_p . \mu_{md}}{K.N.K_{md}}$ (5.3)

xiii. Here *N* is the number density of dust particles per unit volume. The body forces and body couples are neglected. The transportation attributes are unchanged in both the zones and common pressure gradients are applied along the horizontal (*X*) axial direction.

xiv. The fluid velocity vectors in both zones are $u_m(y,t)$, $u_{md}(y,t)$ and the micro-rotation vector $M_*(y,t)$ in the zone, I (lower), $M_d(y,t)$ in the zone, II (upper), and particle-phase velocity $u_p(y,t)$ are assumed to be $(u_m(y,t),0,0)$, $(u_{md}(y,t),0,0)$, $((0,0,M_*(y,t))$, $((0,0,M_d(y,t))$, and $(u_m(y,t),0,0)$.

xv. The fluid temperature vectors in both zones are $T_m(y,t)$, $T_{md}(y,t)$ and the particle phase temperature $T_P(y,t)$ in the zone, II (upper) is assumed to be $(T_m(y,t),0,0)$, $(T_{md}(y,t),0,0)$, and $(T_p(y,t),0,0)$ respectively.

xvi. The fluid layers are mechanically coupled through the mode of momentum exchange. Transferring momentum arises through consistency in velocity and shear stress over the interface. However, we assume that the flow rate and shear pressure are also stable at the interface between two liquids.

xvii. The governing equations for linear fluid velocities (u_m, u_{md}) particle velocity (u_p), micro-rotation (M_*, M_d) and temperature (T_m, T_{md}) particle temperature (T_p) of the interfacial MHD (magnetohydrodynamic) flow under the aforesaid assumed constraints are [24], [74],[2] :

Zone-I (Micropolar fluid).

$$\rho_m \frac{\partial u_m}{\partial t} = -\frac{\partial p}{\partial x} + \kappa_m \frac{\partial M_*}{\partial y} + (\mu_m + \kappa_m)\frac{\partial^2 u_m}{\partial y^2} - \frac{\sigma {B_0}^2(1+Bi.Be)}{(1+Bi.Be)^2+Be^2} u_m , \tag{5.4}$$

$$\rho_m j_m \frac{\partial M_*}{\partial t} = \omega_m \frac{\partial^2 M_*}{\partial y^2} - \kappa_m \left(2M_* + \frac{\partial u_m}{\partial y}\right), \tag{5.5}$$

$$\rho_m C_m \frac{\partial T_m}{\partial t} = K_m \frac{\partial^2 T_m}{\partial y^2} + \mu_m \left(\frac{\partial u_m}{\partial y}\right)^2 + \kappa_m \left(2M_* + \frac{\partial u_m}{\partial y}\right)^2 + \beta_m \left(\frac{\partial M_*}{\partial y}\right)^2 + \frac{\sigma {B_0}^2(1+Bi.Be)}{(1+Bi.Be)^2+Be^2} {u_m}^2. \tag{5.6}$$

Zone-II (Micropolar dusty fluid).

$$\rho_{md} \frac{\partial u_{md}}{\partial t} = -\frac{\partial p}{\partial x} + \kappa_{md} \frac{\partial M_{md}}{\partial y} + (\mu_{md} + \kappa_{md})\frac{\partial^2 u_{md}}{\partial y^2} - \frac{\sigma {B_0}^2(1+Bi.Be)}{(1+Bi.Be)^2+Be^2} u_{md} - \zeta_T \rho_p \emptyset \frac{(u_{md}-u_p)}{(1-\emptyset)}, \tag{5.7}$$

$$\frac{\partial u_p}{\partial t} = \zeta_T (u_{md} - u_p), \tag{5.8}$$

$$\rho_{md} j_{md} \frac{\partial M_{md}}{\partial t} = \omega_{md} \frac{\partial^2 M_{md}}{\partial y^2} - \kappa_{md} \left(2M_{md} + \frac{\partial u_{md}}{\partial y}\right), \tag{5.9}$$

$$\rho_{md} C_{md} \frac{\partial T_{md}}{\partial t} = K_{md} \frac{\partial^2 T_{md}}{\partial y^2} + \mu_{md} \left(\frac{\partial u_{md}}{\partial y}\right)^2 + \kappa_{md} \left(2M_{md} + \frac{\partial u_{md}}{\partial y}\right)^2 + \beta_{md} \left(\frac{\partial M_{md}}{\partial y}\right)^2 + \frac{\sigma {B_0}^2(1+Bi.Be)}{(1+Bi.Be)^2+Be^2} {u_{md}}^2 + \frac{\rho_p c_p \emptyset (T_p - T_{md})}{\gamma_T (1-\emptyset)} + \zeta_T \rho_p \emptyset \frac{(u_{md}-u_p)^2}{(1-\emptyset)}, \tag{5.10}$$

$$\frac{\partial T_p}{\partial t} = -\frac{(T_p - T_{md})}{\gamma_T}. \tag{5.11}$$

At the channel wall, both velocity and microrotation are prescribed the vanishing classical hyper-stick, and no-slip conditions at the boundaries are considered. Furthermore, velocities, microrotations, temperature vectors, shear stress, and couple stress are continuous at the fluid-fluid interface. Both fluids and boundaries (channel walls) are initially sustained at a constant temperature. The temperatures on both walls are set to T_{w1} and T_{w2}, respectively. The initial and boundary conditions are taken as [24], [74],[2].

Initial conditions: At $t \leq 0$, and $-k \leq y \leq 0$,

$$\left.\begin{aligned} u_m(y,t) &= 0, \\ M_*(y,t) &= 0, \\ T_m(y,t) &= T_0. \end{aligned}\right\} \tag{5.12}$$

For $0 \leq y \leq k$,

$$\left.\begin{aligned} u_{md}(y,t) &= 0, \\ M_{md}(y,t) &= 0, \\ T_{md}(y,t) &= T_0, \\ u_p(y,t) &= 0, \\ T_p(y,t) &= T_0. \end{aligned}\right\} \tag{5.13}$$

Boundary (At channel walls) conditions: At $t > 0$,

$$\left.\begin{aligned} u_m(-k,t) &= 0, \\ M_*(-k,t) &= 0, \\ T_m(-k,t) &= T_{w1}, \\ u_{md}(k,t) &= U_0, \\ u_p(k,t) &= U_0, \\ M_d(k,t) &= 0, \\ T_{md}(k,t) &= T_{w2}, \\ T_p(k,t) &= T_{w2}. \end{aligned}\right\} \tag{5.14}$$

Interface conditions at *y = 0,*

$$\left.\begin{array}{c} u_m(0,t) = u_{md}(0,t), \\ M_*(0,t) = M_d(0,t), \\ T_m(0,t) = T_{md}(0,t), \\ K_m T_{m_y} = K_{md} T_{md_y}, \\ (\mu_m + \kappa_m) U_{m_y} + \kappa_m M_* = (\mu_{md} + \kappa_{md}) U_{md_y} + \kappa_{md} M_{md}. \end{array}\right\} \tag{5.15}$$

The following non-dimensional parameters are introduced:

$$\left.\begin{array}{c} \bar{x} = \frac{x}{k}, \bar{y} = \frac{y}{k}, \overline{u_m} = \frac{u_m}{U_0}, \overline{u_{md}} = \frac{u_{md}}{U_0}, \overline{U_p} = \frac{u_p}{U_0}, \bar{p} = \frac{p}{\rho_m {U_0}^2}, \bar{t} = \frac{tU_0}{k}, \\ \overline{T_m} = \frac{T_m - T_{w1}}{T_{w2} - T_{w1}}, , \overline{T_{md}} = \frac{T_{md} - T_{w2}}{T_{w2} - T_{w1}}, \overline{T_p} = \frac{T_p - T_{w2}}{T_{w2} - T_{w1}}, \overline{M_*} = \frac{M_* k}{U_0}, \overline{M_{md}} = \frac{M_{md} k}{U_0}. \end{array}\right\} \tag{5.16}$$

Here following [27], we assume $\omega_m = (\mu_m + \kappa_m/2) j_m$ and $\omega_{md} = (\mu_{md} + \kappa_{md}/2) j_{md}$ with $j_m = j_{md} = k^2$. After dropping the bars, the equations (5.4) - (5.11) assume the following forms:

Zone-I (Micropolar fluid).

$$\frac{\partial u_m}{\partial t} = -\frac{\partial p}{\partial x} + \frac{1}{Re}\left[\eta_1 \frac{\partial M_*}{\partial y} + (1+\eta_1)\frac{\partial^2 u_m}{\partial y^2} - \frac{Ha^2(1+Bi.Be)}{(1+Bi.Be)^2+Be^2} u_m\right], \tag{5.17}$$

$$\frac{\partial M_*}{\partial t} = \frac{1}{Re}\left[\left(1+\frac{\eta_1}{2}\right)\frac{\partial^2 M_*}{\partial y^2} - \eta_1\left(2M_* + \frac{\partial u_m}{\partial y}\right)\right], \tag{5.18}$$

$$\frac{\partial T_m}{\partial t} = \frac{Ec}{Re}\left[\begin{array}{c} \frac{1}{Pr.Ec}\frac{\partial^2 T_m}{\partial y^2} + \left(\frac{\partial u_m}{\partial y}\right)^2 + \eta_1\left(2M_* + \frac{\partial u_m}{\partial y}\right)^2 + \delta_m\left(\frac{\partial M_m}{\partial y}\right)^2 \\ + \frac{Ha^2(1+Bi.Be)}{(1+Bi.Be)^2+Be^2} {u_m}^2 \end{array}\right]. \tag{5.19}$$

Zone-II (Micropolar dusty fluid)

$$\frac{\partial u_{md}}{\partial t} = -\frac{\partial p}{\partial x} + \frac{r_1}{r_2.Re}\left[\begin{array}{c} \eta_2 \frac{\partial M_d}{\partial y} + (1+\eta_2)\frac{\partial^2 u_{md}}{\partial y^2} - \frac{Ha^2(1+Bi.Be)}{r_1((1+Bi.Be)^2+Be^2)} u_{md} \\ -R\left(u_{md} - u_p\right) \end{array}\right], \tag{5.20}$$

$$\frac{\partial u_p}{\partial t} = \frac{R.r_1.r_3}{r_2.Re}\left(u_{md} - u_p\right), \tag{5.21}$$

$$\frac{\partial M_d}{\partial t} = \frac{r_1}{r_2.Re}\left[\left(1+\frac{\eta_2}{2}\right)\frac{\partial^2 M_d}{\partial y^2} - \eta_2\left(2M_{md} + \frac{\partial u_{md}}{\partial y}\right)\right], \tag{5.22}$$

$$\frac{\partial T_{md}}{\partial t} = \frac{Ec.r_1}{Re.r_2.C_r}\left[\begin{array}{c} \frac{Kr}{Pr.Ec.r_1}\frac{\partial^2 T_{md}}{\partial y^2} + \left(\frac{\partial u_{md}}{\partial y}\right)^2 + \eta_2\left(2M_d + \frac{\partial u_{md}}{\partial y}\right)^2 \\ +\delta_{md}\left(\frac{\partial M_d}{\partial y}\right)^2 + \frac{Ha^2(1+Bi.Be)}{r_1((1+Bi.Be)^2+Be^2)} {u_{md}}^2 \\ + \frac{2}{3}\frac{R.K_r}{Pr.Ec.r_1}\left(T_p - T_{md}\right) + R\left(U_{md} - U_p\right)^2 \end{array}\right], \tag{5.23}$$

$$\frac{\partial T_p}{\partial t} = \frac{2}{3}\frac{R*k_r*C_r*r_3}{C_{Pr}*r_1*Pr}\frac{(T_{md}-T_p)}{Re}. \tag{5.24}$$

Equations (5.12) - (5.15) are considered as initial, interfacial, and boundary conditions with $T_0 = 0, T_{w1} = 0, T_{w2} = 1, U_0 = 1$, and $k = 1$. In equations (5.17) - (5.24) the parameters (see nomenclature) emerging are defined as follows:

$$\left.\begin{array}{c} Re = \frac{\rho_m U_0}{\mu_m},\ \eta_1 = \frac{\kappa_m}{\mu_m}, Ha^2 = \frac{\sigma {B_0}^2 k^2}{\mu_m}, Ec = \frac{U_0}{C_m(T_{w2}-T_{w1})}, Pr = \frac{\mu_m C_m}{K_m} \\ \delta_m = \frac{\beta_m}{\mu_m k^2}, r_1 = \frac{\mu_{md}}{\mu_m}, r_2 = \frac{\rho_{md}}{\rho_d}, \eta_2 = \frac{\kappa_{md}}{\mu_{md}}, R = \frac{K\rho_p k^2}{\mu_{md} m_p}, r_3 = \frac{\rho_{md}}{\rho_p}, K_r = \frac{K_{md}}{K_m}, \\ C_r = \frac{C_{md}}{C_m}, \delta_{md} = \frac{\beta_{md}}{\mu_{md} k^2}, C_{Pr} = \frac{C_{md}}{c_p}, -\frac{\partial p}{\partial x} = Ge(t), K = 6\pi r \mu_{md} U_0. \end{array}\right\} \tag{5.25}$$

Here $Ge(t)$ is the applied time-dependent pressure gradient in the x-axial direction with $t > 0$.

5.2.2 Plane Couette flow of two immiscible, micropolar, and micropolar dusty fluids through a horizontal duct $(-1 \le y \le 1)$

In the absence of an external pressure gradient $\left(-\frac{\partial p}{\partial x} = 0\right)$ and the presence of upper plate movement with $(U_0 = 1)$, the equations (5.17) - (5.24) represent the plane Couette flow in the channel. Hence the equations of generalized Couette flow have been updated accordingly.

5.3 Engineering design quantities

5.3.1 Skin Friction Coefficients

When the fluid flows over the channel walls (boundaries), it exerts a frictional effect on these surfaces, obstructing forward motion and causing skin friction (shear stress). The skin-friction coefficient is used to quantify this effect. The expressions for skin friction coefficients at the lower and upper walls are defined as follows:

At lower wall $\left(C_f\right)_{y=-1} = \frac{2}{Re}\left[(1+\eta_1)\frac{\partial u_m}{\partial y} + \eta_1 M_*\right]_{y=-1}$. (5.26)

At upper wall $\left(C_f\right)_{y=1} = \frac{2r_1}{r_2 Re}\left[(1+\eta_1)\frac{\partial u_{md}}{\partial y} + \eta_1 M_d\right]_{y=1}$. (5.27)

5.3.2 Nusselt Numbers

Nusselt number is a key parameter in MHD nuclear and energy generator systems. It quantifies the rate of heat transfer from the bulk flow to the boundaries and also expresses the relative contribution of thermal convection heat transfer to thermal conduction heat transfer. The expressions for Nusselt number on both walls take the form:

At lower plate $(N_u)_{y=-1} = \left(-\frac{\partial T_m}{\partial y}\right)_{y=-1}$, (5.28)

At upper plate $(N_u)_{y=1} = \left(-\frac{\partial T_{md}}{\partial y}\right)_{y=1}$. (5.29)

5.4 Profiles computation for generalized Couette flow

To obtain the velocity, micro-rotation, and temperature profiles for generalized MHD (magnetohydrodynamic) Couette flow of immiscible micropolar and micropolar dusty fluids in the respective zone, replace the approximation of the spatial components of the I and II order derivatives obtained by using MCB-DQM (modified cubic b-spline differential quadrature method). Hence the system of coupled partial equations (5.17) - (5.24) is numerically solved with the initial and boundary condition equations (5.12) - (5.15) and the linear velocities, angular velocity component (microrotation), and temperature profiles of both fluids and particles are readily obtained. The equations (5.17) - (5.24) can be updated as follows:

Zone-I (Micropolar fluid).

$$\frac{\partial u_m}{\partial t} = Ge(t) + \frac{1}{Re}\begin{bmatrix}\eta_1 \sum_{j=1}^{N} a^*{}_{ij} M_*(y_j,t) + (1+\eta_1)\left(\sum_{j=1}^{N} b^*{}_{ij} u_m(y_j,t)\right) \\ -\frac{Ha^2(1+Bi.Be)}{(1+Bi.Be)^2+Be^2} u_m(y_j,t)\end{bmatrix}, \quad (5.30)$$

$$\frac{\partial M_*}{\partial t} = \frac{1}{Re}\left[\left(1+\frac{\eta_1}{2}\right)\left(\sum_{j=1}^{N} b^*{}_{ij} M_*(y_j,t)\right) - \eta_1 \begin{pmatrix} 2M_*(y_j,t) \\ +\sum_{j=1}^{N} a^*{}_{ij} u_m(y_j,t)\end{pmatrix}\right], \quad (5.31)$$

$$\frac{\partial T_m}{\partial t} = \frac{Ec}{Re}\begin{bmatrix} \frac{1}{Pr.Ec}\left(\sum_{j=1}^{N} b^*{}_{ij} T_m(y_j,t)\right) + \left(\sum_{j=1}^{N} a^*{}_{ij} u_m(y_j,t)\right)^2 + \\ \eta_1\left(2M_*(y_j,t) + \sum_{j=1}^{N} a^*{}_{ij} u_1(y_j,t)\right)^2 + \delta_m\left(\sum_{j=1}^{N} a^*{}_{ij} M_*(y_j,t)\right)^2 \\ + \frac{Ha^2(1+Bi.Be)}{(1+Bi.Be)^2+Be^2} u_m(y_j,t)^2 \end{bmatrix}. \quad (5.32)$$

Zone-II (Micropolar dusty fluid).

$$\frac{\partial u_{md}}{\partial t} = Ge(t) + \frac{r_1}{r_2.Re}\begin{bmatrix} \eta_2\left(\sum_{j=1}^{N} a^*{}_{ij} M_d(y_j,t)\right) + \\ (1+\eta_2)\left(\sum_{j=1}^{N} b^*{}_{ij} u_{md}(y_j,t)\right) \\ -\frac{Ha^2(1+Bi.Be)}{r_1((1+Bi.Be)^2+Be^2)} u_{md}(y_j,t) \\ -\ R\left(u_{md}(y_j,t) - u_p(y_j,t)\right) \end{bmatrix}, \quad (5.33)$$

$$\frac{\partial u_p}{\partial t} = \frac{R.r_1.r_3}{r_2.Re}\left[u_{md}(y_j,t) - u_p(y_j,t)\right], \quad (5.34)$$

$$\frac{\partial M_d}{\partial t} = \frac{r_1}{r_2.Re}\left[\left(1+\frac{\eta_2}{2}\right)\left(\sum_{j=1}^{N} b^*{}_{ij} M_d(y_j,t)\right) - \eta_2\begin{pmatrix} 2M_d(y_j,t) \\ +\sum_{j=1}^{N} a^*{}_{ij} u_{md}(y_j,t) \end{pmatrix}\right], \quad (5.35)$$

$$\frac{\partial T_{md}}{\partial t} = \frac{Ec.r_1}{Re.r_2.C_r}\begin{bmatrix} \frac{Kr}{Pr.Ec.r_1}\left(\sum_{j=1}^{N} a^*{}_{ij} T_{md}(y_j,t)\right) + \left(\sum_{j=1}^{N} a^*{}_{ij} u_{md}(y_j,t)\right)^2 + \\ \eta_2\begin{pmatrix} 2M_d(y_j,t) + \\ \sum_{j=1}^{N} a^*{}_{ij} u_{md}(y_j,t) \end{pmatrix}^2 + \delta_{md}\left(\sum_{j=1}^{N} a^*{}_{ij} M_d(y_j,t)\right)^2 \\ + \frac{Ha^2(1+Bi.Be)}{r_1((1+Bi.Be)^2+Be^2)} u_{md}(y_j,t)^2 + \\ \frac{2}{3}\frac{R.K_r}{Pr.Ec.r_1}\left(T_p(y_j,t) - T_{md}(y_j,t)\right) \\ +R\ \left(u_{md}(y_j,t) - u_p(y_j,t)\right)^2 \end{bmatrix}, \quad (5.36)$$

$$\frac{\partial T_p}{\partial t} = \frac{2}{3}\frac{R*k_r*C_r*r_3}{C_{Pr}*r_1*Pr}\left[\frac{\left(T_{md}(y_j,t) - T_p(y_j,t)\right)}{Re}\right]. \quad (5.37)$$

Thus, equations (5.31) - (5.37) are reduced into a system of ordinary differential equations in time, that is, for *i=1, 2, 3…, N*, and the system is solved by the robust four-step third-order SSP-RK43 scheme (1.69) - (1.72). The velocities and microrotation in both zones are obtained as follows:

In the first step, for *i=1,2,3…, N.*

Zone-I ($-k \le y \le 0$) (Micropolar fluid):

$$u_{m_1} = u_{m_0} + \frac{\Delta t}{2}\left(Ge(t) + \frac{1}{Re}\begin{bmatrix} \eta_1\left(\sum_{j=1}^{N} a^*{}_{ij} M_{*_0}(y_j,t)\right) \\ -\frac{Ha^2(1+Bi.Be)}{(1+Bi.Be)^2+Be^2} u_{m_0}(y_j,t) \\ +(1+\eta_1)\left(\sum_{j=1}^{N} b^*{}_{ij} u_{m_0}(y_j,t)\right) \end{bmatrix}\right), \tag{5.38}$$

$$M_{*_1} = M_{*_0} + \frac{\Delta t}{2}\left(\frac{1}{Re}\begin{bmatrix} \left(1+\frac{\eta_1}{2}\right)\left(\sum_{j=1}^{N} b^*{}_{ij} M_{*_0}(y_j,t)\right) - \\ \eta_1\left(2M_{*_0}(y_j,t) + \sum_{j=1}^{N} a^*{}_{ij} u_{m_0}(y_j,t)\right) \end{bmatrix}\right), \tag{5.39}$$

$$T_{m_1} = T_{m_0} + \frac{\Delta t}{2}\left(\frac{Ec}{Re}\begin{bmatrix} \frac{1}{Pr.Ec}\left(\sum_{j=1}^{N} b^*{}_{ij} T_{m_0}(y_j,t)\right) + \left(\sum_{j=1}^{N} a^*{}_{ij} u_{m_0}(y_j,t)\right)^2 \\ +\eta_1\left(2M_{*_0}(y_j,t) + \sum_{j=1}^{N} a^*{}_{ij} u_{m_0}(y_j,t)\right)^2 + \\ \delta_m\left(\sum_{j=1}^{N} a^*{}_{ij} M_{*_0}(y_j,t)\right)^2 + \frac{Ha^2(1+Bi.Be)}{(1+Bi.Be)^2+Be^2} u_{m_0}(y_j,t)^{\,2} \end{bmatrix}\right). \tag{5.40}$$

Zone-II *(0 ≤ y ≤ k)* (Micropolar dusty fluid):

$$u_{md_1} = u_{md_0} + \frac{\Delta t}{2}\left(Ge(t) + \frac{r_1}{r_2.Re}\begin{bmatrix} \eta_2 \sum_{j=1}^{N} a^*{}_{ij} M_{md_0}(y_j,t) + \\ (1+\eta_2)\left(\sum_{j=1}^{N} \beta^*{}_{ij} u_{md_0}(y_j,t)\right) - \\ \frac{Ha^2(1+Bi.Be)}{r_1((1+Bi.Be)^2+Be^2)} u_{md_0}(y_j,t) \\ -R\left(u_{2_0}(y_j,t) - u_{p_0}(y_j,t)\right) \end{bmatrix}\right), \tag{5.41}$$

$$u_{p_1} = u_{p_0} + \frac{\Delta t}{2}\left(\frac{R.r_1.r_3}{r_2.Re}\left[u_{md_0}(y_j,t) - u_{p_0}(y_j,t)\right]\right), \tag{5.42}$$

$$M_{md_1} = M_{*_0} + \frac{\Delta t}{2}\left(\frac{r_1}{r_2.Re}\begin{bmatrix} \left(1+\frac{\eta_2}{2}\right)\left(\sum_{j=1}^{N} b^*{}_{ij} M_{md_0}(y_j,t)\right) \\ -\eta_2\left(2M_{md_0}(y_j,t) + \sum_{j=1}^{N} a^*{}_{ij} u_{md_0}(y_j,t)\right) \end{bmatrix}\right), \tag{5.43}$$

$$T_{md_1} = T_{md_0} + \frac{\Delta t}{2}\left(\frac{Ec.r_1}{Re.r_2.C_r}\left[\begin{array}{c} \frac{Kr}{Pr.Ec.r_1}\left(\sum_{j=1}^{N} b^*{}_{ij} T_{md_0}(y_j,t)\right) \\ +\left(\sum_{j=1}^{N} a^*{}_{ij} u_{md_0}(y_j,t)\right)^2 \\ +\eta_2 \begin{pmatrix} 2M_{d_0}(y_j,t) + \\ \sum_{j=1}^{N} a^*{}_{ij} u_{md_0}(y_j,t) \end{pmatrix}^2 + \\ \delta_{md}\left(\sum_{j=1}^{N} a^*{}_{ij} M_{md_0}(y_j,t)\right)^2 + \\ \frac{Ha^2(1+Bi.Be)}{r_1((1+Bi.Be)^2+Be^2)} u_{md_0}(y_j,t)^2 \\ +\frac{2}{3}\frac{R.K_r}{Pr.Ec.r_1}\left(T_{p_0}(y_j,t) - T_{md_0}(y_j,t)\right) + \\ \frac{R.C_r.r_3}{Ec}\left(u_{md_0}(y_j,t) - u_{p_0}(y_j,t)\right)^2 \end{array} \right] \right), \tag{5.44}$$

$$T_{p_1} = T_{p_0} + \frac{\Delta t}{2}\left(\frac{2}{3}\frac{R*k_r*C_r*r_3}{C_{Pr}*r_1*Pr}\frac{\left(T_{md_0}(y_j,t) - T_{p_0}(y_j,t)\right)}{Re} \right). \tag{5.45}$$

At the first step of the method, the initial, interfacial, and boundary condition equations (5.12) - (5.15) are considered favourably.

In the second step for *i=1,2,3…, N.*

Zone-I ($-k \le y \le 0$) (Micropolar fluid):

$$u_{m_2} = u_{m_1} + \frac{\Delta t}{2}\left(Ge(t) + \frac{1}{Re}.\left[\begin{array}{c} \eta_1 \sum_{j=1}^{N} a^*{}_{ij} M_{*_1}(y_j,t) + \\ (1+\eta_1)\left(\sum_{j=1}^{N} b^*{}_{ij} u_{m_1}(y_j,t)\right) \\ -\frac{Ha^2(1+Bi.Be)}{(1+Bi.Be)^2+Be^2} u_{m_1}(y_j,t) \end{array} \right] \right), \tag{5.46}$$

$$M_{*_2} = M_{*_1} + \frac{\Delta t}{2}\left(\frac{1}{Re}\left[\begin{array}{c} \left(1+\frac{\eta_1}{2}\right)\left(\sum_{j=1}^{N} b^*{}_{ij} M_{*_1}(y_j,t)\right) \\ -\eta_1\left(2M_{*_1}(y_j,t) + \sum_{j=1}^{N} a^*{}_{ij} u_{m_1}(y_j,t)\right) \end{array} \right] \right), \tag{5.47}$$

$$T_{m_2} = T_{m_1} + \frac{\Delta t}{2}\left(\frac{Ec}{Re}\left[\begin{array}{c} \frac{1}{Pr.Ec}\left(\sum_{j=1}^{N} b^*{}_{ij} T_{m_1}(y_j,t)\right) + \left(\sum_{j=1}^{N} a^*{}_{ij} u_{m_1}(y_j,t)\right)^2 \\ +\eta_1\left(2M_{*_1}(y_j,t) + \sum_{j=1}^{N} a^*{}_{ij} u_{m_1}(y_j,t)\right)^2 + \\ \delta_m\left(\sum_{j=1}^{N} a^*{}_{ij} M_{*_1}(y_j,t)\right)^2 + \frac{Ha^2(1+Bi.Be)}{(1+Bi.Be)^2+Be^2} u_{m_1}(y_j,t)^2 \end{array} \right] \right), \tag{5.48}$$

Zone-II *(0 ≤ y ≤ k)* (Micropolar dusty fluid):

$$u_{md_2} = u_{md_1} + \frac{\Delta t}{2}\left(Ge(t) + \frac{r_1}{r_2.Re}\begin{bmatrix} \eta_2 \sum_{j=1}^{N} a^*{}_{ij} M_{d_1}(y_j,t) + \\ (1+\eta_2)\left(\sum_{j=1}^{N} b^*{}_{ij} u_{md_1}(y_j,t)\right) \\ -\frac{Ha^2(1+Bi.Be)}{r_1((1+Bi.Be)^2+Be^2)} u_{md_1}(y_j,t) \\ -\ R\left(u_{md_1}(y_j,t) - u_{p_1}(y_j,t)\right) \end{bmatrix}\right), \tag{5.49}$$

$$u_{p_2} = u_{p_1} + \frac{\Delta t}{2}\left(\frac{R.r_1.r_3}{r_2.Re}\left[u_{md_1}(y_j,t) - u_{p_1}(y_j,t)\right]\right), \tag{5.50}$$

$$M_{d_2} = M_{d_1} + \frac{\Delta t}{2}\left(\frac{r_1}{r_2.Re}\begin{bmatrix} \left(1+\frac{\eta_2}{2}\right)\left(\sum_{j=1}^{N} b^*{}_{ij} M_{d_1}(y_j,t)\right) \\ -\eta_2\left(2M_{d_1}(y_j,t) + \sum_{j=1}^{N} a^*{}_{ij} u_{md_1}(y_j,t)\right) \end{bmatrix}\right), \tag{5.51}$$

$$T_{md_2} = T_{md_1} + \frac{\Delta t}{2}.\left(\frac{Ec.r_1}{Re.r_2.C_r}\begin{bmatrix} \frac{Kr}{Pr.Ec.r_1}\left(\sum_{j=1}^{N} b^*{}_{ij} T_{md_1}(y_j,t)\right) \\ +\left(\sum_{j=1}^{N} a^*{}_{ij} u_{md_1}(y_j,t)\right)^2 \\ +\eta_2\left(2M_{d_1}(y_j,t) + \sum_{j=1}^{N} a^*{}_{ij} u_{md_1}(y_j,t)\right)^2 + \\ \delta_{md}\left(\sum_{j=1}^{N} a^*{}_{ij} M_{d_1}(y_j,t)\right)^2 \\ +\frac{Ha^2(1+Bi.Be)}{r_1((1+Bi.Be)^2+Be^2)} u_{md_1}(y_j,t)^2 \\ +\frac{2}{3}\frac{R.K_r}{Pr.Ec.r_1}\left(T_{p_1}(y_j,t) - T_{md_1}(y_j,t)\right) + \\ R\left(u_{md_1}(y_j,t) - u_{p_1}(y_j,t)\right)^2 \end{bmatrix}\right), \tag{5.52}$$

$$T_{p_2} = T_{p_1} + \frac{\Delta t}{2}\left(\frac{2}{3}\frac{R*k_r*C_r*r_3}{C_{Pr}*r_1*Pr}\frac{\left(T_{md_1}(y_j,t) - T_{p_1}(y_j,t)\right)}{Re}\right). \tag{5.53}$$

In the second step of the method, the initial, interfacial, and boundary condition equations (5.12) - (5.15) are considered favourably.

In the third step for *i=1,2,3…,N*.

Zone-I ($-k \le y \le 0$) (Micropolar fluid):

$$u_{m_3} = \frac{2.u_{m_0}}{3} + \frac{u_{m_2}}{3} + \frac{\Delta t}{6}\left(Ge(t) + \frac{1}{Re}.\begin{bmatrix} \eta_1 \sum_{j=1}^{N} a^*{}_{ij} M_{*_2}(y_j,t) + \\ (1+\eta_1)\left(\sum_{j=1}^{N} b^*{}_{ij} u_{m_2}(y_j,t)\right) \\ -\frac{Ha^2(1+Bi.Be)}{(1+Bi.Be)^2+Be^2} u_{m_2}(y_j,t) \end{bmatrix}\right), \tag{5.54}$$

$$M_{*_3} = \frac{2.M_{*_0}}{3} + \frac{M_{*_2}}{3} + \frac{\Delta t}{6}\left(\frac{1}{Re}\begin{bmatrix}\left(1+\frac{\eta_1}{2}\right)\left(\sum_{j=1}^{N} b^*{}_{ij} M_{*_2}(y_j,t)\right) \\ -\eta_1\left(2M_{*_2}(y_j,t) + \sum_{j=1}^{N} a^*{}_{ij} u_{*_2}(y_j,t)\right)\end{bmatrix}\right), \quad (5.55)$$

$$T_{m_3} = \frac{2.T_{m_0}}{3} + \frac{T_{m_2}}{3} + \frac{\Delta t}{6}\left(\frac{Ec}{Re}\begin{bmatrix}\frac{1}{Pr.Ec}\left(\sum_{j=1}^{N} b^*{}_{ij} T_{m_2}(y_j,t)\right) \\ +\left(\sum_{j=1}^{N} a^*{}_{ij} u_{m_2}(y_j,t)\right)^2 + \\ \eta_1\left(2M_{m_2}(y_j,t) + \sum_{j=1}^{N} a^*{}_{ij} u_{m_2}(y_j,t)\right)^2 \\ +\delta_m\left(\sum_{j=1}^{N} a^*{}_{ij} M_{*_2}(y_j,t)\right)^2 + \\ \frac{Ha^2(1+Bi.Be)}{(1+Bi.Be)^2+Be^2} u_{m_2}(y_j,t)^{\,2}\end{bmatrix}\right), \quad (5.56)$$

Zone-II *(0 ≤ y ≤ k)* (Micropolar dusty fluid):

$$u_{md_3} = \frac{2.u_{md_0}}{3} + \frac{u_{md_2}}{3} + \frac{\Delta t}{6}\left(Ge(t) + \frac{r_1}{r_2.Re}\begin{bmatrix}\eta_2 \sum_{j=1}^{N} a^*{}_{ij} M_{d_2}(y_j,t) + \\ (1+\eta_2)\left(\sum_{j=1}^{N} b^*{}_{ij} u_{md_2}(y_j,t)\right) \\ -\frac{Ha^2(1+Bi.Be)}{r_1((1+Bi.Be)^2+Be^2)} u_{md_2}(y_j,t) \\ -\ R\left(u_{md_2}(y_j,t) - u_{p_2}(y_j,t)\right)\end{bmatrix}\right), \quad (5.57)$$

$$u_{p_3} = \frac{2.u_{p_0}}{3} + \frac{u_{p_2}}{3} + \frac{\Delta t}{6}\left(\frac{R.r_1.r_3}{r_2.Re}\left[u_{md_2}(y_j,t) - u_{p_2}(y_j,t)\right]\right), \quad (5.58)$$

$$M_{d_3} = \frac{2.M_{d_0}}{3} + \frac{M_{d_2}}{3} + \frac{\Delta t}{6}\left(\frac{r_1}{r_2.Re}\begin{bmatrix}\left(1+\frac{\eta_2}{2}\right)\left(\sum_{j=1}^{N} b^*{}_{ij} M_{d_2}(y_j,t)\right) \\ -\eta_2\begin{pmatrix}2M_{d_2}(y_j,t) \\ +\sum_{j=1}^{N} a^*{}_{ij} u_{md_2}(y_j,t)\end{pmatrix}\end{bmatrix}\right), \quad (5.59)$$

$$T_{md_3} = \frac{2.T_{md_0}}{3} + \frac{T_{md_2}}{3} +$$

$$\frac{\Delta t}{6}\left(\frac{Ec.r_1}{Re.r_2.C_r}\begin{bmatrix}\frac{Kr}{Pr.Ec.r_1}\left(\sum_{j=1}^{N} b^*{}_{ij}T_{md_2}(y_j,t)\right)\\ +\left(\sum_{j=1}^{N} a^*{}_{ij}u_{md_2}(y_j,t)\right)^2+\\ \eta_2\left(2M_{d_2}(y_j,t)+\sum_{j=1}^{N} a^*{}_{ij}u_{md_2}(y_j,t)\right)^2\\ +\delta_{md}\left(\sum_{j=1}^{N} a^*{}_{ij}M_{d_2}(y_j,t)\right)^2\\ +\frac{Ha^2(1+Bi.Be)}{r_1((1+Bi.Be)^2+Be^2)}u_{md_2}(y_j,t)^2\\ +\frac{2}{3}\frac{R.K_r}{Pr.Ec.r_1}\left(T_{p_2}(y_j,t)-T_{md_2}(y_j,t)\right)+\\ R\left(u_{md_2}(y_j,t)-u_{p_2}(y_j,t)\right)^2\end{bmatrix}\right), \quad (5.60)$$

$$T_{p_3}=\frac{2.T_{p_0}}{3}+\frac{T_{p_2}}{3}+\frac{\Delta t}{6}.\left(\frac{2}{3}\frac{R*k_r*C_r*r_3}{C_{Pr}*r_1*Pr}\frac{\left(T_{md_1}(y_j,t)-T_{p_1}(y_j,t)\right)}{Re}\right). \quad (5.61)$$

In the third step of the method, the initial, interfacial, and boundary condition equations (5.12) - (5.15) are considered favourably.

At the fourth step for *i=1,2,3…, N*.

Zone-I ($-k \le y \le 0$) (Micropolar fluid):

$$u_{m_4}=u_{m_3}+\frac{\Delta t}{2}\left(Ge(t)+\frac{1}{Re}.\begin{bmatrix}\eta_1\sum_{j=1}^{N} a^*{}_{ij}M_{m_3}(y_j,t)+\\ (1+\eta_1)\left(\sum_{j=1}^{N} b^*{}_{ij}u_{m_3}(y_j,t)\right)\\ -\frac{Ha^2(1+Bi.Be)}{(1+Bi.Be)^2+Be^2}u_{m_3}(y_j,t)\end{bmatrix}\right), \quad (5.62)$$

$$M_{*_4}=M_{*_3}+\frac{\Delta t}{2}\left(\frac{1}{Re}\begin{bmatrix}\left(1+\frac{\eta_1}{2}\right)\left(\sum_{j=1}^{N} b^*{}_{ij}M_{*_3}(y_j,t)\right)\\ -\eta_1\left(2M_{*_3}(y_j,t)+\sum_{j=1}^{N} a^*{}_{ij}u_{m_3}(y_j,t)\right)\end{bmatrix}\right), \quad (5.63)$$

$$T_{m_4}=T_{m_3}+\frac{\Delta t}{2}\left(\frac{Ec}{Re}\begin{bmatrix}\frac{1}{Pr.Ec}\left(\sum_{j=1}^{N} b^*{}_{ij}T_{m_3}(y_j,t)\right)+\left(\sum_{j=1}^{N} a^*{}_{ij}u_{m_3}(y_j,t)\right)^2\\ +\eta_1\left(2M_{m_3}(y_j,t)+\sum_{j=1}^{N} a^*{}_{ij}u_{m_3}(y_j,t)\right)^2\\ +\delta_m\left(\sum_{j=1}^{N} a^*{}_{ij}M_{m_3}(y_j,t)\right)^2+\\ \frac{Ha^2(1+Bi.Be)}{(1+Bi.Be)^2+Be^2}u_{m_3}(y_j,t)^2\end{bmatrix}\right), \quad (5.64)$$

Zone-II *(0 ≤ y ≤ k)* (Micropolar dusty fluid):

$$u_{md_4} = u_{md_3} + \frac{\Delta t}{2}\left(Ge(t) + \frac{r_1}{r_2.Re}\begin{bmatrix} \eta_2 \sum_{j=1}^{N} a^*{}_{ij} M_{d_3}(y_j,t) + \\ (1+\eta_2)\left(\sum_{j=1}^{N} b^*{}_{ij} u_{md_3}(y_j,t)\right) \\ -\frac{Ha^2(1+Bi.Be)}{r_1((1+Bi.Be)^2+Be^2)} u_{md_3}(y_j,t) \\ -\ R\left(u_{md_3}(y_j,t) - u_{p_3}(y_j,t)\right) \end{bmatrix}\right), \tag{5.65}$$

$$u_{p_4} = u_{p_3} + \frac{\Delta t}{2}\left(\frac{R.r_1.r_3}{r_2.Re}\left[u_{md_3}(y_j,t) - u_{p_3}(y_j,t)\right]\right), \tag{5.66}$$

$$M_{md_4} = M_{md_3} + \frac{\Delta t}{2}\left(\frac{r_1}{r_2.Re}\begin{bmatrix} \left(1+\frac{\eta_2}{2}\right)\left(\sum_{j=1}^{N} b^*{}_{ij} M_{d_3}(y_j,t)\right) \\ -\eta_2\left(2M_{d_3}(y_j,t) + \sum_{j=1}^{N} a^*{}_{ij} u_{md_3}(y_j,t)\right) \end{bmatrix}\right), \tag{5.67}$$

$$T_{md_4} = T_{md_3} + \frac{\Delta t}{2}.\left(\frac{Ec.r_1}{Re.r_2.C_r}\begin{bmatrix} \frac{Kr}{Pr.Ec.r_1}\left(\sum_{j=1}^{N} b^*{}_{ij} T_{md_3}(y_j,t)\right) \\ +\left(\sum_{j=1}^{N} a^*{}_{ij} u_{md_3}(y_j,t)\right)^2 \\ +\eta_2\begin{pmatrix} 2M_{d_3}(y_j,t) + \\ \sum_{j=1}^{N} a^*{}_{ij} u_{md_3}(y_j,t) \end{pmatrix}^2 + \\ \delta_{md}\left(\sum_{j=1}^{N} a^*{}_{ij} M_{md_3}(y_j,t)\right)^2 \\ +\frac{Ha^2(1+Bi.Be)}{r_1((1+Bi.Be)^2+Be^2)} u_{md_3}(y_j,t)^2 \\ +\frac{2}{3}\frac{R.K_r}{Pr.Ec.r_1}\left(T_{p_3}(y_j,t) - T_{md_3}(y_j,t)\right) + \\ R\left(u_{md_3}(y_j,t) - u_{p_3}(y_j,t)\right)^2 \end{bmatrix}\right), \tag{5.68}$$

$$T_{p_4} = T_{p_3} + \frac{\Delta t}{2}\left(\frac{2}{3}\frac{R*k_r*C_r*r_3}{C_{Pr}*r_1*Pr}\frac{\left(T_{md_3}(y_j,t) - T_{p_3}(y_j,t)\right)}{Re}\right). \tag{5.69}$$

At the fourth step of the method, the initial, interfacial, and boundary condition equations (5.12) - (5.15) are considered favourably.

Hence the fluid (linear) velocity and angular velocity (Eringen microrotation) and temperatures profiles, i. e. u_m, M_*, T_m, of micropolar fluid in zone-I, and also the fluid velocity (linear) and particle velocity components, angular velocity, and temperature profiles. u_{md}, u_p $M_d, T_{md}, T_p$for micropolar dusty fluid in zone-II can be numerically obtained at the fourth step of MCB-DQM for the genialized Couette flow and plane Couette flow.

5.5 Result and Analysis of Generalized Couette flow

The time-dependent unidirectional generalized hydromagnetic Couette flow of two immiscible, electro-conductive, dissipative, micropolar, and micropolar-dusty fluids with heat transfer has been examined theoretically. The two-fluid flow coupled problem equations (5.17) - (5.24) in the corresponding regions with stable interface have been numerically solved by modified cubic B-spline differential quadrature method, and velocity, temperature profiles of fluids, and dust particles have been obtained. The analysis of skin friction coefficient and Nusselt number at both upper and lower boundaries of the duct have also been computed. The results are discussed in due course with the following prescribed values of all parameters (unless otherwise indicated): Ge=5, $t = 0.5, \eta_1 = 0.5, \eta_2 = 0.5, Ha^2 = 2, Be = 2, Bi = 2, Re$=2, R=2, r_1=0.5, r_2=0.5, r_3=100, C_r=0.5, Ec=0.5, $Kr = 0.5, Pr = 2, \delta_1 = 2, \delta_2 = 2, Cr_r$=0.5. This data represents real MHD generator duct flows and is consistent with relevant publications – see [35-38]. The simulation results are verified for the velocity profile by comparing them with the limiting case (the non-MHD, non-dusty, single Newtonian Couette flow for which $Ha^2 = 0, Be = 0, Bi = 0$, R=0, $\eta_1 = 0, \eta_2 = 0$, r_1=1, r_2=1 Ge=0). The limiting case numerical result and the exact solution shows strong agreement, as seen in Figure 5.2, and the parabolic laminar flow profile is captured across the channel span.

5.5.1 Analysis of velocity profiles for genialized Couette flow

Figure 5.3-Figure 5.10 represents the effect of various fluid parameters on fluids and particle velocity, and it is cited in Figure 5.3, Figure 5.4, and Figure 5.10 that both fluid and particle velocity increase with time, Hall parameter ($Be = \sigma\beta B_0$) and Ion-slip parameter (Bi). The magnetic resistive force is decreased as Be and Bi are increased, creating an acceleration in the main flow, which increases fluid and particle-phase velocities.

The Reynolds number $Re = \frac{\rho_m U_0 h}{\mu_m}$ is the non-dimensional parameter which describes the ratio of inertial to viscous forces. Higher Re in the two-fluid medium indicates lower

viscous forces. The viscous forces decrease as the Reynolds number increases, resulting in a growing pattern in fluid velocities (See Figure 5.5).

Figure 5.6 and Figure 5.7 show that increasing the micropolar parameters $\eta_1 = \frac{\kappa_m}{\mu_m}$ of micropolar fluid and $\eta_2 = \frac{\kappa_{md}}{\mu_{md}}$ of micropolar-dusty fluid (which increase the vortex viscosities $\kappa_m$and κ_{md}) elevate the magnitudes of velocity profiles of the fluids and particle-phase increase in the respective regions. Therefore, increasing the spin of the microelements produces flow acceleration. Because η_1 is a characteristic of micropolar fluid alone, it has a weaker effect on micropolar-dusty fluid as well; similarly, $\eta_2$is a feature of micropolar-dusty fluid alone and therefore has a less dramatic impact on micropolar fluid also. This happens due to the continuous coupling across the interface.

The Hartmann number squared, $Ha^2 = \frac{\sigma B_0^2 k^2}{\mu_m}$ expresses the square of the ratio of the Lorentz magnetic drag force to the viscous hydrodynamic force. When Ha^2 is unity, these two forces are balanced. When $Ha > 1$, magnetic drag exceeds viscous force and vice versa for $Ha < 1$. The influence of the transverse magnetic field on the hydromagnetic flow and thermal characteristics can be analyzed by changing this number. According to Figure 5.8, increasing Ha^2 significantly elevates the magnetic retarding force and results in a depletion in the velocity fields in both regions. This may be attributed to the effect of an applied transverse magnetic field on both plates, which causes resistance to fluid movement through the Lorentz force, which substantially damps the flow.

Figure 5.9 indicates that only the dust particle velocity increases with an enhancement of particle concentration parameter R, and no variation in fluid velocities is observed.

5.5.2 Analysis of microrotation profiles for genialized Couette flow

Figure 5.11-Figure 5.17illustrates the effects of various fluid parameters on microrotations (angular velocities). It is observed from Figure 5.11 that the microrotation increases with time and attains a steady state after a significant time has elapsed. According to Figure 5.12, increasing Ha^2 manifests in a boost in microrotation

in the lower region fluid; however, this response changes to a decrease in the upper region. Figure 5.14 shows that increasing micropolar parameters, η_1 of the micropolar fluid, decreases the microrotation profiles in both regions. However, a less marked decline is observed in the micropolar fluid region as compared to the micropolar dusty fluid region. Figure 5.13, Figure 5.17, and Figure 5.16 show that as the micropolar parameter of the micropolar dusty fluid η_2, Hall effect (Be) and Ion-slip parameter (Bi) increase, microrotation consistently decreases in the lower region fluid (reduced spin of microelements), and the response is modified to an increasing nature in the upper region (i.e., a faster spin of microelements). Figure 5.15 indicates that the microrotation profiles in both regions noticeably decrease with an increment in Reynolds number Re.

5.5.3 Analysis of temperature profiles for genialized Couette flow

The nonlinear and flow-dependent viscous dissipation terms are also included in the numerical computations. Figure 5.18-Figure 5.27exhibit the effect of various fluid parameters on temperature profiles of micropolar and micropolar dusty fluids. It is evident from Figure 5.18 that the temperature profiles of both region fluids increase with progression in time. Elevation in the ratio of viscosity r_1 leads to an increase in the temperatures in both regions (Figure 5.19). According to Figure 5.20, increasing Ha^2 (i.e., a boost in magnetic field strength) amplifies the impedance to the flow and increases temperatures. Figure 5.21 shows that increasing Reynolds number Re reduces the viscous force hence temperature profiles of both fluids are increased. Figure 5.22 visualizes the effect of the Eckert number ***(Ec)*** on temperature evolution in the channelling regime. *Ec* provides a measure of kinetic energy dissipated via internal friction to the enthalpy difference across the channel. It is observed that the temperature of fluids and particles increases with $\boldsymbol{Ec}$ since greater mechanical energy is converted to heat which energizes the regime. It is noted from Figure 5.23, that increasing the Prandtl number $(\boldsymbol{Pr})$ i.e., ratio of viscous diffusivity to thermal diffusivity enhances the temperature profiles of both fluids and particles. It can be seen from Figure 5.27,

Figure 5.25*,* and Figure 5.24that the temperature profiles of fluids and particles in both regions rise with an increment in the micropolar parameter of micropolar dusty fluid, η_2, Hall parameter (Be) and Ion-slip parameter (Bi). The temperature in both region fluids decreases with greater values of density ratio r_1 and micropolar parameter of the lower region fluid, η_1 (see Figure 5.26 and Figure 5.28).

5.5.4 Analysis of skin-friction coefficients for genialized Couette flow

As the immiscible fluids flow internally over the boundaries of the channel, the maximum resistance to the flow is experienced. Since the only laminar flow is considered, the flow will not become chaotic at some point in the flow path, although Hartmann-Stokes layers will develop in the presence of a magnetic field. Frictional forces are applied to the boundary surface impeding flow- this is known as skin friction drag. Table 5.1 shows that skin friction increases with time *(t)*, Reynolds number (Re), Hall parameter (Be) and Ion-slip parameter (Bi) at the lower wall of the channel i.e., the flow is accelerated at the lower wall. However, a slight decrement is induced with an increment in the micropolar parameter of the lower zone fluid η_1, the micropolar parameter of the upper zone fluid η_2 and Hartmann number, Ha^2 but remains constant with increasing values of particle concertation parameter R. At the upper wall, a decrease in skin friction co-efficient is induced with rising values of time *(t)*, Reynolds number Re, Hall parameter (Be), and Ion-slip parameter (Bi) .When η_1 , η_2, and Ha^2 are increased, the skin co-efficient improves slightly but remains invariant with modification in particle concentration parameter *R*. It is important to note that modern MHD generators are increasingly exploiting stronger magnetic fields with the advent of more powerful magnets. This amplifies the contribution of Hall currents and ion slip-neglecting these effects, therefore, leads to under-prediction in the skin friction coefficient at the lower wall and over-prediction at the upper wall. The Hall and ion slip effects will also modify the structure of the Hartmann-Stokes layers at the boundaries. The inclusion of Hall and ion slip current effects, therefore, provides for a more realistic appraisal of thermofluid characteristics in practical applications since the

change in the magnitude and direction of the current density leads to a significant modification in Lorentz electromagnetic force, as noted by Kayukawa [247].

5.5.5 Analysis of the Nusselt numbers for genialized Couette flow

The Nusselt number, which is equal to the dimensionless temperature gradient at the wall, also quantifies the ratio of convection heat transfer to conductive heat transfer at the surface. Table 5.2 shows that the Nusselt number increases at the upper wall and decreases at the lower wall with time *(t),* Reynolds number (Re), Eckert number *(Ec),* Prandtl number (Pr), Hall parameter (Be), Ion-slip parameter (Bi), the micropolar parameter of micropolar dusty fluid (η_2) and micropolar parameter of lower region fluid (η_1). At the lower plate, the Nusselt number increases, whereas it exhibits a decrement at the upper wall with an increment in Hartmann number squared, Ha^2. Nusselt number however remains constant at both channel walls with particle concertation parameter (R). The Nusselt number at the upper wall shows a decreasing nature with an increase in the thermal conductivity ratio k_r whereas it does not change at the lower wall.

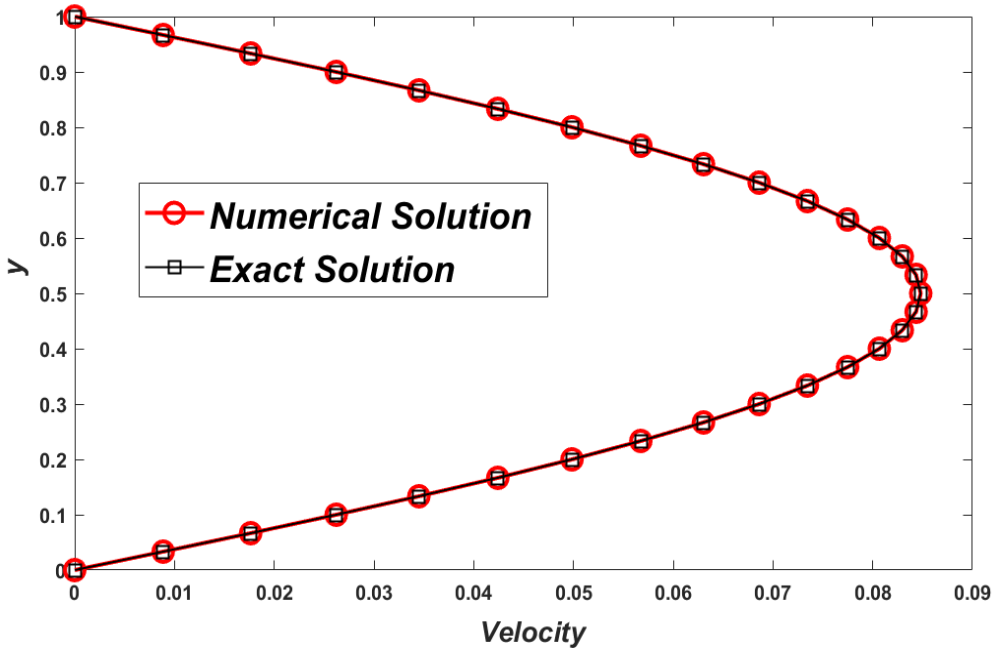

Figure 5.2: Numerical vs. exact solution

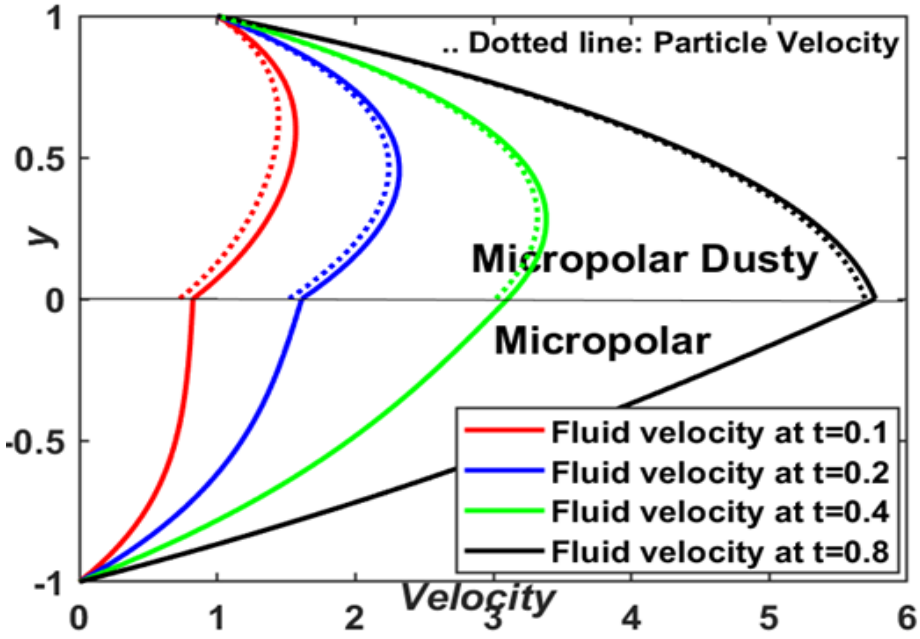

Figure 5.3: Generalized Couette flow velocity with time

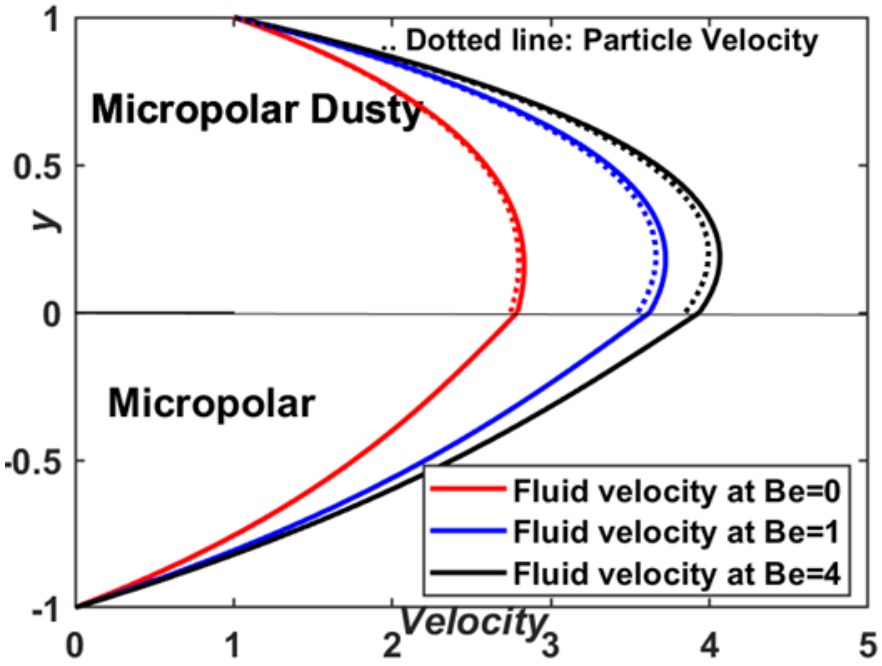

Figure 5.4: Generalized Couette flow velocity with Hall parameter

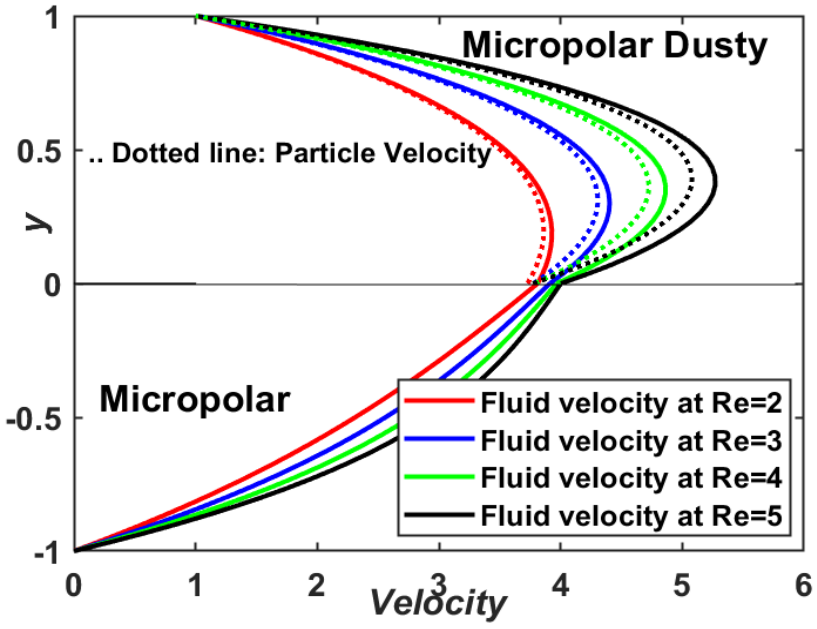

Figure 5.5: Generalized Couette flow velocity with Reynolds number

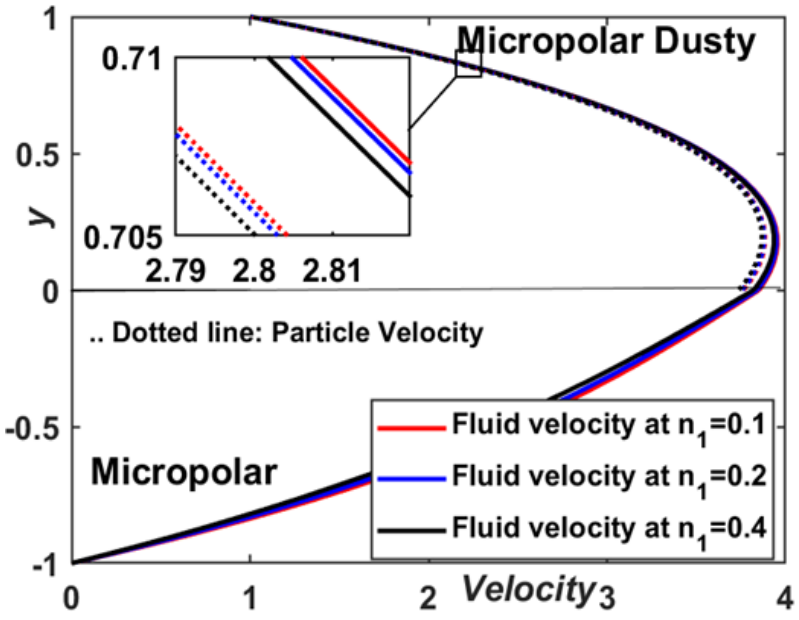

Figure 5.6: Generalized Couette flow velocity with a micropolar parameter of lower fluid

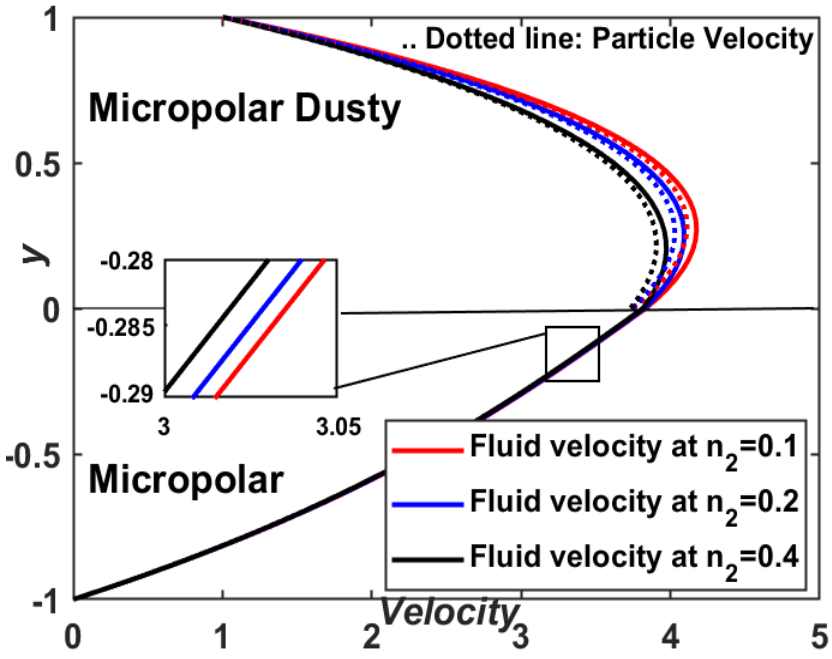

Figure 5.7: Generalized Couette flow velocity with a micropolar parameter of the upper fluid

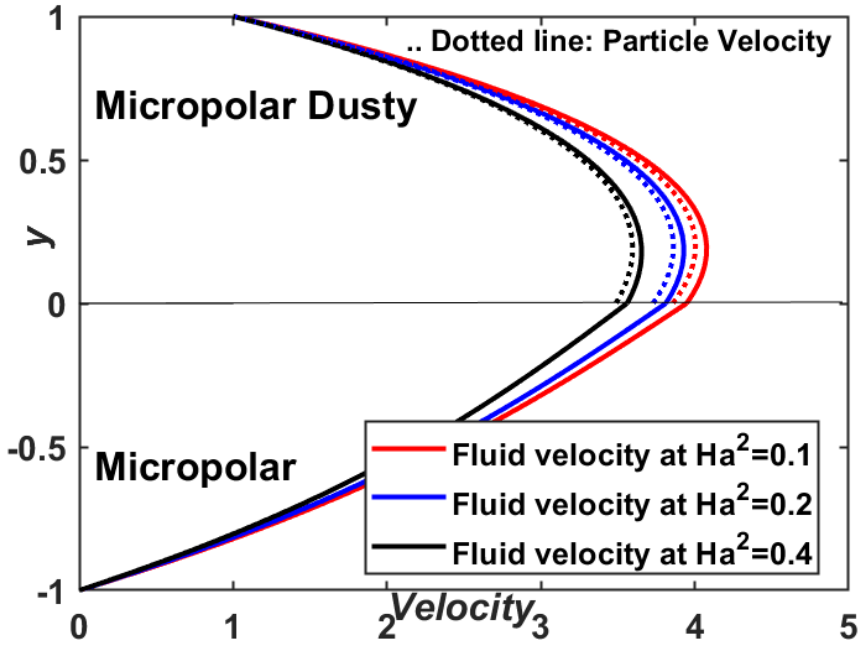

Figure 5.8: Generalized Couette flow velocity with Hartmann number

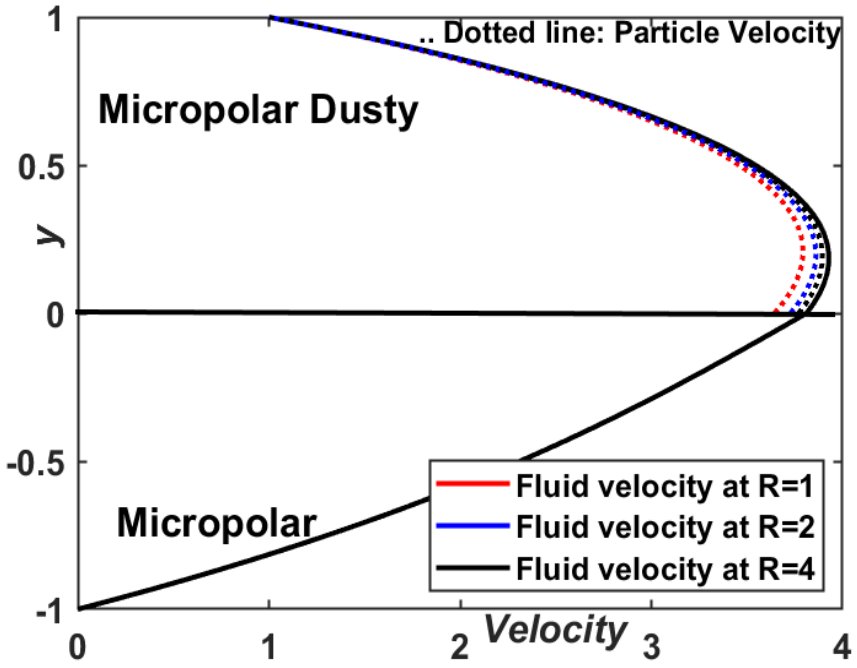

Figure 5.9: Generalized Couette flow velocity with particle concertation parameter

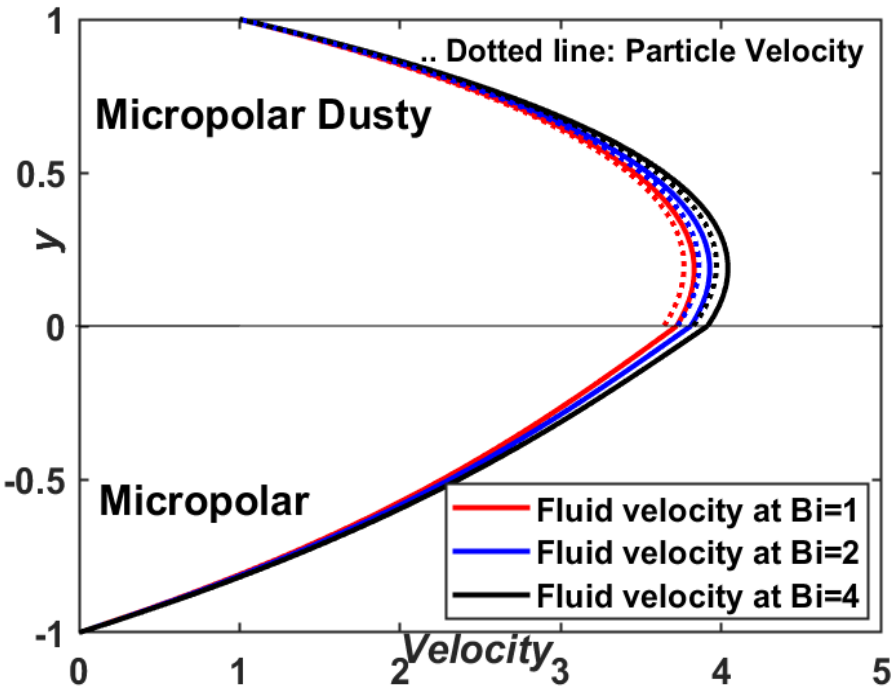

Figure 5.10: Generalized Couette flow velocity with Ion-slip parameter

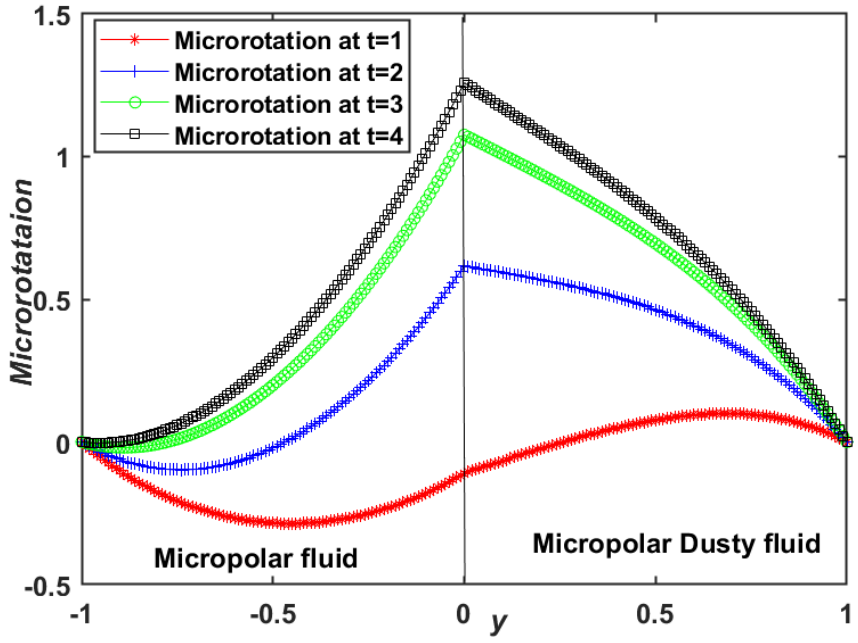

Figure 5.11: Generalized Couette flow microrotation with time

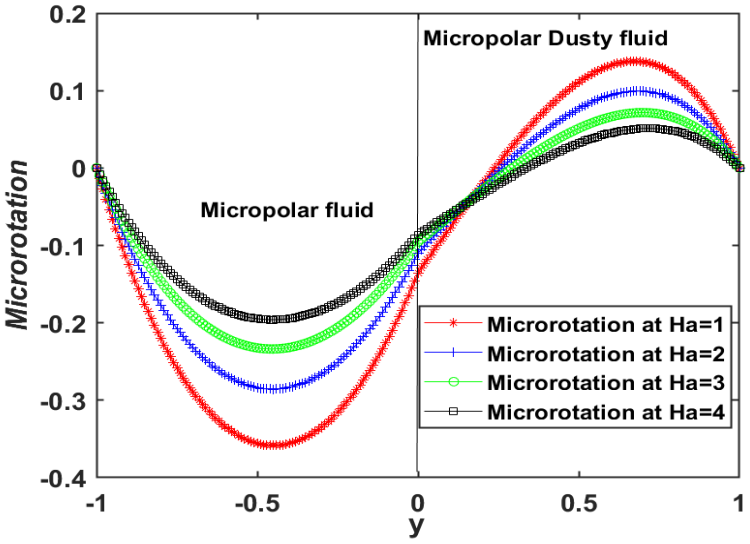

Figure 5.12: Generalized Couette flow microrotation with Hartmann parameter

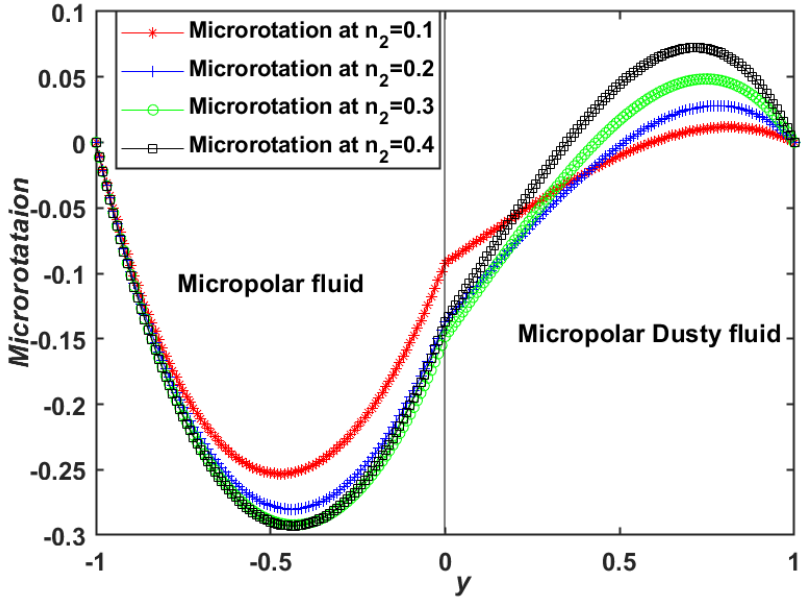

Figure 5.13: Generalized Couette flow microrotation with a micropolar parameter of the upper fluid

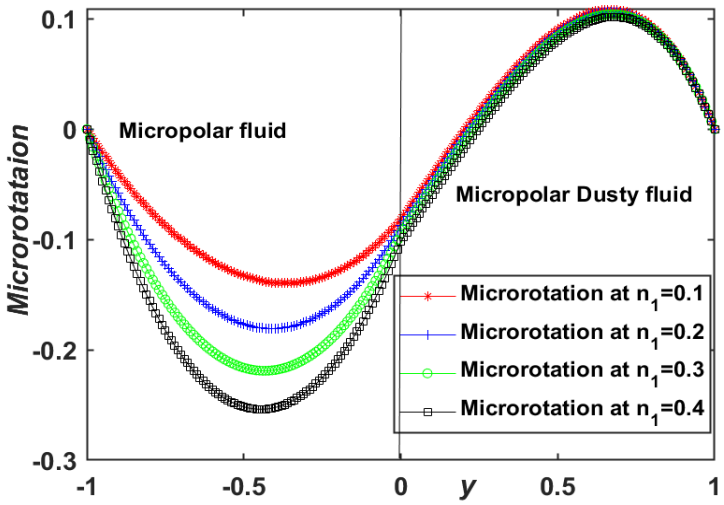

Figure 5.14: Generalized Couette flow microrotation with a micropolar parameter of lower fluid

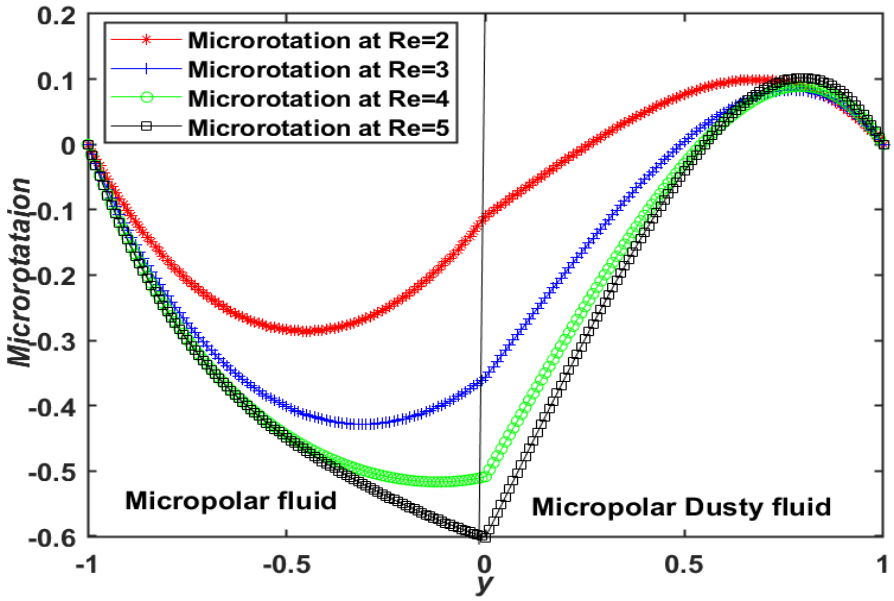

Figure 5.15: Generalized Couette flow microrotation with Reynolds number

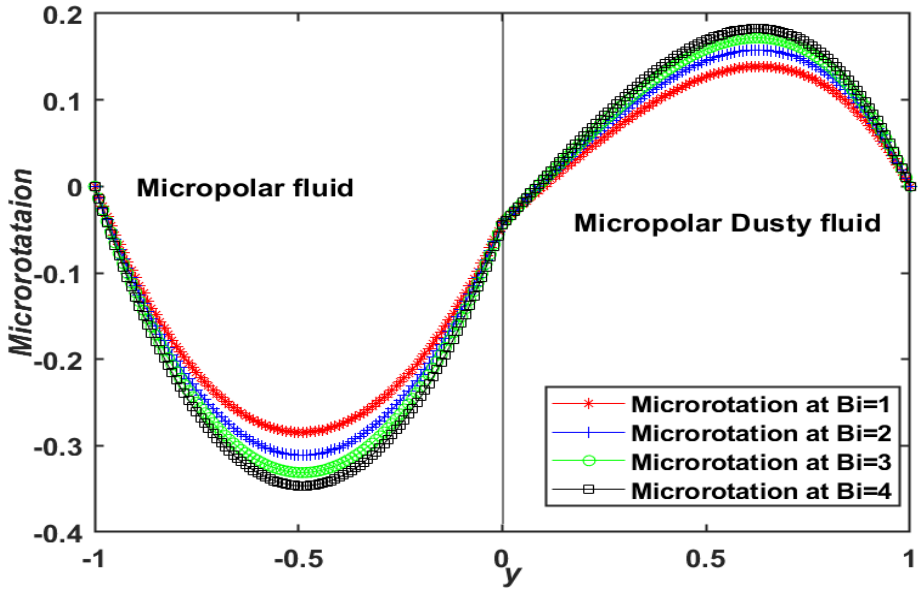

Figure 5.16: Generalized Couette flow microrotation with Ion-slip parameter

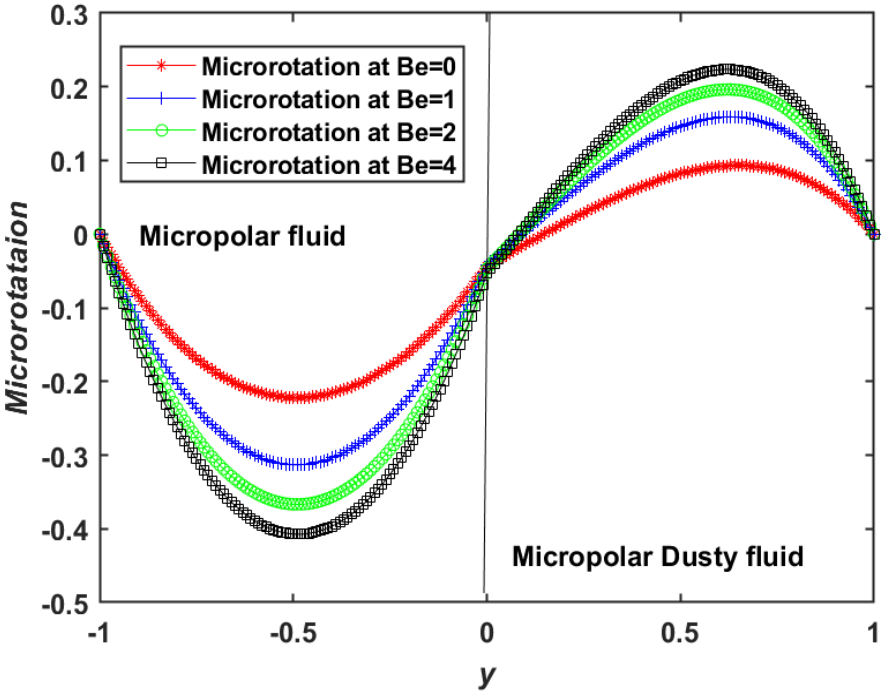

Figure 5.17: Generalized Couette flow microrotation with Hall parameter

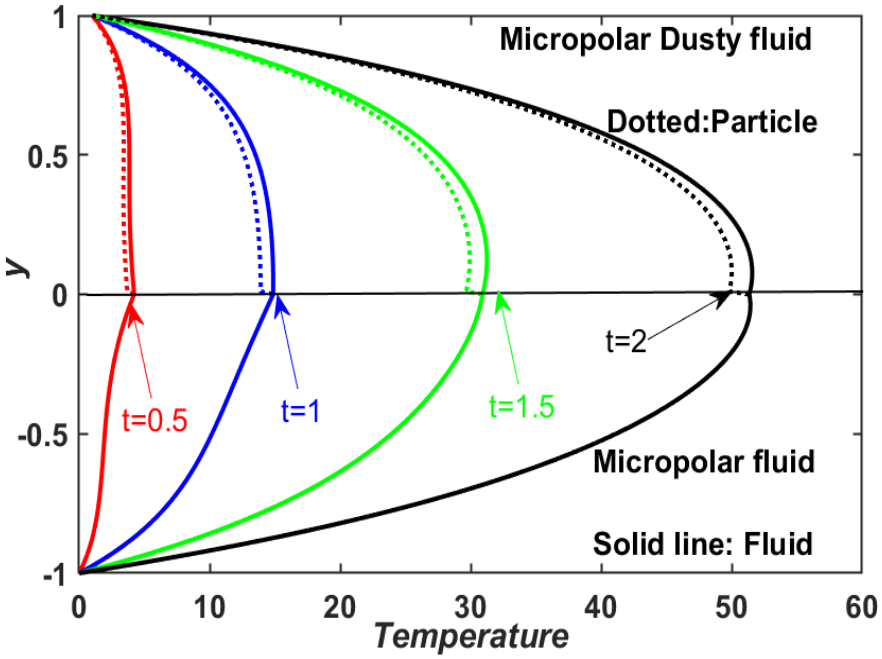

Figure 5.18: Generalized Couette flow temperature with time

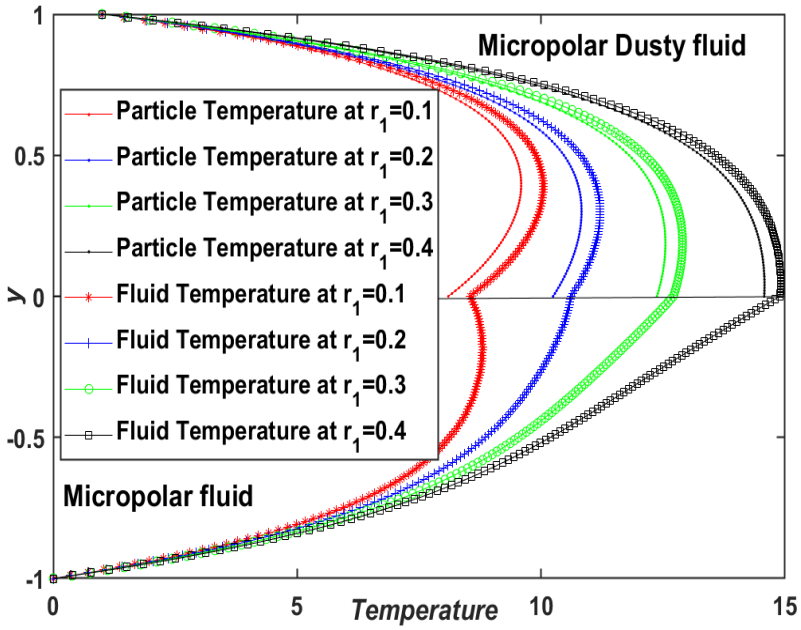

Figure 5.19: Generalized Couette flow temperature with a ratio of viscosity

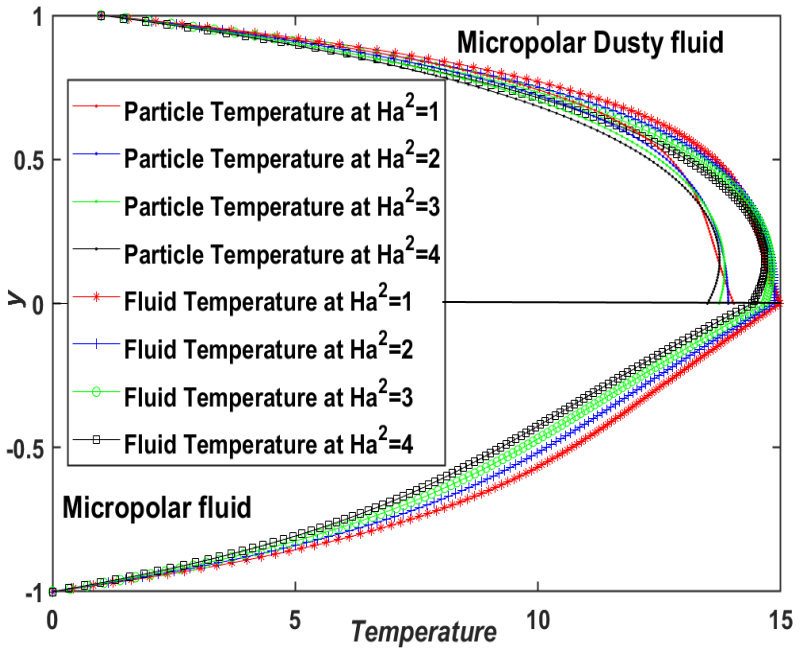

Figure 5.20: Generalized Couette flow temperature with Hartmann number

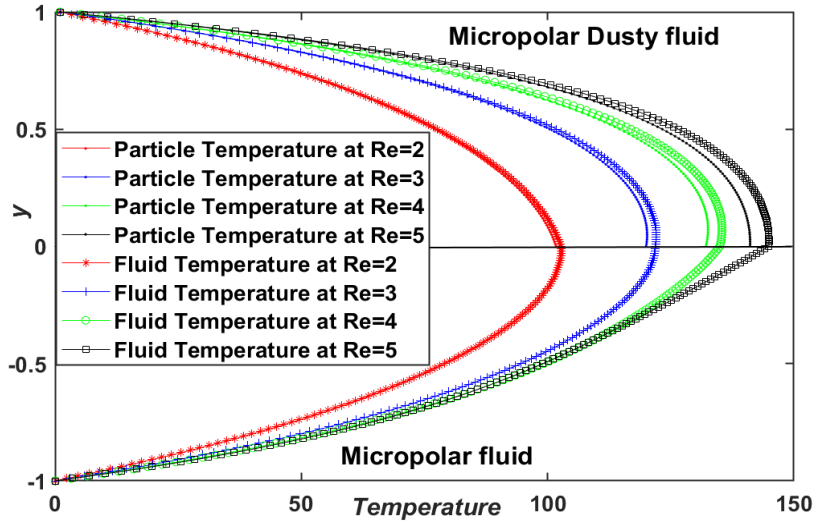

Figure 5.21: Generalized Couette flow temperature with Reynolds number

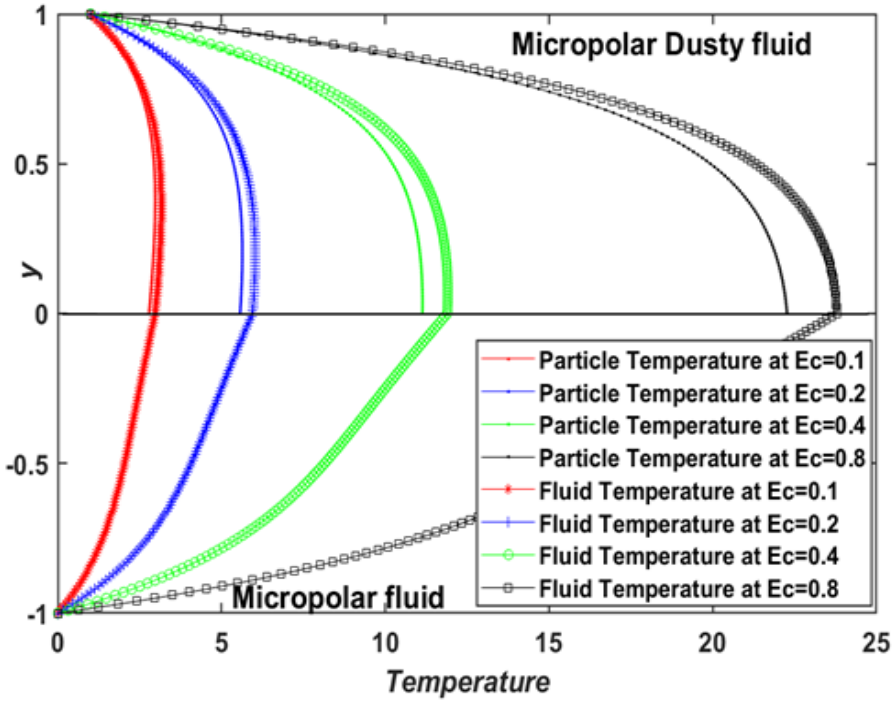

Figure 5.22: Generalized Couette flow temperature Eckert number

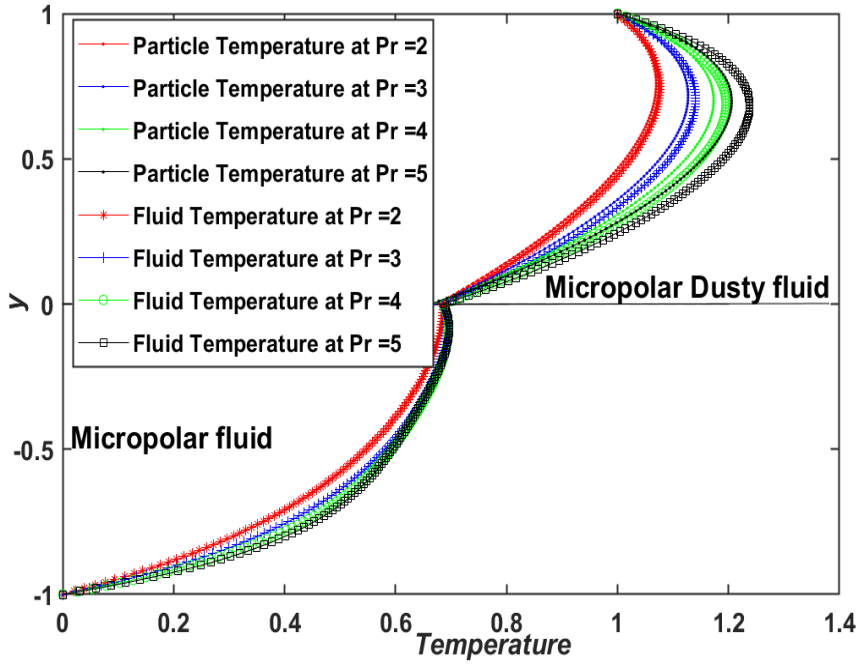

Figure 5.23: Generalized Couette flow temperature with Prandtl number

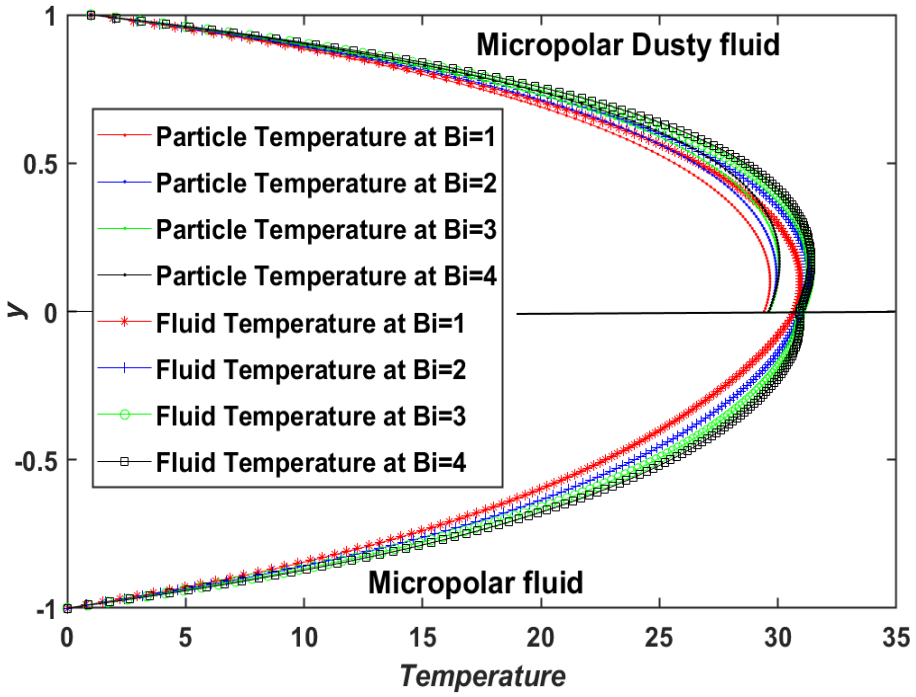

Figure 5.24: Generalized Couette flow temperature with Ion-slip parameter

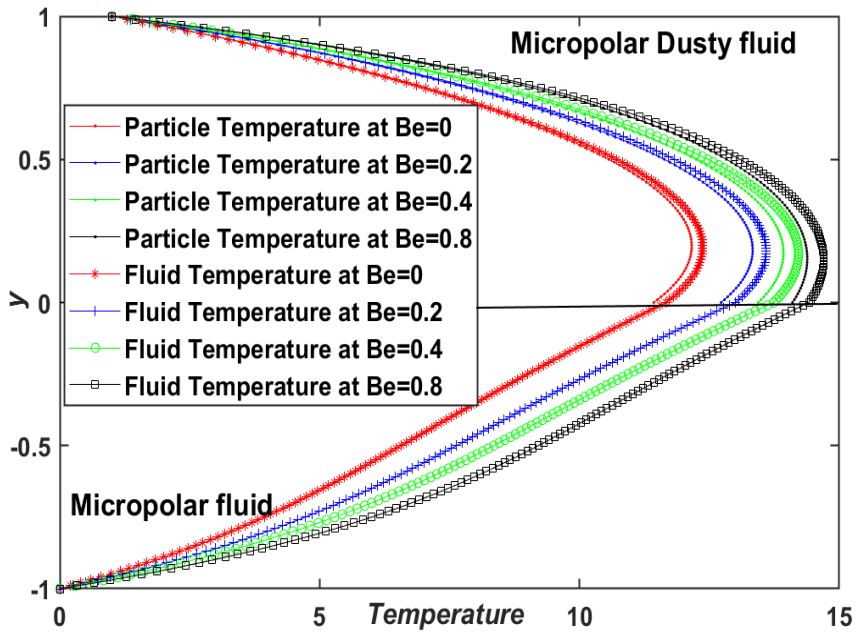

Figure 5.25: Generalized Couette flow temperature profiles with Hall parameter

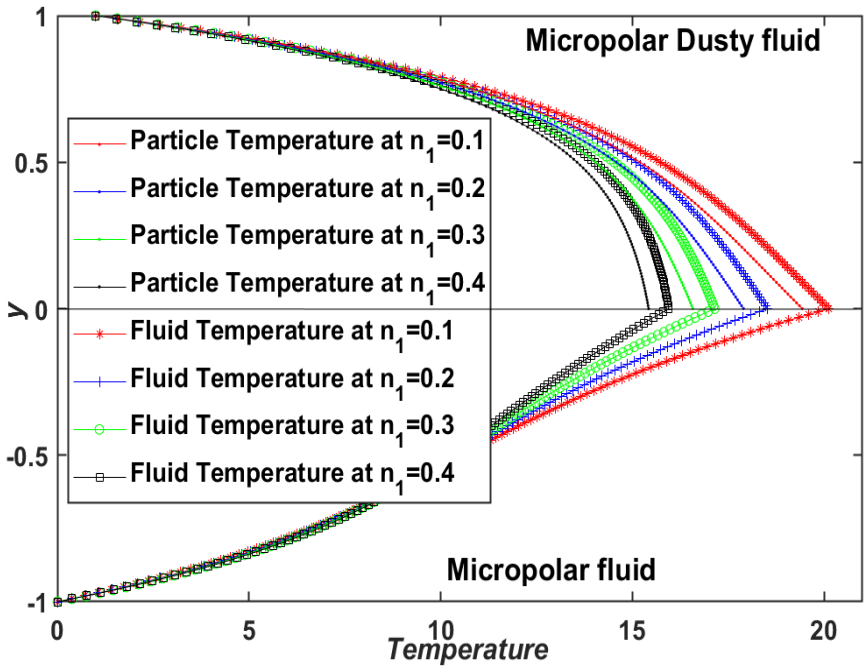

Figure 5.26: Generalized Couette flow temperature with a micropolar parameter of lower fluid

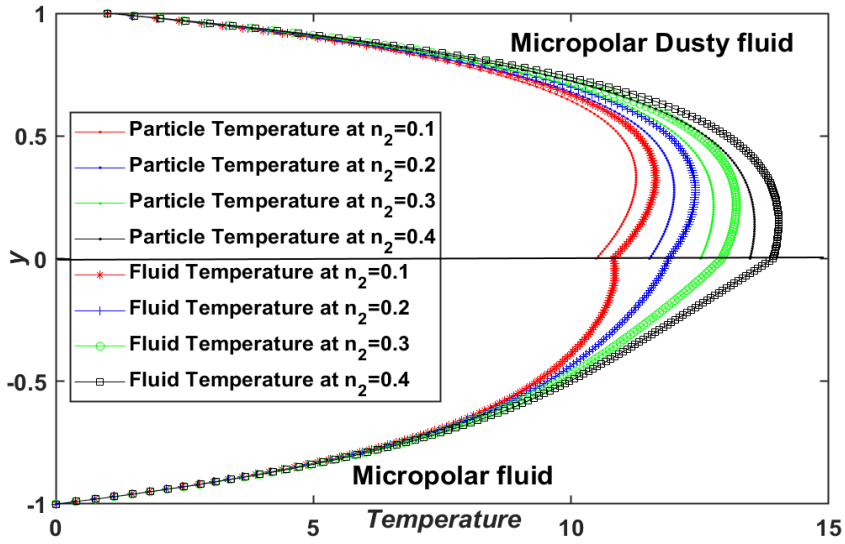

Figure 5.27: Generalized Couette flow temperature with a micropolar parameter of the upper fluid

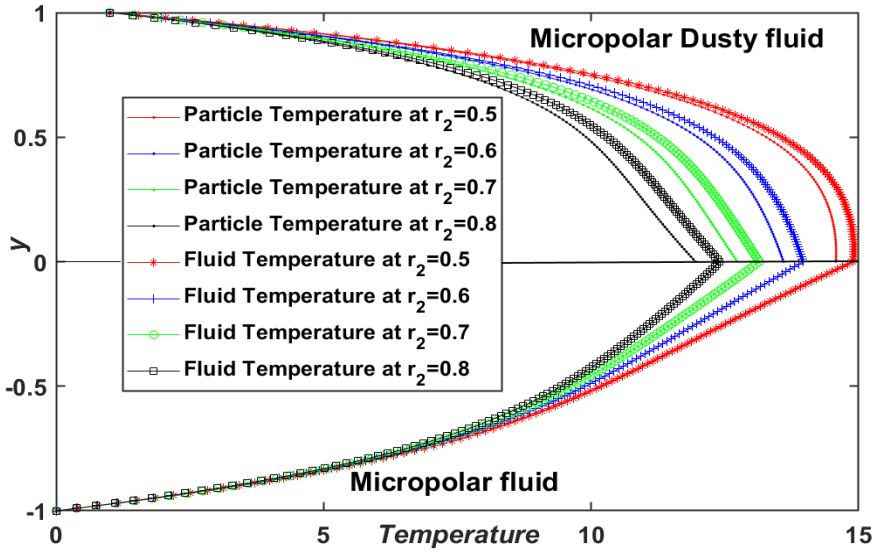

Figure 5.28: Generalized Couette flow temperature with a ratio of the density

Table 5.1:Skin friction Coefficients in generalized Couette flow with varying parameters (plates = Plt)

t	*Lower Plt*	*Upper Plt*	η_2	*Lower Plt*	*Upper Plt*	*Be*	*Lower Plt*	*Upper Plt*
0.1	*3.914577*	*-5.03428*	*0.1*	*8.978459*	*-14.4407*	*0*	*7.175638*	*-7.88893*
0.2	*5.499268*	*-7.96846*	*0.2*	*8.955957*	*-13.6545*	*1*	*8.595216*	*-11.1443*
0.4	*7.853986*	*-10.8048*	*0.3*	*8.937793*	*-12.9805*	*2*	*8.911331*	*-11.8856*
0.8	*11.86768*	*-14.765*	*0.4*	*8.923136*	*-12.3965*	*4*	*9.119304*	*-12.3772*
Re	*Lower Plt*	*Upper Plt*	Ha^2	*Lower Plt*	*Upper Plt*	*R*	*Lower Plt*	*Upper Plt*
2	*8.911331*	*-11.8856*	*1*	*9.136863*	*-12.4189*	*1*	*8.911333*	*-11.8856*
3	*10.66685*	*-15.8778*	*2*	*8.911331*	*-11.8856*	*2*	*8.911331*	*-11.8856*
4	*12.26886*	*-19.5165*	*3*	*8.695507*	*-11.3788*	*3*	*8.91133*	*-11.8857*
5	*13.73152*	*-22.7994*	*4*	*8.488902*	*-10.8966*	*4*	*8.91133*	*-11.8857*
η_1	*Lower Plt*	*Upper Plt*	*Bi*	*Lower Plt*	*Upper Plt*			
0.1	*10.17517*	*-11.913*	*1*	*8.764204*	*-11.5398*			
0.2	*9.79548*	*-11.9073*	*2*	*8.911331*	*-11.8856*			
0.3	*9.464052*	*-11.9008*	*3*	*9.015624*	*-12.1318*			
0.4	*9.171692*	*-11.8936*	*4*	*9.084507*	*-12.2948*			

Table 5.2: Nusselt numbers at the upper and lower walls (plates = Plt) in generalized Couette with various parameters

t	*Lower Plt*	*Upper Plt*	Ha^2	*Lower Plt*	*Upper Plt*	*Re*	*Lower Plt*	*Upper Plt*
0.5	*-10.6939*	*18.2945*	*1*	*-43.0247*	*57.7629*	*2*	*-39.6009*	*53.5489*
1	*-39.6009*	*53.5489*	*2*	*-39.6009*	*53.5489*	*3*	*-41.1022*	*70.1412*
1.5	*-82.8666*	*99.0824*	*3*	*-36.5677*	*49.8127*	*4*	*-42.4534*	*86.9392*
2	*-132.946*	*147.186*	*4*	*-33.8719*	*46.489*	*5*	*-44.2968*	*104.621*
Ec	*Lower Plt*	*Upper Plt*	*Pr*	*Lower Plt*	*Upper Plt*	*Bi*	*Lower Plt*	*Upper Plt*
0.1	*-7.92018*	*9.92662*	*2*	*-39.6009*	*53.54888*	*1*	*-37.5084*	*50.97172*
0.2	*-15.8404*	*20.8322*	*3*	*-48.6417*	*70.42561*	*2*	*-39.6009*	*53.54888*
0.4	*-31.6807*	*42.6433*	*4*	*-56.7456*	*85.78423*	*3*	*-41.1507*	*55.45682*
0.8	*-63.3614*	*86.2656*	*5*	*-64.243*	*99.96635*	*4*	*-42.2057*	*56.75519*
Be	*Lower Plt*	*Upper Plt*	*R*	*Lower Plt*	*Upper Plt*	η_1	*Lower Plt*	*Upper Plt*
0	*-20.6741*	*30.16*	*1*	*-39.6004*	*53.57657*	*0.1*	*-36.8681*	*58.28132*
0.2	*-25.4591*	*36.0918*	*2*	*-39.6009*	*53.54888*	*0.2*	*-37.5684*	*56.94946*
0.4	*-29.0338*	*40.5148*	*3*	*-39.6011*	*53.53989*	*0.3*	*-38.2685*	*55.73181*
0.8	*-33.6803*	*46.2526*	*4*	*-39.6013*	*53.53548*	*0.4*	*-38.95*	*54.60394*

5.6 Profiles computation for plane Couette flow

As the plane Couette flow is induced by only upper plate movement and there is no external pressure provided from any direction in the channel, so at each step of SSP-RK43 schemes (1.69) - (1.72) in DQM, the systems of coupled partial differential equations (5.17) - (5.24) are considered with $\left(-\frac{\partial p}{\partial x} = 0\right)$. The velocity, temperature, and angular velocity profiles of micropolar and micropolar dusty fluids, and dust particle velocity are calculated similarly to the computation performed for generalized Couette flow in section 5.4

5.6.1 Analysis of velocity profiles for plane Couette flow

Figure 5.29-Figure 5.36 represents the effect of various fluid parameters on fluids and particle velocity, and it is cited from Figure 5.29 that in the absence of external pressure gradient, both fluid and particle velocity increased with time. It became stable for a higher value of time. Hall parameter($Be = \sigma\beta B_0$) and Ion-slip parameter (Bi) also affect the velocity but the magnitude is little less as compared to genialized Couette flow case; Hence the magnetic resistive force is decreased as Be and Bi are increased, creating an acceleration in the main flow, which increases fluid and particle-phase velocities the profile slightly and get stable for higher values (see Figure 5.30-Figure 5.31). If the flow is induced by constantly applied pressure from the *x*-direction, it is known as the generalized Couette flow. The Reynold's number $Re = \frac{\rho_1 U_0 h}{\mu_1}$ is the non-dimensional parameter which is defined as the ratio of inertial to viscous forces. Lower viscous forces are referred to as higher Re values in the fluid medium. As the Reynolds number rises, viscous forces decrease, causing an increasing correlation of fluid velocities (See Figure 5.5- generalized Couette flow with *Re)*. Figure 5.32 shows that if there is no external pressure on fluids, rising the *Re,* value decreases the velocity profiles. The parameter Hartmann number $Ha^2 = \frac{\sigma B_0^2 k^2}{\mu_m}$ calculates the results of a

transverse magnetic field. According to Figure 5.33, increasing $Ha^2$the allows the velocity fields in both regions to decrease. This may be attributed to the effect of an applied transverse magnetic field on both plates, which causes resistance to fluid movement through the Lorentz force, which appears to draw fluid velocities down. Increasing the micropolar parameters $\eta_1 = \frac{\kappa_m}{\mu_m}$, $\eta_2 = \frac{\kappa_{md}}{\mu_{md}}$ of both fluids, increase the vortex viscosities $\kappa_1$and κ_2; hence the velocity profiles of the fluids and particle-phase increase slightly in respective regions. This happens because there is no external pressure is provided, and upper plat movement generates more force than vortex viscosity (see Figure 5.34-Figure 5.35). Figure 5.36 indicates that only the dust particle velocity increases with an enhancement of particle concentration parameter R, and no variation in fluid velocities is observed.

5.6.2 Analysis of micropolar profiles for plane Couette flow

Figure 5.37-Figure 5.43 represents the effect of various fluid parameters on microrotations (angular velocities), and it is observed from Figure 5.37 that the microrotation decreases with time and reaches a steady-state after a higher value. According to Figure 5.38, increasing Ha^2 microrotation increases in both regionsFigure 5.49 and Figure 5.50 show that enhancing the Hall (Be) and Ion-slip parameter (Bi) decreases microrotation in both region fluids. Figure 5.41 shows that increasing the micropolar parameters η_1 of micropolar fluid, microrotation profiles in both regions increase slightly while profiles get a significant increment with the micropolar parameters η_2 of micropolar dusty fluid (see Figure 5.42). Figure 5.43 exhibits that the Microrotation profiles in both regions increase with Re in the absence of applied pressure.

5.6.3 Analysis of temperature profiles for plane Couette flow

The nonlinear and flow-dependent viscous dissipation terms are not skipped during the simulation. Figure 5.44-Figure 5.52 exhibits the effect of various fluid parameters on heat transfer profiles of micropolar and micropolar dusty fluids, and it is observed in

Figure 5.44, Figure 5.50, Figure 5.47, Figure 5.52, Figure 5.53, and Figure 5.54 that the temperature profiles of both regions fluids increase with time, Hartman number Ha^2(effect transverse magnetic field applied to both plates), Eckert number *(*Ec- which provides the ratio of the advective mass transfer to the heat dissipation potential*),* the micropolar parameter of micropolar dusty fluid η_2, and the ratio of viscosity r_1 and density r_2. The increment in the Ion-slip parameter (*Bi*), Hall parameter (*Be*), and micropolar parameter of micropolar fluid η_1 cause a decline in the temperatures in both regions (see Figure 5.49, Figure 5.50, and Figure 5.51). Figure 5.45 shows that if the flow is carried out by upper plate movement (Couette flow), increasing Reynold's number Re reduces the temperature profiles in both the regions while Figure 5.21 shows that if the flow is carried out by constant pressure increasing Reynold's number Re reduces the viscous force hence temperature profiles of both fluids have increasing nature. It is cited from Figure 5.48, increasing the Prandtl number (*Pr*), which is the ratio of viscous diffusivity to thermal diffusivity, enhancing the temperature profiles of fluid and particle in the upper region, and changing its nature from increasing to decreasing in the lower area.

5.6.4 Analysis of skin-friction coefficient for plane Couette flow

As fluid flows over the plates, the flow becomes chaotic at some point in the flow path. The existence of vortices indicates that turbulent flow has a fluctuating and unstable pattern of flow. So frictional forces are applied to the plate surface preventing fluid moves; this is known as skin friction drag. Table 5.3 shows that at the lower plate of the channel, skin friction increases with time *(t)*, the micropolar parameter η_1 of lower region fluid, micropolar parameter η_2, Hall (*Be*), and Ion-slip parameter (*Bi*). It shows a slight decrement with Reynolds number (*Re*), and Hartman number Ha^2 but remains constant with increasing values of particle concertation parameter R. On the upper plate, the skin friction coefficient is declined by rising values of time *t*, η_1, η_2, *Be,* and

Bi. When and Ha^2 and *Re* increase, the co-efficient improves slightly and it does not change with *R*.

5.6.5 Analysis of Nusselt number for plane Couette flow

The Nusselt number, which is equal to the dimensionless temperature gradient at the plates and is calculated at the channel wall only, is a measure of convection heat transfer at the surface. Table 2 shows that the Nusselt number increases at the upper plate and decreases at the lower plate with time *(t),* Eckert number *(Ec)*, Hartman Number Ha^2*,* the micropolar parameter (η_2) of micropolar dusty fluid. The Nusselt number decreases at the upper plate and increases at the lower plate with Reynold's number (*Re*)*,* Hall (*Be*), and Ion-slip parameter (*Bi*). micropolar parameter (η_1). It remains constant at both the plates with particle concertation parameter (*R*)*.* The Nusselt number changes at the upper plate and shows decreasing nature with the ratio of thermal conductivity *kr* and does not change at the lower plate. The effect of the Prandtl number (*Pr*) shows that at both plates, the Nusselt number is enhanced.

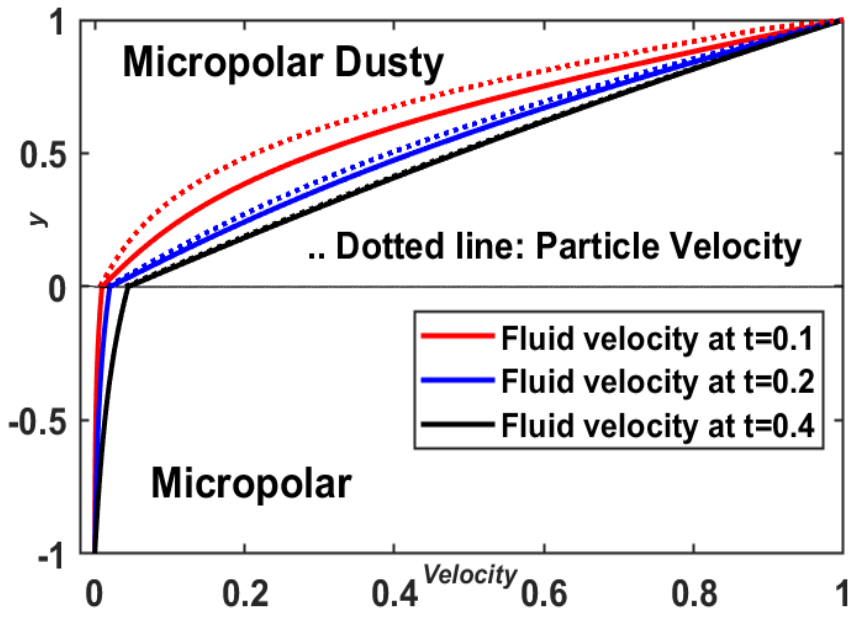

Figure 5.29: Velocity under Couette flow with time

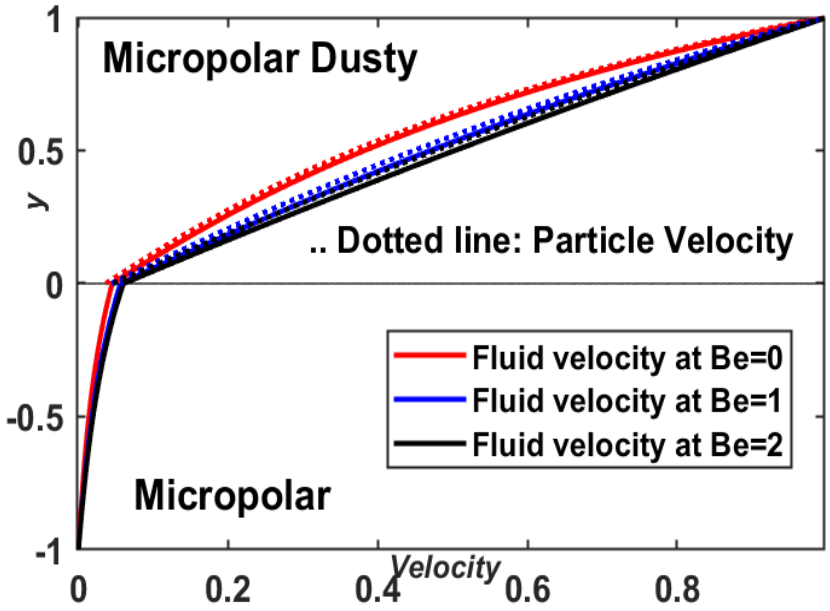

Figure 5.30: Velocity under Couette flow with hall parameter

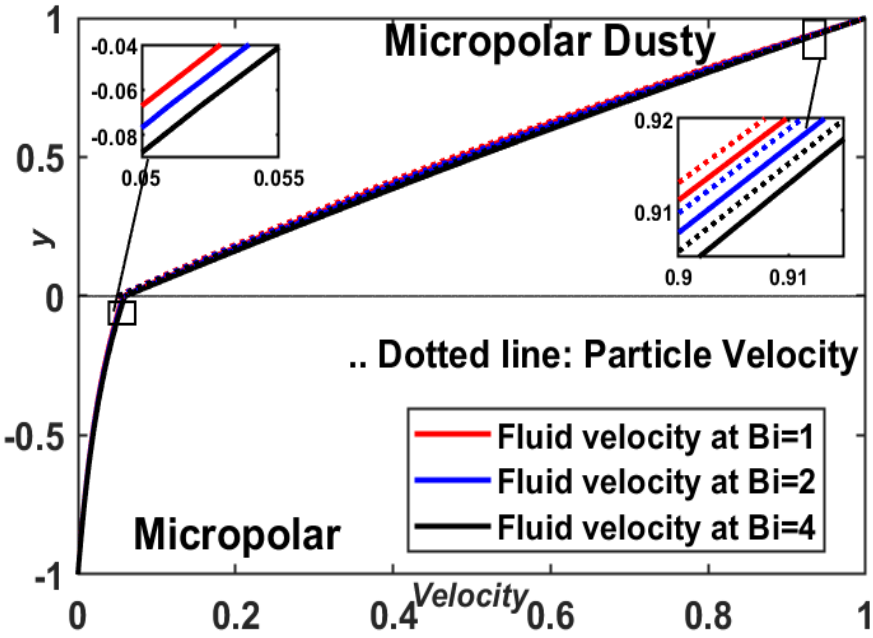

Figure 5.31:Velocity under Couette flow with Ion-slip parameter

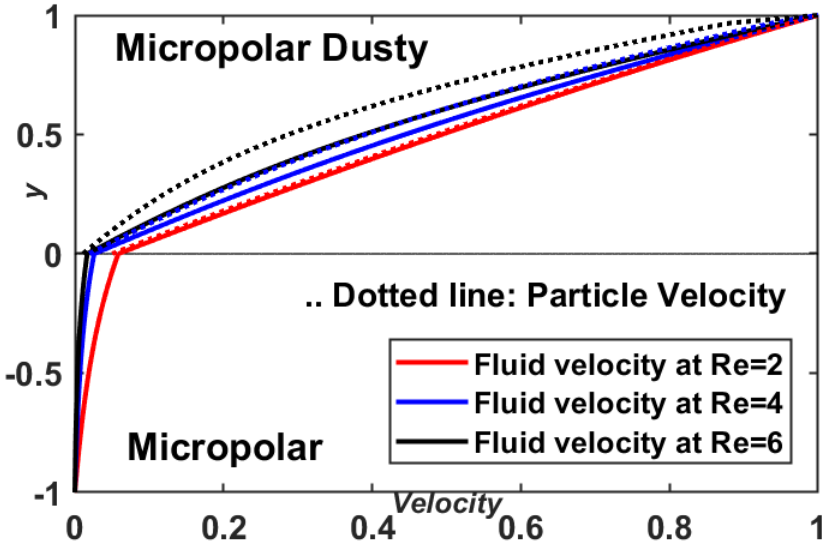

Figure 5.32:Velocity under Couette flow with Reynolds number

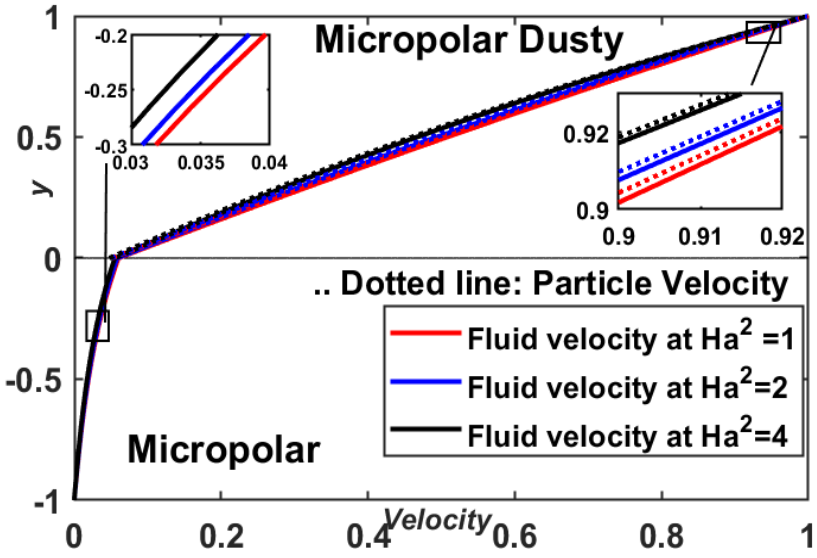

Figure 5.33:Velocity under Couette flow with Hartman Number

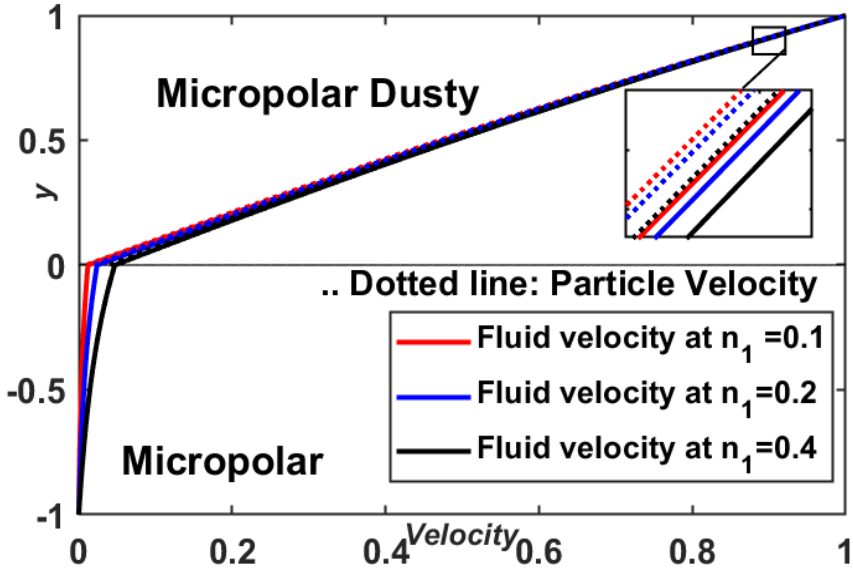

Figure 5.34:Velocity under Couette flow with lower fluid micropolar parameter

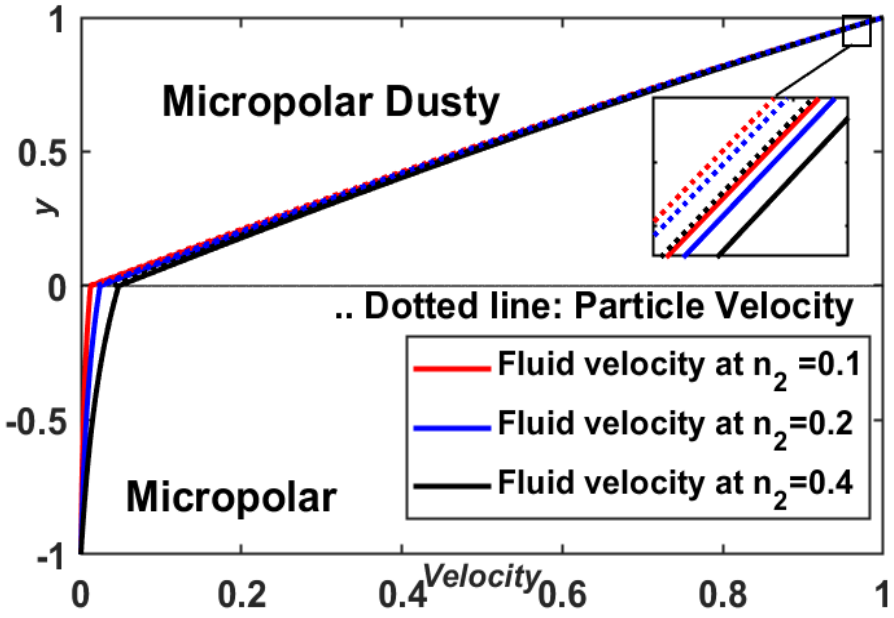

Figure 5.35:Velocity under Couette flow with upper fluid micropolar parameter

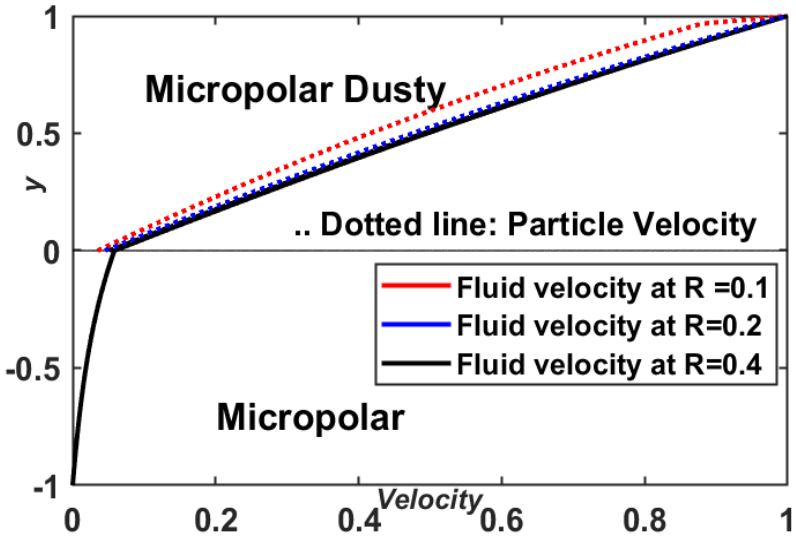

Figure 5.36:Velocity under Couette flow with particle concentration parameter

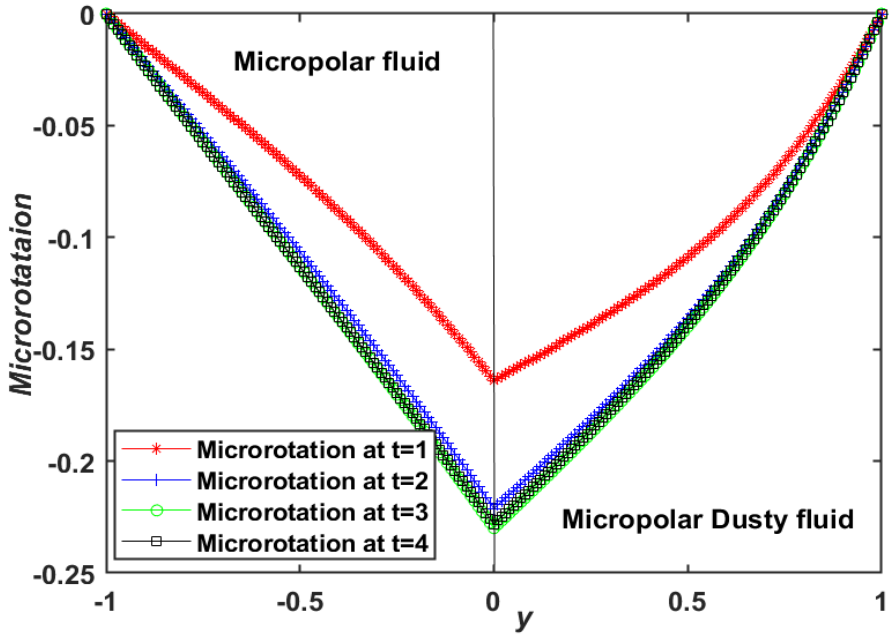

Figure 5.37:Microrotation under Couette flow with time

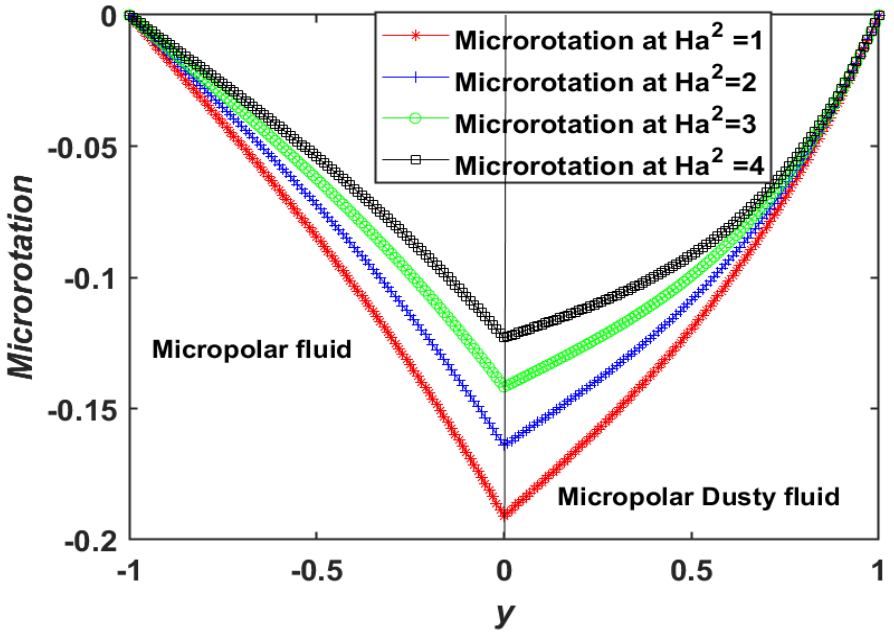

Figure 5.38:Microrotation under Couette flow with Hartman Number

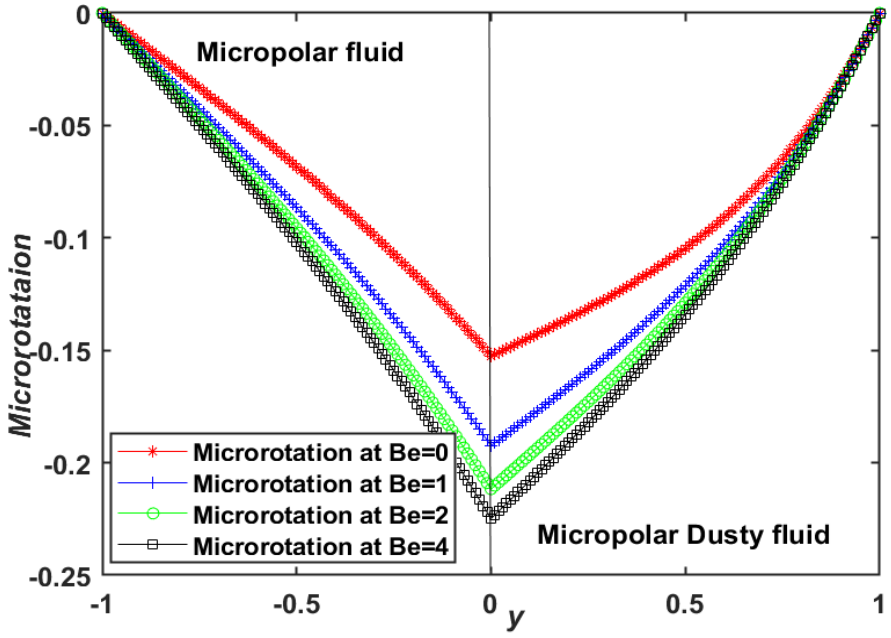

Figure 5.39:Microrotation under Couette flow with hall parameter

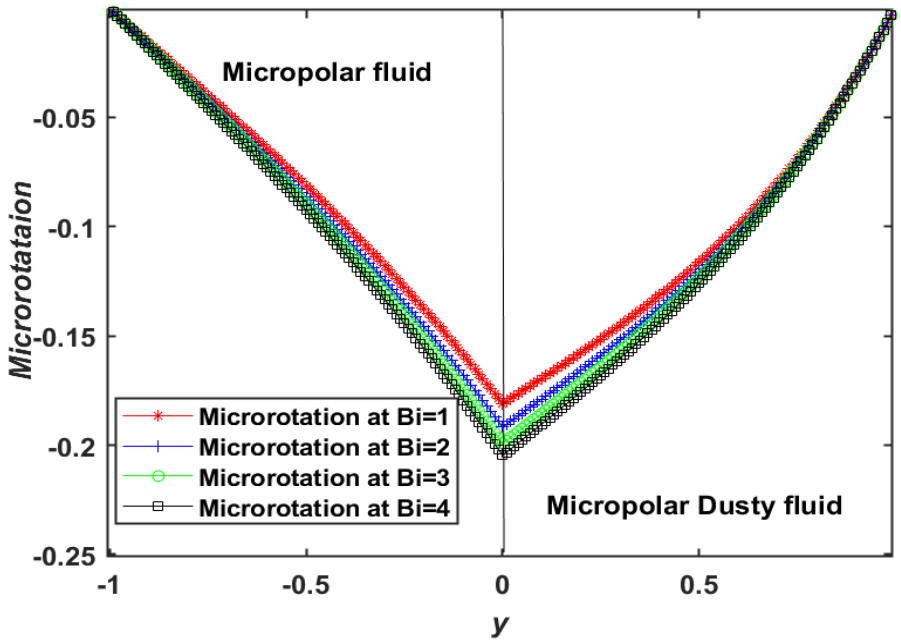

Figure 5.40:Microrotation under Couette flow with Ion-slip parameter

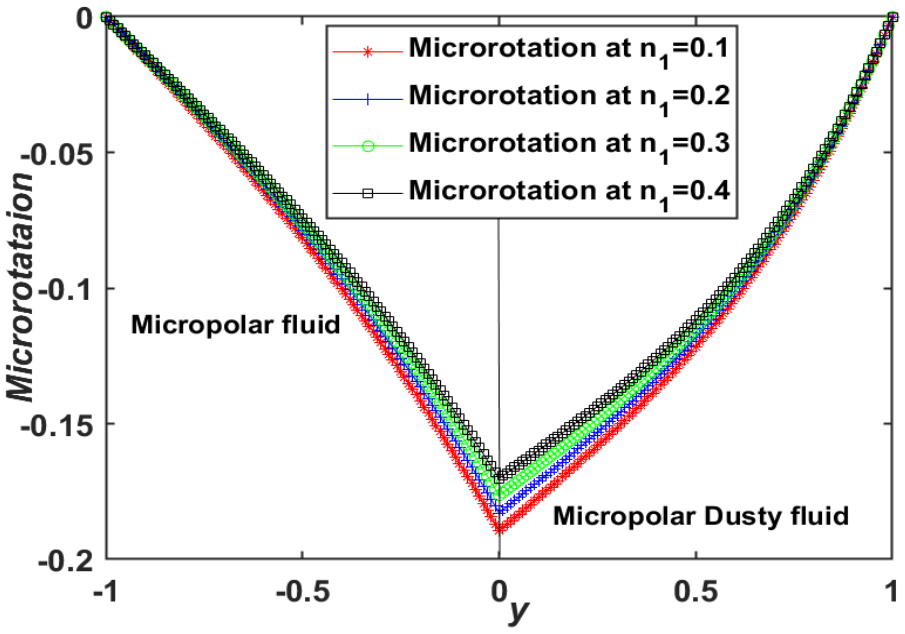

Figure 5.41:Microrotation under Couette flow with lower fluid micropolar parameter

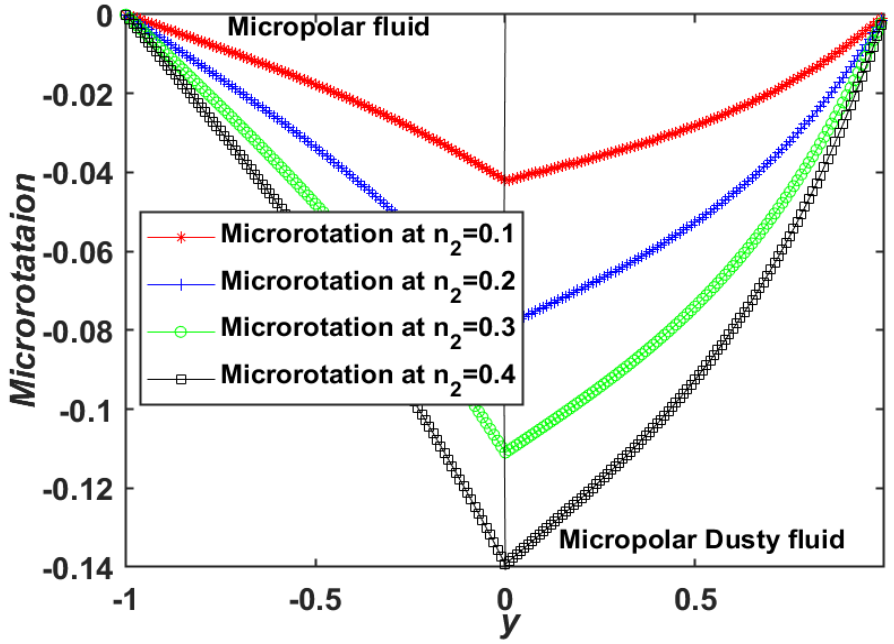

Figure 5.42: Microrotation under Couette flow with upper fluid micropolar parameter

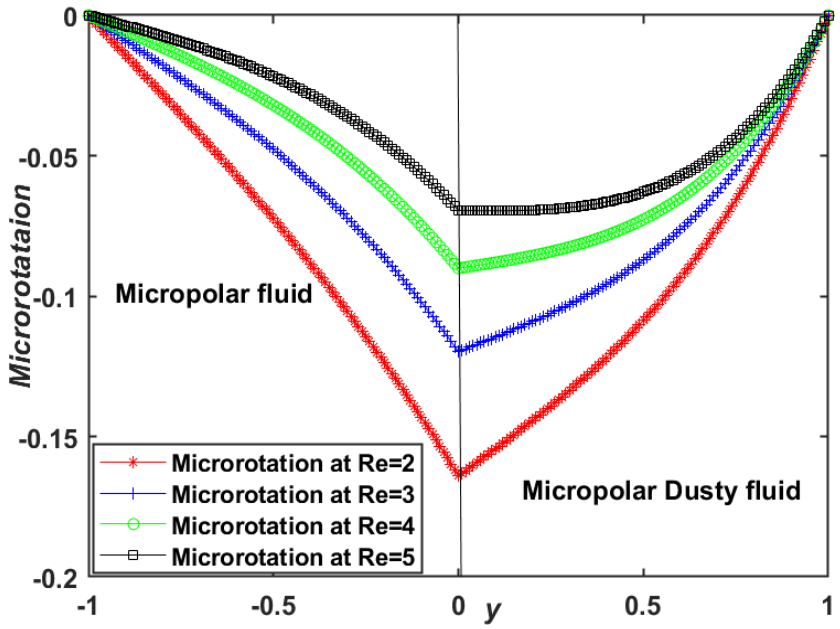

Figure 5.43:Microrotation under Couette flow with *Re*

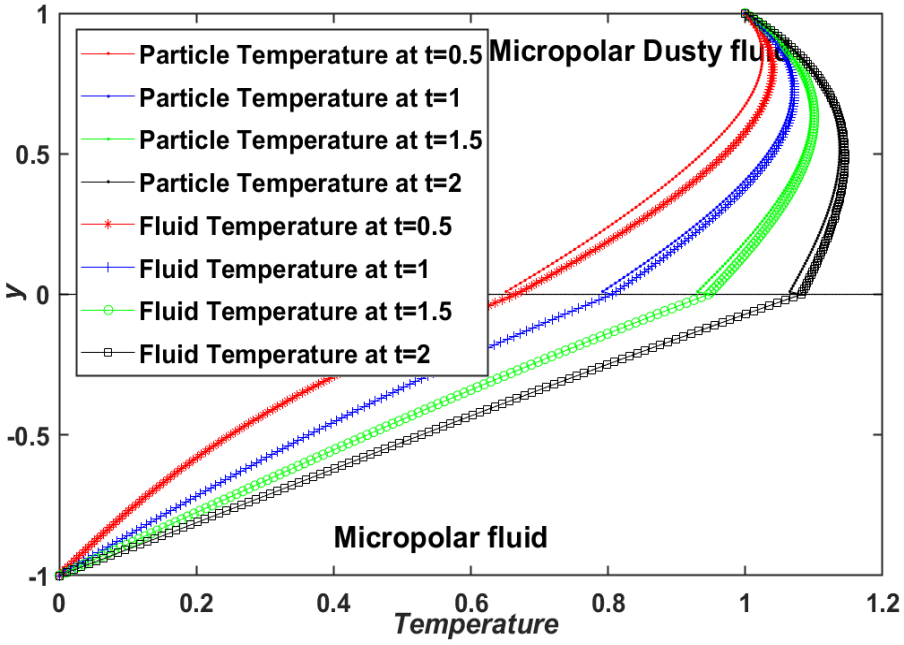

Figure 5.44:Temperature under Couette flow with time

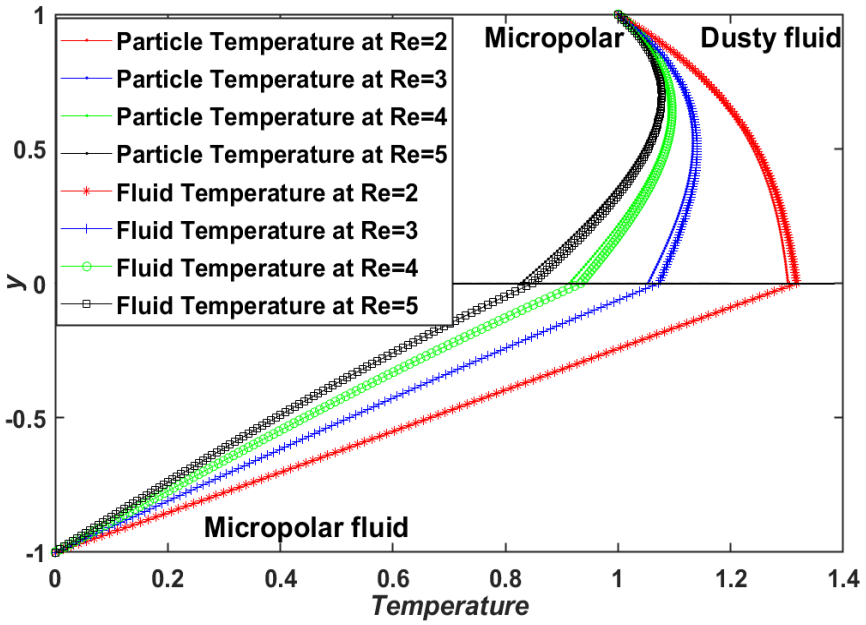

Figure 5.45:Temperature under Couette flow with *Re*

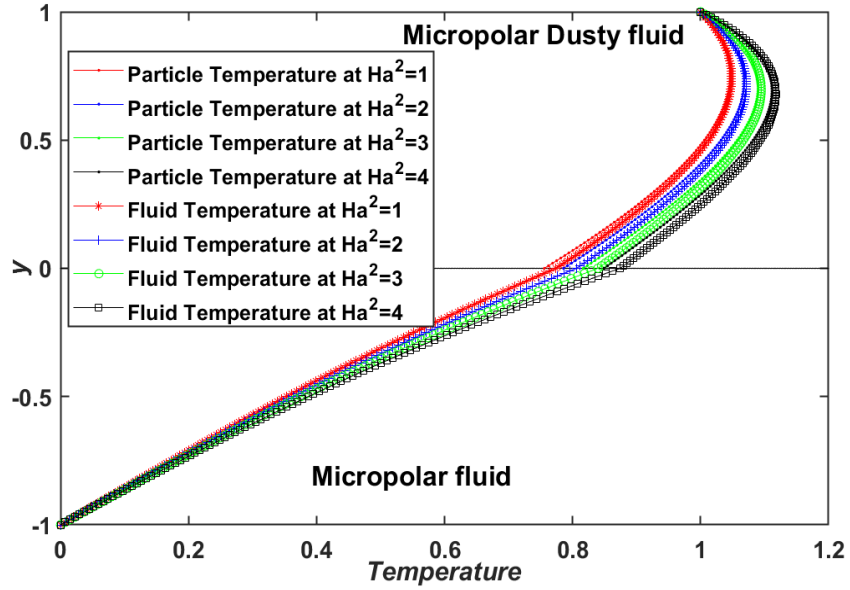

Figure 5.46:Temperature under Couette flow with Hartman Number

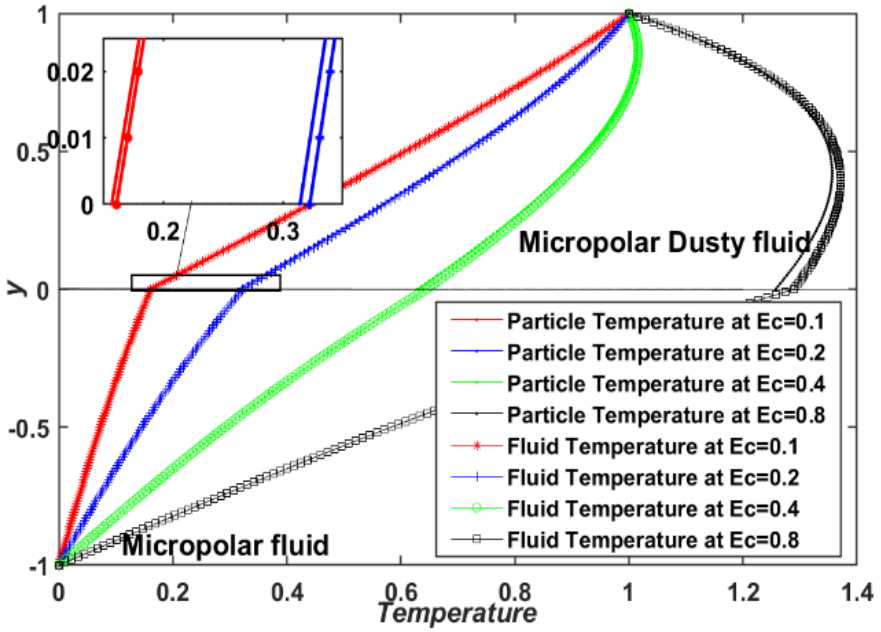

Figure 5.47:Temperature Couette flow with Eckert number

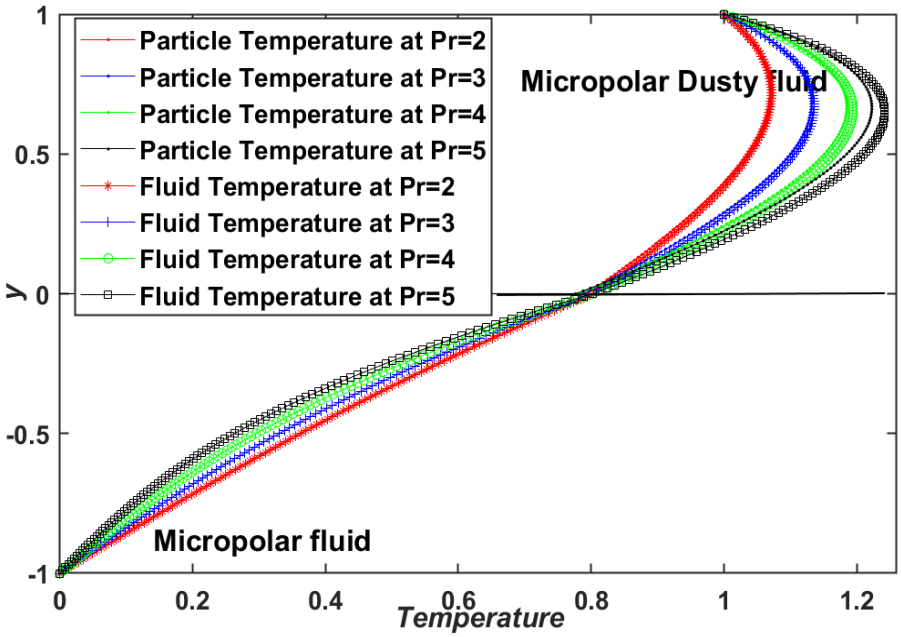

Figure 5.48:Temperature Couette flow with Prandtl number

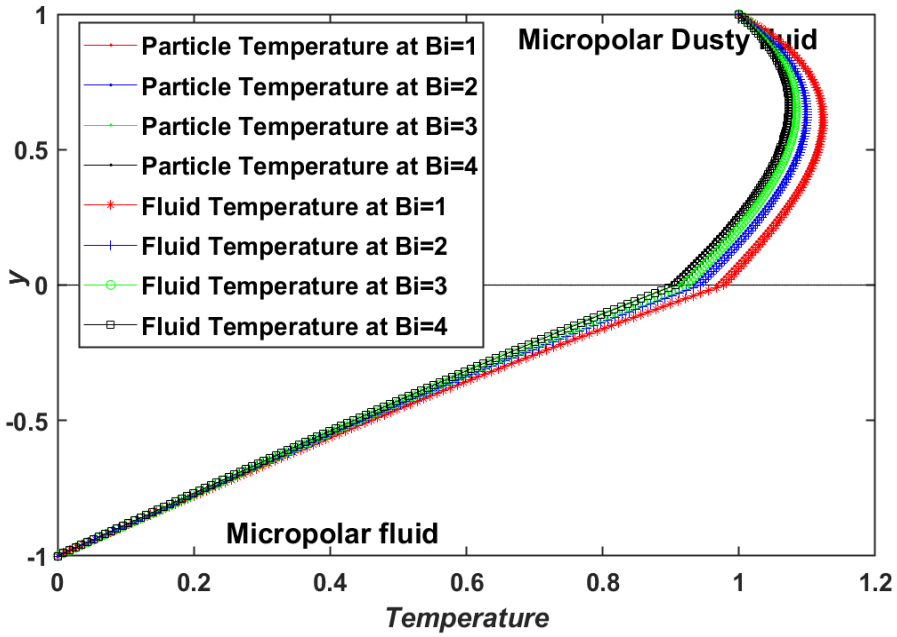

Figure 5.49:Temperature Couette flow with Ion-slip parameter

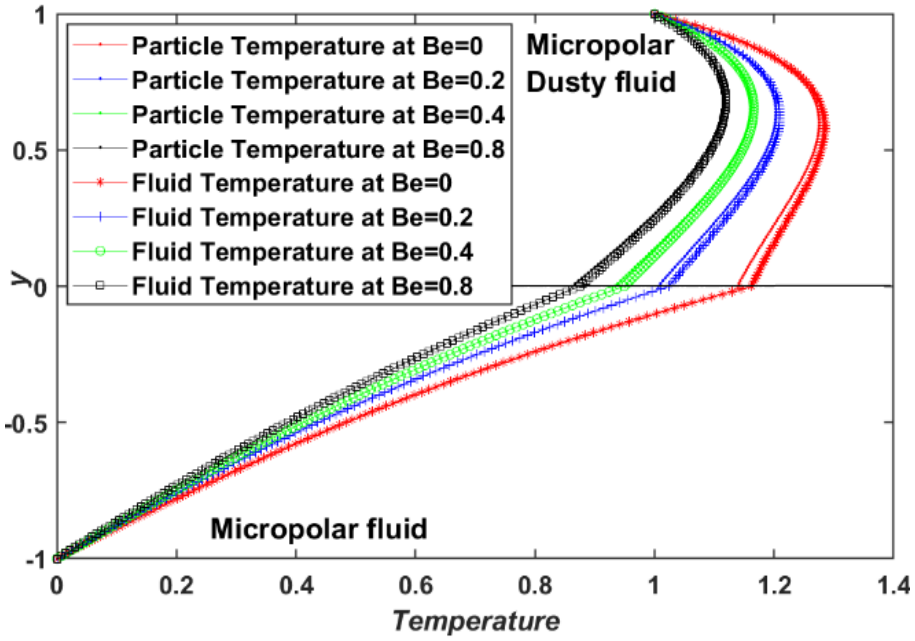

Figure 5.50:Temperature Couette flow with Hall parameter

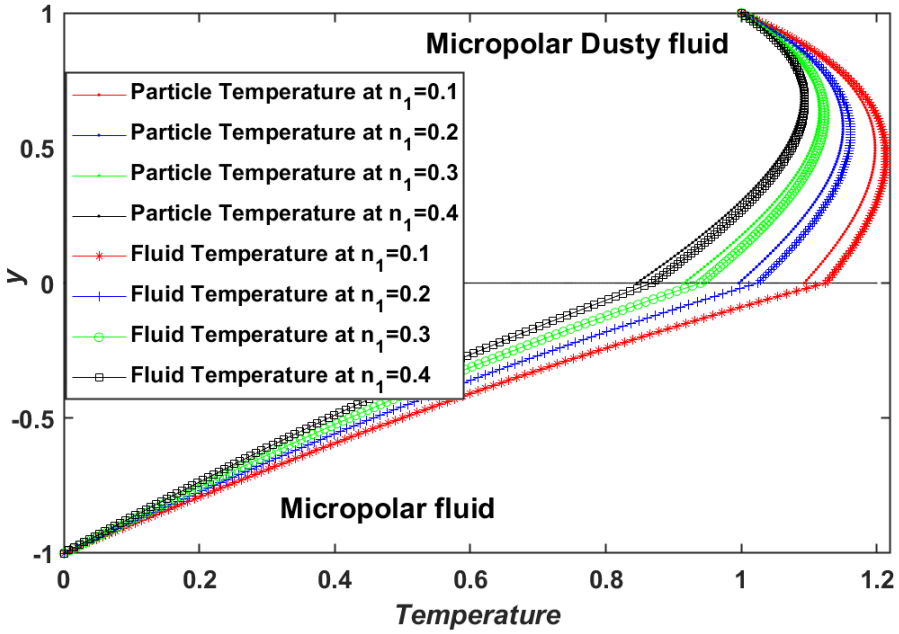

Figure 5.51:Temperature Couette flow with lower fluid micropolar parameter

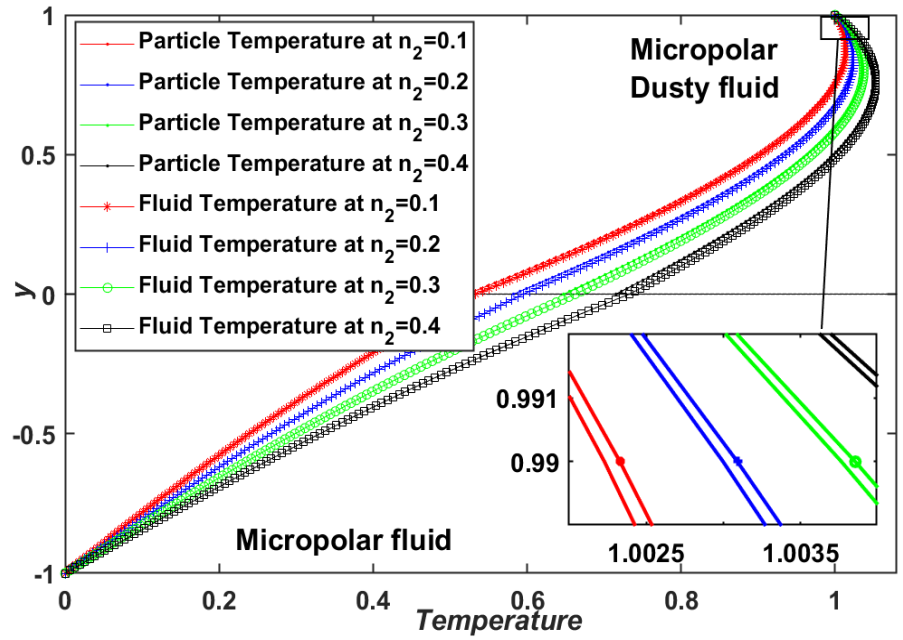

Figure 5.52: Temperature Couette flow with upper fluid micropolar parameter

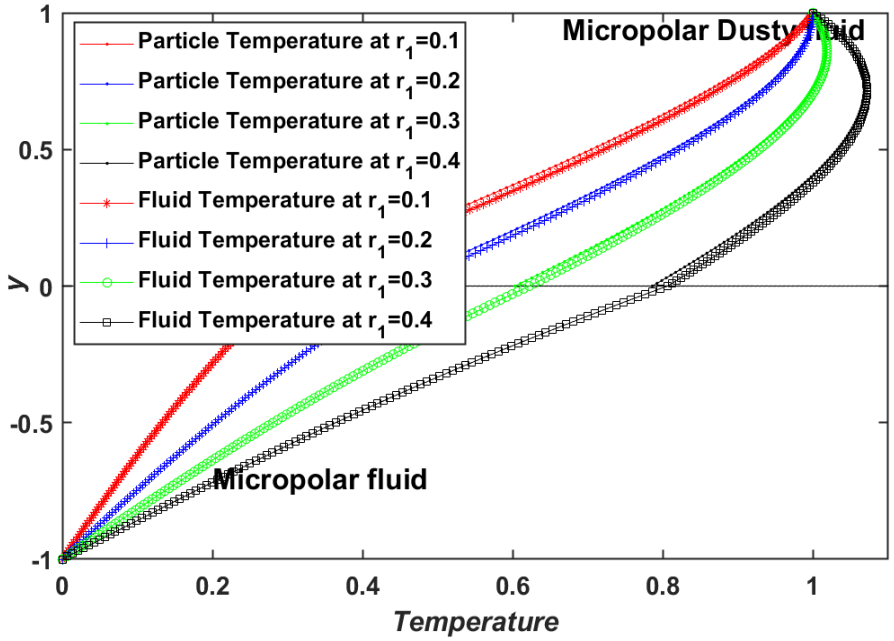

Figure 5.53:Temperature Couette flow with the ratio of viscosities

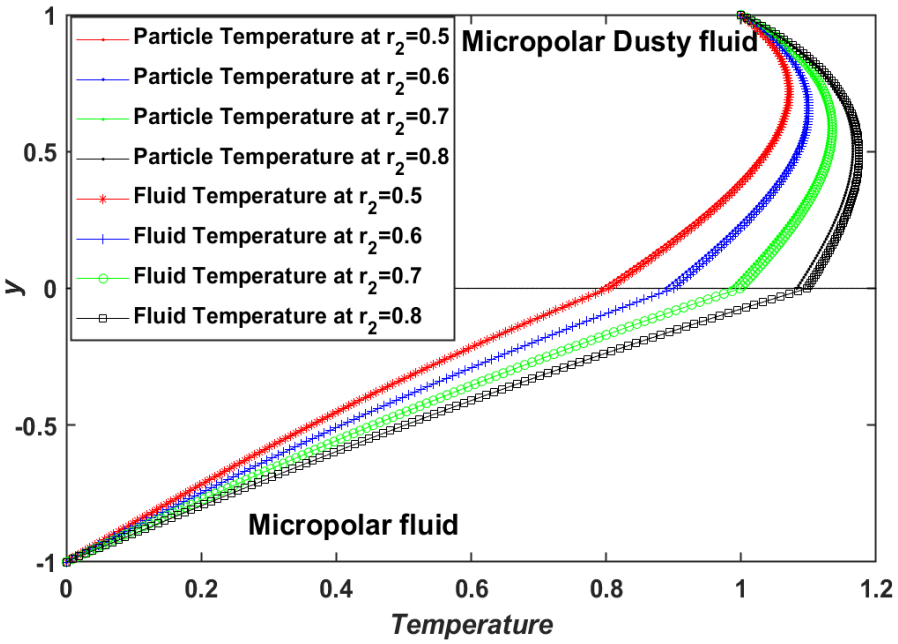

Figure 5.54:Temperature Couette flow with the ratio of densities

Table 5.3: Skin friction Coefficients in plane Couette flow with varying parameters

t	*Lower Plt*	*Upper Plt*	η_2	*Lower Plt*	*Upper Plt*	*Be*	*Lower Plt*	*Upper Plt*
0.1	*0.001994*	*2.53042*	*0.1*	*0.011379*	*1.808388*	*0*	*0.031701*	*2.571262*
0.2	*0.011004*	*1.91909*	*0.2*	*0.021177*	*1.759846*	*1*	*0.041652*	*1.795886*
0.4	*0.031873*	*1.67237*	*0.3*	*0.029698*	*1.715515*	*2*	*0.043806*	*1.635953*
0.8	*0.091465*	*1.55249*	*0.4*	*0.03718*	*1.674432*	*4*	*0.04521*	*1.532623*
Re	*Lower Plt*	*Upper Plt*	Ha^2	*Lower Plt*	*Upper Plt*	*R*	*Lower Plt*	*Upper Plt*
2	*0.043806*	*1.63595*	*1*	*0.045328*	*1.523962*	*1*	*0.043807*	*1.635974*
3	*0.024719*	*1.71059*	*2*	*0.043806*	*1.635953*	*2*	*0.043806*	*1.635953*
4	*0.016142*	*1.80477*	*3*	*0.042338*	*1.744747*	*3*	*0.043806*	*1.635947*
5	*0.011009*	*1.91909*	*4*	*0.040922*	*1.850523*	*4*	*0.043806*	*1.635944*
η_1	*Lower Plt*	*Upper Plt*	*Bi*	*Lower Plt*	*Upper Plt*			
0.1	*0.006325*	*1.68128*	*1*	*0.042807*	*1.709937*			
0.2	*0.014167*	*1.66972*	*2*	*0.043806*	*1.635953*			
0.3	*0.023194*	*1.65831*	*3*	*0.044512*	*1.583959*			
0.4	*0.033144*	*1.64705*	*4*	*0.044976*	*1.549814*			

Table 5.4: Nusselt numbers at the walls in plane Couette with various parameters

t	*Lower Plt*	*Upper Plt*	Ha^2	*Lower Plt*	*Upper Plt*	*Re*	*Lower Plt*	*Upper Plt*
0.5	*-0.42518*	*0.42597*	*1*	*-0.68843*	*0.39078*	*2*	*-0.70544*	*0.53587*
1	*-0.70544*	*0.53587*	*2*	*-0.70544*	*0.53587*	*3*	*-0.53386*	*0.47905*
1.5	*-0.8997*	*0.59438*	*3*	*-0.72334*	*0.67768*	*4*	*-0.41561*	*0.41503*
2	*-1.07893*	*0.6605*	*4*	*-0.74205*	*0.8164*	*5*	*-0.32323*	*0.33214*
Ec	*Lower Plt*	*Upper Plt*	*Pr*	*Lower Plt*	*Upper Plt*	*Bi*	*Lower Plt*	*Upper Plt*
0.1	*-0.141*	*-0.69332*	*2*	*-0.70544*	*0.535872*	*1*	*-0.71746*	*0.63221*
0.2	*-0.2821*	*-0.38602*	*3*	*-0.61494*	*0.900611*	*2*	*-0.70544*	*0.535872*
0.4	*-0.5643*	*0.22858*	*4*	*-0.518*	*1.23576*	*3*	*-0.69736*	*0.468403*
0.8	*-1.1287*	*1.45776*	*5*	*-0.42919*	*1.532756*	*4*	*-0.69223*	*0.424198*
Be	*Lower Plt*	*Upper Plt*	*R*	*Lower Plt*	*Upper Plt*	η_1	*Lower Plt*	*Upper Plt*
0	*-0.90402*	*1.78722*	*1*	*-0.70512*	*0.535481*	*0.1*	*-0.9592*	*0.934201*
0.2	*-0.82619*	*1.35921*	*2*	*-0.70544*	*0.535872*	*0.2*	*-0.8788*	*0.813828*
0.4	*-0.7845*	*1.10391*	*3*	*-0.70561*	*0.536065*	*0.3*	*-0.8114*	*0.709249*
0.8	*-0.7435*	*0.82678*	*4*	*-0.70574*	*0.536196*	*0.4*	*-0.7542*	*0.617364*

5.7 Conclusions

A theoretical model of the transient magnetohydrodynamic generalized and plane Couette flow of dual immiscible non-Newtonian micropolar and micropolar dusty fluids in a horizontal duct with heat transfer, viscous heating, Hall current, and ion slip effects has been developed. The robust modified cubic B-spline differential quadrature method (MCB-DQM) has been deployed to numerically solve the transformed, dimensionless boundary value problem. Extensive visualization of linear velocity, microrotation (angular momentum), and temperature profiles of both fluid and particle phases have been presented. Validation with exact solutions has also been included for the linear velocity field. A parametric study of the impact of all key thermophysical and electromagnetic parameters on thermo-fluidic characteristics has been conducted. The main conclusions of the current study are summarized as follows:

(i) For the regulating condition of non-dusty, single fluid Newtonian Couette flow, the modified cubic B-spline differential quadrature approach was found to be in good agreement with exact solutions.

(ii) Fluid velocities, microrotation (angular momentum), and temperature profiles of both fluids and particles are enhanced with time, and for a higher time, the particle and fluid velocities are the same.

(iii) The micropolar parameter η_1 of lower region fluid influences the velocities and temperatures of upper region (micropolar dusty) fluid and the impact of parameter η_2 of the upper region, fluid is also being seen in lower region fluid velocities and temperatures.

(iv) In the generalized Couette flow scheme, the Hall(Be) and Ion-slip(Bi) parameters significantly increase the velocity and temperature of both fluids and the

angular velocity of micropolar dusty fluid whereas they decrease the microrotation of micropolar fluid.

(v) Hartmann number (Ha^2) exhibits an inverse relationship with the velocities of the fluid and particle phases and their temperatures

(vi) Reynolds number *(Re)* affects the fluid and particle velocities and their temperatures with a directly proportional relation. However, *Re* shows an inverse relationship with the angular velocity.

(vii) Dust particle and fluid temperatures are both increased with an enhancement in Eckert number *(Ec),* the ratio of viscosities r_1 and Prandtl number *(Pr).*

(viii) The external pressure gradient affects the velocity, microrotation, and temperature profiles, and because of that, the generalized Couette flow velocity magnitudes are higher than plane Couette flow.

Overall, the Modified cubic B-spline differential quadrature method (MCB-DQM) achieves excellent accuracy and is a versatile method for addressing unsteady viscous multi-fluid non-Newtonian transport in MHD duct flows. The current work has provided a good benchmark for more general computational fluid dynamics simulations. However, it has neglected magnetic induction effects since it was assumed that the magnetic Reynolds number is sufficiently small to ignore the magnetic field distortion. Future work may include induced magnetic field phenomena in dusty flows from rotating disks (Von Karman swirl flows), pulsating plates, etc., including MHD and heat transfer, especially electro and magneto micropolar rotating dusty flows, and will be deported imminently.

Chapter 6

Ion-slip and Hall effect on the two-dimensional interface between immiscible dusty and pure (non-dusty) fluids by differential quadrature method

6.1 Introduction

Viscous magnetohydrodynamic flows in ducts and channels arise in many diverse branches of engineering, including loop systems in nuclear duct transport [248] and electromagnetic flow control [249], [250], and DC electromagnetic pumps [251]. When an electrically conducting fluid (e. g., plasma, ionic liquid, etc.) interacts with a magnetic field, it generates an electric field due to charge separation, which mobilizes an electric current. The interaction between this created electric current and the imposed magnetic field produces the Lorentz force, which acts in the opposite direction of the fluid motion and is a resistive force. Therefore, greater power must be expended to drive the fluid [252]. The Navier-Stokes viscous flow model is modified with additional magnetic body force terms to simulate such flows. Ramos and Winowich [253] presented finite-difference numerical solutions for viscous MHD flow in a two-dimensional duct. He solved the coupled Navier–Stokes and Maxwell equations at low magnetic Reynolds numbers, noting that axial velocity profiles exhibit the M shape as the fluid approaches and passes the electrode. He further identified a sharp gradient in electrical in the vicinity of the electrodes and significant pressure enhancement with

greater magnetic field strength. Sezgin [254] employed a dual reciprocal boundary element method (BEM) to compute the hydromagnetic viscous flow in a 3-D rectangular duct under an external transverse static magnetic field with induction effects. He considered the case where the walls parallel to the applied magnetic field are conducting and the other two walls duct normal to the magnetic field are insulators. With a greater Hartmann number, it was found that Hartmann-Stokes boundary layers arise close to the insulated boundaries for both the velocity and the induced magnetic field whereas in the core region a more uniform flow distribution is computed.

A significant modification was observed in the wall skin friction at a high magnetic field due to the couple stress effect. MHD duct flow applications in smart liquid metal robotics were considered by Chiolerio and Quadrelli [255] over a wide range of magnetic Reynolds numbers and magnetic field intensity. Magnetic ionic lubricant flows in ducts were addressed for astronautical applications (damping of components) by Okaniwa and Hayama [256]. Singh and Lal [257] deployed a finite element algorithm to simulate the impact of an inclined applied magnetic field and wall electrical conductivity on MHD square duct channel flows. He noted that flow deceleration is produced with increasing increments of in-wall conductivity increases, and the volumetric flow rate is maximum for the case when the magnetic field is parallel.

The above studies neglected Hall current and ion slip effects [258]. Hall currents are mobilized in magnetohydrodynamics when a magnetic field deflects an electric current. In conducting materials, this leads to the so-called Hall effect. When electric current flows through a metal strip, electrons move laterally from one side of the material to the other. The Lorentz magnetic force is generated in the vicinity of an external magnetic field, which acts on the electrons. This causes a deviation in the path of the electrons and results in a greater concentration of electrons on one side than on the other. A voltage is generated, which is perpendicular to the direction in which the current flows. This classic Hall effect induces a secondary (cross) flow in

magnetohydrodynamics. Hall current may significantly modify transport characteristics in fuel cell design and chemical or nuclear duct flow processing systems. Under strong magnetic fields, ions can also slip relative to each other. This is particularly important in the new generation of magnetic ionic liquids being deployed in energy generator systems and electromagnetic pumps [259]. Hall effects are essentially important when the ratio between the fluid electron-cyclotron frequency and the electron-atom-collision frequency is high (the Hall parameter).

Additionally, when the electromagnetic (Lorentz) force is very large, the diffusion velocity of ions is significant; therefore, the diffusional velocity of ions and electrons must be incorporated in MHD flow models featuring ion slip. Mathematical models of MHD flows with Hall, and ion slip phenomena are therefore more sophisticated than Lorentz body force models. Several researchers have used such models. Da Silva *et al.* [260] implemented a hybrid (generalized integral transform) method to analyze transient unsteady magnetohydrodynamic convection with temperature-dependent transport properties, Hall current, and ion-slip effects in a duct. They computed the effects of time-dependent pressure gradient and inflow perpendicular to the duct walls on velocity and temperature potentials. Javeri [261] used a Kantorowitsch method of variational calculus to compute the collective effects of the Hall effect, ion slip, and viscosity variation on flow and heat transfer in a duct with finely segmented electrodes. Vighnesam and Takhar [262] considered the hydromagnetic channel flow with thermal convection and Hall and Ion-slip effects. They derived exact solutions for the velocity components, magnetic field components, axial and transverse components of the skin friction, temperature, and heat transfer rate. They noted that flow instability arises for significant Hall parameter and ion-slip parameter values. Bég *et al.* [263] deployed an electrothermal network solver (PSPICE) to compute the hydromagnetic viscous plasma flow in a rotating channel under an oblique magnetic field with Hall current effects. They found that primary flow acceleration is generated with an increase in Hall current parameter, whereas secondary flow deceleration is induced. Shamshuddin *et al.* [264]

used MATLAB and generalized differential quadrature (GDQ) to simulate the effects of Hall current, viscous heating, and Ohmic dissipation on stretching sheet magnetized non-Newtonian polymer flow with slip. They considered both pseudoplastic and dilatant liquids and observed a strong modification in both primary and secondary velocity field and temperature distribution with a more significant Hall effect, including strong flow reversal in the secondary velocity. Bég *et al.* [241] used a Keller box finite difference method to analyze the non-isothermal hydromagnetic heat and momentum transfer in a permeable regime with Hall and ion slip currents and Joule heating. They observed that with increment in both Hall and ion slip parameters, there is an elevation in primary shear stress function and heat transfer rate (Nusselt number), whereas the secondary shear stress is suppressed. Further studies of Hall and ion slip effects in MHD duct flows include Bég *et al.* [41] (for micropolar Hall generator systems), [39] (for chemically reacting heat and mass transfer with Soret and Difour effects in an MHD Hall generator duct), Sheri *et al*. [242] (transient radiative convection flows) and Krishna [265] (on viscoelastic electroconductive polymer flows). These studies confirmed the substantial modification in velocity distributions with Hall and ion slip effects.

The above studies were confined to single-phase flow. However, in many industrial systems, including nuclear power ducts [246], MHD flows may be two-phase. Suspensions arise which contain particles, and a single-phase model is not sufficient. These so-called dusty fluids or fluid-particle suspensions are multi-phase. They can be simulated with the Saffman model [50], which provides a promising approach for analyzing the influence of suspended particles on laminar flows when there is a homogenous distribution of identical particles in the dusty fluid. The Saffman model deploys two parameters to evaluate the influence of the dust, namely the concentration of dust and a relaxation time τ quantifying the rate at which the velocity of a dust particle adjusts to changes in the gas velocity and is a function of the size of the individual particles. Marble [51] later refined the Saffman dusty model for engineering

applications. Several researchers have utilized the dusty model to investigate fluid-particle suspension transport, including Gupta and Gupta [266], who considered duct flow with a transient pressure gradient. Mitra and Bhattacharyya [155] extended the dusty model to consider magnetohydrodynamic channel flows over a range of Hartmann numbers. Datta and Dalal [267] considered dusty flow and thermal convection in an annular regime under a pulsatile pressure gradient. They noted that a strong acceleration in both fluid and particle phases accompanies an elevation in oscillation frequency. Furthermore, the heat transfer rate is strongly modified at a large volume fraction of the dust particles and high oscillation frequencies. Motivated by applications in MHD energy generator systems, several researchers have also examined magnetized flows of dusty fluids in duct systems. Takhar *et al*. [67] studied the Hall current and rotation (Ekman number) on time-dependent hydromagnetic dusty flow in a revolving duct. Aboul-Hassan and Attia [268] considered thermal convection and Hall current effects in dusty channel flows. Ramesh *et al.* [269] examined hydrodynamic wall slip and Hall current impact on pumping non-Newtonian dusty (fluid-particle) suspensions in a deformable micropump. Mahantesh [270] computed the Hall current on the boundary layer flow of a dusty magnetic fluid over a permeable stretching sheet with the Runge-Kutta-Fehlberg fourth-fifth order method, noting that a large mass concentration of dust particles strongly decelerates the flow increases momentum boundary layer thickness.

The above studies were confined to a single fluid or suspension. However, interfacial effects arise when two immiscible fluids are considered in many applications. These are relevant to various chemical processing operations and are known as two-fluid systems [271] arise in which immiscible liquids have an interface between them. Relevant applications include shear flow instability in polymer interfacial transport [272], lubricated pipelining in core-annular dynamics [273], [274] and fabrication of cryogels [275], and magnetic ionic liquid-water pumping in robotics [276]. These fluids may be Newtonian or non-Newtonian, or dusty. Several recent investigations have

considered dusty interfacial flows. Chandrawat *et al.* [171] computed the time-dependent flow of immiscible dissipative dusty (fluid-particle suspension) and non-dusty fluids in a duct with heat transfer. They observed that particle and fluid temperatures in respective regions increase with an enhancement in time, Eckert number, and the ratio of viscosities.

In contrast, they are depleted with Reynolds number and Prandtl number. They also found that elevation in the ratio of thermal conductivities boosts the temperature magnitudes of both dust particles and fluid in only one region. In contrast, there is no substantial modification in the temperature of the pure non-dusty fluid. Magnetohydrodynamic immiscible flow with heat transfer in a duct has been studied by Živojin *et al.* [277], who considered Newtonian liquids between isothermal walls with an applied electric and inclined magnetic field. Chandrawat *et al.* [189] recently considered the influence of Ion slip and Hall effects on unsteady MHD duct flow and heat transfer of immiscible micropolar and dusty micropolar fluids with viscous heating.

A mathematical model is developed for an unsteady two-dimensional flow of electrically conducting immiscible dusty and non-dusty fluids with interface evolution (moving) through a horizontal channel in the present work. Hall current and ion slip effects are incorporated in the model as they are important in novel magnetic ionic working fluids in robotics and nuclear engineering [276]. The Saffman two-phase model is deployed for the dusty fluid, and the Newtonian model is used for the non-dusty liquid. Hyper-stick and no-slip boundary conditions are utilized. A single momentum equation is coupled for evaluating the interface profiles using the VOF (Volume of fluid) approach. The enhanced B-spline differential quadrature method [278] is used to numerically solve the transformed, dimensionless coupled-partial differential equations with appropriate boundary conditions. The impact of Froude number, capillary number, wave number, Reynolds number, amplitude, viscosity ratio, and time on the interface profile is computed. For constrained values of the control

parameters, three applied pressure gradients are studied: constant *Ge=10*, periodic *Ge= 10Sin(t)*, and decaying *Ge= e^{-t}*. Detailed visualization of the interface tracking is included, and a comprehensive discussion is presented. The current study constitutes a novel contribution to the scientific literature. The simulations provide an important insight into interfacial magnetofluid dynamics of dusty/pure liquid transport, and a useful benchmark for computational fluid dynamics approaches with commercial software.

6.2 Magnetohydrodynamic Immiscible Flow Model

The following assumptions are made for time-dependent interface tracking between two immiscible fluids through a horizontal duct (channel).

Consider the two-dimensional, unsteady MHD laminar flow of electrically conducting, immiscible, dusty, and non-dusty fluids in a horizontal duct. The following assumptions are invoked for time-dependent interface tracking between two immiscible fluids through the duct (channel).

i. Owing to viscosity jump primarily, an interfacial instability occurs.

ii. Both fluids are viscous, incompressible, and are assumed to have electrical conductivity, σ, and can flow in the region between two horizontal parallel non-porous plates. The duct walls (plates) in the *x*-*y* plane, as depicted in Figure 6.1.

iii. Hall current and ion slip effects are present.

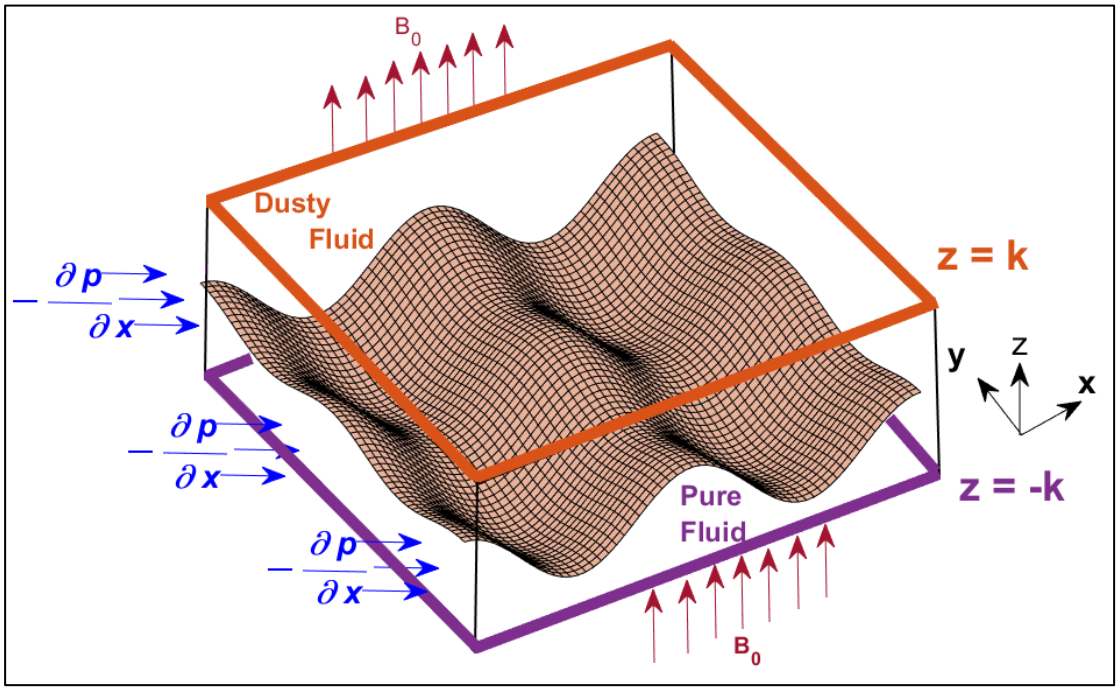

Figure 6.1: Geometry of two-dimensional interface between immiscible dusty and pure fluids in magnetohydrodynamic duct flow

iv. Both plates are stable while the flow gets momentum by the uniform pressure gradient applied from x-direction and maximum flow velocity is U_0.

v. An external uniform static magnetic field B_0 is imposed on the fluids in the z-direction.

vi. The effect of an applied transverse magnetic field on both fluids generates resistance to fluid movement through the Lorentz force, which is orthogonal to the applied magnetic field and produces the following magnetic body force acting on both fluids [74][279]:

$$J \times B_0 = \frac{\sigma {B_0}^2[(1+Bi.Be)u_i+Be*u_j]}{(1+Bi.Be)^2+Be^2}. \tag{6.1}$$

Here J is the current density, B_0 is the external magnetic field, σ is the electric conductivity, Bi is the ion slip parameter, Be is the Hall parameter, u_i, u_j are velocity fields.

vii. Let ρ_d, μ_d be the density and viscosity of dusty fluid which lies in $(l_1 \leq y \leq k)$ and possesses a linear fluid velocity u_d.

viii. The non-dusty fluid has a density ρ_n and viscosity μ_n and occupies the region $(-k \leq y \leq l_1)$ and possesses a linear fluid velocity u_n.

ix. Owing to a viscosity jump primarily, interfacial instability occurs; the evolution of the interface is analyzed by using horizontal attenuation in the initial interface phase.

x. The flow of these immiscible fluids receives momentum in the *x*-direction via applied common pressure gradients with an average density given by $\rho^* = \rho_n + N_s(\rho_d - \rho_n)$ and the viscosity $\mu^* = \mu_n + N_s(\mu_d - \mu_n)$.

xi. We do allow for the possibility of a jump across the interface. The volume fraction function describes the interface movement of immiscible fluids of various densities and viscosities N_i.

xii. Let the initial interface be $l_1 y_m + A_1 cos(B_1 x + A_2 cos(B_2 y))$ where y_m is the average depth of interface, A_1, B_1 are the *x*-directional amplitude and wavenumber, A_2, B_2 are the *y*- directional amplitude and wavenumber.

xiii. The volume fraction function N_i is transported by the average velocity field U following Li and Renardy [81]: $\frac{\partial N_i}{\partial t} + U.\nabla N_i = 0.$ (6.2)

xiv. The mean flow velocity U is driven by a single momentum equation, with the resultant velocity field shared between the transitions:

$$\rho^*\left(\frac{\partial U}{\partial t}+U.\nabla U\right)=-\nabla p+\mu^*\nabla^2U+\rho^*g+F. \tag{6.3}$$

xv. Here g is the gravitational acceleration, F is a body force, and $-\nabla p$ is the applied pressure term. The body force F is modeled as a surface tension force by the continuum surface force (CSF) model, and the surface tension is reconstructed as a volume force

$$F_s=\sigma\omega\nabla N_i,\omega=-\frac{\nabla^2N_i}{\|\nabla N_i\|};\text{ Hence }F_s=-\sigma\frac{\frac{\partial^2N_i}{\partial x^2}+\frac{\partial^2N_i}{\partial y^2}}{\sqrt{\left(\frac{\partial N_i}{\partial x}\right)^2+\left(\frac{\partial N_i}{\partial y}\right)^2}}\left(\frac{\partial N_i}{\partial x}+\frac{\partial N_i}{\partial y}\right). \tag{6.4}$$

xvi. It is also assumed that the particle phase is sufficiently dilute such that the interactions between any two particles are ignored. The dust particle size (radius *r*) is also relatively tiny in scale. Hence the net dust effect on the fluid particles is equivalent to the following additional force per unit volume [24], [74]:

$$D_f=\zeta_T\rho_p\left(U-u_p\right). \tag{6.5}$$

Here $\zeta_T=\frac{6\pi r\mu^*}{m_p}$ is the volume transfer coefficient with an average mass of dust particle m_p , density ρ_p , velocity u_p, and radius r.

Using the above assumption, adopting U^*, U_p as the *x*-directional fluid and particle velocity and V^*, V_p are the *y*-directional fluid and particle velocity, then by virtue of equations (6.1) - (6.5) the governing transport equations for the two-fluid dusty/non-dusty channel flow and two-dimensional interface tracking can be shown to be simulated by the following system of coupled partial differential equations:

$$\frac{\partial N_i}{\partial t}+U^*\frac{\partial N_i}{\partial x}+V^*\frac{\partial N_i}{\partial y}=0, \tag{6.6}$$

$$\frac{\partial U^*}{\partial t}+U^*\frac{\partial U^*}{\partial x}+V^*\frac{\partial U^*}{\partial y}=\begin{pmatrix}\frac{Ge(t)}{\rho^*}+\frac{\mu^*}{\rho^*}\left(\frac{\partial^2 U^*}{\partial x^2}+\frac{\partial^2 U^*}{\partial y^2}\right)-\frac{\zeta_T\rho_p\left(U^*-U_p\right)}{\rho^*}+\frac{\rho^* g}{\rho^*}-\\ -\frac{\sigma {B_0}^2}{\rho^*}\left(\frac{(1+Bi.Be)}{(1+Bi.Be)^2+Be^2}\,U^*-\frac{Be}{(1+Bi.Be)^2+Be^2}\,V^*\right)\\ \frac{\sigma}{\rho^*}\frac{\frac{\partial^2 N_i}{\partial x^2}+\frac{\partial^2 N_i}{\partial y^2}}{\sqrt{\left(\frac{\partial N_i}{\partial x}\right)^2+\left(\frac{\partial N_i}{\partial y}\right)^2}}\left(\frac{\partial N_i}{\partial x}+\frac{\partial N_i}{\partial y}\right)\end{pmatrix}, \tag{6.7}$$

$$\frac{\partial U_p}{\partial t}=\zeta_T\left(U^*-U_p\right), \tag{6.8}$$

$$\frac{\partial V^*}{\partial t}+U^*\frac{\partial V^*}{\partial x}+V^*\frac{\partial V^*}{\partial y}=\begin{pmatrix}\frac{Ge(t)}{\rho^*}+\frac{\mu^*}{\rho^*}\left(\frac{\partial^2 V^*}{\partial x^2}+\frac{\partial^2 V^*}{\partial y^2}\right)-\frac{\zeta_T\rho_p\left(V^*-V_p\right)}{\rho^*}+\frac{\rho^* g}{\rho^*}-\\ -\frac{\sigma {B_0}^2}{\rho^*}\left(\frac{Be}{(1+Bi.Be)^2+Be^2}\,U^*-\frac{(1+Bi.Be)}{(1+Bi.Be)^2+Be^2}\,V^*\right)\\ \frac{\sigma}{\rho^*}\frac{\frac{\partial^2 N_i}{\partial x^2}+\frac{\partial^2 N_i}{\partial y^2}}{\sqrt{\left(\frac{\partial N_i}{\partial x}\right)^2+\left(\frac{\partial N_i}{\partial y}\right)^2}}\left(\frac{\partial N_i}{\partial x}+\frac{\partial N_i}{\partial y}\right)\end{pmatrix}, \tag{6.9}$$

$$\frac{\partial V_p}{\partial t}=\zeta_T\left(V^*-V_p\right). \tag{6.10}$$

Introducing the non-dimensional parameters

$$\left.\begin{gathered}\bar{x}=\frac{x}{k},\bar{y}=\frac{y}{k},\overline{U^*}=\frac{U^*}{U_0},\overline{U_p}=\frac{U_p}{U_0},\overline{V^*}=\frac{V^*}{V_0},\overline{V_p}=\frac{V_p}{V_0},\\ \bar{p}=\frac{p}{\rho^*{U_0}^2},r_1=\frac{\rho_d}{\rho_n},K=6\pi r\mu_d U_0,\\ r_2=\frac{\mu_d}{\mu_n},\bar{t}=\frac{tU_0}{k},r_{nd}=\frac{\rho_n+\rho_d}{\rho_p},Ha^2=\frac{\sigma {B_0}^2k^2}{\mu_n},\\ Ca=\frac{\mu^*U_0}{\sigma},Re=\frac{\rho_n U_0}{\mu_n},Fr=\frac{{U_0}^2}{gk},R=\frac{Kk^2\rho_p}{\mu_d m_p}.\end{gathered}\right\} \tag{6.11}$$

Post-substitution of equation (6.11) into the above equations (6.6) - (6.10), the final dimensionless equations representing the unsteady two-dimensional flow of immiscible dusty and non-dusty fluids with interface evolution in the duct assume the form.

$$\frac{\partial N_i}{\partial t}=-U^*\frac{\partial N_i}{\partial x}-V^*\frac{\partial N_i}{\partial y}, \tag{6.12}$$

$$\frac{\partial U^*}{\partial t} = \begin{pmatrix} \frac{Ge(t)}{1+C_s(r_1-1)} - U^*\frac{\partial U^*}{\partial x} - V^*\frac{\partial U^*}{\partial y} + \frac{(1+C_s(r_2-1))}{Re(1+C_s(r_1-1))}\left(\frac{\partial^2 U^*}{\partial x^2}+\frac{\partial^2 U^*}{\partial y^2}\right) \\ -\frac{Ha^2}{Re(1+C_s(r_1-1))}\left(\frac{(1+Bi.Be)}{(1+Bi.Be)^2+Be^2}\,U^* - \frac{Be}{(1+Bi.Be)^2+Be^2}\,V^*\right) \\ -\frac{R(1+C_s(r_2-1))}{Re(1+C_s(r_1-1))}(U^*-U_p) + \frac{1}{Fr} - \\ \frac{1+C_s(r_1-1)}{Re*Ca(1+C_s(r_2-1))}\frac{\frac{\partial^2 N_i}{\partial x^2}+\frac{\partial^2 N_i}{\partial y^2}}{\sqrt{\left(\frac{\partial N_i}{\partial x}\right)^2+\left(\frac{\partial N_i}{\partial y}\right)^2}}\left(\frac{\partial N_i}{\partial x}+\frac{\partial N_i}{\partial y}\right) \end{pmatrix}, \tag{6.13}$$

$$\frac{\partial U_p}{\partial t} = \frac{Rr_{nd}(1+C_s(r_2-1))}{Re(1+r_1)}(U^*-U_p), \tag{6.14}$$

$$\frac{\partial V^*}{\partial t} = \begin{pmatrix} \frac{(1+C_s(r_2-1))}{Re(1+C_s(r_1-1))}\left(\frac{\partial^2 V^*}{\partial x^2}+\frac{\partial^2 V^*}{\partial y^2}\right) - U^*\frac{\partial V^*}{\partial x} - V^*\frac{\partial V^*}{\partial y} \\ -\frac{Ha^2}{Re(1+C_s(r_1-1))}\left(\frac{Be}{(1+Bi.Be)^2+Be^2}\,U^* - \frac{(1+Bi.Be)}{(1+Bi.Be)^2+Be^2}\,V^*\right) \\ -\frac{R(1+C_s(r_2-1))}{Re(1+C_s(r_1-1))}(V^*-V_p) + \frac{1}{Fr} - \\ \frac{1+C_s(r_1-1)}{Re*Ca(1+C_s(r_2-1))}\frac{\frac{\partial^2 N_i}{\partial x^2}+\frac{\partial^2 N_i}{\partial y^2}}{\sqrt{\left(\frac{\partial N_i}{\partial x}\right)^2+\left(\frac{\partial N_i}{\partial y}\right)^2}}\left(\frac{\partial N_i}{\partial x}+\frac{\partial N_i}{\partial y}\right) \end{pmatrix}, \tag{6.15}$$

$$\frac{\partial V_p}{\partial t} = \frac{Rr_{nd}(1+C_s(r_2-1))}{Re(1+r_1)}(V^*-V_p). \tag{6.16}$$

The classical no-slip and hyper-stick conditions are considered at the boundaries. These conditions can be written as follows in numerical terms.

Initial conditions: At $t \leq 0$, and Boundary conditions: At $t > 0$,

$$\left.\begin{array}{c} U^* = V^* = V_p = U_p = 0, \\ C_i(x,y,0) = a_0\cos(\theta y + b_0\cos(\theta x), \\ U^*(-k,-k,t) = U^*(k,k,t) = 0, \\ U^*(-k,-k,t) = U^*(k,k,t) = 0, \\ V^*(-k,-k,t) = V^*(k,k,t) = 0, \\ U_p(-k,-k,t) = U_p(k,k,t) = 0, \\ V_p(-k,-k,t) = V_p(k,k,t) = 0. \end{array}\right\} \tag{6.17}$$

6.3 Computation of two-dimensional interface

Using the above approximations (1.43) - (1.54), the system of the coupled partial differential equations (6.12)-(6.16) provides the two-dimensional interface profile, and it is obtained by the differential quadrature SSP-RK43 scheme (1.69)-(1.72). The interface is calculated in the fourth step as

For the first stage ($i = 1,2,3 \dots, N$ and $j = 1,2,3 \dots, N$),

$$N_{i_1} = N_{i_0} + \frac{\Delta t}{2}.\left(-U_1^*\left(\sum_{i=1}^{N} a_{ij} N_{i_0}(x_i, y, t)\right) - V_1^* \sum_{j=1}^{N} a_{ij} N_{i_0}\left(x, y_j, t\right)\right), \tag{6.18}$$

$$U_1^* = U^*{}_0(x_i, y, t) + \frac{\Delta t}{2}\left(\begin{array}{c} \frac{Ge(t)}{1+C_s(r_1-1)} - U^*{}_0(x_i, y, t)\left(\sum_{i=1}^{N} a_{ij} U^*{}_0(x_i, y, t)\right) \\ -V_0^*\left(x, y_j, t\right)\left(\sum_{j=1}^{N} a_{ij}^* V_0^*\left(x, y_j, t\right)\right) \\ \frac{\left(1+C_s(r_2-1)\right)}{Re\left(1+C_s(r_1-1)\right)}\left(\begin{array}{c}\sum_{i=1}^{N} b_{ij} U^*{}_0(x_i, y, t) \\ +\sum_{j=1}^{N} b_{ij}^* U_0^*\left(x, y_j, t\right)\end{array}\right) \\ -\frac{Ha^2}{Re\left(1+C_s(r_1-1)\right)}\left(\begin{array}{c}\frac{(1+Bi.Be)}{(1+Bi.Be)^2+Be^2}\, U^*{}_0(x_i, y, t) - \\ \frac{Be}{(1+Bi.Be)^2+Be^2}\, V_0^*\left(x, y_j, t\right)\end{array}\right) \\ -\frac{R\left(1+C_s(r_2-1)\right)}{Re\left(1+C_s(r_1-1)\right)}\left(U^*{}_0(x_i, y, t) - U_p(x_i, y, t)\right) \\ +\frac{1}{Fr} - \frac{1+C_s(r_1-1)}{Re*Ca\left(1+C_s(r_2-1)\right)}. \\ \left(\begin{array}{c}\frac{\left(\begin{array}{c}\sum_{i=1}^{N} b_{ij} N_{i_0}(x_i, y, t) \\ +\sum_{j=1}^{N} b_{ij}^* N_{i_0}(x, y_j, t)\end{array}\right)}{\sqrt{\begin{array}{c}\left(\sum_{i=1}^{N} a_{ij} N_{i_0}(x_i, y, t)\right)^2 \\ +\left(\sum_{j=1}^{N} a_{ij} N_{i_0}(x, y_j, t)\right)^2\end{array}}}\left(\begin{array}{c}\sum_{i=1}^{N} a_{ij} N_{i_0}(x_i, y, t) \\ +\sum_{j=1}^{N} a_{ij} N_{i_0}\left(x, y_j, t\right)\end{array}\right)\end{array}\right)\end{array}\right), \tag{6.19}$$

$$U_{p_1} = U_{p_0}(x_i, y, t) + \frac{\Delta t}{2}\left(\frac{Rr_{nd}\left(1+C_s(r_2-1)\right)}{Re(1+r_1)}\left(U^*{}_0(x_i, y, t) - U_{p_0}(x_i, y, t)\right)\right), \tag{6.20}$$

$$V_1^* = V^*{}_0(x, y_j, t) + \frac{\Delta t}{2}\left(\begin{array}{c} \frac{Ge(t)}{1+C_s(r_1-1)} - U^*{}_0(x_i, y, t)\left(\sum_{i=1}^{N} a_{ij} V^*{}_0(x_i, y, t)\right) \\ -V_0^*(x, y_j, t)\left(\sum_{j=1}^{N} a_{ij}^* V_0^*(x, y_j, t)\right) \\ \frac{(1+C_s(r_2-1))}{Re(1+C_s(r_1-1))}\left(\begin{array}{c}\sum_{i=1}^{N} b_{ij} V^*{}_0(x_i, y, t) \\ +\sum_{j=1}^{N} b_{ij}^* V_0^*(x, y_j, t)\end{array}\right) \\ -\frac{Ha^2}{Re(1+C_s(r_1-1))}\left(\begin{array}{c}\frac{Be}{(1+Bi.Be)^2+Be^2}\, U^*{}_0(x_i, y, t) - \\ \frac{(1+Bi.Be)}{(1+Bi.Be)^2+Be^2}\, V_0^*(x, y_j, t)\end{array}\right) \\ -\frac{R\,(1+C_s(r_2-1))}{Re(1+C_s(r_1-1))}\left(V^*{}_0(x, y_j, t) - V_p(x, y_j, t)\right) \\ +\frac{1}{Fr} - \frac{1+C_s(r_1-1)}{Re*Ca(1+C_s(r_2-1))}. \end{array}\right), \quad (6.21)$$

$$\left(\begin{array}{c} \frac{\left(\begin{array}{c}\sum_{i=1}^{N} b_{ij} N_{i_0}(x_i, y, t) \\ +\sum_{j=1}^{N} b_{ij}^* N_{i_0}(x, y_j, t)\end{array}\right)}{\sqrt{\left(\sum_{i=1}^{N} a_{ij} N_{i_0}(x_i, y, t)\right)^2 + \left(\sum_{j=1}^{N} a_{ij} N_{i_0}(x, y_j, t)\right)^2}} \left(\begin{array}{c}\sum_{i=1}^{N} a_{ij} N_{i_0}(x_i, y, t) \\ +\sum_{j=1}^{N} a_{ij} N_{i_0}(x, y_j, t)\end{array}\right) \end{array}\right)$$

$$V_{p_1} = V_{p_0}(x, y_j, t) + \frac{\Delta t}{2}\left(\frac{Rr_{nd}\,(1+C_s(r_2-1))}{Re(1+r_1)}\left(V^*{}_0(x, y_j, t) - V_{p_0}(x, y_j, t)\right)\right). \quad (6.22)$$

For the second stage

$$N_{i_2} = N_{i_1} + \frac{\Delta t}{2}.\left(-U_2^*\left(\sum_{i=1}^{N} a_{ij} N_{i_1}(x_i, y, t)\right) - V_2^* \sum_{j=1}^{N} a_{ij} N_{i_2}(x, y_j, t)\right), \quad (6.23)$$

$$U_2^* = U^*{}_1 + \frac{\Delta t}{2}\left(\begin{array}{l} \frac{Ge(t)}{1+C_s(r_1-1)} - U^*{}_1(x_i,y,t)\left(\sum_{i=1}^{N} a_{ij}U^*{}_1(x_i,y,t)\right) \\ -V_1^*(x,y_j,t)\left(\sum_{j=1}^{N} a_{ij}^* V_1^*(x,y_j,t)\right) \\ \frac{(1+C_s(r_2-1))}{Re(1+C_s(r_1-1))}\left(\begin{array}{l}\sum_{i=1}^{N} b_{ij}U^*{}_1(x_i,y,t) \\ +\sum_{j=1}^{N} b_{ij}^* U_1^*(x,y_j,t)\end{array}\right) \\ -\frac{Ha^2}{Re(1+C_s(r_1-1))}\left(\begin{array}{l}\frac{(1+Bi.Be)}{(1+Bi.Be)^2+Be^2}\ U^*{}_1(x_i,y,t) - \\ \frac{Be}{(1+Bi.Be)^2+Be^2}\ V_1^*(x,y_j,t)\end{array}\right) \\ -\frac{R\,(1+C_s(r_2-1))}{Re(1+C_s(r_1-1))}\left(U^*{}_1(x_i,y,t) - U_{p_1}(x_i,y,t)\right) \\ +\frac{1}{Fr} - \frac{1+C_s(r_1-1)}{Re*Ca(1+C_s(r_2-1))}. \\ \left(\begin{array}{l}\frac{\left(\begin{array}{l}\sum_{i=1}^{N} b_{ij}N_{i_1}(x_i,y,t) \\ +\sum_{j=1}^{N} b_{ij}^* N_{i_1}(x,y_j,t)\end{array}\right)}{\sqrt{\left(\sum_{i=1}^{N} a_{ij}N_{i_1}(x_i,y,t)\right)^2 + \left(\sum_{j=1}^{N} a_{ij}N_{i_1}(x,y_j,t)\right)^2}}\left(\begin{array}{l}\sum_{i=1}^{N} a_{ij}N_{i_1}(x_i,y,t) \\ +\sum_{j=1}^{N} a_{ij}N_{i_1}(x,y_j,t)\end{array}\right)\end{array}\right)\end{array}\right), \tag{6.24}$$

$$U_{p_2} = U_{p_1} + \frac{\Delta t}{2}\left(\frac{Rr_{nd}\,(1+C_s(r_2-1))}{Re(1+r_1)}\left(U^*{}_1(x_i,y,t) - U_{p_1}(x_i,y,t)\right)\right), \tag{6.25}$$

$$V_2^* = V^*{}_1 + \frac{\Delta t}{2}\left(\begin{array}{l} \frac{Ge(t)}{1+C_s(r_1-1)} - U^*{}_1(x_i,y,t)\left(\sum_{i=1}^{N} a_{ij}V^*{}_1(x_i,y,t)\right) \\ -V_1^*(x,y_j,t)\left(\sum_{j=1}^{N} a_{ij}^* V_1^*(x,y_j,t)\right) \\ \frac{(1+C_s(r_2-1))}{Re(1+C_s(r_1-1))}\left(\begin{array}{l}\sum_{i=1}^{N} b_{ij}V^*{}_1(x_i,y,t) \\ +\sum_{j=1}^{N} b_{ij}^* V_1^*(x,y_j,t)\end{array}\right) \\ -\frac{Ha^2}{Re(1+C_s(r_1-1))}\left(\begin{array}{l}\frac{Be}{(1+Bi.Be)^2+Be^2}\ U^*{}_1(x_i,y,t) - \\ \frac{(1+Bi.Be)}{(1+Bi.Be)^2+Be^2}\ V_1^*(x,y_j,t)\end{array}\right) \\ -\frac{R\,(1+C_s(r_2-1))}{Re(1+C_s(r_1-1))}\left(V^*{}_1(x,y_j,t) - V_{p_1}(x,y_j,t)\right) \\ +\frac{1}{Fr} - \frac{1+C_s(r_1-1)}{Re*Ca(1+C_s(r_2-1))}. \\ \left(\begin{array}{l}\frac{\left(\begin{array}{l}\sum_{i=1}^{N} b_{ij}N_{i_1}(x_i,y,t) \\ +\sum_{j=1}^{N} b_{ij}^* N_{i_1}(x,y_j,t)\end{array}\right)}{\sqrt{\left(\sum_{i=1}^{N} a_{ij}N_{i_1}(x_i,y,t)\right)^2 + \left(\sum_{j=1}^{N} a_{ij}N_{i_1}(x,y_j,t)\right)^2}}\left(\begin{array}{l}\sum_{i=1}^{N} a_{ij}N_{i_1}(x_i,y,t) \\ +\sum_{j=1}^{N} a_{ij}N_{i_1}(x,y_j,t)\end{array}\right)\end{array}\right)\end{array}\right), \tag{6.26}$$

$$V_{p_2} = V_{p_1} + \frac{\Delta t}{2}\left(\frac{Rr_{nd}\,(1+C_s(r_2-1))}{Re(1+r_1)}\left(V^*{}_1(x_i,y,t) - V_{p_1}(x_i,y,t)\right)\right). \tag{6.27}$$

For the third stage-

$$N_{i_3} = \frac{2N_{i_0}}{3} + \frac{N_{i_2}}{3} + \frac{\Delta t}{6}.\left(-U_3^*\left(\sum_{i=1}^{N} a_{ij}N_{i_2}(x_i,y,t)\right) - V_3^*\sum_{j=1}^{N} a_{ij}N_{i_2}\left(x,y_j,t\right)\right), \tag{6.28}$$

$$U_3^* = \frac{2U_0^*}{3} + \frac{U_2^*}{3} + \frac{\Delta t}{6}\left(\begin{array}{c} \frac{Ge(t)}{1+C_s(r_1-1)} - U^*{}_2(x_i,y,t)\left(\sum_{i=1}^{N} a_{ij}U^*{}_2(x_i,y,t)\right) \\ -V_2^*\left(x,y_j,t\right)\left(\sum_{j=1}^{N} a_{ij}^*V_2^*\left(x,y_j,t\right)\right) \\ \frac{(1+C_s(r_2-1))}{Re(\,1+C_s(r_1-1))}\left(\begin{array}{c}\sum_{i=1}^{N} b_{ij}U^*{}_2(x_i,y,t) \\ +\sum_{j=1}^{N} b_{ij}^*U_2^*\left(x,y_j,t\right)\end{array}\right) \\ -\frac{Ha^2}{Re(\,1+C_s(r_1-1))}\left(\begin{array}{c}\frac{(1+Bi.Be)}{(1+Bi.Be)^2+Be^2}\;U^*{}_2(x_i,y,t) - \\ \frac{Be}{(1+Bi.Be)^2+Be^2}\;V_2^*\left(x,y_j,t\right)\end{array}\right) \\ -\frac{R\,(1+C_s(r_2-1))}{Re(\,1+C_s(r_1-1))}\left(U^*{}_2(x_i,y,t) - U_{p_2}(x_i,y,t)\right) \\ +\frac{1}{Fr} - \frac{1+C_s(r_1-1)}{Re*Ca(\,1+C_s(r_2-1))}. \\ \left(\begin{array}{c}\frac{\left(\begin{array}{c}\sum_{i=1}^{N} b_{ij}N_{i_2}(x_i,y,t) \\ +\sum_{j=1}^{N} b_{ij}^*N_{i_2}(x,y_j,t)\end{array}\right)}{\sqrt{\begin{array}{c}\left(\sum_{i=1}^{N} a_{ij}N_{i_2}(x_i,y,t)\right)^2 \\ +\left(\sum_{j=1}^{N} a_{ij}N_{i_2}(x,y_j,t)\right)^2\end{array}}}\left(\begin{array}{c}\sum_{i=1}^{N} a_{ij}N_{i_2}(x_i,y,t) \\ +\sum_{j=1}^{N} a_{ij}N_{i_2}\left(x,y_j,t\right)\end{array}\right)\end{array}\right)\end{array}\right), \tag{6.29}$$

$$U_{p_3} = \frac{2U_{p_0}}{3} + \frac{U_{p_2}}{3} + \frac{\Delta t}{6}\left(\frac{Rr_{nd}\,(1+C_s(r_2-1))}{Re(1+r_1)}\left(U^*{}_2(x_i,y,t) - U_{p_2}(x_i,y,t)\right)\right), \tag{6.30}$$

$$V_3^* = \frac{2V_0^*}{3} + \frac{V_2^*}{3} + \frac{\Delta t}{6}\left(\begin{array}{c} \frac{Ge(t)}{1+C_s(r_1-1)} - U^*{}_2(x_i,y,t)\left(\sum_{i=1}^{N} a_{ij}V^*{}_2(x_i,y,t)\right) \\ -V_2^*(x,y_j,t)\left(\sum_{j=1}^{N} a_{ij}^* V_2^*(x,y_j,t)\right) \\ \frac{(1+C_s(r_2-1))}{Re(1+C_s(r_1-1))}\left(\begin{array}{c}\sum_{i=1}^{N} b_{ij}V^*{}_2(x_i,y,t) \\ +\sum_{j=1}^{N} b_{ij}^* V_2^*(x,y_j,t)\end{array}\right) \\ -\frac{Ha^2}{Re(1+C_s(r_1-1))}\left(\begin{array}{c}\frac{Be}{(1+Bi.Be)^2+Be^2}\ U^*{}_2(x_i,y,t) - \\ \frac{(1+Bi.Be)}{(1+Bi.Be)^2+Be^2}\ V_2^*(x,y_j,t)\end{array}\right) \\ -\frac{R\,(1+C_s(r_2-1))}{Re(1+C_s(r_1-1))}\left(V^*{}_2(x,y_j,t) - V_{p_2}(x,y_j,t)\right) \\ +\frac{1}{Fr} - \frac{1+C_s(r_1-1)}{Re*Ca(1+C_s(r_2-1))}. \\ \left(\begin{array}{c} \frac{\left(\begin{array}{c}\sum_{i=1}^{N} b_{ij}N_{i_2}(x_i,y,t) \\ +\sum_{j=1}^{N} b_{ij}^* N_{i_2}(x,y_j,t)\end{array}\right)}{\sqrt{\left(\sum_{i=1}^{N} a_{ij}N_{i_2}(x_i,y,t)\right)^2 + \left(\sum_{j=1}^{N} a_{ij}N_{i_2}(x,y_j,t)\right)^2}}\left(\begin{array}{c}\sum_{i=1}^{N} a_{ij}N_{i_2}(x_i,y,t) \\ +\sum_{j=1}^{N} a_{ij}N_{i_2}(x,y_j,t)\end{array}\right) \end{array}\right) \end{array}\right), \tag{6.31}$$

$$V_{p_3} = \frac{2V_{p_0}}{3} + \frac{V_{p_2}}{3} + \frac{\Delta t}{6}\left(\frac{Rr_{nd}\,(1+C_s(r_2-1))}{Re(1+r_1)}\left(V^*{}_2(x_i,y,t) - V_{p_2}(x_i,y,t)\right)\right). \tag{6.32}$$

For the fourth stage-

$$N_i = N_{i_3} + \frac{\Delta t}{2}.\left(-U^*\left(\sum_{i=1}^{N} a_{ij}N_{i_3}(x_i,y,t)\right) - V^*\sum_{j=1}^{N} a_{ij}N_{i_3}(x,y_j,t)\right), \tag{6.33}$$

$$U^* = U^*{}_3 + \frac{\Delta t}{2}\left(\begin{array}{c} \frac{Ge(t)}{1+C_s(r_1-1)} - U^*{}_3(x_i,y,t)\left(\sum_{i=1}^{N} a_{ij}U^*{}_3(x_i,y,t)\right) \\ -V_3^*(x,y_j,t)\left(\sum_{j=1}^{N} a_{ij}^* V_3^*(x,y_j,t)\right) \\ \frac{(1+C_s(r_2-1))}{Re(1+C_s(r_1-1))}\left(\begin{array}{c}\sum_{i=1}^{N} b_{ij}U^*{}_3(x_i,y,t) \\ +\sum_{j=1}^{N} b_{ij}^* U_3^*(x,y_j,t)\end{array}\right) \\ -\frac{Ha^2}{Re(1+C_s(r_1-1))}\left(\begin{array}{c}\frac{(1+Bi.Be)}{(1+Bi.Be)^2+Be^2}\,U^*{}_3(x_i,y,t) - \\ \frac{Be}{(1+Bi.Be)^2+Be^2}\,V_3^*(x,y_j,t)\end{array}\right) \\ -\frac{R\,(1+C_s(r_2-1))}{Re(1+C_s(r_1-1))}\left(U^*{}_3(x_i,y,t) - U_{p_3}(x_i,y,t)\right) \\ +\frac{1}{Fr} - \frac{1+C_s(r_1-1)}{Re*Ca(1+C_s(r_2-1))}. \\ \left(\begin{array}{c}\frac{\left(\begin{array}{c}\sum_{i=1}^{N} b_{ij}N_{i_3}(x_i,y,t) \\ +\sum_{j=1}^{N} b_{ij}^* N_{i_3}(x,y_j,t)\end{array}\right)}{\sqrt{\left(\sum_{i=1}^{N} a_{ij}N_{i_3}(x_i,y,t)\right)^2 + \left(\sum_{j=1}^{N} a_{ij}N_{i_3}(x,y_j,t)\right)^2}}\left(\begin{array}{c}\sum_{i=1}^{N} a_{ij}N_{i_3}(x_i,y,t) \\ +\sum_{j=1}^{N} a_{ij}N_{i_3}(x,y_j,t)\end{array}\right)\end{array}\right)\end{array}\right), \tag{6.34}$$

$$U_p = U_{p_3} + \frac{\Delta t}{2}\left(\frac{Rr_{nd}\,(1+C_s(r_2-1))}{Re(1+r_1)}\left(U^*{}_3(x_i,y,t) - U_{p_3}(x_i,y,t)\right)\right), \tag{6.35}$$

$$V^* = V^*{}_3 + \frac{\Delta t}{2}\left(\begin{array}{c} \frac{Ge(t)}{1+C_s(r_1-1)} - U^*{}_3(x_i,y,t)\left(\sum_{i=1}^{N} a_{ij}V^*{}_3(x_i,y,t)\right) \\ -V_3^*(x,y_j,t)\left(\sum_{j=1}^{N} a_{ij}^* V_3^*(x,y_j,t)\right) \\ \frac{(1+C_s(r_2-1))}{Re(1+C_s(r_1-1))}\left(\begin{array}{c}\sum_{i=1}^{N} b_{ij}V^*{}_3(x_i,y,t) \\ +\sum_{j=1}^{N} b_{ij}^* V_3^*(x,y_j,t)\end{array}\right) \\ -\frac{Ha^2}{Re(1+C_s(r_1-1))}\left(\begin{array}{c}\frac{Be}{(1+Bi.Be)^2+Be^2}\,U^*{}_3(x_i,y,t) - \\ \frac{(1+Bi.Be)}{(1+Bi.Be)^2+Be^2}\,V_3^*(x,y_j,t)\end{array}\right) \\ -\frac{R\,(1+C_s(r_2-1))}{Re(1+C_s(r_1-1))}\left(V^*{}_3(x,y_j,t) - V_{p_3}(x,y_j,t)\right) \\ +\frac{1}{Fr} - \frac{1+C_s(r_1-1)}{Re*Ca(1+C_s(r_2-1))}. \\ \left(\begin{array}{c}\frac{\left(\begin{array}{c}\sum_{i=1}^{N} b_{ij}N_{i_3}(x_i,y,t) \\ +\sum_{j=1}^{N} b_{ij}^* N_{i_3}(x,y_j,t)\end{array}\right)}{\sqrt{\left(\sum_{i=1}^{N} a_{ij}N_{i_3}(x_i,y,t)\right)^2 + \left(\sum_{j=1}^{N} a_{ij}N_{i_3}(x,y_j,t)\right)^2}}\left(\begin{array}{c}\sum_{i=1}^{N} a_{ij}N_{i_3}(x_i,y,t) \\ +\sum_{j=1}^{N} a_{ij}N_{i_3}(x,y_j,t)\end{array}\right)\end{array}\right)\end{array}\right), \tag{6.36}$$

$$V_p = V_{p_3} + \frac{\Delta t}{2}\left(\frac{Rr_{nd}\,(1+C_s(r_2-1))}{Re(1+r_1)}\left(V^*{}_3(x_i,y,t) - V_{p_3}(x_i,y,t)\right)\right). \quad (6.37)$$

In every stage, the initial and boundary conditions are taken as Equation (6.17) with $k = 1$.

6.4 Results And Discussion

Figure 6.2-Figure 6.18 shows the evolution of the interface between the two (dusty and non-dusty) liquids for the effects of critical parameters, including time, amplitude, wave number, particulate concentration parameter, and applied pressure gradients.

Figure 6.2-Figure 6.6 visualize the interface track at different times. It is apparent that initially, the interface is smooth with small-time but owing to externally applied constant pressure gradient and upper region particulate concentration parameter, a significant vertical prolongation is observed. The undulating pattern repeats quicker for a more extended period. Then, the interface (topology) develops and finally becomes stable. The particulate concentration and magnetic parameters strongly influence the flow, which is also affected by different viscosity ratios. Hence, a very substantial sinusoidal interface is computed, first at a short time. After that, the wave's crest travels rapidly; however, the wave's amplitude decreases at high time values.

Figure 6.7 indicates that in the absence of particulate concentration parameter (non-dusty case, i. e. no contamination) and magnetic parameter (electrically non-conducting case, i. e. *Ha = 0*), it is evident that greater smoothness is achieved at the interface and stability in the interface is established faster. It is important to note that the inclusion of Hall and ion slip parameters modifies the classical Lorentz body force terms. For example, in Eqn. (6.9), the new terms are of the form, $-\frac{\sigma {B_0}^2}{\rho^*}\left(\frac{Be}{(1+Bi.Be)^2+Be^2}\,U^* - \frac{(1+Bi.Be)}{(1+Bi.Be)^2+Be^2}\,V^*\right)$. The Hall and ion slip effects will change the overall influence of the magnetic field on the regime. Hartmann-Stokes layers at the boundaries of the duct

will be modified, and individual fluid and particle velocities will also be affected. This will morph the interface topology in the duct since the change in the magnitude and direction of the current density leads to a significant modification in Lorentz electromagnetic force. Magnetized two-fluid dusty/non-dusty duct flow will deviate significantly from classical two-fluid dusty/non-dusty flow characteristics. This will be prominent at the interface as computed in Figure 6.7. The simultaneous effects of time and pressure gradient (considered in due course) will also significantly act to distort the interface structure.

The pattern of the interface growth with all three applied pressure gradients (constant, periodic, and decaying) at a given time (t=10) is depicted in Figure 6.6**,** Figure 6.7**,** and Figure 6.9**.** Inspection of these plots reveals that the displacement is initially large at the wave's peak and then significantly decreases. The profiles of the constant pressure gradient are more stable than in the decaying pressure gradient case, and the interface of decaying pressure is smoother and more stable than in the periodic pressure gradient case. Therefore, the nature of the pressure gradient applied in the two-fluid duct flow regime significantly influences the topology of the interface.

Figure 6.10-Figure 6.12 represents the effect of a constant pressure gradient on the interface profile, and it is observed that the smoothness of the interface is maintained with lower pressure magnitudes. However, the sinusoidal undulation occurs faster with higher pressure gradient values, and the interface does not become stable as the number of cusps on the curvature is observed to grow.

It is observed from Figure 6.13-Figure 6.15 that for a small value of wave number, the interface is stable, and the vertical undulation with some cusp on the curvature is witnessed with a more excellent value of θ. It is noteworthy that in the computations, the wavenumbers value varies from π to 3π. Over this range a notable evolution in the interface topology is computed.

It is also noticed that the qualitative characteristics of this flow are sustained. As expected, the interface starts to shift vertically and does not break the smoothness of curvature if the amplitude is enhanced (see Figure 6.16-Figure 6.18).

Overall, the MCB-DQM computations successfully capture the evolution in the interface with different combinations of magnetic, concentration (dusty), and pressure gradient parameters. Excellent visualization is achieved, and the plots provide a useful benchmark for alternative computational fluid dynamics (CFD) simulations with commercial software tools, including ANSYS FLUENT, ADINA-F, and CFD-ACE.

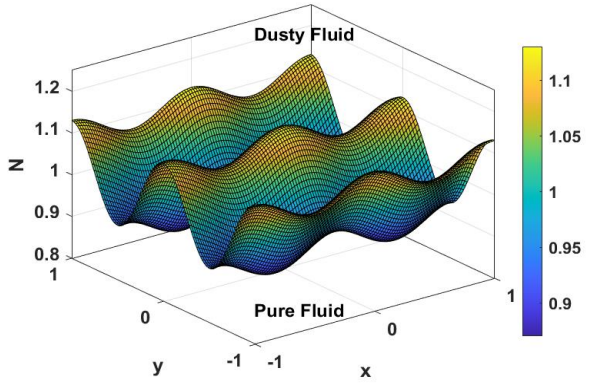

Figure 6.2:Two-dimension interface at *t=0.1*

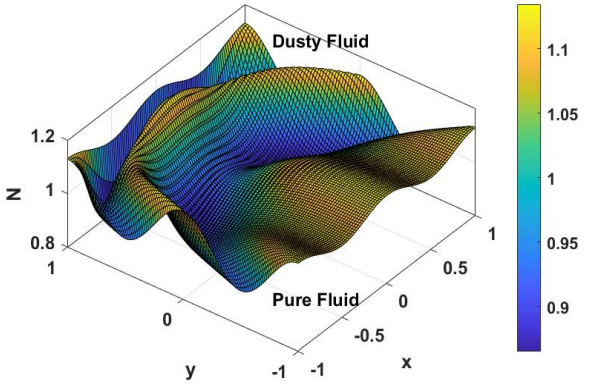

Figure 6.3: Two-dimension interface at *t=0.5*

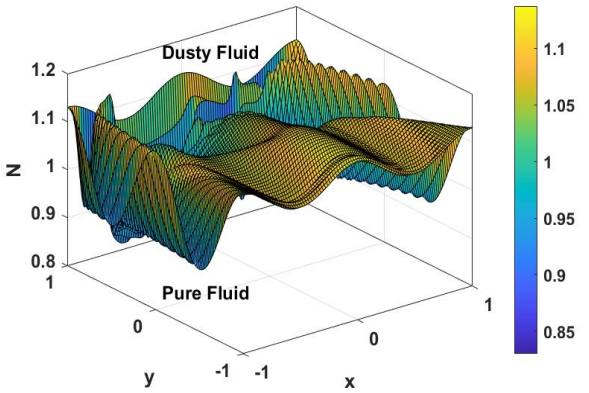

Figure 6.4:Two-dimension interface at *t=1*

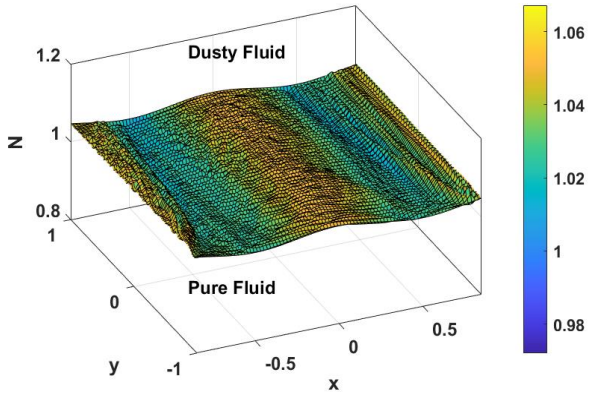

Figure 6.5:Two-dimension interface at *t=5*

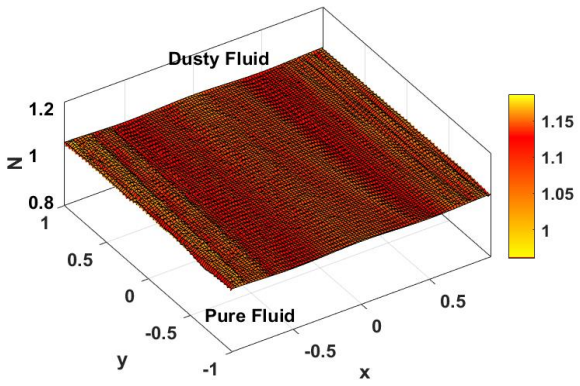

Figure 6.6:Two-dimension interface at *t=10*

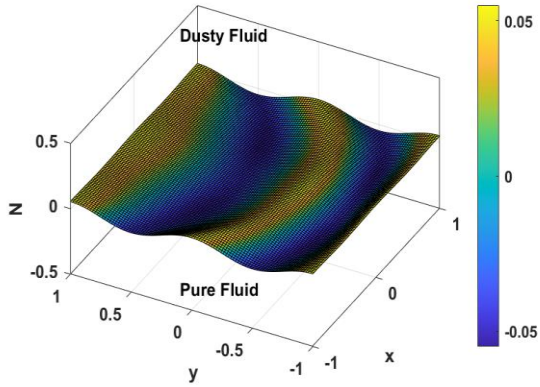

Figure 6.7:Two-dimension interface at *t=0.5, R=Ha=Be=Bi=0*

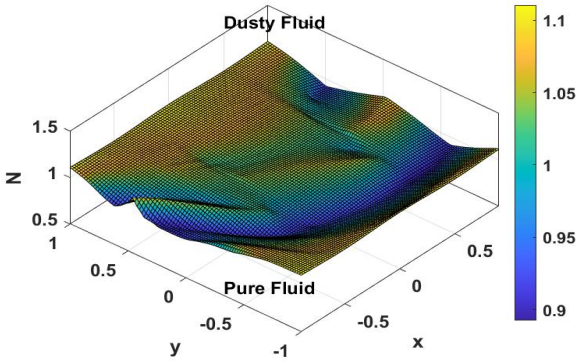

Figure 6.8:Two-dimension interface with decaying pressure gradient at *t=10*

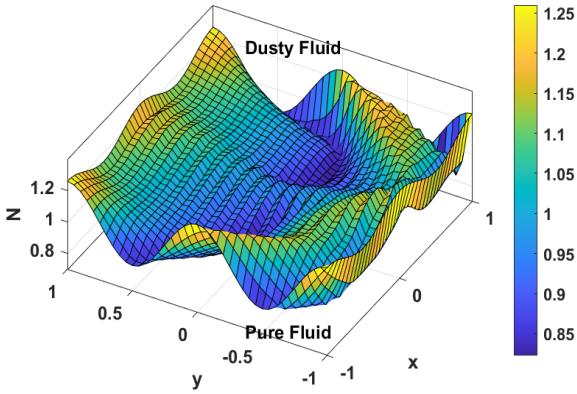

Figure 6.9:Two-dimension interface with periodic pressure gradient at *t=10*

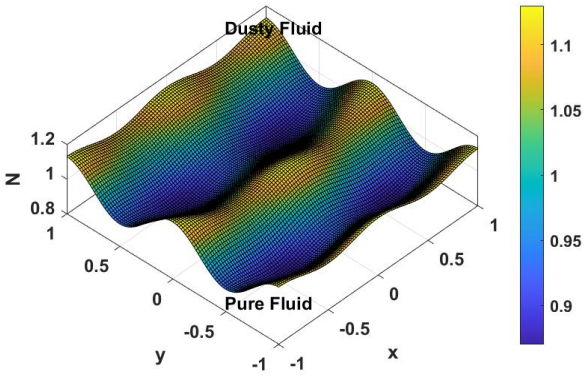

Figure 6.10: 2D interface with *Ge=0,t=1*

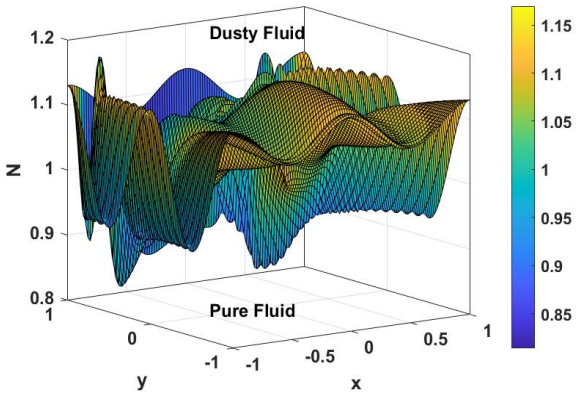

Figure 6.11: 2D interface with *Ge=20, t=1*

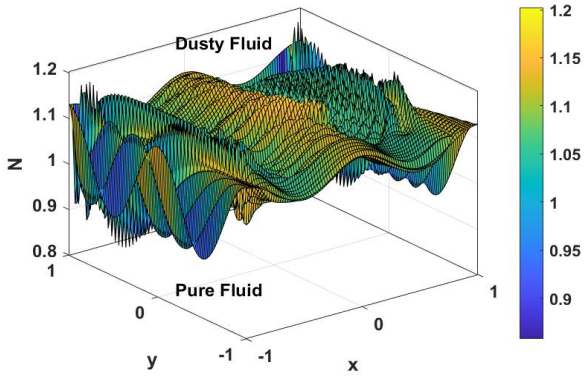

Figure 6.12: 2D interface with *Ge=50 at t=1*

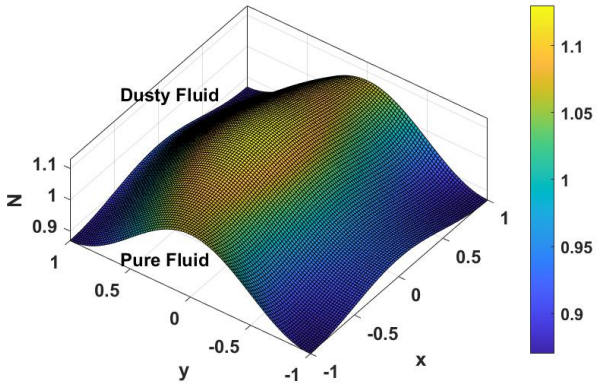

Figure 6.13: 2D interface at $\theta = \pi$

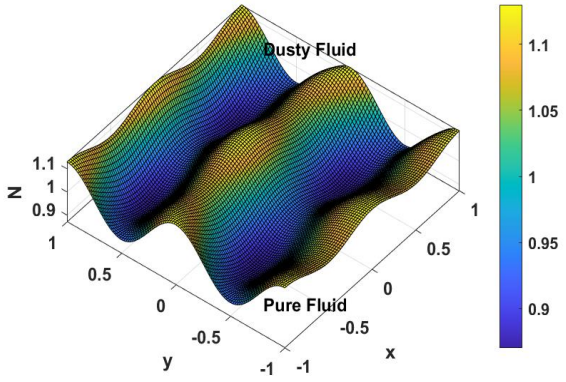

Figure 6.14:Two-dimension interface at $\theta=2\pi$

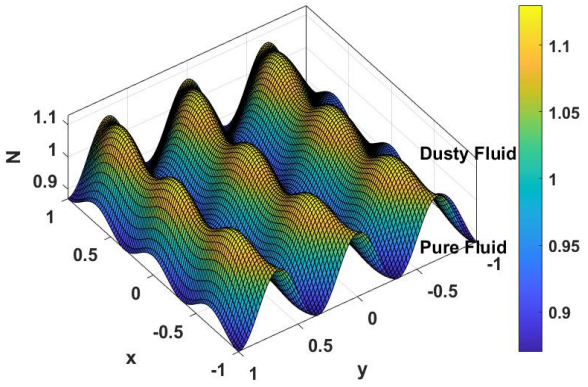

Figure 6.15:Two-dimension interface at $\theta=3\pi$

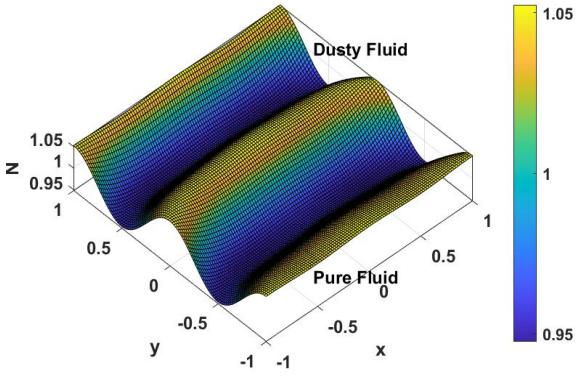

Figure 6.16: 2D interface track at $a_0 = b_0 = 0.05$

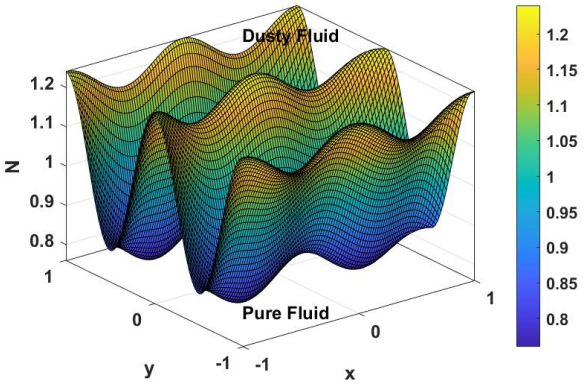

Figure 6.17: 2D interface track at $a_0 = b_0 = 0.1$

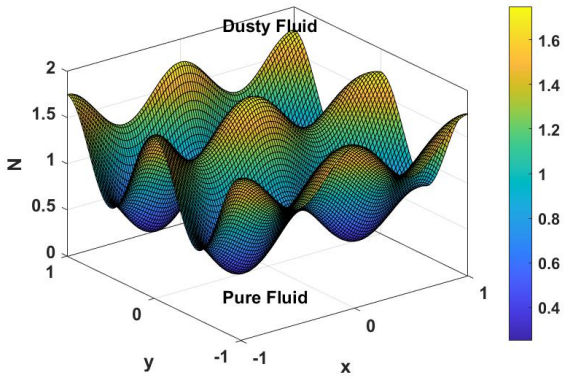

Figure 6.18: Two-dimension interface track with $a_0 = b_0 = 0.5$

6.5 Conclusion

A theoretical and numerical study of the interface tracking in the unsteady two-dimensional flow of electrically conducting immiscible dusty and non-dusty fluids through a horizontal duct has been presented. Hall current and ion slip effects are incorporated into the model. Saffman's two-phase model is deployed for the dusty fluid, and the Newtonian model is used for the non-dusty liquid. Hyper-stick and no-slip boundary conditions are utilized. A single momentum equation is coupled for evaluating the interface profiles using the VOF (Volume of fluid) approach. The modified cubic B-spline differential quadrature method (MCB-DQM) has been successfully applied to simulate the flow. Interface tracking has been examined at different values of Froude number, capillary number, magnetic (Hartmann) number, Hall and ion slip numbers, wave number, Reynolds number, amplitude, viscosity ratio, and time on the interface profile is computed. Three applied pressure gradients have also been examined for constrained values of the control parameters: constant $Ge = 10$, periodic $Ge = 10Sin(t)$, and decaying $Ge = e^{-t}$. Detailed visualization of the interface tracking is included. The main findings of the present simulations can be summarized as follows:

(i) In the absence of particulate concentration parameter (non-dusty case, i. e., no contamination) and magnetic parameter (electrically non-conducting case, i. e. $Ha = 0$), a greater smoothness is achieved at the interface, and stability in the interface is established faster. The presence of magnetic body force, Hall current, and ionslip effects in addition to dusty effects (particle concentration presence), therefore, delays the attainment of a stable interface and reduces the smoothness.

(ii) A smoother interface is computed in a short time. Still, it is significantly elongated in the vertical direction due to the effects of externally applied constant pressure gradient and dustiness (particulate concentration) in the upper zone above the interface. A pronounced sinusoidal interface is computed, first at a short time, and subsequently, the wave's crest travels rapidly, although there is a decrement in the height of the wave at high time values.

(iii) For all three cases of applied pressure gradients (constant, periodic, and decaying) at a given time ($t=10$), the displacement is initially large at the peak of the wave and subsequently is depleted substantially. The profiles of the constant pressure gradient are more stable than the decaying pressure gradient case. In contrast, the interface of decaying pressure is smoother and more stable than the periodic pressure gradient case.

(iv) At low wavenumber values, the interface is stable. However, a vertical undulation with some cusp on the curvature is computed with a more significant wave number.

(v) For the constant pressure gradient, the smoothness of the interface is maintained with lower pressure magnitudes. However, the sinusoidal undulation occurs faster with higher pressure gradient values, and the interface does not become stable as the number of cusps on the curvature is observed to increase.

The current MCB-DQM approach has robustly simulated the evolution numerically in the interface with different magnetic, concentration (dusty), and pressure gradient parameters. However, only dusty and Newtonian fluids have been considered. Future investigations may address electro-conductive polymers (ECPs), which are also of great interest in robotic, nuclear, and chemical process engineering duct transport. These may be simulated with viscoelastic flow models combined with the Saffman dusty model, and efforts in this direction are currently being explored.

Chapter 7

Conclusions and recommendations

7.1 Considered problems and main findings

For the unsteady flow problems of some immiscible fluids, this thesis presents a detailed mathematical model and numerical solution using the modified cubic B-spline-Differential Quadrature method (MCB-DQM).

In Chapter 2, the unsteady flow of two immiscible (Eringen micropolar and Newtonian) fluids through a horizontal channel with stable and moving interface schemes has been considered. An externally imposed continuous pressure gradient induces the flow in both the schemes and the system of coupled partial differential is formulated for fluid flow movement. The velocity of both fluids and angular momentum of Eringen micropolar fluids have been calculated through MCB-DQM. The effects of critical parameters on fluid velocities and interface profiles can be summarized as

i. The micropolar fluid is exclusively present in the lower zone, and the influence of the micropolar component on fluid velocity has been seen in both regions under the stable interface scheme.

ii. Under the stable interface scheme, the fluid velocities and micro-rotation rises for static pressure, fluctuate with periodic, and decline with decaying pressure gradients with time

iii. Under the moving scheme, the interface's vertical extending is prominent at first, and the undulating repetition happens faster. The interface remains stable for a more extended period when a constant pressure gradient is provided.

iv. The interface becomes stable quickly with time as the micropolar parameter is curtailed for the case where a constant pressure gradient induces the flow under the moving scheme

Chapter 3 explored the unsteady flow of two immiscible Eringen micropolar and Saffman dusty fluids in a horizontal channel with both stable and moving interface schemes. The derived system of the coupled partial differential equation for both scheme flows is solved by strong stability MCB-DQM. The effects of the emerging hydrodynamic control parameters on fluid and particle velocities, microrotation (angular velocity component), and interface evolution have been computed and visualized graphically. The core findings of the present analysis can be summarized in the following points:

i. Under the scheme-2a (Dusty and micropolar fluid with stable interface) flow, accelerating, oscillating and decelerating behavior in the fluids and particle velocities and micro-rotation profile with time is observed in respective zones depending on whether the hydrodynamics is triggered by constant, periodic, or decaying pressure gradients, respectively.

ii. The intensities of the fluid and particle velocities and the micro-rotation grow with the constant pressure gradient.

iii. For all scenarios of an applied pressure gradient, elevating the Reynolds number leads to significant improvement in fluid and particle velocities, as well as a micro-rotation profile under the scheme-2a

iv. However, the micropolar fluid is confined to the lower zone. Still, it causes a decrease in both fluid and particle linear velocities and micro-rotation magnitudes (i.e., slowing in the angular spin of the micro-elements in the micropolar fluid) when the flow is induced by all scenarios of an applied pressure gradient.

v. Raising the dust particle concentration parameter enhances particle velocity in scheme-2a flow in all three applied pressure gradient instances. On the other

hand, this parameter is coupled to Saffman dusty fluid, which is only seen in the higher zone. It affects the lower zone fluid's microrotation profile; as a result, microrotation profiles elevate somewhat for constant and periodic pressure gradient situations and fall slightly for decaying pressure cases.

vi. Under scheme-2b (Dusty and micropolar fluid with moving interface), tracking the interface between the two immiscible liquids is also discovered with variation in time and other fluid parameters. It is emphasized that initially, the vertical elongation of the interface is significant, and after that, the shape evolves with time. Hence the undulating sequence occurs faster for a longer duration of time. The qualitative features of this flow are retained with variation in Reynolds number, time, amplitude, wave number, particulate concentration parameter, viscosity ratio, and applied pressure gradients.

Chapter 4 includes the generalized Couette flow of two immiscible Saffman dusty (fluid-particle suspension) and pure (nondusty) fluids through the horizontal duct with heat transfer. The heat transfer, mass transfer, and interface tracking analysis are numerically proposed using MCB-DQM. The flow is explored under three different geometries: first for nonporous plates with the stable interface, second for porous plates with the sight of suction and injection, and third for nonporous plates with interface evolution.

i. In the limiting scenario of single nondusty fluid flow, the exact solution is shown to be in good agreement with the modified cubic B-spline differential quadrature technique.

ii. For the flow under schemes 3a (Dusty and non-dusty fluid through porous plates) and 3b (Dusty and non-dusty fluid through non-porous plates), an increasingly oscillatory and decreasing behavior in the fluid's velocities and particle velocity with time is computed when the flow is induced by constant, periodic, and decaying pressure gradients, respectively.

iii. Increasing the Reynolds number in the stable interface schemes generates a marked enhancement in the fluid and particle-phase velocities for all three applied constant, periodic, and decaying pressure gradient cases. However, in the case of periodic gradient under scheme-3b, the velocities are observed to be decreasing near the interface.

iv. Elevation in the particle concentration parameter increases the velocities of dust particles with all three applied pressure gradient scenarios in the stable interface schemes

v. In scheme-3a, an increase in the ratio of viscosities is associated with a significant decrease in dust particle and fluid velocities in the dusty fluid area and a slight decrease in pure fluid velocities. The conduct of fluids and particle velocities for the periodic pressure gradient differs from the constant and decaying pressure gradient scenario in the scheme-3b flow. When a periodic pressure gradient is applied, the velocity profiles in both locations decrease. In contrast, pure fluid velocity rises moderately for both constant and decaying applied pressure gradients, and dusty fluid and particle velocity change from declining to increasing trends towards the interface. The suction effect and the coupling nature of fluids might account for the observed differences.

vi. The qualitative features of fluids and particle temperature profiles under scheme-3a and 3b are similar to all control parameters.

vii. Dust particle and fluid temperatures in respective regions increase with an enhancement in time, Eckert number, and the ratio of viscosities (i.e., heating of the channeling regime). In contrast, they decrease with Reynolds and Prandtl numbers (i.e., cooling of the channeling regimes). Temperatures decline slightly in both regions with an increase in particle concentration parameters.

viii. Elevation in the ratio of thermal conductivities produces a notable enhancement in temperature magnitudes of both dust particles and fluid in region II. However, the pure fluids do not exhibit any shift in the temperature.

ix. Under scheme-3c (Dusty and non-dusty fluid with moving interface), tracking the interface between the two immiscible liquids is also simulated with varying times. It is noticed that initially, the vertical elongation of the interface is significant, and subsequently, the topology evolves with time. Therefore, the undulating sequence occurs faster for a more considerable time, and the qualitative features of this flow are retained with high time and amplitude.

Chapter 5 aims to investigate the effects of Ion slip, Viscous dissipation, Joule heating, and Hall current on time-dependent plain and genialized Couette flow of two immiscible fluids. In the horizontal duct with heat transmission, two non-Newtonian incompressible magnetohydrodynamic fluids are considered: micropolar and dusty (fluid-particle suspension).

i. The Modified cubic B-spline differential quadrature method agrees with obtained numerical results in the limiting case of fluid flow, with the exact solution.

ii. Fluid velocities, microrotation, and temperature profiles of fluids and particles accelerate with time.

iii. The micropolar parameter η_1 only available in lower region fluids, but it also affects the velocities and temperatures of upper region fluids. Similarly micropolar parameter η_2 of the upper region, fluid affects the velocities and temperatures of lower region fluids.

iv. The Hall(Be) and Ion-slip(Bi) parameters are increasing the velocity, temperature of both fluids, and angular velocity of micropolar dusty fluid while the microrotation of micropolar fluid is lessening it.

v. Hartmann number (Ha^2) is inversely proportional to the velocities of the fluid and particle phases and their temperatures

vi. Reynold's number *(Re)* affects the fluid and particle velocities and their temperatures with a directly proportional relation. While *(Re)* is inversely proportional to the angular velocity.

Numerical computation of the interface tracking in the unsteady two-dimensional stream of electrically conducting immiscible dusty (Saffman's two-phase) and nondusty (Newtonian model) fluids via a horizontal channel is provided in Chapter 6. The model features Hall current and ion slip characteristics, and the detailed visualization of the interface tracking is included with the effect of Froude number, capillary number, magnetic (Hartmann) number, Hall and ion slip numbers, wave number, Reynolds number, amplitude, viscosity ratio, and time on the interface values. The main findings of the present simulations can be summarized as follows:

i. In the absence of the particle concentration parameter (nondusty case, i. e. no contaminants) and the magnetic parameter (electrically non-conducting issue, i. e. $Ha = 0$), the interface achieves more smoothness establishes stability sooner. The existence of magnetic body force, Hall current, ion slip effects, and dusty effects (the presence of particle concentration) causes a delay in the achievement of a stable interface and lowers smoothness.

ii. The effects of an externally imposed continuous pressure gradient and dustiness (particle density) in the top section just above the interface result in a smoother interface that is calculated in a short amount of time but is considerably extended in the vertical direction. A prominent sinusoidal interface is computed, initially at relatively low time values. Then the wave's crest travels swiftly, while the elevation of the wave declines at large time values.

iii. The interface tracks by an externally enforced constant pressure gradient are generally more stable than decaying pressure gradient profiles for high time. In contrast, the traces of the decaying pressure gradient are smoother and more stable than the periodic pressure gradient.

7.2 The main difficulties encountered.

The nonlinear system of coupled partial differential equations for immiscible fluid flow temperature field is the most complex to solve. However, numerical techniques can be implemented. It's intended to employ correct approximations of derivatives to convert nonlinear differential equations to a system of equations. In the case of numerical approaches, the stability of convergence criteria must be checked, and proper premises must be established to use these boundary and interfacial conditions.

7.3 Recommendations for future work

The current MCB-DQM approach systematically simulates the immiscible fluid flow problems with interface evolution. However, only micropolar, dusty, nondusty, micropolar-dusty, and Newtonian fluids have been considered with different magnetic, concentration (dusty), micro-rotation, and pressure gradient parameters. Future investigations may address electro-conductive polymers (ECPs), which are also of great interest in robotic, nuclear, and chemical process engineering duct transport. These may be simulated with viscoelastic flow models combined with the Saffman dusty model, and efforts in this direction are currently being explored. Excellent visualization is achieved, and the plots provide a valuable benchmark for alternative computational fluid dynamics (CFD) simulations with commercial software tools, including ANSYS FLUENT, ADINA-F, and CFD-ACE.

References

[1] M. Devakar and A. Raje, “A study on the unsteady flow of two immiscible micropolar and Newtonian fluids through a horizontal channel: A numerical approach,” *Eur. Phys. J. Plus*, vol. 133, no. 5, 2018, doi: 10.1140/epjp/i2018-12011-5.

[2] M. Devakar and A. Raje, “A magnetohydrodynamic time dependent model of immiscible newtonian and micropolar fluids through a porous channel: A numerical approach,” *J. Appl. Fluid Mech.*, vol. 12, no. 2, pp. 603–615, 2019, doi: 10.29252/jafm.12.02.28548.

[3] M. Devakar and A. Raje, “Modelling and analysis of the unsteady flow and heat transfer of immiscible micropolar and Newtonian fluids through a pipe of circular cross section,” *J. Brazilian Soc. Mech. Sci. Eng.*, vol. 40, no. 6, 2018, doi: 10.1007/s40430-018-1233-2.

[4] R. Dyja, E. Gawronska, and A. Grosser, “Numerical Problems Related to Solving the Navier-Stokes Equations in Connection with the Heat Transfer with the Use of FEM,” in *Procedia Engineering*, 2017, vol. 177, pp. 78–85, doi: 10.1016/j.proeng.2017.02.187.

[5] A. Eringen, “Theory of Micropolar Fluids,” *Indiana Univ. Math. J.*, vol. 16, no. 1, pp. 1–18, 1966, doi: 10.1512/iumj.1967.16.16001.

[6] A. C. Eringen, “Simple microfluids,” *Int. J. Eng. Sci.*, vol. 2, no. 2, pp. 205–217, 1964, doi: 10.1016/0020-7225(64)90005-9.

[7] C. K. Chen, Y. T. Yang, and K. H. Chang, “The effect of thermal radiation on entropy generation due to micro-polar fluid flow along a wavy surface,” *Entropy*, vol. 13, no. 9, pp. 1595–1610, 2011, doi: 10.3390/e13091595.

[8] F. Shakeri Aski, S. J. Nasirkhani, E. Mohammadian, and A. Asgari,

"Application of Adomian decomposition method for micropolar flow in a porous channel," *Propuls. Power Res.*, vol. 3, no. 1, pp. 15–21, 2014, doi: 10.1016/j.jppr.2014.01.004.

[9] S. K. Pandey and D. Tripathi, "Unsteady peristaltic flow of micro-polar fluid in a finite channel," *Zeitschrift fur Naturforsch. - Sect. A J. Phys. Sci.*, vol. 66, no. 3–4, pp. 181–192, 2011, doi: 10.1515/zna-2011-3-407.

[10] M. A. Abbas, N. Faraz, Y. Q. Bai, and Y. Khan, "Analytical study of the non orthogonal stagnation point flow of a micro polar fluid," *Journal of King Saud University - Science*, vol. 29, no. 1. pp. 126–132, 2017, doi: 10.1016/j.jksus.2015.05.004.

[11] Aurangzaib, M. Sharif Uddin, K. Bhattacharyya, and S. Shafie, "Micropolar fluid flow and heat transfer over an exponentially permeable shrinking sheet," *Propuls. Power Res.*, vol. 5, no. 4, pp. 310–317, 2016, doi: 10.1016/j.jppr.2016.11.005.

[12] M. M. Rashidi, M. Ashraf, B. Rostami, M. T. Rastegari, and S. Bashir, "Mixed convection boundary-layer flow of a micro polar fluid towards a heated shrinking sheet by homotopy analysis method," *Therm. Sci.*, vol. 20, no. 1, pp. 21–34, 2016, doi: 10.2298/TSCI130212096R.

[13] D. Srinivasacharya and M. Shiferaw, "Flow of Micropolar Fluid Between Parallel Plates with Soret and Dufour Effects," *Arab. J. Sci. Eng.*, vol. 39, no. 6, pp. 5085–5093, 2014, doi: 10.1007/s13369-014-1016-8.

[14] S. Jangili and O. Anwar Bég, "Homotopy study of entropy generation in magnetized micropolar flow in a vertical parallel plate channel with buoyancy effect," *Heat Transf. Res.*, vol. 49, no. 6, pp. 529–553, 2018, doi: 10.1615/HeatTransRes.2018018305.

[15] K. S. Mekheimer and M. A. E. Kot, "The micropolar fluid model for blood flow through a tapered artery with a stenosis," *Acta Mech. Sin. Xuebao*, vol. 24, no. 6, pp. 637–644, 2008, doi: 10.1007/s10409-008-0185-7.

[16] L. Wang, Y. Jian, and F. Li, "The flow of micropolar fluids through a microparallel corrugated channel," *Eur. Phys. J. Plus*, vol. 131, no. 9, 2016, doi: 10.1140/epjp/i2016-16338-5.

[17] P. Aparna, N. Pothanna, J. V. R. Murthy, and K. Sreelatha, "Flow generated by slow steady rotation of a permeable sphere in a micro-polar fluid," *Alexandria Eng. J.*, vol. 56, no. 4, pp. 679–685, 2017, doi: 10.1016/j.aej.2017.01.018.

[18] T. Govinda Rao, J. V. Ramana Murthy, and G. S. Bhaskara Rao, "Longitudinal oscillations of a circular cylinder in a micro-polar fluid: case of resonance," *Sadhana - Acad. Proc. Eng. Sci.*, vol. 44, no. 3, 2019, doi: 10.1007/s12046-018-1004-x.

[19] L. Wang, X. Chu, J. Wan, and C. Xiu, "Implementation of micropolar fluids model and hydrodynamic behavior analysis using user-defined function in FLUENT," *Adv. Mech. Eng.*, vol. 12, no. 7, 2020, doi: 10.1177/1687814020943052.

[20] O. A. Bég, J. Zueco, and T. B. Chang, "Numerical analysis of hydromagnetic gravity-driven thin film micropolar flow along an inclined plane," *Chem. Eng. Commun.*, 2011, doi: 10.1080/00986445.2010.512534.

[21] E. I. Saad and M. S. Faltas, "Thermophoresis of a spherical particle straddling the interface of a semi-infinite micropolar fluid," *J. Mol. Liq.*, vol. 312, 2020, doi: 10.1016/j.molliq.2020.113289.

[22] S. A. M. Mehryan, M. Izadi, and M. A. Sheremet, "Analysis of conjugate natural convection within a porous square enclosure occupied with micropolar nanofluid using local thermal non-equilibrium model," *J. Mol. Liq.*, vol. 250, pp. 353–368, 2018, doi: 10.1016/j.molliq.2017.11.177.

[23] A. Kumar and J. Chawla, "Effect of Mass and Heat Transfer in Oscillatory Two Dimensional Flow of a Micro Polar Fluid Over an Infinite Permeable Plate in a Porous Medium Under the Existence of Magnetic Field," *Int. J. Eng. Technol. Manag. Res.*, vol. 5, no. 2, pp. 33–45, 2020, doi:

10.29121/ijetmr.v5.i2.2018.144.

[24] S. S. Ghadikolaei, K. Hosseinzadeh, M. Hatami, and D. D. Ganji, "MHD boundary layer analysis for micropolar dusty fluid containing Hybrid nanoparticles (Cu-Al2O3) over a porous medium," *J. Mol. Liq.*, vol. 268, pp. 813–823, 2018, doi: 10.1016/j.molliq.2018.07.105.

[25] S. S. Ghadikolaei, K. Hosseinzadeh, M. Yassari, H. Sadeghi, and D. D. Ganji, "Boundary layer analysis of micropolar dusty fluid with TiO2 nanoparticles in a porous medium under the effect of magnetic field and thermal radiation over a stretching sheet," *J. Mol. Liq.*, vol. 244, pp. 374–389, 2017, doi: 10.1016/j.molliq.2017.08.111.

[26] S. S. Ghadikolaei, K. Hosseinzadeh, and D. D. Ganji, "MHD raviative boundary layer analysis of micropolar dusty fluid with graphene oxide (Go)-engine oil nanoparticles in a porous medium over a stretching sheet with joule heating effect," *Powder Technology*, vol. 338. pp. 425–437, 2018, doi: 10.1016/j.powtec.2018.07.045.

[27] H. Kaneez, M. Nawaz, and Y. Elmasry, "Role of hybrid nanostructures and dust particles on transport of heat energy in micropolar fluid with memory effects," *J. Therm. Anal. Calorim.*, 2020, doi: 10.1007/s10973-020-10284-y.

[28] M. D. Cowley, "The Electromagnetodynamics of Fluids. By W. F. Hughes and F. J. Young. John Wiley, 1966. 648 pp. 6. 12s.," *Journal of Fluid Mechanics*, vol. 34, no. 4. pp. 820–821, 1968, doi: 10.1017/S0022112068212260.

[29] T. Javed and M. A. Siddiqui, "Energy transfer through mixed convection within square enclosure containing micropolar fluid with non-uniformly heated bottom wall under the MHD impact," *J. Mol. Liq.*, vol. 249, pp. 831–842, 2018, doi: 10.1016/j.molliq.2017.11.124.

[30] A. Tetbirt, M. N. Bouaziz, and M. Tahar Abbes, "Numerical study of magnetic effect on the velocity distribution field in a macro/micro-scale of a micropolar and viscous fluid in vertical channel," *J. Mol. Liq.*, vol. 216, pp. 103–110,

2016, doi: 10.1016/j.molliq.2015.12.088.

[31] H. A. Nabwey and A. Mahdy, “Transient flow of micropolar dusty hybrid nanofluid loaded with Fe3O4-Ag nanoparticles through a porous stretching sheet,” *Results Phys.*, vol. 21, 2021, doi: 10.1016/j.rinp.2020.103777.

[32] S. Ahmad and S. Nadeem, “Thermal analysis in buoyancy driven flow of hybrid nanofluid subject to thermal radiation,” *Int. J. Ambient Energy*, 2020, doi: 10.1080/01430750.2020.1861090.

[33] M. R. Eid and F. Mabood, “Entropy analysis of a hydromagnetic micropolar dusty carbon NTs-kerosene nanofluid with heat generation: Darcy–Forchheimer scheme,” *J. Therm. Anal. Calorim.*, vol. 143, no. 3, pp. 2419–2436, 2021, doi: 10.1007/s10973-020-09928-w.

[34] O. D. Makinde, K. G. Kumar, S. Manjunatha, and B. J. Gireesha, “Effect of nonlinear thermal radiation on MHD boundary layer flow and melting heat transfer of micro-polar fluid over a stretching surface with fluid particles suspension,” *Defect Diffus. Forum*, vol. 378, pp. 125–136, 2017, doi: 10.4028/www.scientific.net/DDF.378.125.

[35] V. M. Soundalgekar and R. N. Aranake, “Effects of couple stresses on MHD Couette flow,” *Nucl. Eng. Des.*, vol. 49, no. 3, pp. 197–203, 1978, doi: 10.1016/0029-5493(78)90142-5.

[36] K. L. Hsiao, “Micropolar nanofluid flow with MHD and viscous dissipation effects towards a stretching sheet with multimedia feature,” *Int. J. Heat Mass Transf.*, vol. 112, pp. 983–990, 2017, doi: 10.1016/j.ijheatmasstransfer.2017.05.042.

[37] L. Zhang, M. M. Bhatti, M. Marin, and K. S. Mekheimer, “Entropy analysis on the blood flow through anisotropically tapered arteries filled with magnetic zinc-oxide (ZnO) nanoparticles,” *Entropy*, vol. 22, no. 10, 2020, doi: 10.3390/E22101070.

[38] M. Ashraf, N. Jameel, and K. Ali, "MHD non-Newtonian micropolar fluid flow and heat transfer in channel with stretching walls," *Appl. Math. Mech. (English Ed.*, vol. 34, no. 10, pp. 1263–1276, 2013, doi: 10.1007/s10483-013-1743-7.

[39] O. Anwar Beg *et al.*, "Computation of Non-isothermal Thermo-convective Micropolar Fluid Dynamics in a Hall MHD Generator System with Non-linear Distending Wall," *Int. J. Appl. Comput. Math.*, vol. 6, no. 2, 2020, doi: 10.1007/s40819-020-0792-y.

[40] M. D. Shamshuddin, S. R. Sheri, and O. A. Bég, "Oscillatory dissipative conjugate heat and mass transfer in chemically reacting micropolar flow with wall couple stress: A finite element numerical study," *Proc. Inst. Mech. Eng. Part E J. Process Mech. Eng.*, vol. 233, no. 1, pp. 48–64, 2019, doi: 10.1177/0954408917743372.

[41] O. A. Bég *et al.*, "Unsteady nonlinear magnetohydrodynamic micropolar transport phenomena with Hall and Ion-slip current effects: Numerical study," *Int. J. Appl. Electromagn. Mech.*, vol. 65, no. 2, pp. 371–403, 2021, doi: 10.3233/JAE-201508.

[42] G. Lukaszewicz, "Micropolar Fluids: Theory and Applications.," *J. Fluid Mech.*, vol. 401, pp. 378–381, 1999, doi: 10.1017/s0022112099236889.

[43] G. F. Carrier, "Shock waves in a dusty gas," *J. Fluid Mech.*, vol. 4, no. 4, pp. 376–382, 1958, doi: 10.1017/S0022112058000513.

[44] L. M. Iilla and G. Volpicelli, "Flow of fluid-particle suspensions from liquid-fluidized beds," *Ind. Eng. Chem. Fundam.*, vol. 2, no. 3, pp. 194–199, 1963, doi: 10.1021/i160007a006.

[45] K. K. Sankara and L. V. K. V. Sarma, "On the steady flow produced in fluid-particle suspension by an infinite rotating disk with surface suction," *Int. J. Eng. Sci.*, vol. 23, no. 8, pp. 875–886, 1985, doi: 10.1016/0020-7225(85)90104-1.

[46] M. S. Alam Sarker, “Effect of coriolis force on vorticity covariance in MHD turbulent flow of dusty fluid,” *Int. J. Energy Res.*, vol. 21, no. 15, pp. 1399–1403, 1997, doi: 10.1002/(sici)1099-114x(199712)21:15<1399::aid-er342>3.0.co;2-5.

[47] O. Igra, I. Elperin, and G. Ben-Dor, “Dusty gas flow in a converging-diverging nozzle,” *J. Fluids Eng. Trans. ASME*, vol. 121, no. 4, pp. 908–913, 1999, doi: 10.1115/1.2823554.

[48] D. H. Michael, “The steady motion of a sphere in a dusty gas,” *J. Fluid Mech.*, vol. 31, no. 1, pp. 175–192, 1968, doi: 10.1017/S0022112068000091.

[49] K. Tseronis, I. K. Kookos, and C. Theodoropoulos, “Modelling mass transport in solid oxide fuel cell anodes: a case for a multidimensional dusty gas-based model,” *Chem. Eng. Sci.*, vol. 63, no. 23, pp. 5626–5638, 2008, doi: 10.1016/j.ces.2008.07.037.

[50] P. G. Saffman, “On the stability of laminar flow of a dusty gas,” *J. Fluid Mech.*, vol. 13, no. 1, pp. 120–128, 1962, doi: 10.1017/S0022112062000555.

[51] F. E. Marble, “Dynamics of Dusty Gases,” *Annu. Rev. Fluid Mech.*, vol. 2, no. 1, pp. 397–446, 1970, doi: 10.1146/annurev.fl.02.010170.002145.

[52] R. Duraiswami and A. Prosperetti, “Linear pressure waves in fogs,” *J. Fluid Mech.*, vol. 299, pp. 187–215, 1995, doi: 10.1017/S0022112095003478.

[53] A. Chauvière and J. Chaskalovic, “Dusty debris in tornadoes modelled by high Reynolds number two cells vortices,” *Int. J. Eng. Sci.*, vol. 43, no. 19–20, pp. 1486–1497, 2005, doi: 10.1016/j.ijengsci.2005.08.001.

[54] M. A. Allaham and J. Peddieson, “The flow induced by a rotating disk in a particulate suspension,” *Int. J. Eng. Sci.*, vol. 31, no. 7, pp. 1025–1034, 1993, doi: 10.1016/0020-7225(93)90110-G.

[55] S. V. Manuilovich, “Dusty-gas flow in a channel with horizontalwalls,” *Fluid Dyn.*, vol. 47, no. 1, pp. 84–100, 2012, doi: 10.1134/S0015462812010097.

[56] M. Bilal, S. Khan, F. Ali, M. Arif, I. Khan, and K. S. Nisar, "Couette flow of viscoelastic dusty fluid in a rotating frame along with the heat transfer," *Sci. Rep.*, vol. 11, no. 1, 2021, doi: 10.1038/s41598-020-79795-w.

[57] A. N. Osiptsov, "Mathematical modeling, of dusty-gas boundary layers," *Appl. Mech. Rev.*, vol. 50, no. 6, pp. 357–370, 1997, doi: 10.1115/1.3101716.

[58] L. Debnath and A. K. Ghosh, "On unsteady hydromagnetic flows of a dusty fluid between two oscillating plates," *Appl. Sci. Res.*, vol. 45, no. 4, pp. 353–365, 1988, doi: 10.1007/BF00457067.

[59] D. Dey, "Dusty Hydromagnetic Oldryod Fluid Flow in a Horizontal Channel with Volume Fraction and Energy Dissipation," *Int. J. Heat Technol.*, vol. 34, no. 3, pp. 415–422, 2016, doi: 10.18280/ijht.340310.

[60] N. Datta, D. C. Dalal, and S. K. Mishra, "Unsteady heat transfer to pulsatile flow of a dusty viscous incompressible fluid in a channel," *Int. J. Heat Mass Transf.*, vol. 36, no. 7, pp. 1783–1788, 1993, doi: 10.1016/S0017-9310(05)80164-4.

[61] K. Vajravelu, K. V. Prasad, and P. S. Datti, "Hydromagnetic fluid flow and heat transfer at a stretching sheet with fluid-particle suspension and variable fluid properties," *J. Fluids Eng. Trans. ASME*, vol. 135, no. 1, 2013, doi: 10.1115/1.4007802.

[62] S. K. Kumar and L. V. K. V. Sarma, "Fluid-particle suspension flow past a stretching sheet," *Int. J. Eng. Sci.*, vol. 29, no. 1, pp. 123–132, 1991, doi: 10.1016/0020-7225(91)90082-E.

[63] D. C. Dalal, N. Datta, and S. K. Mukherjea, "Unsteady natural convection of a dusty fluid in an infinite rectangular channel," *Int. J. Heat Mass Transf.*, vol. 41, no. 3, pp. 547–562, 1998, doi: 10.1016/S0017-9310(97)00189-0.

[64] W. Gretler and R. Regenfelder, "Variable-energy blast waves generated by a piston moving in a dusty gas," *J. Eng. Math.*, vol. 52, no. 4, pp. 321–336, 2005,

doi: 10.1007/s10665-005-2731-7.

[65] M. Saqib, I. Khan, and S. Shafie, “Generalized magnetic blood flow in a cylindrical tube with magnetite dusty particles,” *J. Magn. Magn. Mater.*, vol. 484, pp. 490–496, 2019, doi: 10.1016/j.jmmm.2019.03.032.

[66] H. M. Park and D. E. Rosner, “Combined inertial and thermophoretic effects on particle deposition rates in highly loaded dusty-gas systems,” *Chem. Eng. Sci.*, vol. 44, no. 10, pp. 2233–2244, 1989, doi: 10.1016/0009-2509(89)85158-9.

[67] H. S. Takhar, P. C. Ram, and S. S. Singh, “Unsteady MHD flow of a dusty viscous liquid in a rotating channel with hall currents,” *Int. J. Energy Res.*, vol. 17, no. 1, pp. 69–74, 1993, doi: 10.1002/er.4440170109.

[68] A. J. Chamkha, “Analytical solutions for flow of a dusty fluid between two porous flat plates,” *J. Fluids Eng. Trans. ASME*, vol. 116, no. 2, pp. 354–356, 1994, doi: 10.1115/1.2910280.

[69] O. A. Bég, H. S. Takhar, R. Bhargava, S. Rawat, and V. R. Prasad, “Numerical study of heat transfer of a third grade viscoelastic fluid in non-Darcy porous media with thermophysical effects,” *Phys. Scr.*, vol. 77, no. 6, 2008, doi: 10.1088/0031-8949/77/06/065402.

[70] S. Mukhopadhyay, R. Usha, and E. G. Tulapurkara, “Numerical study of concentrated fluid-particle suspension flow in a wavy channel,” *Int. J. Numer. Methods Fluids*, vol. 59, no. 10, pp. 1125–1155, 2009, doi: 10.1002/fld.1858.

[71] T. A. Bég, M. M. Rashidi, O. A. Bég, and N. Rahimzadeh, “Differential transform semi-numerical analysis of biofluid-particle suspension flow and heat transfer in non-Darcian porous media,” *Comput. Methods Biomech. Biomed. Engin.*, vol. 16, no. 8, pp. 896–907, 2013, doi: 10.1080/10255842.2011.643470.

[72] G. Palani and K. Y. Kim, “Free convection of a dusty-gas flow along a semi-

infinite vertical cylinder," *Int. J. Numer. Methods Fluids*, vol. 63, no. 4, pp. 517–532, 2010, doi: 10.1002/fld.2082.

[73] A. J. Chamkha, "Solutions for fluid-particle flow and heat transfer in a porous channel," *Int. J. Eng. Sci.*, vol. 34, no. 12, pp. 1423–1439, 1996, doi: 10.1016/0020-7225(96)00036-5.

[74] H. A. Attia, W. Abbas, and M. A. M. Abdeen, "Ion slip effect on unsteady Couette flow of a dusty fluid in the presence of uniform suction and injection with heat transfer," *J. Brazilian Soc. Mech. Sci. Eng.*, vol. 38, no. 8, pp. 2381–2391, 2016, doi: 10.1007/s40430-015-0311-y.

[75] R. Scardovelli and S. Zaleski, "Direct numerical simulation of free-surface and interfacial flow," *Annu. Rev. Fluid Mech.*, vol. 31, pp. 567–603, 1999, doi: 10.1146/annurev.fluid.31.1.567.

[76] R. W. Yeung, "Numerical methods in free-surface flows.," *Annu. Rev. Fluid Mech.*, vol. 14, M. Va, pp. 395–442, 1982, doi: 10.1146/annurev.fl.14.010182.002143.

[77] S. O. Unverdi and G. Tryggvason, "A front-tracking method for viscous, incompressible, multi-fluid flows," *J. Comput. Phys.*, vol. 100, no. 1, pp. 25–37, 1992, doi: 10.1016/0021-9991(92)90307-K.

[78] V. Cristini, J. Bławzdziewicz, and M. Loewenberg, "Drop breakup in three-dimensional viscous flows," *Phys. Fluids*, vol. 10, no. 8, pp. 1781–1783, 1998, doi: 10.1063/1.869697.

[79] S. Osher and J. A. Sethian, "Fronts propagating with curvature-dependent speed: Algorithms based on Hamilton-Jacobi formulations," *J. Comput. Phys.*, vol. 79, no. 1, pp. 12–49, 1988, doi: 10.1016/0021-9991(88)90002-2.

[80] N. Scapin, P. Costa, and L. Brandt, "A volume-of-fluid method for interface-resolved simulations of phase-changing two-fluid flows," *J. Comput. Phys.*, vol. 407, p. 109251, Apr. 2020, doi: 10.1016/j.jcp.2020.109251.

[81] J. Li and Y. Renardy, “Numerical Study of Flows of Two Immiscible Liquids at Low Reynolds Number,” *SIAM Rev.*, vol. 42, no. 3, pp. 417–439, 2000, doi: 10.1137/S0036144599354604.

[82] J. C. Umavathi and O. Anwar Bég, “Effects of thermophysical properties on heat transfer at the interface of two immisicible fluids in a vertical duct: Numerical study,” *Int. J. Heat Mass Transf.*, vol. 154, 2020, doi: 10.1016/j.ijheatmasstransfer.2020.119613.

[83] C. S. Yih, “Instability due to viscosity stratification,” *J. Fluid Mech.*, vol. 27, no. 2, pp. 337–352, 1967, doi: 10.1017/S0022112067000357.

[84] R. B. DeBar, “Fundamentals of the KRAKEN code. [Eulerian hydrodynamics code for compressible nonviscous flow of several fluids in two-dimensional (axially symmetric) region],” 1974.

[85] D. L. Youngs, “Time-dependent multi-material flow with large fluid distortion.,” 1982.

[86] K. Kannan, D. Kedelty, and M. Herrmann, “An in-cell reconstruction finite volume method for flows of compressible immiscible fluids,” *J. Comput. Phys.*, 2018, doi: 10.1016/j.jcp.2018.07.006.

[87] A. Baniabedalruhman, “A coupled volume-of-fluid and level set method in interDyMFoam solver,” 2020, doi: 10.21595/vp.2020.21342.

[88] W. Tauber, S. O. Unverdi, and G. Tryggvason, “The nonlinear behavior of a sheared immiscible fluid interface,” *Phys. Fluids*, vol. 14, no. 8, pp. 2871–2885, 2002, doi: 10.1063/1.1485763.

[89] B. Dong, Y. Y. Yan, W. Li, and Y. Song, “Lattice Boltzmann simulation of viscous fingering phenomenon of immiscible fluids displacement in a channel,” *Comput. Fluids*, vol. 39, no. 5, pp. 768–779, 2010, doi: 10.1016/j.compfluid.2009.12.005.

[90] J. Li, “Calcul d’Interface Affine par Morceaux,” *Comptes Rendus - Academie*

des Sciences, Serie II: Mecanique, Physique, Chimie, Astronomie, vol. 320, no. 8. pp. 391–396, 1995.

[91] Y. Zhao, H. H. Tan, and B. Zhang, "A high-resolution characteristics-based implicit dual time-stepping VOF method for free surface flow simulation on unstructured grids," *J. Comput. Phys.*, vol. 183, no. 1, pp. 233–273, 2002, doi: 10.1006/jcph.2002.7196.

[92] V. R. Gopala and B. G. M. van Wachem, "Volume of fluid methods for immiscible-fluid and free-surface flows," *Chem. Eng. J.*, vol. 141, no. 1–3, pp. 204–221, 2008, doi: 10.1016/j.cej.2007.12.035.

[93] G. Biswas, "Variant of a volume-of-fluid method for surface tension-dominant two-phase flows," *Sadhana - Acad. Proc. Eng. Sci.*, vol. 38, no. 6, pp. 1127–1133, 2013, doi: 10.1007/s12046-013-0222-5.

[94] Y. Y. Shan, C. Shu, and Z. L. Lu, "Application of local MQ-DQ method to solve 3D incompressible viscous flows with curved boundary," *C. - Comput. Model. Eng. Sci.*, vol. 25, no. 2, pp. 99–113, 2008, doi: 10.3970/cmes.2008.025.099.

[95] C. Shu, *Differential Quadrature and Its Application in Engineering*. 2000.

[96] R. Bellman, B. G. Kashef, and J. Casti, "Differential quadrature: A technique for the rapid solution of nonlinear partial differential equations," *J. Comput. Phys.*, vol. 10, no. 1, pp. 40–52, 1972, doi: 10.1016/0021-9991(72)90089-7.

[97] J. R. Quan and C. T. Chang, "New insights in solving distributed system equations by the quadrature method-II. Numerical experiments," *Comput. Chem. Eng.*, vol. 13, no. 9, pp. 1017–1024, 1989, doi: 10.1016/0098-1354(89)87043-7.

[98] W. Zhang and X. Wang, "Elastoplastic buckling analysis of thick rectangular plates by using the differential quadrature method," *Comput. Math. with Appl.*, vol. 61, no. 1, pp. 44–61, 2011, doi: 10.1016/j.camwa.2010.10.028.

[99] R. C. Mittal and R. Rohila, "A study of one dimensional nonlinear diffusion equations by Bernstein polynomial based differential quadrature method," *J. Math. Chem.*, vol. 55, no. 2, pp. 673–695, 2017, doi: 10.1007/s10910-016-0703-y.

[100] Y. Ding, L. M. Zhu, X. J. Zhang, and H. Ding, "Stability analysis of milling via the differential quadrature method," *J. Manuf. Sci. Eng. Trans. ASME*, vol. 135, no. 4, 2013, doi: 10.1115/1.4024539.

[101] C. Shu and B. E. Richards, "Application of generalized differential quadrature to solve two-dimensional incompressible Navier-Stokes equations," *Int. J. Numer. Methods Fluids*, vol. 15, no. 7, pp. 791–798, 1992, doi: 10.1002/fld.1650150704.

[102] A. Korkmaz and I. Daı, "Cubic B-spline differential quadrature methods and stability for Burgers' equation," *Eng. Comput. (Swansea, Wales)*, vol. 30, no. 3, pp. 320–344, 2013, doi: 10.1108/02644401311314312.

[103] M. S. Hashmi, M. Wajiha, S. W. Yao, A. Ghaffar, and M. Inc, "Cubic spline based differential quadrature method: A numerical approach for fractional Burger equation," *Results Phys.*, vol. 26, 2021, doi: 10.1016/j.rinp.2021.104415.

[104] C. Bota, B. Căruntu, D. Ţucu, M. Lăpădat, and M. S. Paşca, "A Least squares differential quadrature method for a class of nonlinear partial differential equations of fractional order," *Mathematics*, vol. 8, no. 8, 2020, doi: 10.3390/MATH8081336.

[105] O. Demir, D. Balkan, R. C. Peker, M. Metin, and A. Arikoglu, "Vibration analysis of curved composite sandwich beams with viscoelastic core by using differential quadrature method," *J. Sandw. Struct. Mater.*, vol. 22, no. 3, pp. 743–770, 2020, doi: 10.1177/1099636218767491.

[106] M. A. Patil and R. Kadoli, "Influence of Winkler and viscoelastic foundation on free vibration of functionally graded beam integrated with Terfenol-D

layer," *J. Brazilian Soc. Mech. Sci. Eng.*, vol. 42, no. 11, 2020, doi: 10.1007/s40430-020-02677-9.

[107] A. Başhan, "A mixed method approach to Schrödinger equation: Finite difference method and quartic B-spline based differential quadrature method," *Int. J. Optim. Control Theor. Appl.*, vol. 9, no. 2, pp. 223–235, 2021, doi: 10.11121/IJOCTA.01.2019.00709.

[108] A. C. Eringen, "Mechanics of Micromorphic Continua," in *Mechanics of Generalized Continua*, 1968, pp. 18–35.

[109] J. Peddieson, "An application of the micropolar fluid model to the calculation of a turbulent shear flow," *Int. J. Eng. Sci.*, vol. 10, no. 1, pp. 23–32, 1972, doi: 10.1016/0020-7225(72)90072-9.

[110] O. A. Bég, V. Ramachandra Prasad, B. Vasu, N. Bhaskar Reddy, Q. Li, and R. Bhargava, "Free convection heat and mass transfer from an isothermal sphere to a micropolar regime with Soret/Dufour effects," *Int. J. Heat Mass Transf.*, vol. 54, no. 1–3, pp. 9–18, 2011, doi: 10.1016/j.ijheatmasstransfer.2010.10.005.

[111] C. KANG and A. ERINGEN, "The effect of microstructure on the rheological properties of blood," *Bull. Math. Biol.*, vol. 38, no. 2, pp. 135–159, 1976, doi: 10.1016/s0092-8240(76)80030-4.

[112] M. Devakar and T. K. V. Iyengar, "Unsteady flows of a micropolar fluid between parallel plates using state space approach," *Eur. Phys. J. Plus*, vol. 128, no. 4, pp. 1–13, 2013, doi: 10.1140/epjp/i2013-13041-1.

[113] F. Selimefendigil, H. F. Öztop, and A. J. Chamkha, "Role of magnetic field on forced convection of nanofluid in a branching channel," *Int. J. Numer. Methods Heat Fluid Flow*, vol. 30, no. 4, pp. 1755–1772, 2020, doi: 10.1108/HFF-10-2018-0568.

[114] A. S. Dogonchi, T. Tayebi, N. Karimi, A. J. Chamkha, and H. Alhumade, "Thermal-natural convection and entropy production behavior of hybrid

nanoliquid flow under the effects of magnetic field through a porous wavy cavity embodies three circular cylinders," *J. Taiwan Inst. Chem. Eng.*, vol. 124, pp. 162–173, 2021, doi: 10.1016/j.jtice.2021.04.033.

[115] Y. Menni, A. Azzi, and A. Chamkha, "Enhancement of convective heat transfer in smooth air channels with wall-mounted obstacles in the flow path: A review," *Journal of Thermal Analysis and Calorimetry*, vol. 135, no. 4. pp. 1951–1976, 2019, doi: 10.1007/s10973-018-7268-x.

[116] J. Raza, F. Mebarek-Oudina, and A. J. Chamkha, "Magnetohydrodynamic flow of molybdenum disulfide nanofluid in a channel with shape effects," *Multidiscip. Model. Mater. Struct.*, vol. 15, no. 4, pp. 737–757, 2019, doi: 10.1108/MMMS-07-2018-0133.

[117] M. Veera Krishna and A. J. Chamkha, "Hall and ion slip effects on MHD rotating boundary layer flow of nanofluid past an infinite vertical plate embedded in a porous medium," *Results Phys.*, vol. 15, 2019, doi: 10.1016/j.rinp.2019.102652.

[118] Y. Menni, A. J. Chamkha, N. Massarotti, H. Ameur, N. Kaid, and M. Bensafi, "Hydrodynamic and thermal analysis of water, ethylene glycol and water-ethylene glycol as base fluids dispersed by aluminum oxide nano-sized solid particles," *Int. J. Numer. Methods Heat Fluid Flow*, vol. 30, no. 9, pp. 4349–4386, 2020, doi: 10.1108/HFF-10-2019-0739.

[119] S. N.S, B. J. Gireesha, B. Mahanthesh, P. B.C, and A. J. Chamkha, "Entropy generation analysis of magneto-nanoliquids embedded with aluminium and titanium alloy nanoparticles in microchannel with partial slips and convective conditions," *Int. J. Numer. Methods Heat Fluid Flow*, vol. 29, no. 10, pp. 3638–3658, 2019, doi: 10.1108/HFF-06-2018-0301.

[120] B. Kumar, G. S. Seth, R. Nandkeolyar, and A. J. Chamkha, "Outlining the impact of induced magnetic field and thermal radiation on magneto-convection flow of dissipative fluid," *Int. J. Therm. Sci.*, vol. 146, 2019, doi:

10.1016/j.ijthermalsci.2019.106101.

[121] Y. Menni, A. Azzi, and A. Chamkha, "Modeling and analysis of solar air channels with attachments of different shapes," *Int. J. Numer. Methods Heat Fluid Flow*, vol. 29, no. 5, pp. 1815–1845, 2019, doi: 10.1108/HFF-08-2018-0435.

[122] A. J. Chamkha, I. V. Miroshnichenko, and M. A. Sheremet, "Numerical analysis of unsteady conjugate natural convection of hybrid water-based nanofluid in a semicircular cavity," *J. Therm. Sci. Eng. Appl.*, vol. 9, no. 4, 2017, doi: 10.1115/1.4036203.

[123] S. Parvin and A. J. Chamkha, "An analysis on free convection flow, heat transfer and entropy generation in an odd-shaped cavity filled with nanofluid," *Int. Commun. Heat Mass Transf.*, vol. 54, pp. 8–17, 2014, doi: 10.1016/j.icheatmasstransfer.2014.02.031.

[124] Y. Menni, A. J. Chamkha, and A. Azzi, "Fluid flow and heat transfer over staggered + shaped obstacles," *J. Appl. Comput. Mech.*, vol. 6, no. 4, pp. 741–756, 2020, doi: 10.22055/JACM.2018.26277.1316.

[125] A. J. Chamkha, "Non-darcy fully developed mixed convection in a porous medium channel with heat generation/absorption and hydromagnetic effects," *Numer. Heat Transf. Part A Appl.*, vol. 32, no. 6, pp. 653–675, 1997, doi: 10.1080/10407789708913911.

[126] A. J. Chamkha, "On laminar hydromagnetic mixed convection flow in a vertical channel with symmetric and asymmetric wall heating conditions," *Int. J. Heat Mass Transf.*, vol. 45, no. 12, pp. 2509–2525, 2002, doi: 10.1016/S0017-9310(01)00342-8.

[127] A. J. Chamkha, "Unsteady laminar hydromagnetic fluid-particle flow and heat transfer in channels and circular pipes," *Int. J. Heat Fluid Flow*, vol. 21, no. 6, pp. 740–746, 2000, doi: 10.1016/S0142-727X(00)00031-X.

[128] M. Ghalambaz, A. Doostani, E. Izadpanahi, and A. J. Chamkha, "Conjugate natural convection flow of Ag–MgO/water hybrid nanofluid in a square cavity," *J. Therm. Anal. Calorim.*, vol. 139, no. 3, pp. 2321–2336, 2020, doi: 10.1007/s10973-019-08617-7.

[129] A. J. Chamkha, M. A. Mansour, A. M. Rashad, H. Kargarsharifabad, and T. Armaghani, "Magnetohydrodynamic mixed convection and entropy analysis of nanofluid in gamma-shaped porous cavity," *J. Thermophys. Heat Transf.*, vol. 34, no. 4, pp. 836–847, 2020, doi: 10.2514/1.T5983.

[130] S. Parvin, R. Nasrin, M. A. Alim, N. F. Hossain, and A. J. Chamkha, "Thermal conductivity variation on natural convection flow of water-alumina nanofluid in an annulus," *Int. J. Heat Mass Transf.*, vol. 55, no. 19–20, pp. 5268–5274, 2012, doi: 10.1016/j.ijheatmasstransfer.2012.05.035.

[131] P. S. Reddy, P. Sreedevi, and A. J. Chamkha, "MHD boundary layer flow, heat and mass transfer analysis over a rotating disk through porous medium saturated by Cu-water and Ag-water nanofluid with chemical reaction," *Powder Technol.*, vol. 307, pp. 46–55, 2017, doi: 10.1016/j.powtec.2016.11.017.

[132] A. J. Chamkha, "MHD-free convection from a vertical plate embedded in a thermally stratified porous medium with Hall effects," *Appl. Math. Model.*, vol. 21, no. 10, pp. 603–609, 1997, doi: 10.1016/S0307-904X(97)00084-X.

[133] R. B. Bird, "Transport phenomena," *Applied Mechanics Reviews*, vol. 55, no. 1. 2002, doi: 10.1115/1.1424298.

[134] J. C. Umavathi, A. J. Chamkha, M. H. Manjula, and A. Al-Mudhaf, "Flow and heat transfer of a couple-stress fluid sandwiched between viscous fluid layers," *Can. J. Phys.*, vol. 83, no. 7, pp. 705–720, 2005, doi: 10.1139/p05-032.

[135] J. C. Umavathi, J. Prathap Kumar, and A. J. Chamkha, "Convective flow of two immiscible viscous and couple stress permeable fluids through a vertical channel," *Turkish J. Eng. Environ. Sci.*, vol. 33, no. 4, pp. 221–243, 2009, doi:

10.3906/muh-0905-29.

[136] J. P. Kumar, J. C. Umavathi, A. J. Chamkha, and I. Pop, "Fully-developed free-convective flow of micropolar and viscous fluids in a vertical channel," *Appl. Math. Model.*, vol. 34, no. 5, pp. 1175–1186, 2010, doi: 10.1016/j.apm.2009.08.007.

[137] J. Srinivas and J. V. R. Murthy, "Flow of two immiscible couple stress fluids between two permeable beds," *J. Appl. Fluid Mech.*, vol. 9, no. 1, pp. 501–507, 2016, doi: 10.18869/acadpub.jafm.68.224.24013.

[138] J. Srinivas, J. V. Ramana Murthy, and K. S. Sai, "Entropy generation analysis of the flow of twoimmiscible couple stress fluids between two porous beds," *Comput. Therm. Sci.*, vol. 7, no. 2, pp. 123–137, 2015, doi: 10.1615/ComputThermalScien.2015012175.

[139] J. Srinivas and J. V. Ramana Murthy, "Thermal analysis of a flow of immiscible couple stress fluids in a channel," *J. Appl. Mech. Tech. Phys.*, vol. 57, no. 6, pp. 997–1005, 2016, doi: 10.1134/S0021894416060067.

[140] A. Borrelli, G. Giantesio, and M. C. Patria, "Reverse flow in magnetoconvection of two immiscible fluids in a vertical channel," *J. Fluids Eng. Trans. ASME*, vol. 139, no. 10, 2017, doi: 10.1115/1.4036670.

[141] G. Tryggvason *et al.*, "A Front-Tracking Method for the Computations of Multiphase Flow," *J. Comput. Phys.*, vol. 169, no. 2, pp. 708–759, 2001, doi: 10.1006/jcph.2001.6726.

[142] A. Riaz and H. A. Tchelepi, "Numerical simulation of immiscible two-phase flow in porous media," *Phys. Fluids*, vol. 18, no. 1, 2006, doi: 10.1063/1.2166388.

[143] K. Vajravelu, P. V. Arunachalam, and S. Sreenadh, "Unsteady Flow of Two Immiscible Conducting Fluids Between Two Permeable Beds," *J. Math. Anal. Appl.*, vol. 196, no. 3, pp. 1105–1116, 1995, doi: 10.1006/jmaa.1995.1463.

[144] J. C. Umavathi, A. J. Chamkha, A. Mateen, and A. Al-Mudhaf, "Unsteady two-fluid flow and heat transfer in a horizontal channel," *Heat Mass Transf. und Stoffuebertragung*, vol. 42, no. 2, pp. 81–90, 2005, doi: 10.1007/s00231-004-0565-x.

[145] R. Katta, R. K. Chandrawat, and V. Joshi, "A Numerical study of the unsteady flow of two immiscible micro polar and Newtonian fluids through a horizontal channel using DQM with B-Spline basis function," *J. Phys. Conf. Ser.*, vol. 1531, no. 1, 2020, doi: 10.1088/1742-6596/1531/1/012090.

[146] K. Ramesh and V. Joshi, "Numerical Solutions for Unsteady Flows of a Magnetohydrodynamic Jeffrey Fluid Between Parallel Plates Through a Porous Medium," *Int. J. Comput. Methods Eng. Sci. Mech.*, vol. 20, no. 1, pp. 1–13, 2019, doi: 10.1080/15502287.2018.1520322.

[147] M. Devakar, A. Raje, and S. Kumar, "Numerical Study on an Unsteady Flow of an Immiscible Micropolar Fluid Sandwiched Between Newtonian Fluids Through a Channel," *J. Appl. Mech. Tech. Phys.*, vol. 59, no. 6, pp. 980–991, 2018, doi: 10.1134/S0021894418060032.

[148] R. Niefer and P. N. Kaloni, "On the motion of a micropolar fluid drop in a viscous fluid," *J. Eng. Math.*, vol. 14, no. 2, pp. 107–116, 1980, doi: 10.1007/BF00037621.

[149] M. S. Faltas and E. I. Saad, "Slow motion of spherical droplet in a micropolar fluid flow perpendicular to a planar solid surface," *Eur. J. Mech. B/Fluids*, vol. 48, pp. 266–276, 2014, doi: 10.1016/j.euromechflu.2014.04.010.

[150] E. I. Saad, "Motion of a viscous droplet bisecting a free surface of a semi-infinite micropolar fluid," *Eur. J. Mech. B/Fluids*, vol. 59, pp. 57–69, 2016, doi: 10.1016/j.euromechflu.2016.04.009.

[151] Y. Menni, A. J. Chamkha, and A. Azzi, "Nanofluid transport in porous media: A review," *Spec. Top. Rev. Porous Media*, vol. 10, no. 1, pp. 49–64, 2019, doi: 10.1615/SpecialTopicsRevPorousMedia.2018027168.

[152] Y. Menni, A. J. Chamkha, and A. Azzi, "Nanofluid flow in complex geometries—A review," *Journal of Nanofluids*, vol. 8, no. 5. pp. 893–916, 2019, doi: 10.1166/jon.2019.1663.

[153] D. H. Michael and D. A. Miller, "Plane parallel flow of a dusty gas," *Mathematika*, vol. 13, no. 1, pp. 97–109, 1966, doi: 10.1112/S0025579300004289.

[154] J. Peddieson, "Some unsteady parallel flows of particulate suspensions," *Appl. Sci. Res.*, vol. 32, no. 3, pp. 239–268, 1976, doi: 10.1007/BF00411778.

[155] P. Mitra and P. Bhattacharyya, "Unsteady hydromagnetic laminar flow of a conducting dusty fluid between two parallel plates started impulsively from rest," *Acta Mech.*, vol. 39, no. 3–4, pp. 171–182, 1981, doi: 10.1007/BF01170340.

[156] P. Mitra and P. Bhattacharyya, "Flow of a Dusty Gas Between Two Parallel Plates One Stationary and Other Oscillating.," *Def. Sci. J.*, vol. 31, no. 3, pp. 211–223, 1981, doi: 10.14429/dsj.31.6359.

[157] P. Mitra and P. Bhattacharyya, "On the Hydromagnetic Flow of a Dusty Fluid Between Two Parallel Plates, One Being Stationary and the Other Oscillating," *J. Phys. Soc. Japan*, vol. 50, no. 3, pp. 995–1001, 1981, doi: 10.1143/JPSJ.50.995.

[158] H. A. Attia, W. Abbas, M. A. M. Abdeen, and M. S. Emam, "Effect of porosity on the flow of a dusty fluid between parallel plates with heat transfer and uniform suction and injection," *Eur. J. Environ. Civ. Eng.*, vol. 18, no. 2, pp. 241–251, 2014, doi: 10.1080/19648189.2013.860923.

[159] H. A. Attia, "Unsteady MHD flow and heat transfer of dusty fluid between parallel plates with variable physical properties," *Appl. Math. Model.*, vol. 26, no. 9, pp. 863–875, 2002, doi: 10.1016/S0307-904X(02)00049-5.

[160] H. A. Attia and K. M. Ewis, "Magnetohydrodynamic flow of continuous dusty

particles and non-Newtonian Darcy fluids between parallel plates," *Adv. Mech. Eng.*, vol. 11, no. 6, 2019, doi: 10.1177/1687814019857349.

[161] V. Singh and G. Singh, "Unsteady magnetohydrodynamic flow of a dusty fluid between two oscillating plates under varying constant pressure gradient," *Novi Sad J. Math.*, vol. 41, no. 2, pp. 123–129, 2011.

[162] A. Kucaba-Pięta1, "Microchannels flow modelling with the micropolar fluid theory," *Bull. Polish Acad. Sci. Tech. Sci.*, vol. 52, no. 3, pp. 209–214, 2004.

[163] O. A. Beg, H. S. Takhar, R. Bhargava, S. Sharma, and T. K. Hung, "Mathematical modeling of biomagnetic flow in a micropolar fluid-saturated darcian porous medium," *Int. J. Fluid Mech. Res.*, vol. 34, no. 5, pp. 403–424, 2007, doi: 10.1615/InterJFluidMechRes.v34.i5.20.

[164] S. Apparao, N. B. Naduviiiamani, and M. D. Patil, "Lubrication characteristics of porous inclined stepped composite bearings with couple stress fluids," *Tribol. Online*, vol. 8, no. 3, pp. 234–241, 2013, doi: 10.2474/trol.8.234.

[165] H. H. Sherief, M. S. Faltas, and K. E. Ragab, "Motion of a slip spherical particle near a planar micropolar-viscous interface," *Eur. J. Mech. B/Fluids*, vol. 89, pp. 274–288, 2021, doi: 10.1016/j.euromechflu.2021.06.004.

[166] J. C. Umavathl, J. Prathap Kumar, and A. J. Chamkha, "Flow and heat transfer of a micropolar fluid sandwiched between viscous fluid layers," *Can. J. Phys.*, vol. 86, no. 8, pp. 961–973, 2008, doi: 10.1139/P08-022.

[167] A. K. Singh, A. K. Singh, and N. P. Singh, "Generalised couette flow of two immiscible viscous fluids with heat transfer using Brinkman model," *Heat Mass Transf. und Stoffuebertragung*, vol. 40, no. 6–7, pp. 517–523, 2004, doi: 10.1007/s00231-003-0421-4.

[168] A. K. Singh, "Convective flow of two immiscible viscous fluids using Brinkman model," *Indian J. Pure Appl. Phys.*, vol. 43, no. 6, pp. 415–421, 2005.

[169] Reena Mittal and U. S. Rana, "Effect of dust particles on a layer of micropolar ferromagnetic fluid heated from below saturating a porous medium," *Appl. Math. Comput.*, vol. 215, no. 7, pp. 2591–2607, 2009, doi: 10.1016/j.amc.2009.08.063.

[170] J. Srinivas, J. V. R. Murthy, and O. A. Bég, "Entropy generation analysis of radiative heat transfer effects on channel flow of two immiscible couple stress fluids," *J. Brazilian Soc. Mech. Sci. Eng.*, vol. 39, no. 6, pp. 2191–2202, 2017, doi: 10.1007/s40430-017-0752-6.

[171] R. K. Chandrawat, V. Joshi, O. Anwar Bég, and D. Tripathi, "Computation of unsteady generalized Couette flow and heat transfer in immiscible dusty and non-dusty fluids with viscous heating and wall suction effects using a modified cubic B-spine differential quadrature method," *Heat Transf.*, vol. 51, no. 1, pp. 99–139, 2022, doi: 10.1002/htj.22299.

[172] J. C. Umavathi, I. C. Liu, and M. Shekar, "Unsteady mixed convective heat transfer of two immiscible fluids confined between long vertical wavy wall and parallel flat wall," *Appl. Math. Mech. (English Ed.*, vol. 33, no. 7, pp. 931–950, 2012, doi: 10.1007/s10483-012-1596-6.

[173] O. A. Bég, A. Zaman, N. Ali, S. A. Gaffar, and E. T. Bég, "Numerical computation of nonlinear oscillatory two-immiscible magnetohydrodynamic flow in dual porous media system: FTCS and FEM study," *Heat Transf. - Asian Res.*, vol. 48, no. 4, pp. 1245–1263, 2019, doi: 10.1002/htj.21429.

[174] M. Norouzi, S. Dorrani, H. Shokri, and O. Anwar Bég, "Linear Stability Analysis and CFD Simulation of Thermal Viscous Fingering Instability in Anisotropic Porous Media," *J. Eng. Mech.*, vol. 147, no. 4, p. 04021006, 2021, doi: 10.1061/(asce)em.1943-7889.0001906.

[175] M. Norouzi, S. Dorrani, H. Shokri, and O. Anwar Bég, "Effects of viscous dissipation on miscible thermo-viscous fingering instability in porous media," *Int. J. Heat Mass Transf.*, vol. 129, pp. 212–223, 2019, doi:

10.1016/j.ijheatmasstransfer.2018.09.048.

[176] R. B. DeBar, "Fundamentals of the KRAKEN code," *Tech. Rep.*, no. March, p. UCID-17366, 1974, [Online]. Available: http://www.osti.gov/energycitations/product.biblio.jsp?osti_id=7227630%5Cn http://www.ntis.gov/search/product.aspx?ABBR=UCID17366.

[177] E. G. Puckett, A. S. Almgren, J. B. Bell, D. L. Marcus, and W. J. Rider, "A high-order projection method for tracking fluid interfaces in variable density incompressible flows," *J. Comput. Phys.*, vol. 130, no. 2, pp. 269–282, 1997, doi: 10.1006/jcph.1996.5590.

[178] W. J. Rider and D. B. Kothe, "Reconstructing Volume Tracking," *J. Comput. Phys.*, vol. 141, no. 2, pp. 112–152, 1998, doi: 10.1006/jcph.1998.5906.

[179] Rider and Kothe, "[Rider]Reconstructing Volume Tracking(1998).pdf," *J. Comput. Phys.*, 1998.

[180] A. Pathak and M. Raessi, "A three-dimensional volume-of-fluid method for reconstructing and advecting three-material interfaces forming contact lines," *J. Comput. Phys.*, vol. 307, pp. 550–573, 2016, doi: 10.1016/j.jcp.2015.11.062.

[181] A. Bajpayee and A. H. Techet, "Fast volume reconstruction for 3D PIV," *Exp. Fluids*, vol. 58, no. 8, 2017, doi: 10.1007/s00348-017-2373-3.

[182] J. R. Quan and C. T. Chang, "New insights in solving distributed system equations by the quadrature method-I. Analysis," *Comput. Chem. Eng.*, vol. 13, no. 7, pp. 779–788, 1989, doi: 10.1016/0098-1354(89)85051-3.

[183] F. Civan, "Comment on 'application of generalized quadrature to solve two-dimensional incompressible Navier–Stokes equations', By C. Shu and B. E. Richards," *International Journal for Numerical Methods in Fluids*, vol. 17, no. 10. pp. 921–922, 1993, doi: 10.1002/fld.1650171007.

[184] C. Shu, Y. Y. Shan, and N. Qin, "Development of a local MQ-DQ-based stencil adaptive method and its application to solve incompressible Navier-

Stokes equations," *Int. J. Numer. Methods Fluids*, vol. 55, no. 4, pp. 367–386, 2007, doi: 10.1002/fld.1467.

[185] R. Jiwari and A. S. Alshomrani, "A new algorithm based on modified trigonometric cubic B-splines functions for nonlinear Burgers'-type equations," *Int. J. Numer. Methods Heat Fluid Flow*, vol. 27, no. 8, pp. 1638–1661, 2017, doi: 10.1108/HFF-05-2016-0191.

[186] Geeta Arora, V. Joshi, and R. C. Mittal, "Numerical Simulation of Nonlinear Schrödinger Equation in One and Two Dimensions," *Math. Model. Comput. Simulations*, vol. 11, no. 4, pp. 634–648, 2019, doi: 10.1134/S2070048219040070.

[187] R. C. Mittal and R. K. Jain, "Numerical solutions of nonlinear Burgers' equation with modified cubic B-splines collocation method," *Appl. Math. Comput.*, vol. 218, no. 15, pp. 7839–7855, 2012, doi: 10.1016/j.amc.2012.01.059.

[188] R. K. Chandrawat, V. Joshi, and S. Kanchan, "Numerical simulation of interface tracking between two immiscible micropolar and dusty fluids," *Mater. Today Proc.*, 2021, doi: 10.1016/j.matpr.2021.08.069.

[189] R. K. Chandrawat, V. Joshi, and O. Anwar Bég, "Ion Slip and Hall Effects on Generalized Time-Dependent Hydromagnetic Couette Flow of Immiscible Micropolar and Dusty Micropolar Fluids with Heat Transfer and Dissipation: A Numerical Study," *J. Nanofluids*, vol. 10, no. 3, pp. 431–446, 2021, doi: 10.1166/jon.2021.1792.

[190] J. Zueco, P. Eguía, E. Granada, J. L. Míguez, and O. A. Bég, "An electrical network for the numerical solution of transient mhd couette flow of a dusty fluid: Effects of variable properties and hall current," *Int. Commun. Heat Mass Transf.*, vol. 37, no. 10, pp. 1432–1439, 2010, doi: 10.1016/j.icheatmasstransfer.2010.07.025.

[191] Beg, "Keller Box and Smoothed Particle Hydrodynamic Numerical Simulation

of Two-Phase Transport in Blood Purification Auto-Transfusion Dialysis Hybrid Device with Stokes and Darcy Number Effects," *J. Adv. Biotechnol. Bioeng.*, 2013, doi: 10.12970/2311-1755.2013.01.02.4.

[192] O. A. Bég, M. M. Rashidi, N. Rahimzadeh, T. A. Bég, and T. K. Hung, "Homotopy simulation of two-phase thermo-hemodynamic filtration in a high permeability blood purification device," *J. Mech. Med. Biol.*, vol. 13, no. 4, 2013, doi: 10.1142/S0219519413500668.

[193] M. M. Bhatti, A. Zeeshan, N. Ijaz, O. Anwar Bég, and A. Kadir, "Mathematical modelling of nonlinear thermal radiation effects on EMHD peristaltic pumping of viscoelastic dusty fluid through a porous medium duct," *Eng. Sci. Technol. an Int. J.*, vol. 20, no. 3, pp. 1129–1139, 2017, doi: 10.1016/j.jestch.2016.11.003.

[194] W. Ibrahim and D. Gamachu, "Dusty Nanofluid Past a Centrifugally Stretching Surface," *Math. Probl. Eng.*, vol. 2020, 2020, doi: 10.1155/2020/9163081.

[195] M. Gnaneswara Reddy and M. Ferdows, "Species and thermal radiation on micropolar hydromagnetic dusty fluid flow across a paraboloid revolution," *Journal of Thermal Analysis and Calorimetry*, vol. 143, no. 5. pp. 3699–3717, 2021, doi: 10.1007/s10973-020-09254-1.

[196] S. F. Ahmed, M. G. Hafez, and Y. M. Chu, "Conversion of energy equation for fiber suspensions in dusty fluid turbulent flow," *Results Phys.*, vol. 19, 2020, doi: 10.1016/j.rinp.2020.103341.

[197] B. J. Gireesha, B. M. Shankaralingappa, B. C. Prasannakumar, and B. Nagaraja, "MHD flow and melting heat transfer of dusty Casson fluid over a stretching sheet with Cattaneo–Christov heat flux model," *Int. J. Ambient Energy*, pp. 1–9, 2020, doi: 10.1080/01430750.2020.1785938.

[198] H. Tariq and A. A. Khan, "Peristaltic flow of a dusty electrically conducting fluid through a porous medium in an endoscope," *SN Appl. Sci.*, vol. 2, no. 12, 2020, doi: 10.1007/s42452-020-03850-4.

[199] H. I. Meyer and A. O. Garder, “Mechanics of two immiscible fluids in porous media,” *J. Appl. Phys.*, vol. 25, no. 11, pp. 1400–1406, 1954, doi: 10.1063/1.1721576.

[200] B. J. Briscoe, C. J. Lawrence, and W. G. P. Mietus, “Review of immiscible fluid mixing,” *Adv. Colloid Interface Sci.*, vol. 81, no. 1, pp. 1–17, 1999, doi: 10.1016/S0001-8686(99)00002-0.

[201] G. Li, Y. Oka, M. Furuya, and M. Kondo, “Experiments and MPS analysis of stratification behavior of two immiscible fluids,” *Nucl. Eng. Des.*, vol. 265, pp. 210–221, 2013, doi: 10.1016/j.nucengdes.2013.09.006.

[202] S. Jachalski, D. Peschka, A. Münch, and B. Wagner, “Impact of interfacial slip on the stability of liquid two-layer polymer films,” *J. Eng. Math.*, vol. 86, no. 1, pp. 9–29, 2014, doi: 10.1007/s10665-013-9651-8.

[203] Ž. Stamenković, D. Nikodijević, D. Milenković, B. Blagojević, and J. Nikodijevic, “Flow and heat transfer of two immiscible fluids in the presence of uniform inclined magnetic field,” *Math. Probl. Eng.*, vol. 2011, 2011, doi: 10.1155/2011/132302.

[204] M. Mori, M. Natori, and Z. Guo-Feng, “A finite element analysis of a free surface drainage problem of two immiscible fluids,” *Int. J. Numer. Methods Fluids*, vol. 9, no. 5, pp. 569–582, 1989, doi: 10.1002/fld.1650090507.

[205] H. Tang and L. C. Wrobel, “Modelling the interfacial flow of two immiscible liquids in mixing processes,” *Int. J. Eng. Sci.*, vol. 43, no. 15–16, pp. 1234–1256, 2005, doi: 10.1016/j.ijengsci.2005.03.011.

[206] T. Wan, S. Aliabadi, and C. Bigler, “A hybrid scheme based on finite element/volume methods for two immiscible fluid flows,” *Int. J. Numer. Methods Fluids*, vol. 61, no. 8, pp. 930–944, 2009, doi: 10.1002/fld.1997.

[207] P. T. Than, F. Rosso, and D. D. Joseph, “Instability of Poiseuille flow of two immiscible liquids with different viscosities in a channel,” *Int. J. Eng. Sci.*, vol.

25, no. 2, pp. 189–204, 1987, doi: 10.1016/0020-7225(87)90005-X.

[208] A. A. Yagodnitsyna, A. V. Kovalev, and A. V. Bilsky, "Flow patterns of immiscible liquid-liquid flow in a rectangular microchannel with T-junction," *Chem. Eng. J.*, vol. 303, pp. 547–554, 2016, doi: 10.1016/j.cej.2016.06.023.

[209] Y. Zhou, Q. W. Ma, and S. Yan, "MLPG_R method for modelling 2D flows of two immiscible fluids," *Int. J. Numer. Methods Fluids*, vol. 84, no. 7, pp. 385–408, 2017, doi: 10.1002/fld.4353.

[210] R. H. McLean, C. W. Manry, and W. W. Whitaker, "Displacement Mechanics in Primary Cementing," *J. Pet. Technol.*, vol. 19, no. 02, pp. 251–260, 1967, doi: 10.2118/1488-pa.

[211] S. Pelipenko and I. A. Frigaard, "Mud removal and cement placement during primary cementing of an oil well," *J. Eng. Math.*, vol. 48, no. 1, pp. 1–26, 2004, doi: 10.1023/B:ENGI.0000009499.63859.f0.

[212] H. Tang, L. C. Wrobel, and Z. Fan, "Tracking of immiscible interfaces in multiple-material mixing processes," *Comput. Mater. Sci.*, vol. 29, no. 1, pp. 103–118, 2004, doi: 10.1016/j.commatsci.2003.07.002.

[213] M. M. Bhatti, A. Riaz, L. Zhang, S. M. Sait, and R. Ellahi, "Biologically inspired thermal transport on the rheology of Williamson hydromagnetic nanofluid flow with convection: an entropy analysis," *J. Therm. Anal. Calorim.*, vol. 144, no. 6, pp. 2187–2202, 2021, doi: 10.1007/s10973-020-09876-5.

[214] R. E. Abo-Elkhair, M. M. Bhatti, and K. S. Mekheimer, "Magnetic force effects on peristaltic transport of hybrid bio-nanofluid (Au–Cu nanoparticles) with moderate Reynolds number: An expanding horizon," *Int. Commun. Heat Mass Transf.*, vol. 123, 2021, doi: 10.1016/j.icheatmasstransfer.2021.105228.

[215] K. L. Hsiao, "To promote radiation electrical MHD activation energy thermal extrusion manufacturing system efficiency by using Carreau-Nanofluid with

parameters control method," *Energy*, vol. 130, pp. 486–499, 2017, doi: 10.1016/j.energy.2017.05.004.

[216] M. Bibi, A. Zeeshan, M. Y. Malik, and K. U. Rehman, "Numerical investigation of the unsteady solid-particle flow of a tangent hyperbolic fluid with variable thermal conductivity and convective boundary," *Eur. Phys. J. Plus*, vol. 134, no. 6, 2019, doi: 10.1140/epjp/i2019-12651-9.

[217] M. Bibi, A. Zeeshan, and M. Y. Malik, "Numerical analysis of unsteady flow of three-dimensional Williamson fluid-particle suspension with MHD and nonlinear thermal radiations," *Eur. Phys. J. Plus*, vol. 135, no. 10, 2020, doi: 10.1140/epjp/s13360-020-00857-z.

[218] K. L. Hsiao, "Stagnation electrical MHD nanofluid mixed convection with slip boundary on a stretching sheet," *Appl. Therm. Eng.*, vol. 98, pp. 850–861, 2016, doi: 10.1016/j.applthermaleng.2015.12.138.

[219] K. L. Hsiao, "Combined electrical MHD heat transfer thermal extrusion system using Maxwell fluid with radiative and viscous dissipation effects," *Appl. Therm. Eng.*, vol. 112, pp. 1281–1288, 2017, doi: 10.1016/j.applthermaleng.2016.08.208.

[220] S. Haider, N. Ijaz, A. Zeeshan, and Y. Z. Li, "Magneto-hydrodynamics of a solid-liquid two-phase fluid in rotating channel due to peristaltic wavy movement," *Int. J. Numer. Methods Heat Fluid Flow*, vol. 30, no. 5, pp. 2501–2516, 2020, doi: 10.1108/HFF-02-2019-0131.

[221] M. Fakour, A. Vahabzadeh, D. D. Ganji, and M. Hatami, "Analytical study of micropolar fluid flow and heat transfer in a channel with permeable walls," *J. Mol. Liq.*, vol. 204, pp. 198–204, 2015, doi: 10.1016/j.molliq.2015.01.040.

[222] H. H. Sherief, M. S. Faltas, and S. El-Sapa, "Interaction between two rigid spheres moving in a micropolar fluid with slip surfaces," *Journal of Molecular Liquids*, vol. 290. 2019, doi: 10.1016/j.molliq.2019.111165.

[223] J. Srinivas and J. V. Ramana Murthy, “Second law analysis of the flow of two immiscible micropolar fluids between two porous beds,” *J. Eng. Thermophys.*, vol. 25, no. 1, pp. 126–142, 2016, doi: 10.1134/S1810232816010124.

[224] J. Srinivas and J. V. Ramana Murthy, “Thermodynamic analysis for the mhd flow of two immiscible micropolar fluids between two parallel plates,” *Front. Heat Mass Transf.*, vol. 6, no. 1, 2015, doi: 10.5098/hmt.6.4.

[225] M. Veera Krishna, M. Gangadhar Reddy, and A. J. Chamkha, “Heat and mass transfer on MHD free convective flow over an infinite nonconducting vertical flat porous plate,” *Int. J. Fluid Mech. Res.*, vol. 46, no. 1, pp. 1–25, 2019, doi: 10.1615/INTERJFLUIDMECHRES.2018025004.

[226] M. Veera Krishna, “Hall and ion slip impacts on unsteady MHD free convective rotating flow of Jeffreys fluid with ramped wall temperature,” *Int. Commun. Heat Mass Transf.*, vol. 119, 2020, doi: 10.1016/j.icheatmasstransfer.2020.104927.

[227] M. V. Krishna, M. G. Reddy, and A. J. Chamkha, “Heat and mass transfer on unsteady mhd flow through an infinite oscillating vertical porous surface,” *J. Porous Media*, vol. 24, no. 1, pp. 81–100, 2021, doi: 10.1615/JPORMEDIA.2020025021.

[228] K. V. Prasad, K. Vajravelu, P. S. Datti, and B. T. Raju, “MHD flow and heat transfer in a power-law liquid film at a porous surface in the presence of thermal radiation,” *J. Appl. Fluid Mech.*, vol. 6, no. 3, pp. 385–395, 2013, doi: 10.36884/jafm.6.03.19563.

[229] M. V. Krishna and A. J. Chamkha, “Hall and ion slip effects on magnetohydrodynamic convective rotating flow of Jeffreys fluid over an impulsively moving vertical plate embedded in a saturated porous medium with Ramped wall temperature,” *Numer. Methods Partial Differ. Equ.*, vol. 37, no. 3, pp. 2150–2177, 2021, doi: 10.1002/num.22670.

[230] M. V. Krishna and A. J. Chamkha, “Hall and ion slip effects on MHD rotating

flow of elastico-viscous fluid through porous medium," *Int. Commun. Heat Mass Transf.*, vol. 113, 2020, doi: 10.1016/j.icheatmasstransfer.2020.104494.

[231] M. Veera Krishna, N. Ameer Ahamad, and A. J. Chamkha, "Radiation absorption on MHD convective flow of nanofluids through vertically travelling absorbent plate," *Ain Shams Eng. J.*, vol. 12, no. 3, pp. 3043–3056, 2021, doi: 10.1016/j.asej.2020.10.028.

[232] Y. Menni, A. J. Chamkha, A. Azzi, and C. Zidani, "Numerical analysis of fluid flow and heat transfer characteristics of a new kind of vortex generators by comparison with those of traditional vortex generators," *Int. J. Fluid Mech. Res.*, vol. 47, no. 1, pp. 23–42, 2020, doi: 10.1615/InterJFluidMechRes.2019026753.

[233] M. Veera Krishna, N. A. Ahamad, and A. J. Chamkha, "Numerical investigation on unsteady MHD convective rotating flow past an infinite vertical moving porous surface," *Ain Shams Eng. J.*, vol. 12, no. 2, pp. 2099–2109, 2021, doi: 10.1016/j.asej.2020.10.013.

[234] Y. Menni, A. Azzi, and A. J. Chamkha, "Computational thermal analysis of turbulent forced-convection flow in an air channel with a flat rectangular fin and downstream v-shaped baffle," *Heat Transf. Res.*, vol. 50, no. 18, pp. 1781–1818, 2019, doi: 10.1615/HeatTransRes.2019026143.

[235] Y. Menni, A. Chamkha, C. Zidani, and B. Benyoucef, "Baffle orientation and geometry effects on turbulent heat transfer of a constant property incompressible fluid flow inside a rectangular channel," *Int. J. Numer. Methods Heat Fluid Flow*, vol. 30, no. 6, pp. 3027–3052, 2020, doi: 10.1108/HFF-12-2018-0718.

[236] Y. Menni, A. Azzi, A. J. Chamkha, and S. Harmand, "Effect of wall-mounted V-baffle position in a turbulent flow through a channel: Analysis of best configuration for optimal heat transfer," *Int. J. Numer. Methods Heat Fluid Flow*, vol. 29, no. 10, pp. 3908–3937, 2019, doi: 10.1108/HFF-06-2018-0270.

[237] Y. Menni, A. Azzi, A. J. Chamkha, and S. Harmand, "Analysis of fluid dynamics and heat transfer in a rectangular duct with staggered baffles," *J. Appl. Comput. Mech.*, vol. 5, no. 2, pp. 231–248, 2019, doi: 10.22055/JACM.2018.26023.1305.

[238] G. Arora and V. Joshi, "A computational approach using modified trigonometric cubic B-spline for numerical solution of Burgers' equation in one and two dimensions," *Alexandria Eng. J.*, vol. 57, no. 2, pp. 1087–1098, 2018, doi: 10.1016/j.aej.2017.02.017.

[239] O. A. Bég, J. Zueco, and H. S. Takhar, "Unsteady magnetohydrodynamic Hartmann-Couette flow and heat transfer in a Darcian channel with Hall current, ionslip, viscous and Joule heating effects: Network numerical solutions," *Communications in Nonlinear Science and Numerical Simulation*, vol. 14, no. 4. pp. 1082–1097, 2009, doi: 10.1016/j.cnsns.2008.03.015.

[240] J. Zueco, O. A. Bég, and L. M. López-Ochoa, "Non-linear transient hydromagnetic partially ionised dissipative Couette flow in a non-Darcian porous medium channel with Hall, ionslip and Joule heating effects," *Prog. Comput. Fluid Dyn.*, vol. 11, no. 2, pp. 116–129, 2011, doi: 10.1504/PCFD.2011.038837.

[241] O. A. Bég, S. Abdul Gaffar, V. R. Prasad, and M. J. Uddin, "Computational solutions for non-isothermal, nonlinear magneto-convection in porous media with hall/ionslip currents and ohmic dissipation," *Eng. Sci. Technol. an Int. J.*, vol. 19, no. 1, pp. 377–394, 2016, doi: 10.1016/j.jestch.2015.08.009.

[242] S. R. Sheri, O. Anwar Bég, P. Modugula, and A. Kadir, "Computation of transient radiative reactive thermosolutal magnetohydrodynamic convection in inclined mhd hall generator flow with dissipation and cross diffusion," *Comput. Therm. Sci.*, vol. 11, no. 6, pp. 541–563, 2019, doi: 10.1615/ComputThermalScien.2019026405.

[243] A. Yamanishi, S. Ohmori, K. Tsuru, T. Tachiiri, H. Kusajima, and K. Momo,

"Combined influence of ibudilast and ticlopidine · HC1 - Pharmacokinetics and safety assessment in rats -," *Japanese Pharmacol. Ther.*, vol. 27, no. 10, pp. 40–41, 1999.

[244] A. H. Eraslan, "Temperature distributions in MHD channels with Hall effect," *AIAA J.*, vol. 7, no. 1, pp. 186–188, 1969, doi: 10.2514/3.5072.

[245] M. Nawaz and T. Zubair, "Finite element study of three dimensional radiative nano-plasma flow subject to Hall and ion slip currents," *Results Phys.*, vol. 7, pp. 4111–4122, 2017, doi: 10.1016/j.rinp.2017.10.035.

[246] Q. Wu, D. W. L. Schubring, and J. J. Sienicki, "Feasibility analysis of two-phase MHD energy conversion for liquid metal cooled reactors," *Nucl. Eng. Des.*, vol. 237, no. 20–21, pp. 2114–2119, 2007, doi: 10.1016/j.nucengdes.2007.02.009.

[247] N. Kayukawa, "Open-cycle magnetohydrodynamic electrical power generation: A review and future perspectives," *Progress in Energy and Combustion Science*, vol. 30, no. 1. pp. 33–60, 2004, doi: 10.1016/j.pecs.2003.08.003.

[248] H. R. Kim, J. E. Cha, J. M. Kim, H. Y. Nam, and B. H. Kim, "DC magnetic field effect on a liquid sodium channel flow," *Nucl. Eng. Des.*, vol. 238, no. 1, pp. 280–284, 2008, doi: 10.1016/j.nucengdes.2007.06.007.

[249] E. Schuster, L. Luo, and M. Krstić, "MHD channel flow control in 2D: Mixing enhancement by boundary feedback," *Automatica*, vol. 44, no. 10, pp. 2498–2507, 2008, doi: 10.1016/j.automatica.2008.02.018.

[250] E. Spong, J. A. Reizes, and E. Leonardi, "Efficiency improvements of electromagnetic flow control," *Int. J. Heat Fluid Flow*, vol. 26, no. 4 SPEC. ISS., pp. 635–655, 2005, doi: 10.1016/j.ijheatfluidflow.2005.04.001.

[251] B. K. Jha, B. Y. Isah, and I. J. Uwanta, "Combined effect of suction/injection on MHD free-convection flow in a vertical channel with thermal radiation," *Ain Shams Eng. J.*, vol. 9, no. 4, pp. 1069–1088, 2018, doi:

10.1016/j.asej.2016.06.001.

[252] J. Lee, M. A. Huerta, and G. Zha, “Low magnetic Reynolds number hypersonic MHD flow using high order WENO schemes,” 2009, doi: 10.2514/6.2009-459.

[253] J. I. Ramos and N. S. Winowich, “Magnetohydrodynamic channel flow study,” *Phys. Fluids*, vol. 29, no. 4, p. 992, 1986, doi: 10.1063/1.865695.

[254] M. Tezer-Sezgin, “Boundary element method solution of MHD flow in a rectangular duct,” *Int. J. Numer. Methods Fluids*, vol. 18, no. 10, pp. 937–952, 1994, doi: 10.1002/fld.1650181004.

[255] A. Chiolerio and M. B. Quadrelli, “Smart Fluid Systems: The Advent of Autonomous Liquid Robotics,” *Advanced Science*, vol. 4, no. 7. 2017, doi: 10.1002/advs.201700036.

[256] T. Okaniwa and M. Hayama, “The application of ionic liquids into space lubricants,” *[Conference] Esmats 2013*, no. September, pp. 25–27, 2013.

[257] B. Singh and J. Lal, “Effect of magnetic field orientation and wall conductivity on mhd channel flows using finite element method,” *Comput. Methods Appl. Mech. Eng.*, vol. 40, no. 2, pp. 159–170, 1983, doi: 10.1016/0045-7825(83)90088-9.

[258] J. A. Shercliff, “Engineering Magnetohydrodynamics. G. W. Sutton and A. Sherman. McGraw-Hill, London. 1965. 548 pp. Diagrams. £6 12s.,” *J. R. Aeronaut. Soc.*, vol. 70, no. 665, pp. 606–606, 1966, doi: 10.1017/s0001924000057857.

[259] B. K. Jha and C. A. Apere, “Combined effect of hall and ion-slip currents on unsteady MHD couette flows in a rotating system,” *J. Phys. Soc. Japan*, vol. 79, no. 10, 2010, doi: 10.1143/JPSJ.79.104401.

[260] B. N. M. da Silva, G. E. Assad, and J. A. de Lima, “Analysis of the hall and ion-slip effects in a MHD channel flow: A hybrid approach,” in *International Symposium on Advances in Computational Heat Transfer*, 2017, pp. 1811–

1827, doi: 10.1615/ichmt.2017.1930.

[261] V. Javeri, “Influence of hall effect and ion slip on velocity and temperature fields in an MHD channel,” *Wärme- und Stoffübertragung*, vol. 7, no. 4, pp. 226–235, 1974, doi: 10.1007/BF01445311.

[262] N. V. Vighnesam and H. S. Takhar, “Hall and Ion-Slip Effects in MHD Couette Flow with Heat Transfer,” *IEEE Trans. Plasma Sci.*, vol. 7, no. 3, pp. 178–182, 1979, doi: 10.1109/TPS.1979.4317226.

[263] O. A. Bég, L. Sim, J. Zueco, and R. Bhargava, “Numerical study of magnetohydrodynamic viscous plasma flow in rotating porous media with Hall currents and inclined magnetic field influence,” *Commun. Nonlinear Sci. Numer. Simul.*, vol. 15, no. 2, pp. 345–359, 2010, doi: 10.1016/j.cnsns.2009.04.008.

[264] M. D. Shamshuddin, S. U. Khan, O. Anwar Bég, and T. A. Bég, “Hall current, viscous and Joule heating effects on steady radiative 2-D magneto-power-law polymer dynamics from an exponentially stretching sheet with power-law slip velocity: A numerical study,” *Therm. Sci. Eng. Prog.*, vol. 20, 2020, doi: 10.1016/j.tsep.2020.100732.

[265] M. Veera Krishna, “Hall and ion slip effects on mhd laminar flow of an elastico-viscous (Walter’s-b) fluid,” *Heat Transf.*, vol. 49, no. 4, pp. 2311–2329, 2020, doi: 10.1002/htj.21722.

[266] R. K. Gupta and S. C. Gupta, “Flow of a dustry gas through a channel with arbitrary time varying pressure gradient,” *Zeitschrift für Angew. Math. und Phys. ZAMP*, vol. 27, no. 1, pp. 119–125, 1976, doi: 10.1007/BF01595248.

[267] N. Datta and D. C. Dalal, “Pulsatile flow and heat transfer of a dusty fluid through an infinitely long annular pipe,” *Int. J. Multiph. Flow*, vol. 21, no. 3, pp. 515–528, 1995, doi: 10.1016/0301-9322(94)00064-Q.

[268] A. L. Aboul-Hassan and H. A. Attia, “Hydromagnetic flow of a dusty fluid in a

rectangular channel with Hall current and heat transfer," *Can. J. Phys.*, vol. 80, no. 5, pp. 579–589, 2002, doi: 10.1139/p01-125.

[269] K. Ramesh, D. Tripathi, O. A. Bég, and A. Kadir, "Slip and Hall Current Effects on Jeffrey Fluid Suspension Flow in a Peristaltic Hydromagnetic Blood Micropump," *Iran. J. Sci. Technol. - Trans. Mech. Eng.*, vol. 43, no. 4, pp. 675–692, 2019, doi: 10.1007/s40997-018-0230-5.

[270] B. Mahanthesh, "Hall Effect on Two-Phase Laminar Boundary Layer flow of Dusty Liquid due to Stretching of an Elastic Flat Sheet," *Mapana - J. Sci.*, vol. 16, no. 3, pp. 13–26, 2017, doi: 10.12723/mjs.42.2.

[271] J. M. Rallison, "Fundamentals of Two-Fluid Dynamics. By D. D. JOSEPH and Y. Y. RENARDY. Springer, 1993. Part I: Mathematical theory and applications, 443 pp., DM 168. Part II: Lubricated transport, drops and miscible liquids, 445 pp., DM 168," *Journal of Fluid Mechanics*, vol. 282. pp. 405–406, 1995, doi: 10.1017/S0022112095220184.

[272] W. G. C. Boyd, "Shear-flow In stability at the interface between two viscous fluids," *J. Fluid Mech.*, vol. 128, pp. 507–528, 1983, doi: 10.1017/S0022112083000580.

[273] H. H. Hu and D. D. Joseph, "Lubricated pipelining: Stability of core-annular flow. part 2," *J. Fluid Mech.*, vol. 205, pp. 359–396, 1989, doi: 10.1017/S0022112089002077.

[274] L. Preziosi, K. Chen, and D. D. Joseph, "Lubricated pipelining: Stability of core-annular flow," *J. Fluid Mech.*, vol. 201, pp. 323–356, 1989, doi: 10.1017/S0022112089000960.

[275] T. Guan *et al.*, "Slug flow hydrodynamics of immiscible fluids within a rectangular microchannel towards size-controllable fabrication of dextran-based cryogel beads," *Chem. Eng. J.*, vol. 369, pp. 116–123, 2019, doi: 10.1016/j.cej.2019.03.062.

[276] H. Wang, G. Jiang, Q. Han, and Y. Cheng, "Formation of magnetic ionic liquid-water Janus droplet in assembled 3D-printed microchannel," *Chem. Eng. J.*, vol. 406, 2021, doi: 10.1016/j.cej.2020.126098.

[277] S. M. Živojin, D. D. Nikodijević, B. D. Blagojević, and S. R. Savić, "MHD flow and heat transfer of two immiscible fluids between moving plates," *Trans. Can. Soc. Mech. Eng.*, vol. 34, no. 3–4, pp. 351–372, 2010, doi: 10.1139/tcsme-2010-0021.

[278] R. K. Chandrawat, V. Joshi, and O. A. Bég, "Numerical Study of Interface Tracking for the Unsteady Flow of Two Immiscible Micropolar and Newtonian Fluids Through a Horizontal Channel with an Unstable Interface," *J. Nanofluids*, vol. 10, no. 4, pp. 552–563, 2021, doi: 10.1166/jon.2021.1805.

[279] M. Ramzan, H. Gul, J. D. Chung, S. Kadry, and Y. M. Chu, "Significance of Hall effect and Ion slip in a three-dimensional bioconvective Tangent hyperbolic nanofluid flow subject to Arrhenius activation energy," *Sci. Rep.*, vol. 10, no. 1, 2020, doi: 10.1038/s41598-020-73365-w.

Research publication

1. R. K. Chandrawat, V. Joshi, and O. A. Bég, "Numerical study of time dependent flow of immiscible Saffman dusty (fluid-particle suspension) and Eringen micropolar fluids in a duct with a modified cubic B-spline Differential Quadrature method," **Int. Commun. Heat Mass Transf.**, vol. 130, no. November 2021, doi: 10.1016/j.icheatmasstransfer.2021.105758.
   [SCI-Impact factor 5.683, SJR-1.33- Q1]

2. R. K. Chandrawat, V. Joshi, O. Anwar Bég, and D. Tripathi, "Computation of unsteady generalized Couette flow and heat transfer in immiscible dusty and non-dusty fluids with viscous heating and wall suction effects using a modified cubic B-spine differential quadrature method," **Heat Transf.**, vol. 51, no. 1, pp. 99–139, 2022, doi: 10.1002/htj.22299.
   [Scopus, SJR-0.41-Q2]

3. R. K. Chandrawat, V. Joshi, and O. Anwar Bég, "Ion Slip and Hall Effects on Generalized Time-Dependent Hydromagnetic Couette Flow of Immiscible Micropolar and Dusty Micropolar Fluids with Heat Transfer and Dissipation: A Numerical Study," **J. Nanofluids**, vol. 10, no. 3, pp. 431–446, 2021, doi: 10.1166/jon.2021.1792.
   [Scopus, SJR-0.389-Q2]

4. R. K. Chandrawat, V. Joshi, and S. Kanchan, "Numerical simulation of interface tracking between two immiscible micropolar and dusty fluids," **Mater. Today Proc.**, 2021, doi: 10.1016/j.matpr.2021.08.069.
   [Scopus, SJR-0.34-Q2]

5. R. K. Chandrawat, V. Joshi, and O. A. Bég, "Numerical Study of Interface Tracking for the Unsteady Flow of Two Immiscible Micropolar and Newtonian Fluids Through a Horizontal Channel with an Unstable Interface," **J. Nanofluids**, vol. 10, no. 4, pp. 552–563, 2021, doi: 10.1166/jon.2021.1805.
   [Scopus, SJR-0.389-Q2]

6. R. K. Chandrawat and V. Joshi, "Numerical Solution of the Time-Depending Flow of Immiscible Fluids with Fuzzy Boundary Conditions," **Int. J. Math. Eng. Manag. Sci**., vol. 6, no. 5, pp. 1315–1330, 2021, doi: 10.33889/ijmems.2021.6.5.079.
[Scopus, SJR-0.23-Q3]

7. R. K. Chandrawat and V. Joshi, "Numerical Study of Ion-Slip and Hall Effect on Couette Flow of Two Immiscible Micropolar and Micropolar Dusty Fluid (Fluid-Particle Suspension) with Heat Transfer," **Int. J. Heat Technol**., vol. 39, no. 4, pp. 1180–1196, 2021, doi: 10.18280/ijht.390416**.[Scopus, SJR-0.28-Q3]**

8. R. Katta, R. K. Chandrawat, and V. Joshi, "A Numerical study of the unsteady flow of two immiscible micropolar and Newtonian fluids through a horizontal channel using DQM with B-Spline basis function," in **Journal of Physics: Conference Series**, 2020, vol. 1531, no. 1, doi: 10.1088/1742-6596/1531/1/012090.**[Scopus, SJR-0.22-Q4]**

9. R. K. Chandrawat, V. Joshi, "Numerical study of the suction effect on unsteady Couette flow of two im-miscible micropolar and dusty fluids through a horizontal channel of porous plates with heat transfer" **FME Transactions** (First revision completed) **[Scopus, SJR-0.41-Q2]**

10. R. K. Chandrawat, V. Joshi, and O. A. Bég, H.J. Leonard "Computation of Ion-slip and Hall effects on two-dimensional interface evolution in the magnetohydrodynamic flow of immiscible dusty and pure (non-dusty) fluids with a modified differential quadrature method (DQM)," **ZAMM Zeitschrift fur Angewandte Mathematik und Mechanik** (under review)
[SCI-Impact factor 1.603, SJR-0.45- Q2]

11. R. K. Chandrawat, V. Joshi, D.Tripathi, S. Sadat, "Numerical Solutions of a time-dependent hydromagnetic Micropolar dusty fluid Between Parallel Plates through an inclined channel," **Pramana- Journal of Physics** (1st review done)
[SCI-Impact factor 2.219, SJR-0.51- Q2]

Conferences

1. Presented the paper titled “Numerical study of the suction effect on unsteady Couette flow of two im-miscible micropolar and dusty fluids through a horizontal channel of porous plates with heat transfer” in PROGRESSIVE RESEARCH IN INDUSTRIAL & MECHANICAL ENGINEERING (PRIME – 2021), 5th -7th August 2021, organized by Department of Mechanical Engineering National Institute of Technology Patna, India.

2. Presented the paper titled “Numerical simulation of interface tracking between two immiscible micropolar and dusty fluids” in INTERNATIONAL CONFERENCE ON FUNCTIONAL MATERIALS, MANUFACTURING, AND PERFORMANCES (ICFMMP-2021), 17-18 September 2021, Organized By Department Of Mechanical Engineering Lovely Professional University Punjab, India.

3. Presented the paper titled “A Numerical study of the unsteady flow of two immiscible micropolar and Newtonian fluids through a horizontal channel using DQM with B-Spline basis function,” in an international conference on RECENT ADVANCES IN FUNDAMENTAL AND APPLIED SCIENCES (RAFAS), November 2019, organized By School Of Chemical Engineering & Physical Sciences Lovely Professional University Punjab, India.